HETERODINUCLEAR CATALYSTS FOR CO_2/EPOXIDE COPOLYMERISATIONS

Gemma Trott



Trinity College

Department of Inorganic Chemistry

University of Oxford

April 2018

A thesis submitted in partial fulfilment of the requirements for the degree of Doctor of Philosophy in Chemistry.

For my parents,

‘Per ardua ad astra’

Declaration

The work presented in this thesis was conducted between October 2014 and April 2018 at Imperial College London and the University of Oxford. This is the work of the author unless otherwise stated.

The copyright of this thesis rests with the author and is made available under a Creative Commons Attribution Non-Commercial No Derivatives licence. Researchers are free to copy, distribute or transmit the thesis on the condition that they attribute it, that they do not use it for commercial purposes and that they do not alter, transform or build upon it. For any reuse or distribution, researchers must make clear to others the licence terms of this work.

Abstract

This thesis describes the preparation of new heterodinuclear catalysts for the selective copolymerisation of epoxides with CO_2 or anhydrides. The catalysts are based on a symmetrical diphenol-tetraamine macrocycle to prepare hetero-complexes coordinated to zinc and magnesium. The coordination sphere is completed by co-ligands derived from carboxylates. Optimisation of the synthesis is carried out to enable a straightforward route to new catalysts through the metathesis of a dibromide complex using a range of potassium salts. The characterisation of these complexes is explored using multinuclear NMR spectroscopy, mass spectrometry, infrared spectroscopy and elemental analysis.

The heterodinuclear complexes are highly active for the copolymerisation of cyclohexene oxide and CO_2, under atmospheric pressures [TOF = 645 h^{-1}, 120 °C, 0.1 mol%, 1 bar]. At higher temperatures (120 °C), excellent selectivity for poly(cyclohexene carbonate) formation (> 99 %) is maintained. The catalysts are highly active under low catalyst loadings, with excellent activities [TOF = 8830 h^{-1}, 120 °C, 0.01 mol%, 20 bar]. Telechelic polymers are produced upon addition of chain transfer agents, and the system is stable under aerobic conditions. A linear increase in molar mass with conversion shows the polymerisation is controlled. The copolymerisation of CO_2 with a range of epoxides is explored, allowing formation of poly(propylene carbonate), albeit with low selectivity [25 %, 60 °C, 0.01 mol%, 20 bar], and high molar mass poly(cyclopentene carbonate) in excellent (> 99 %) selectivity [TOF = 76 h^{-1}, 80 °C, 0.01 mol%, 20 bar].

The catalysts are also tested in the copolymerisation of phthalic anhydride with cyclohexene oxide to yield polyesters in excellent (> 99 %) selectivity. These catalysts are also highly active and well controlled [TOF = 289 h^{-1}, 100 °C, 0.13 mol%]. A range of anhydrides were tested, including succinic anhydride, glutaric anhydride and diphenic anhydride, which generally show high selectivity, although a variation in catalytic activity is observed.

Kinetic studies are carried out to probe the rate equation for the copolymerisations of CO_2 and phthalic anhydride, each with cyclohexene oxide. For the copolymerisation of phthalic anhydride and cyclohexene oxide, the data suggests a zero order dependence on anhydride and first order dependence on catalyst and epoxide. The rate equation determined for the copolymerisation of CO_2 and cyclohexene oxide suggests a first order dependence on catalyst and epoxide, with a zero order dependence on CO_2 pressure, and is in line with previous studies on similar systems. Computational analysis, applying density functional theory, shows that the previously hypothesised homodinuclear 'chain-shuttling' mechanism could be plausible for the analogous heterodinuclear systems.

Acknowledgements

Firstly, I would like to thank my supervisor, Professor Charlotte Williams, for her continued guidance and encouragement. I will always be extremely grateful for the opportunity to carry out my DPhil in your group, as well as the honour to teach back at Trinity College. Your constant belief in me and the advice you've given, both professionally and personally, have always been a great comfort.

I am indebted to all the staff who have helped me run analysis over the years. Thank you to Dr Lisa Haigh, Dr Peter Haycock and Dr Andrew White at Imperial College London, Dr Nick Rees and Dr Chris Durr at the University of Oxford, and Stephen Boyer at London Metropolitan University.

I have been lucky enough to work with a team of incredibly gifted post-docs, all of whom have taught me so much. Giulia, Andrés, Chris, Anish, Seb, Leti, Sumesh, Guun and Frank, it has been an absolute pleasure to work with you all. Special thanks go to Charles for persisting with my inability to grasp computational chemistry – your patience is endless! It is clear to me that I would not have got far without the unwavering support and reassurance of Jenni and PJ. You have both guided me from day one and I am eternally grateful for all your professional direction. Most importantly though, I will treasure all the laughter we have shared and your life-long friendship.

Thank you to every member of the group, past and present, who has made the tough days in the lab that little bit easier. I will remember singing and dancing in the lab, the pub trips, and all the tea breaks very fondly. I wish Alice, Arnaud, Arron, Dom, Jameel,

Shyeni, Charlie, Ni, Tim, Tom, Peck, Greg, Saïd, and every other student, the best in the future. Thank you for all the memories.

A huge thank you to Becca, Floss and Tom for making a wonderful home for us at Byam street – it was such a happy place for me. Your continued encouragement and friendship is forever acknowledged. Katie, Chris and Sarah (and now Oliver!), thank you for making my return to Oxford feel like home. I am grateful to all my other friends who have supported me during, and long before, my doctorate.

Calvin, I have been continually astounded by your kindness and understanding throughout this whole process. I can never put into words how grateful I am for your sacrifices and all the times you made me laugh. For everything you do, thank you.

I am indebted to my family in too many ways to mention. But I am thankful for my grandparents, who always show an interest in what I'm up to, even if my attempts to explain things fall short! Kirsty, thank you for always being there for me and cheering me up. And finally, I owe everything to my incredible parents. Thank you for your enduring support throughout this (very) long journey. You are an inspiration and have taught me everything about sacrifice, hard work and picking yourself back up again. This is for you both.

Thank you all for believing in me.

Abbreviations

AGE	Allyl Glycidyl Ether
Ar	Aryl
ATR-IR	Attenuated Total Reflectance Infrared
BDI	β-Diiminate
cat	Catalyst
CHC	Cyclohexene Carbonate
CHD	Cyclohexane-1,2-diol
CHE	Cyclohexene Anhydride
CHDO	Cyclohexadiene Oxide
CHO	Cyclohexene Oxide
COSY	Correlated Spectroscopy
CPO	Cyclopentene Oxide
CTA	Chain Transfer Agent
C_v	Coefficient of Variation
CXO	3,4-Dioxaepoxide
$Đ$	Dispersity
DABCO	1,4-Diazabicyclo[2.2.2]octane
DCM	Dichloromethane
DEC	Diethyl Carbonate
DFT	Density Functional Theory

$\Delta G^{\dagger}$	Gibbs Transition State Activation Energy
DGA	Diglycolic Anhydride
DMAP	4-Dimethylaminopyridine
DMC	Double Metal Cyanide
DMF	Dimethylformamide
DOSY	Diffusion Ordered NMR Spectroscopy
DP	Degree of Polymerisation
DPA	Diphenic Anhydride
DSC	Differential Scanning Calorimetry
EO	Ethylene Oxide
ESI	Electrospray Ionisation
Et	Ethyl
ETHF	3,4-Epoxytetrahydrofuran
EtOH	Ethanol
GA	Glutaric Anhydride
GPC	Gel Permeation Chromatography
HSQC	Heteronuclear Single Quantum Coherence Spectroscopy
IA	Itaconic Anhydride
IO	Indene Oxide
^{i}Pr	*Iso*-propyl
IR	Infrared

IRC	Intrinsic Reaction Coordinate
k_p	Propagation Rate Constant
k_{obs}	Observed Rate Constant
L	Ligand
LO	Limonene Oxide
M	Lewis Acidic Metal Centre
MA	Maleic Anhydride
MALDI	Matrix Assisted Laser Desorption Ionisation
Me	Methyl
MeOH	Methanol
MO	Menthene Oxide
MOMCl	Chloromethyl Methyl Ether
M_n	Number Average Molar Mass
MS	Mass Spectrometry
MW	Molecular Weight
^{n}Bu	*N*-Butyl
NA	Norbornene Anhydride
NCA	Norcantharidin
NMR	Nuclear Magnetic Resonance
Nu	Nucleophile
OAc	Acetate

OBz	Benzoate
OBz^R	*para*-Substituted Benzoate
PA	Phthalic Anhydride
PCHC	Poly(cyclohexene carbonate)
PCHPE	Poly(cyclohexene phthalate)
PCPC	Poly(cyclopentane carbonate)
PET	Poly(ethylene terephthalate)
PLA	Poly(lactic acid)
PO	Propylene Oxide
PPC	Poly(propylene carbonate)
ppm	Parts Per Million
PPN	Bis(triphenylphosphine)imine
PTFE	Polytetrafluoroethylene
PU	Polyurethane
ROCOP	Ring-Opening Copolymerisation
ROESY	Rotating Frame Overhauser Effect Spectroscopy
ROP	Ring-Opening Polymerisation
RPKA	Reaction Progress Kinetic Analysis
rpm	Revolutions Per Minute
SA	Succinic Anhydride
SEC	Size Exclusion Chromatography

SO	Styrene Oxide
^{t}Bu	*Tert*-butyl
TCE	1,12,2-Tetrachloroethane
T_d	Decomposition Temperature
TFA	Trifluoroacetate
T_g	Glass Transition Temperature
TGA	Thermogravimetric Analysis
THF	Tetrahydrofuran
TMEDA	N,N,N',N'-Tetramethylethylenediamine
TMS	Trimethylsilane
ToF	Time of Flight
TOF	Turnover Frequency
TON	Turnover Number
TFPP	5,10,15,20-tetrakis(pentafluorophenyl)porphyrin
TPP	5,10,15,20-tetraphenylporphyrin
vCHO	Vinyl Cyclohexene Oxide
X	Co-ligand

List of Figures, Tables and Equations

Chapter 1

Figure 1.1 Generic reactions for ring-opening polymerisation (ROP) and ring-opening copolymerisation (ROCOP) to prepare polycarbonates and polyesters.

Figure 1.2 Structures of commonly utilised epoxides and anhydrides.

Figure 1.3 General features of CO_2/epoxide copolymerisations.

Figure 1.4 Porphyrin catalysts for CO_2/epoxide copolymerisation.

Figure 1.5 Metal salen-derived catalysts for CO_2/epoxide copolymerisation.

Figure 1.6 Bifunctional salcy catalysts.

Figure 1.7 Bis(salen) complex with a bimetallic pathway proposed to operate in the absence of co-catalyst and monometallic binary reaction pathway operating in the presence of a co-catalyst.

Figure 1.8 BDI-derived catalysts for CO_2/epoxide copolymerisation.

Figure 1.9 General reactivity of β-diiminate complexes.

Figure 1.10 Bimetallic macrocyclic complexes active under atmospheric pressure of CO_2.

Figure 1.11 Proposed 'chain-shuttling' mechanism for catalyst **[$LZn_2(OAc)_2$]**.

Figure 1.12 A proline-derived dinuclear zinc catalyst (**E**) and an acyclic bis(anilido-aldimine) complex (**F**), active for CHO/CO_2 copolymerisation.

Figure 1.13 Structure and activity comparison for heterodinuclear and homodinuclear catalysts, based on a phenolic macrocycle, in the copolymerisation of CHO/CO_2 and CHO/PA.

Figure 1.14 A heterometallic catalyst, active for CO_2/CHO copolymerisation, based on a macrocyclic tris(salen) ligand, with zinc and rare earth metals.

Table 1.1 Summary of polycarbonates from ROCOP methods, showing a range of T_g values.

Table 1.2 Summary of polyesters from ROCOP methods, showing high T_g values.

Table 1.3 Selected catalysts for the copolymerisation of CHO/CO_2 at elevated pressures.

Table 1.4 Selected catalysts for the copolymerisation of PO/CO_2.

Table 1.5 Selected catalysts active under 1 bar pressure of CO_2 for the copolymerisation in neat CHO.

Chapter 2

Figure 2.1 Example of a ^{1}H NMR spectrum of a crude reaction mixture for the copolymerisation of CO_2 with CHO, in $CDCl_3$.

Figure 2.2 Example of a ^{1}H NMR spectrum of a crude reaction mixture for the copolymerisation of PA with CHO, in $CDCl_3$.

Figure 2.3 Example of a DOSY spectrum analysed in this thesis.

Figure 2.4 Example of a MALDI-ToF spectrum obtained for an α,ω-hydroxyl end-capped polycarbonate sample.

Figure 2.5 Representative *in situ* ATR-IR plot showing the change in absorbance vs. time for three vibrational modes corresponding to poly(cyclohexene carbonate) formation during the CHO/CO_2 copolymerisation.

Figure 2.6 Plot of $\ln([CHO]_0/[CHO])$ vs time for CHO/CO_2 copolymerisation.

Table 2.1 ^{1}H NMR chemical shifts for the reactant and products of CHO/CO_2 copolymerisation, in $CDCl_3$.

Table 2.2 ^{1}H NMR chemical shifts for the reactant and products of CHO/PA copolymerisation, in $CDCl_3$.

Equation 2.1 General method to calculate conversion for the copolymerisation of CO_2 and epoxides.

Equation 2.2 General method to calculate selectivity towards CO_2 linkages for the copolymerisation of CO_2 and epoxides.

Equation 2.3 General method to calculate selectivity towards polymer linkages for the copolymerisation of CO_2 and epoxides.

Equation 2.4 General method to calculate selectivity towards polycarbonate linkages for the copolymerisation of CO_2 and epoxides.

Equation 2.5 Calculation used to find TON.

Equation 2.6 Calculation used to find TOF.

Equation 2.7 Stokes-Einstein equation where D is the diffusion coefficient, k_B the Boltzmann constant, T the temperature, η the solvent viscosity, and r the hydrodynamic radius.

Equations 2.8 The relationship between diffusion coefficient and molecular weight, where A and α are intrinsic constants of the solvent.

Equations 2.9 Calculation of approximate molecular weight from diffusion coefficient.

Equations 2.10 Definition of molar mass parameters and polydispersity.

Equation 2.11 General rate equation for a catalytic reaction of reactants A and B.

Equation 2.12 Isolation of rate orders to determine the order in A, y.

Equation 2.13 Differential equation to determine the order in A.

Equation 2.14 Differential and integrated relationship for a zero order reaction.

Equation 2.15 Differential and integrated relationship for a first order reaction.

Equation 2.16 Differential and integrated relationship for a second order reaction, where $[A]_0$ is defined as the initial concentration of A.

Equations 2.17 Calculations for determining [CHO] at a given normalised absorbance intensity.

Equations 2.18 Calculations to determine C_v, where n_i is the individual data point, N is the total number of data points, μ is the mean and σ is the standard deviation.

Chapter 3

Figure 3.1 Previous attempt to synthesise the heterodinuclear catalyst **[LZnMg(OAc)$_2$]**, resulting in a mixture of **[LMg$_2$(OAc)$_2$]**, **[LZn$_2$(OAc)$_2$]** and **[LZnMg(OAc)$_2$]**.

Figure 3.2 The first synthesis of a pure heterodinuclear complex, **[LZnMgBr$_2$]**, with the macrocyclic scaffold, **LH$_2$**.

Figure 3.3 Representative comparison of heterodinuclear content by ^{1}H NMR spectroscopy, showing a sample of **[LZnMgBr$_2$]** with 92 % heterodinuclear content.

Figure 3.4 The synthesis of a series of heterodinuclear catalysts based on benzoate co-ligands.

Figure 3.5 Comparative ^{1}H NMR spectra in d_4-methanol of complex **[LZnMgBr$_2$]**, before salt metathesis (bottom), and **[LZnMg(OBz^{CF3})$_2$]**, after salt metathesis (top).

Figure 3.6 The synthesis of heterodinuclear catalysts based on acetate co-ligands.

Figure 3.7 ^{1}H NMR spectrum for complex **[LZnMg(OBz)$_2$]**, in d$_8$-THF solvent at 298 K, zoomed in on the ligand aromatic region.

Figure 3.8 ^{1}H NMR spectrum of **[LZnMg(OBz^{CF3})$_2$]** in d$_4$-methanol.

Figure 3.9 ^{1}H NMR spectrum of complex **[LZnMg(OBz^{OMe})$_2$]** in d$_8$-THF before (bottom) and after (middle) the addition of protic MeOH, as well as after all solvents have been removed (top).

Figure 3.10 Representation of possible equilibria in the presence of a binding donor, in this case MeOH.

Figure 3.11 ROESY NMR of **[LZnMg(OBz^{CF3})$_2$]** in d$_4$-methanol at room temperature.

Figure 3.12 Variable temperature ^{1}H NMR spectra of complex **[LZnMg(OBz^{CF3})$_2$]** in d$_4$-methanol, showing the aromatic region.

Figure 3.13 DOSY NMR spectrum of complex **[LZnMg(OBz^{F5})$_2$]** in d$_8$-THF.

Figure 3.14 ^{1}H NMR spectra for **[LZnMg(OBz^{CF3})$_2$]** in d$_4$-methanol before and after exposure to air overnight.

Figure 3.15 Infrared spectrum of **[LZnMg(OAc)$_2$]** taken in air from a powdered sample.

Figure 3.16 MALDI-ToF spectrum of **[LZnMg(OBz)$_2$]**, displaying an *m/z* peak of 759.4 assigned to **[LZnMg(OBz)]$^+$**.

Figure 3.17 ORTEP representation of a) **[LZnMg(O$_2$CPentyl)$_2$]**·MeOH and b) **[LZnMg(OBz^{CF3})$_2$]**·MeOH.

Chapter 4

Figure 4.1 Epoxide copolymerisations focussed on within this work.

Figure 4.2 MALDI-ToF mass spectrum of poly(cyclohexene carbonate) formed from catalyst **[LZnMg(OBz^{CF3})$_2$]** (0.1 mol%).

Figure 4.3 Plot of the polycarbonate M_n (black crosses) and M_w/M_n (blue squares) versus CHO conversion.

Figure 4.4 Comparison of Activities vs Hammett Parameters for catalysts **[LZnMg(OBz^R)$_2$]** in the copolymerisation of CO_2/CHO at 1:1000 catalyst:CHO loading at 80 °C.

Figure 4.5 Comparison of Activities vs terminal carboxylate stretching frequency for catalysts **[LZnMg(OBz^R)$_2$]** in the copolymerisation of CO_2/CHO at 1:1000 catalyst:CHO loading at 80 °C.

Figure 4.6 Range of epoxides tested for the copolymerisation with CO_2.

Figure 4.7 ^{1}H NMR spectrum of the crude reaction mixture for the copolymerisation of vCHO and CO_2, in $CDCl_3$, used to calculate the TON for the copolymerisation.

Figure 4.8 ^{1}H NMR spectrum of the crude reaction mixture for the copolymerisation of ETHF and CO_2, in $CDCl_3$ used to calculate the TON and selectivity for the copolymerisation.

Figure 4.9 ^{1}H NMR spectrum of the crude reaction mixture for the copolymerisation of CPO and CO_2 in $CDCl_3$ at 298 K, used to calculate the TON and selectivity for the copolymerisation.

Figure 4.10 a) Thermal Gravimetric Analysis for a sample of PCPC; b) Second heating cycle for the Differential Scanning Calorimetry plot, showing a glass transition temperature of 65.9 °C.

Figure 4.11 Plot of the polyester M_n (black crosses) and M_w/M_n (blue squares) versus PA conversion for **[LZnMg(OBz^{OMe})$_2$]**.

Figure 4.12 Comparison of Activities vs Hammett Parameters for catalysts **[LZnMg(OBz^R)$_2$]** in the copolymerisation of PA/CHO.

Figure 4.13 Range of anhydrides tested for the copolymerisation with CHO.

Table 4.1 CHO/CO_2 ROCOP Data for Catalysts **[LZnMgBr_2]**, **[LZnMg(OAc)$_2$]** and **[LZnMg(OBz^R)$_2$]** Under 1 bar Pressure of CO_2 at 80 °C.

Table 4.2 CHO/CO_2 ROCOP Data for Selected Catalysts Under 1 bar Pressure of CO_2 at 120 °C.

Table 4.3 Comparison of highly active catalysts under 1 bar pressure of CO_2 for the copolymerisation in neat CHO.

Table 4.4 CHO/CO_2 ROCOP Data for Chain Transfer Agents with catalyst **[LZnMg(OBz^{CF3})$_2$]**.

Table 4.5 CHO/CO_2 ROCOP Data under Aerobic Conditions for catalyst **[LZnMg(OBz^{OMe})$_2$]**.

Table 4.6 CHO/CO_2 ROCOP Data for Catalyst **[LZnMg(OBz^{CF3})$_2$]** Under 20 bar Pressure of CO_2.

Table 4.7 Selected catalysts for the copolymerisation of CHO/CO_2 at elevated pressures.

Table 4.8 Epoxide/CO_2 ROCOP Data for Catalyst **[LZnMg(OBz^{OMe})$_2$]** with a range of epoxides.

Table 4.9 CPO/CO_2 ROCOP Data for Catalyst **[LZnMg(OBz^{OMe})$_2$]** at 80 °C.

Table 4.10 CHO/PA ROCOP Data for **[LZnMgBr_2]** and **[LZnMg(OBz^R)$_2$]**.

Table 4.11 CHO/anhydride ROCOP Data for Catalyst **[LZnMg(OBz^{OMe})$_2$]** with a range of anhydrides.

Chapter 5

Figure 5.1 ATR-IR spectroscopic trace of the copolymerisation of CHO and CO_2.

Figure 5.2 Plots to determine the order in **[LZnMgBr_2]**.

Figure 5.3 Plot of activity (TOF) against pressure for catalyst **[LZnMgBr_2]**.

Figure 5.4 Graphical representation of the propagation pathway for the possible combinations of zinc and magnesium, within the dinuclear framework, with acetate co-ligands.

Figure 5.5 Plot to show a zero order decay from 10 – 99 % consumption of PA.

Figure 5.6 Plots to determine the order in **[LZnMgBr$_2$]** through ATR-IR spectroscopy.

Figure 5.7 Comparative plots for a series of fits for the order in **[LZnMgBr$_2$]** for the copolymerisation of PA and CHO.

Figure 5.8 Plots to determine the order in CHO through ATR-IR spectroscopy.

Table 5.1 Comparison of the coefficient of variation, calculated from the values of t[cat]^x at 99 % PA conversion, to determine the reaction order in catalyst for the copolymerisation of PA and CHO.

Chapter 6

Figure 6.1 General formation of block copolymers from ROP/ROCOP 'switch' catalysis.

Figure 6.2 Attempted synthesis of **L^{1}H$_2$**.

Figure 6.3 Proposed catalyst structure for a trimetallic ligand.

Figure 6.4 Proposed synthesis of **L^{2}H$_2$**.

Figure 6.5 ^{1}H NMR spectrum of **S6** in d_3-MeCN.

Table of Contents

Declaration....3

Abstract....4

Acknowledgements....6

Abbreviations....8

List of Figure, Tables and Equations....13

Chapter 1 – Introduction....27

1.1. Polymers....28

1.1.1. Motivation for sustainable materials....28

1.1.2. Current industrial routes to oxygenated polymers....28

1.1.3. Ring-opening copolymerisation....29

1.1.3.1. Overview....29

1.1.3.2. Monomer scope....31

1.1.3.3. Polycarbonate thermal properties....33

1.1.3.4. Polyester thermal properties....34

1.2. General Features of CO_2/Epoxide Copolymerisations....35

1.2.1. Catalyst requirements....35

1.2.2. Mechanistic considerations....35

1.3. Catalysts for the Copolymerisation of CO_2 and Epoxides....38

1.3.1. Heterogeneous catalysts....38

1.3.2. Porphyrin catalysts....39

1.3.3. Salen catalysts....40

1.3.3.1. Tethered systems....42

1.3.3.2. Dinuclear Salens....44

1.3.4. β-Diiminates....44

1.3.5. Macrocyclic catalysts....46

1.3.6. Other dinucleating ligands....49
1.3.7. Main group catalysis....50
1.3.8. Heteronuclear catalysts....51
1.3.9. Summary....53
1.4. Project Aims....56
1.5. References....57
Chapter 2 – Methodology....61
2.1. NMR Spectroscopy....62
2.1.1. Characterisation of polymers....62
2.1.2. Two dimensional (2D) NMR characterisation techniques....66
2.1.3. Diffusion ordered NMR spectroscopy (DOSY)....66
2.2. Mass Spectrometry....68
2.3. Size Exclusion Chromatography (SEC)....70
2.4. Thermogravimetric Analysis....71
2.5. Differential Scanning Calorimetry....71
2.6. Kinetic methods....72
2.6.1. Polymerisation kinetics....72
2.6.2. Monitoring copolymerisation reactions....74
2.6.3. Treatment of errors....76
2.7. Computational Methods....77
2.8. References....78
Chapter 3 – Synthesis and Structural Studies of Magnesium and Zinc Heterodinuclear Complexes....79
3.1. Introduction....80
3.1.1. Previous synthesis of a heterodinuclear catalyst....80
3.1.2. Aims of this chapter....81
3.2. Synthesis of **[LZnMgBr$_2$]**....82

3.3. Synthesis of Heterodinuclear Catalysts 83
3.3.1. General synthesis of complexes **[LZnMgX$_2$]** 83
3.3.2. Benzoate derivatives 84
3.3.3. Acetate derivatives 86
3.4. NMR Spectroscopy Studies 87
3.4.1. Role of solvent 87
3.4.2. Variable temperature ^{1}H NMR study 93
3.4.3. DOSY NMR studies 95
3.4.4. Air stability tests 95
3.5. IR Spectroscopy 96
3.6. Mass Spectrometry 97
3.7. Crystallography 98
3.8. Conclusions and Future Work 101
3.9. References 102
Chapter 4 – Heterodinuclear Catalysts for Copolymerisations 103
4.1. Introduction 104
4.1.1. Epoxide copolymerisations 104
4.1.2. Chapter aims 105
4.2. Low Pressure CO_2/CHO Copolymerisations 106
4.2.1. Activity under 1 bar pressure of CO_2 106
4.2.2. Activity discussion 108
4.2.3. Effect of chain transfer agents 109
4.2.4. Catalysis under aerobic conditions 111
4.2.5. Effect of co-ligand 111
4.3. High Pressure CO_2/CHO Copolymerisations 115
4.3.1. Activity 115
4.3.2. Discussion 115

4.4. Alternative Epoxides 116
4.4.1. Activity scope 116
4.4.2. Polymer properties 121
4.5. PA/CHO Copolymerisations 122
4.6. Alternative Anhydrides 125
4.7. Conclusions and Future Works 127
4.8. References 128
Chapter 5 – Mechanistic Investigations of a Heterodinuclear Catalyst in Copolymerisation Reactions 131
5.1. Introduction 132
5.1.1. Previous investigations into related systems 132
5.1.2. Aims of the chapter 132
5.2. Rate Equation for CO_2/CHO Copolymerisation 133
5.2.1. Order in epoxide 133
5.2.2. Order in catalyst 134
5.2.3. Order in CO_2 135
5.2.4. Discussion 136
5.3. Computational studies for CO_2/CHO Copolymerisation 138
5.3.1. Calculated reaction pathways for a heterodinuclear catalyst 138
5.3.2. Discussion 141
5.4. Rate Equation for PA/CHO 142
5.4.1. Determining the rate equation for PA/CHO copolymerisation 142
5.4.2. Order in PA 143
5.4.3. Order in catalyst 143
5.4.4. Order in epoxide 146
5.4.5. Discussion 147
5.5. Conclusions 148

5.6. References 149
Chapter 6 – Conclusions and Outlook 150
6.1. Conclusions 151
6.2. Outlook 153
6.2.1. Formations of polyols for polyurethanes 153
6.2.2. Production of block copolymers 154
6.2.3. Catalyst modifications 155
6.2.3.1. Thiol-derived macrocycle 156
6.2.3.2. Extended naphthalene-derived macrocycle 158
6.2.4. Overview 160
6.3. References 161
Chapter 7 – Experimental Procedures and Data 162
7.1. Materials 163
7.1.1. General materials 163
7.1.2. Epoxide synthesis and purification 163
7.1.3. Anhydride purification 164
7.2. Instrumentation 164
7.3. Potassium Salt Synthesis 166
7.3.1. **[KOBz^{OMe}]** 166
7.3.2. **[KOBz^{CF3}]** 166
7.3.3. **[KOBz^{NO2}]** 167
7.3.4. **[KOBz^{NMe2}]** 168
7.3.5. **[KOBz^{F}]** 168
7.3.6. **[KOBz^{F5}]** 169
7.3.7. **[KO$_2$CPentyl]** 170
7.4. Catalyst Synthesis 171
7.4.1. Synthesis of catalyst **[LMgZnBr$_2$]** 171

7.4.2. General procedure for synthesis of carboxylate-based catalysts 172
7.4.3. Complex **[LMgZn(OBz)$_2$]** 173
7.4.4. Complex **[LMgZn(OBz^{OMe})$_2$]** 174
7.4.5. Complex **[LMgZn(OBz^{CF3})$_2$]** 175
7.4.6. Complex **[LMgZn(OBz^{NO2})$_2$]** 176
7.4.7. Complex **[LMgZn(OBz^{NMe2})$_2$]** 177
7.4.8. Complex **[LMgZn(OBz^{F})$_2$]** 178
7.4.9. Complex **[LMgZn(OBz^{F5})$_2$]** 179
7.4.10. Complex **[LMgZn(OAc)$_2$]** 180
7.4.11. Complex **[LMgZn(O$_2$CPentyl)$_2$]** 181
7.5. Copolymerisation of CO_2 and Epoxides 182
7.5.1. Low pressure CO_2/epoxide copolymerisation 182
7.5.2. *In situ* ATR-IR monitoring of CO_2/CHO at low pressures 182
7.5.3. High pressure CO_2/CHO copolymerisation 183
7.6. Copolymerisation of Anydrides and CHO 183
7.6.1. Copolymerisation of PA/CHO 183
7.6.2. *In situ* ATR-IR monitoring of PA/CHO 184
7.6.3. Other anhydride/CHO copolymerisations 184
7.7. References 184
Appendices 185
Appendix A: DOSY NMR Spectra 186
Appendix B: Crystallographic Data 190
Appendix C: SEC Analysis Plots 193
Appendix D: ATR-IR Spectroscopy Plots 203
Appendix E: Concentration vs Time Plots for Table 4.10 231
Appendix F: IRC Plot 232
Appendix References 232

Chapter 1

Introduction

This chapter gives a general introduction into the motivation for synthesising new aliphatic polycarbonates and polyesters, through ring-opening copolymerisation routes. Previous developments in the field of CO_2/epoxide copolymerisation are detailed, including an overview on catalyst classes which are active for this process. The mechanism for CO_2/epoxide copolymerisation is also introduced and the overall aims of the thesis detailed.

1.1. Polymers

1.1.1. Motivation for sustainable materials

The global consumption of polymer materials is currently unsustainable and there remains an ever increasing need to find alternative solutions in production, recycling and waste disposal.[1,2]

The requirement for materials which are durable will continue; therefore, one option to improve sustainability of these products is in their sourcing from renewable resources. Almost all current polymeric materials are derived from crude oil, but in future alternative starting materials should enable substitution to produce both existing and new materials.[3-6] Plant based feedstocks, such as terpenes from waste food streams (like citrus peel) and starch (from sugars or corn starch), have been investigated as sources of monomers.[3,7-10]

Another possible monomer to consider for polymer production is carbon dioxide. The utilisation of carbon dioxide is a desirable means to add value to a significant industrial waste stream.[11] It should be clearly noted here that the use of carbon dioxide in the production of chemicals, including polymers, is unlikely to significantly reduce global atmospheric CO_2 levels. However, it can reduce greenhouse gas emissions associated with polymer production and thus make a meaningful impact on improving the sustainability of this process.[12]

1.1.2. Current industrial routes to oxygenated polymers

Oxygenated polymers, based on polycarbonates and polyesters, are an important class of materials and are generally made through condensation reactions industrially.[13]

Polycarbonates are applied in adhesives, clothing, construction and packaging, with high molar mass polycarbonates used in the production of rigid plastics and films.[14-17] Polycarbonates are currently produced commercially through the copolymerisation of phosgene and bisphenol A. However, these reagents are both highly toxic and petrochemically derived, therefore this process demands more sustainable alternatives.[18]

Polyesters are a major sub-sector of polymers: they account for 70 % of global fibre production, as well as being a leading packaging material.[19] The most widely utilised polyester is the semi-aromatic poly(ethylene terephthalate) (PET) which is generally synthesised by step-growth condensation reactions.[13] This synthetic strategy tends to avoid unwanted cyclisation reactions, however lacks the high levels of control required for the production of sophisticated polymer architectures, such as block copolymers.[5,20,21] Molar masses are usually broad, precise stoichiometries of monomers are required and wasteful small molecules are produced as a by-product of the polycondensation reactions. A major disadvantage in this method is the need to drive the reaction to high conversions to form polymers of high molar mass.

The current commercial polycarbonate and polyester materials often contain aromatic groups to improve material and physical properties. However, aliphatic analogues currently have fewer industrial uses and are primarily explored in this work.

1.1.3. Ring-opening copolymerisation

1.1.3.1. Overview

One well-established route to polyester and polycarbonate materials is through the ring-opening polymerisation (ROP) of lactones or cyclic carbonates, respectively

(Figure 1.1).[13,22] A particularly interesting polyester, synthesised on an industrial scale, is poly(lactic acid) (PLA), which is made through the ROP of lactide.[23,24] PLA materials are used in packaging as well as in medical applications.[25,26] Aliphatic polyesters like PLA are of interest due to their biocompatibility and biodegradability.[27-29]

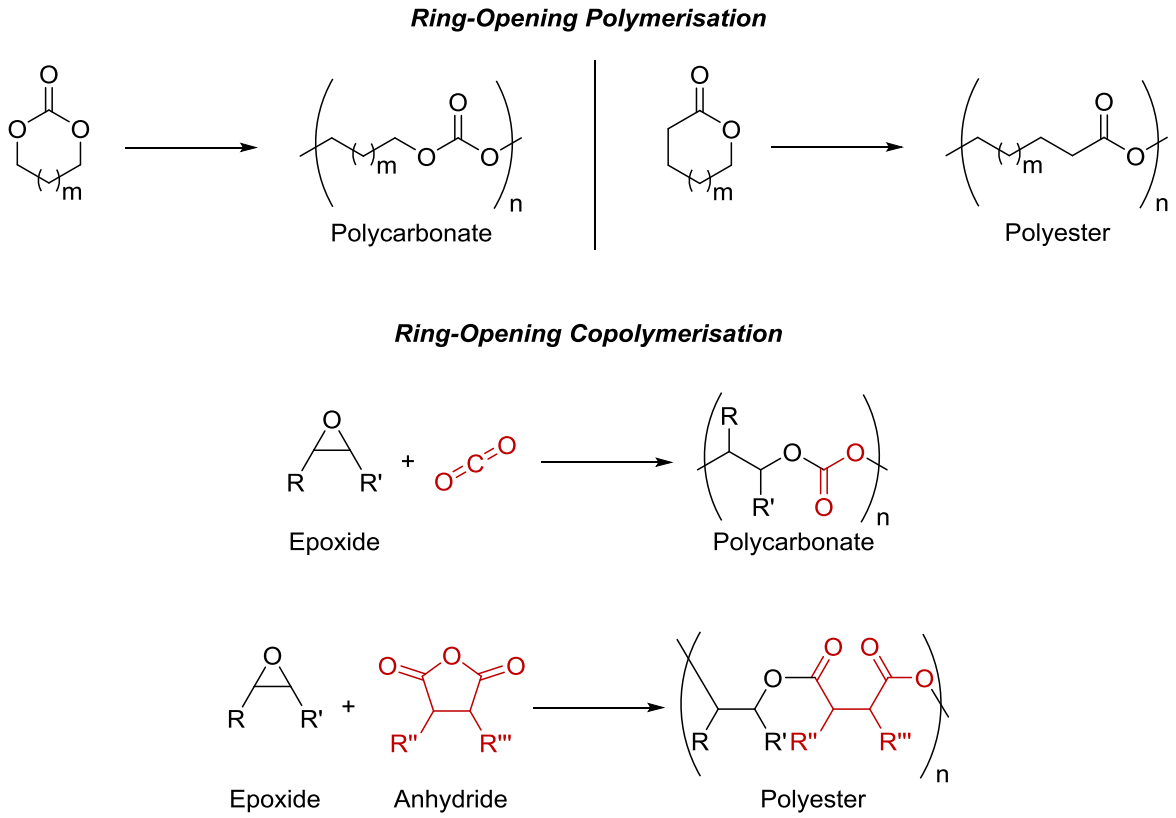


Figure 1.1 – Generic reactions for ring-opening polymerisation (ROP) and ring-opening copolymerisation (ROCOP) to prepare polycarbonates and polyesters.

Although ROP routes often show excellent levels of control, the range of materials available can be limiting. Notably, installing aromatic groups in the polymer is a challenge and changing the ring strain of the cyclic monomers can remove the thermodynamic driving force of the polymerisation.[22]

The ring-opening copolymerisation (ROCOP) of epoxides with CO_2 or anhydrides overcomes many of these problems and has proven to be an effective route to a wide

range of polymers (Figure 1.1).[30-41] Facile monomer substitution can lead to a wide range of materials, including the introduction of aromaticity.[30-41]

A study on the life cycle assessment for the production of polyethercarbonate polyols shows that, by incorporating up to 20 weight % carbon dioxide, a 19 % reduction in greenhouse gas emissions is predicted, in comparison to conventional polyether polyols.[12] It has also been shown that CO_2 from industrial waste streams can be used in the ROCOP with epoxides, to form aliphatic polycarbonates.[11] These low molar mass polyols can be implemented as precursors to highly sought-after polyurethane materials.[42,43]

1.1.3.2. Monomer scope

The ring-opening copolymerisation of epoxides/CO_2 and epoxides/anhydrides provides a straightforward route to a wide range of potential polymer properties by varying the functionality of the monomers (Figure 1.2).[5,37,44-46] This can be important in tailoring polymer properties for different uses, e.g. rigidity, elasticity, thermal stability etc. Academic literature has primarily explored the use of cyclohexene oxide (CHO) and propylene oxide (PO) in the copolymerisation with CO_2, to form aliphatic carbonates.[47] However, aromaticity can be installed through application of monomers such as styrene oxide (SO) or indene oxide (IO).[4,48] Semi-aromatic polyesters are widely formed through the copolymerisation of epoxides with phthalic anhydride (PA).[44]

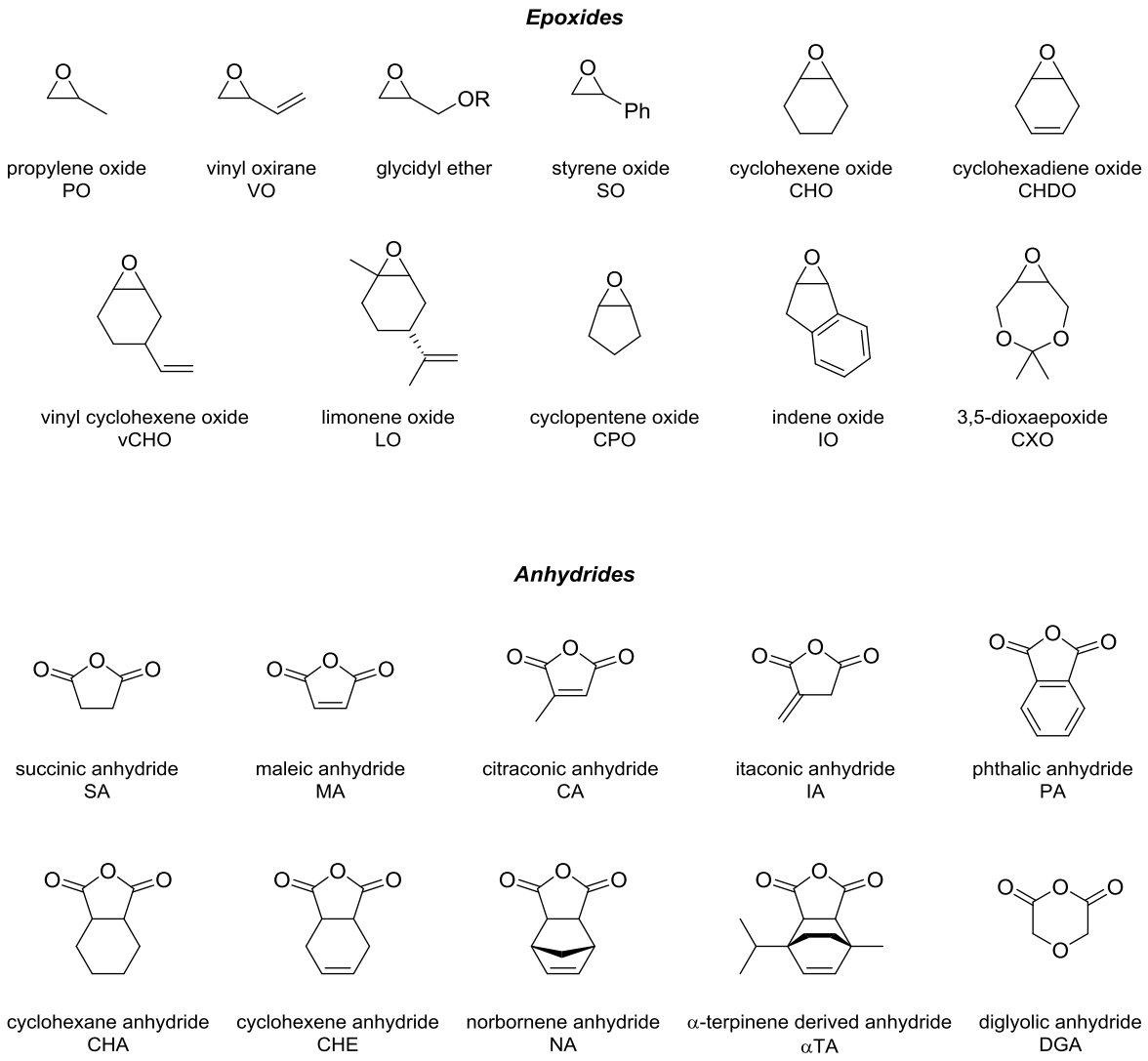


Figure 1.2 – Structures of commonly utilised epoxides and anhydrides.[44,46]

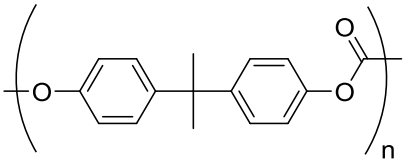
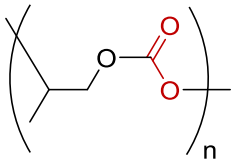
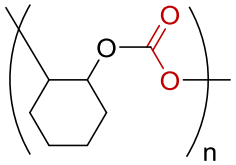
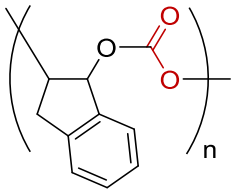
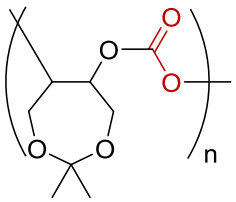
The ability to alter the polymers further through post-modification can also be achieved if monomers are selected with the required functionality.[46] This is often achieved through the incorporation of double bonds into the polymer, with monomers such as cyclohexadiene oxide (CHDO) or vinyl cyclohexadiene oxide (vCHO), which can then be transformed through thiol-ene click, or other, reactions.[49]

One of the more coveted areas of ROCOP design is the utilisation of biorenewable epoxides, such as terpene-based monomers like limonene oxide (LO).[30] Their use in ROCOP with CO_2 would result in a polymer which is 100 % bioderived.[4]

1.1.3.3. Polycarbonate thermal properties

The aromatic polycarbonate produced industrially from bis(phenol) A and phosgene shows an extremely high T_g value of 154 °C, which is currently unobtainable through ROCOP methods (Table 1.1).[48] Implementation of PO or CHO in ROCOP with CO_2 yields aliphatic polymers which show low (30 – 115 °C) T_g values. Therefore, it is necessary to increase the rigidity of the polycarbonate backbone, if higher thermal properties are required. High T_g values have been observed with semi-aromatic polycarbonates, such as poly(indene carbonate) (134 °C), or isotactic copolymers from 3,5-dioxaepoxides (140 °C). [48,50,51]

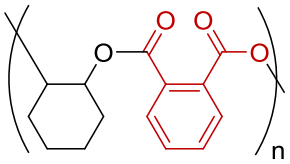
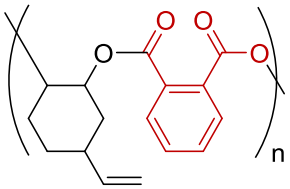
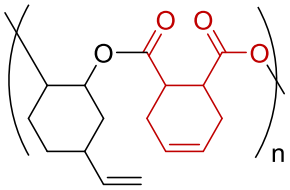
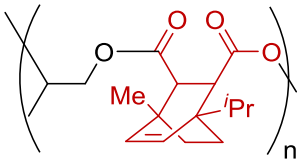
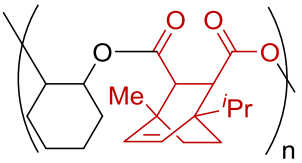
Table 1.1 – Summary of polycarbonates from ROCOP methods, showing a range of T_g values.

Entry	Polymer Structure	Monomers	T_g (°C)
1		Bis(phenol) A/ phosgene	154
2[14,52]		PO/CO_2	30-40
3[14,52,53]		CHO/CO_2	80-115
4[48,50]		IO/CO_2	134
5[51]		CXO/CO_2	140

1.1.3.4. Polyester thermal properties

Varying the monomer combinations in ROCOP of epoxides and anhydrides can lead to a range of physical polymer properties. Of particular importance is the flexibility of the monomers, with rigid polymers requiring a T_g over 90 °C. Some examples of highly rigid aliphatic polyesters are shown in Table 1.2.

Table 1.2 – Summary of polyesters from ROCOP methods, showing high T_g values.

Entry	Polymer Structure	Monomers	T_g (°C)	M_n (g·mol^{-1})
1[54]		CHO/PA	146	13 200
2[54]		vCHO/PA	128	22 100
3[55]		CHO/CHE	95	10 000
4[56]		PO/αTA	109	55 000
5[40]		CHO/αTA	184	8 900

Polyesters with a T_g below 0 °C have use in block formation for thermoplastic elastomers.[57] These low T_g polyesters can be made with highly flexible backbones or through the addition of long aliphatic side chains. Many monomers are suitable for installing these flexible chains; for example, the ROCOP of diglycolic anhydride (DGA) and propylene oxide (PO) yields a material with a T_g of -2 °C.[37]

1.2. General Features of CO_2/Epoxide Copolymerisations

1.2.1. Catalyst requirements

Although significant progress in this field has been made, since its discovery in the 1960's, there remains the challenge to produce new homogeneous catalysts which are highly active, whilst maintaining high selectivities, to allow this process to become industrially viable.[4,58] The polymers produced need to be well controlled with narrow, monomodal molar mass distributions.

Ideally catalysts would also be cheap, safe and straightforward to synthesise on a large scale, as well as being robust to impurities and high temperatures. Most catalysts for the copolymerisation of CO_2 and epoxides consist of an active metal centre, bound within a ligand framework. They must also have an initiator present which can be bound to the metal or added as a co-catalyst.

1.2.2. Mechanistic considerations

First the catalyst must undergo initiation. The initiating group is generally a metal-halide, -alkoxide or -carboxylate bond which ring-opens an equivalent of epoxide, forming a metal-alkoxide (Figure 1.3).[47] The formed intermediate then inserts a molecule of CO_2, entering the propagation cycle.

The metal-carbonate propagating species can then sequentially ring-open an epoxide and insert CO_2, switching from a metal-carbonate to a metal alkoxide and back again. The process continues until the epoxide feedstock is depleted by diffusion limitations, consumption, or through the addition of a quenching reagent which removes the growing polymer chain from the metal irreversibly.

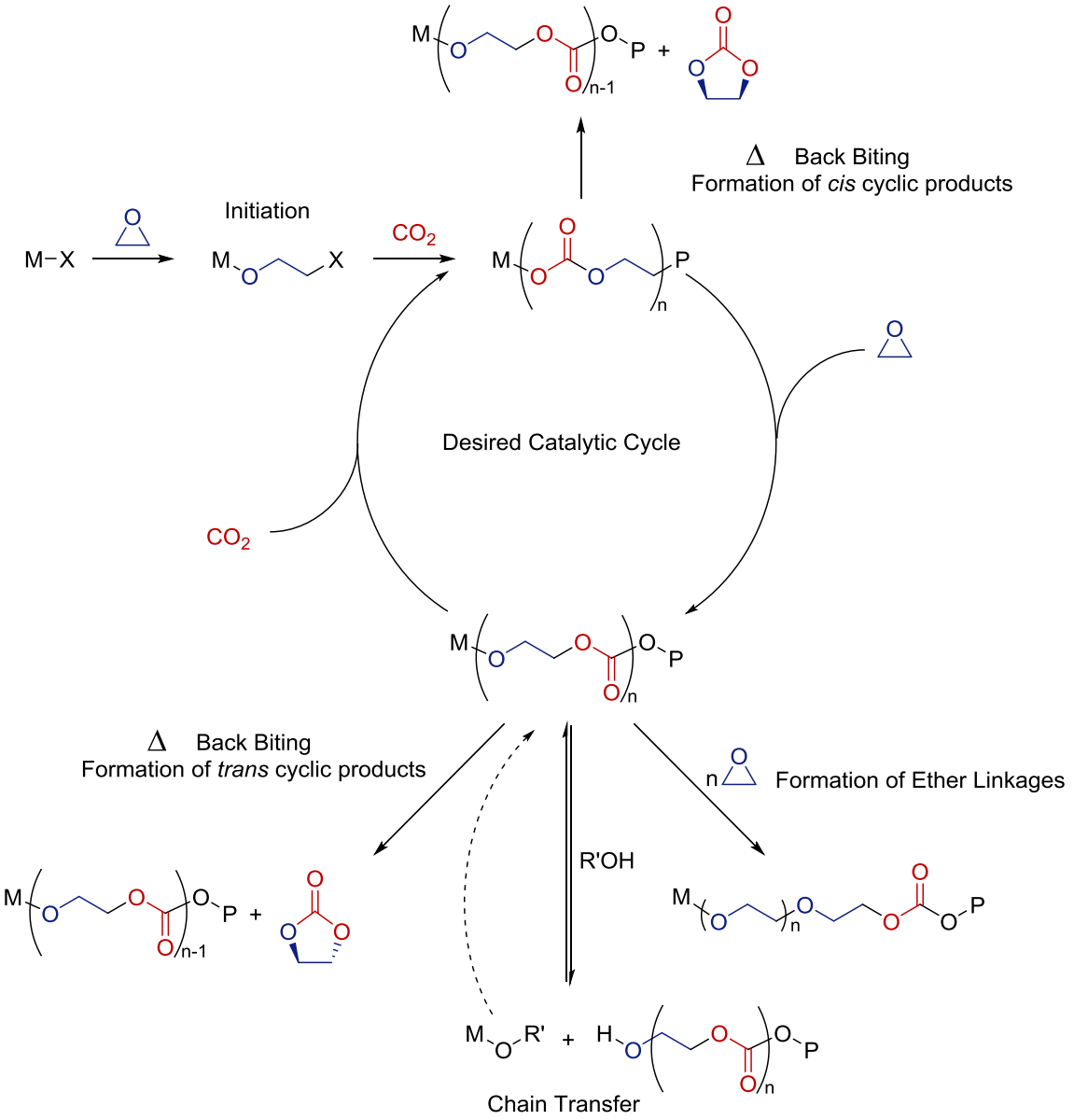


Figure 1.3 – General features of CO_2/epoxide copolymerisations.

Side reactions include the formation of polyether linkages, cyclic products or chain transfer processes. If the propagating metal-alkoxide ring-opens an epoxide, rather than inserting CO_2, an ether linkage forms (Figure 1.3). This process maintains a metal-alkoxide bond which can re-enter the catalytic cycle by inserting CO_2, or continue forming more ether linkages. The growing polymer chain can undergo a back-biting reaction to form a stable five-membered cyclic carbonate (Figure 1.3). This step essentially removes a single polymer unit, reforming the polymer chain with the degree of polymerisation reduced by one (DP-1). Cyclic carbonates are the

thermodynamic product of this reaction and are more likely to form as the reaction temperature is increased. It is therefore a challenge to balance high selectivity for polymer formation, whilst maximising rate.

Protic sources can react with the polymer, forming a free hydroxyl-end capped polymer, and installing a new metal-oxygen initiator (Figure 1.3). If this process is rapid and reversible then narrow dispersity (*Đ*) is maintained. The newly formed initiator can then re-enter the catalytic cycle, growing another polymer chain. This process is known as chain transfer.

This chain transfer process can result in the polymers showing bimodality in epoxide/CO_2 copolymerisation with a range of catalysts.[59-62] Small amounts of residual water can ring-open the epoxide to form diols; polymerisations with bifunctional chain transfer agents have been previously studied by our group.[63,64] In a key study, Darensbourg reported cobalt-salen catalysts preferentially catalyse the hydrolysis of both CHO and PO, forming diols before any copolymerisation reactions occur.[65]

These diols act as a chain transfer agent and result in a mixture of polymers with dihydroxyl end-groups as well as a distribution of polymers which are end-capped with a hydroxyl and the catalyst-derived initiator. This has been observed for several different catalyst classes.[59-61] Catalysts in our group have been developed where the initiators are formed *in situ*, from protonolysis of a metal-aryl bond. This protonolysis installs the epoxide-derived diol on the catalyst which then acts as an initiator, producing monomodal telechelic polymers.[64,66]

Many mechanisms have been proposed for different homogeneous catalyst classes. These are often dependent on the presence and identity of co-catalysts and the ability

of the catalysts to undergo either an intramolecular or intermolecular bimetallic pathway.

1.3. Catalysts for the Copolymerisation of CO_2 and Epoxides

1.3.1. Heterogeneous catalysts

The first report of CO_2/epoxide copolymerisation came from Inuoe in 1969 showing that a mixture of $ZnEt_2$-H_2O and propylene oxide forms polycarbonates under 50-60 bar of CO_2 at 80 °C.[58] This work led to other dialkyl zinc (ZnR_2) reagents, mixed with protic sources, being tested for copolymerisation.[67,68] However, these simple systems showed poor activity, high amounts of ether linkages and produced unwanted side products such as cyclic carbonates.

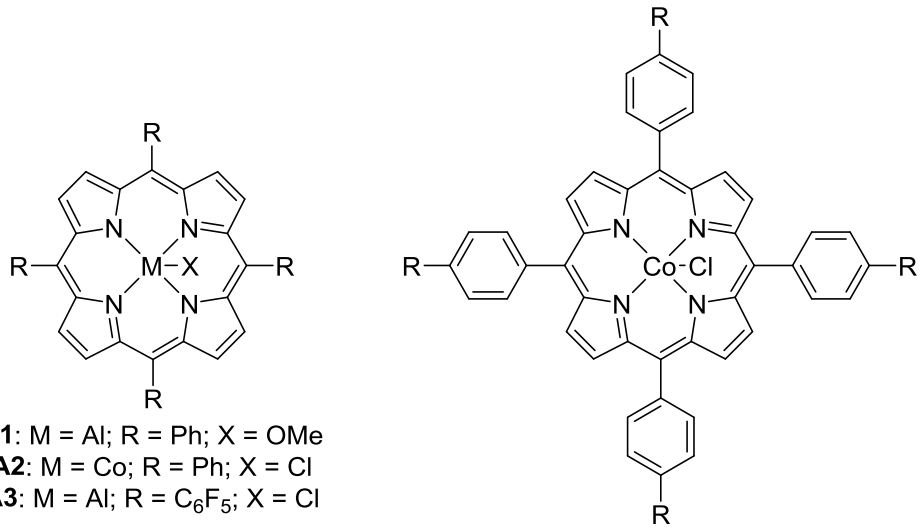
Zinc glutarates were shown to have increased activity to the copolymerisation of CO_2 and propylene oxide.[69-71] It was found that ethylsulphinate groups or increasing the crystallinity of the catalyst significantly improved the activity of polymerisation.[69,71]

A series of double metal cyanide catalysts based on $Zn_3(CoCN_6)_2$ were prepared from reacting $ZnCl_2$ with $K_3(CoCN_6)_2$ before suspending the catalyst in a range of complexing agents.[72] This class of catalysts showed much higher activities than previous heterogeneous catalysts but formed polymers with poor incorporation of carbon dioxide (< 90 %).[72,73] Covestro are already applying these catalysts in the production of polycarbonate materials.[74,75]

Due to relatively low levels of selectivity for polycarbonate formation with heterogeneous systems, the academic literature has focussed on homogeneous catalysts in the last decade. This also normally allows more detailed mechanistic understanding to be extracted from the copolymerisation. This thesis is exclusively concerned with homogeneous catalysis.

1.3.2. Porphyrin catalysts

In 1983 Inoue reported the first example of a homogeneous catalyst for CO_2/epoxide copolymerisation with an aluminium 5,10,15,20-tetraphenylporphyrin (TPP) catalyst (**A1**) (Figure 1.4).[76] Cobalt TPP catalysts (**A2**) were also shown to be active for CHO/CO_2 copolymerisation with a DMAP co-catalyst, resulting in high (> 99 %) polycarbonate selectivity under mild conditions [21 h^{-1}, 80 °C, 0.2 mol%, 50 bar, CHO 7 M in DCM].[77,78] Chisholm has found that 5,10,15,20-tetrakis(pentafluorophenyl)porphyrin (TFPP) catalysts (**A3**) were active for PO/CO_2 copolymerisation in the presence of a co-catalyst, giving high selectivities (up to 98 %) [3 h^{-1}, 25 °C, 0.7 mol%, 50 bar, PO 10 M in $CDCl_3$].[79-81] Rieger has shown that the selectivity towards poly(propylene carbonate) (PPC) can be tuned by changing the ligand substituents in a series of cobalt chloride porphyrin complexes (**A4**-**7**).[82] Catalysts **A4**-**6** were selective for PPC production (up to 90 %) [103 h^{-1}, 30 °C, 0.05 mol%, 30 bar, PO neat], whilst **A7** gave propylene carbonate [11 h^{-1}, 25 °C, 0.05 mol%, 30 bar, PO neat].[82]



A1: M = Al; R = Ph; X = OMe
A2: M = Co; R = Ph; X = Cl
A3: M = Al; R = C_6F_5; X = Cl

A4: R = H
A5: R = OMe
A6: R = O^{i}Pr
A7: R = NO_2

Figure 1.4 – Porphyrin catalysts for CO_2/epoxide copolymerisation.

1.3.3. Salen catalysts

Catalysts based on salen ligands have been widely studied and yield some of the most active catalysts for CO_2/epoxide copolymerisation (Figure 1.5). They have been comprehensively reviewed in the academic literature.[14,45,83] In 2002, Darensbourg reported the first example of a catalyst with a salen ligand, based on chromium, which was air stable, chiral and gave excellent selectivity (> 99 %) for carbonate linkages.[84] Since this discovery, many related catalysts have shown significant advances to yield highly active catalysts.[16,52,83-87] Notably, there are many catalysts in this class which are active for PO/CO_2 copolymerisation – **B2** with a PPNCl co-catalyst produces PPC, with 99 % carbonate and 93 % copolymer selectivity, at a TOF of 192 h^{-1} [60 °C, 0.05 mol%, 34 bar, PO neat].[88]

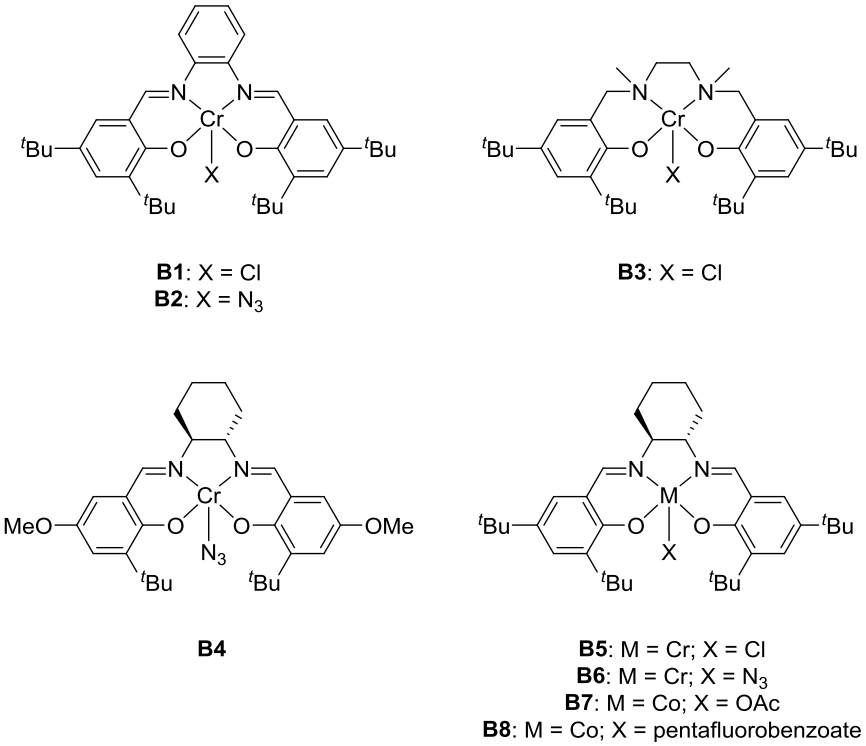


Figure 1.5 – Metal salen-derived catalysts for CO_2/epoxide copolymerisation.

Salans have amine functionality instead of imine functionality, allowing greater flexibility of the ligand, with possible conformational changes, and changes in basicity. High selectivities were observed for **B3** towards CO_2/PO [21 h^{-1}, 25 °C, 15 bar, PO neat] and CO_2/CHO copolymerisation [405 h^{-1}, 60 °C, 0.04 mol%, 34 bar, CHO neat].[89]

Darensbourg reported very high activities for CHO/CO_2 copolymerisation with a chromium salcy complex with [PPN]Cl co-catalyst (**B4**) [1153 h^{-1}, 80 °C, 0.04 mol%, 35 bar, CHO neat].[90] Following on from this, Coates found that cobalt acetate catalysts (**B7**) were highly active towards PO/CO_2 copolymerisation at high CO_2 pressures to give highly selective (> 99 %) copolymers [71 h^{-1}, 25 °C, 0.2 mol%, 55 bar, PO neat].[91] Interestingly, no co-catalysts were required for this copolymerisation; however activities were lower than previous chromium salen catalysts. Developments of these catalysts have yielded highly regioregular polymers with no by-product formation.[92,93]

The precise mechanisms which salen-derived catalysts operate under are still unclear. Epoxide ring-opening is proposed to be rate determining, although there is also a clear CO_2 pressure dependence. [85,86]

Salen catalysts require a Lewis-basic co-catalyst to accelerate the copolymerisation and azide co-ligands have been shown to initiate epoxide ring-opening faster than halides.[60,86,94-96] Successful co-catalysts include neutral nucleophilic species, such as DMAP or phosphines, and ionic ammonium salts. It has been shown that increasing the donor ability of the ligands increases the activity of the chromium (III) centre, although the choice of co-ligand and co-catalyst also affects the catalytic activity.[89,97]

The addition of a co-catalyst results in an equilibrium between metal coordination and 'off-metal' anionic chains.[83] These free anionic polymer chains have been shown to readily form cyclic carbonate by-products from cyclisation reactions.[98] The ratio of catalyst to co-catalyst is also important. When more than 1 co-catalyst equivalent is used a reduction in activity is observed, probably due to the competitive binding of the co-catalyst which hinders the epoxide's approach to the metal centre.[99,100] An excess of co-catalyst retards polymerisation and increases the rate of back biting side reactions to form cyclic by-products.[83,84,96,99]

1.3.3.1. Tethered systems

Increased activities have been observed by covalently bonding the co-catalyst moiety to the catalyst ligand, removing the need to add an exogenous co-catalyst source. Nozaki first reported this in a cobaltate complex with a salcy-type ligand containing piperidinyl and piperidinium arms (**C1**).[62] The piperidinium arms control the nucleophilicity of the propagating chains, increasing the rate of copolymerisation and decreasing the rate of cyclic by-product formation. This catalyst showed very high

selectivity for carbonate formation (> 99 %) and high activity at room temperature [253 h^{-1}, 25 °C, 0.05 mol%, 14 bar, PO neat].[62]

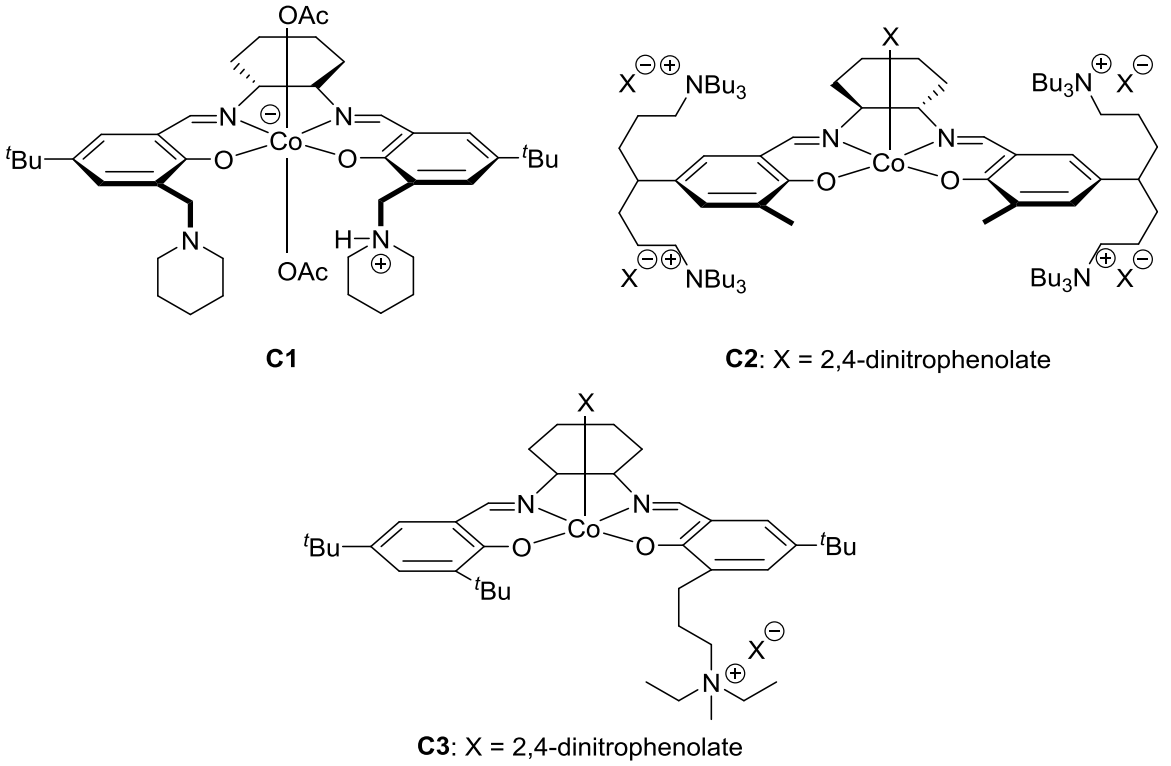
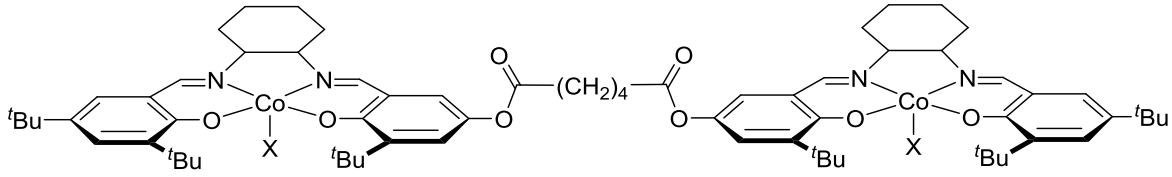


Figure 1.6 – Bifunctional salcy catalysts.

In 2007 Lee then reported a series of highly active bifunctional catalysts, which showed much higher activities to their analogous binary systems, and were active under extremely low catalyst loadings.[101-103] The catalysts with pendant ionic groups (**C2**) have displayed extremely high TOFs for the copolymerisation of PO and CO_2, whilst maintaining excellent (> 99 %) selectivity [26 000 h^{-1}, 80 °C, 0.004 mol%, 20 bar, PO neat].[101-103] Lu has also shown a cobalt salen complex with a tethered quarternary ammonium salt (**C3**) to have high activity and excellent selectivity (> 99 %) for CHO/CO_2 copolymerisation, under low pressures of CO_2 [263 h^{-1}, 50 °C, 0.02 mol%, 1 bar, CHO neat].[52]

1.3.3.2. Dinuclear Salens

Nozaki, and later Rieger, reported dinuclear salen-based catalysts (**C4**).[104,105] In the absence of a co-catalyst, the activities of the dinuclear complexes, in PO/CO_2 copolymerisation, were maintained at high dilution (1:20 000), whereas the mononuclear complexes, which operate via an intermolecular bimetallic pathway, suffer from decreased efficiency.[104,105] This strongly suggests mono- and dinuclear complexes operate under a bimetallic pathway (Figure 1.7).[104,105] In the presence of a co-catalyst, this pathway is exchanged for a binary monometallic reaction where the catalyst bound epoxide can interact with the co-catalyst to ring-open the epoxide.[104,105]



C4: X = pentafluorobenzoate

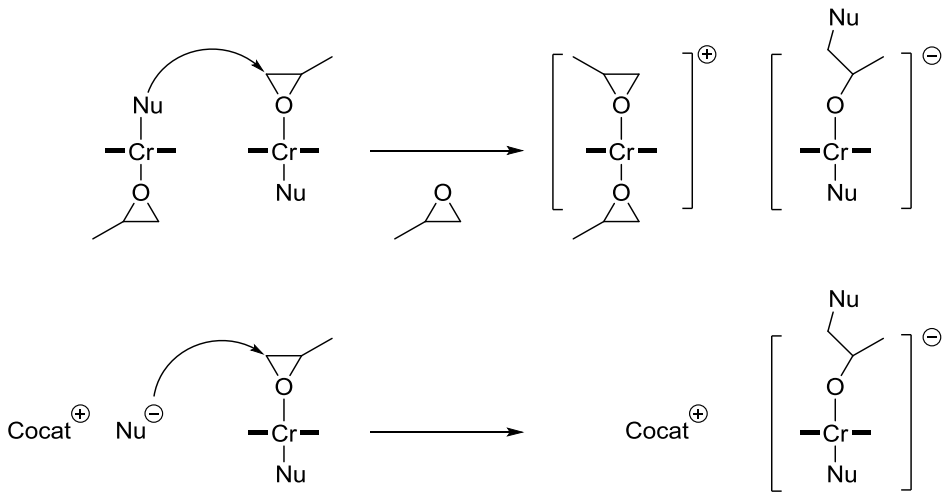
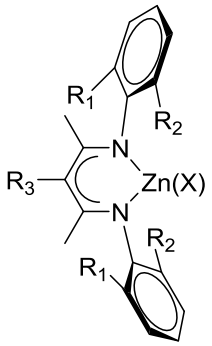


Figure 1.7 – Bis(salen) complex with a bimetallic pathway proposed to operate in the absence of co-catalyst and monometallic binary reaction pathway operating in the presence of a co-catalyst.[104,105]

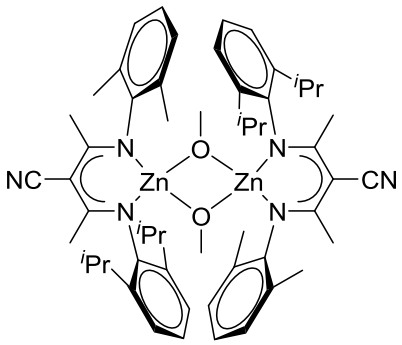
1.3.4. β-Diiminates

The first β-diiminate (BDI) catalysts, reported by Coates and co-workers (**D1**) showed good activity and selectivity (> 96 % PCHC) for CHO/CO_2 copolymerisation

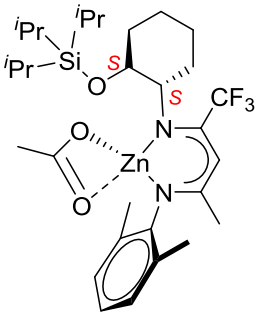
[247 h^{-1}, 50 °C, 0.1 mol%, 7 bar, CHO neat].[106] A wide range of zinc BDI complexes have been synthesised and ligand substituents were shown to exert a significant effect on catalytic activity (**D2-6**).[107] Enantioselective copolymerisation was achieved with C_1-symmetric zinc BDI catalysts (**D7**) to yield isotactic (94 % *ee*) poly(cyclohexene carbonate) (PCHC) at 0 °C, albeit with slow activity [3.9 h^{-1}, 0 °C, 0.05 mol%, 8 bar, CHO 5 M in toluene].[108]



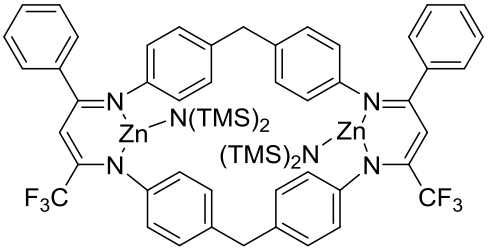
D1: X = OAc; R_1 = ^{i}Pr; R_2 = ^{i}Pr
D2: X = OMe; R_1 = ^{i}Pr; R_2 = ^{i}Pr
D3: X = OMe; R_1 = Et; R_2 = Et
D4: X = OMe; R_1 = ^{i}Pr; R_2 = Et
D5: X = OMe; R_1 = ^{i}Pr; R_2 = Me



D6



D7



D8

Figure 1.8 – BDI-derived catalysts for CO_2/epoxide copolymerisation.

β-Diiminate catalysts have been shown to exist in a monomer/dimer equilibrium which can be altered by changing the substituents on the ligands.[106,107,109,110] Bulky substituents in the *ortho* positions on the N-aryl ligands hinder dimerisation and the complexes exist as unreactive monomers in solution (Figure 1.9).[109] However, if these positions do not contain adequate steric bulk, the dimers formed are too tightly bound, restricting catalysis. A bimetallic mechanism was proposed to operate due to

the observations that the highly reactive, loosely bound dimeric species show enhanced activities for CO_2/CHO copolymerisation.[109]

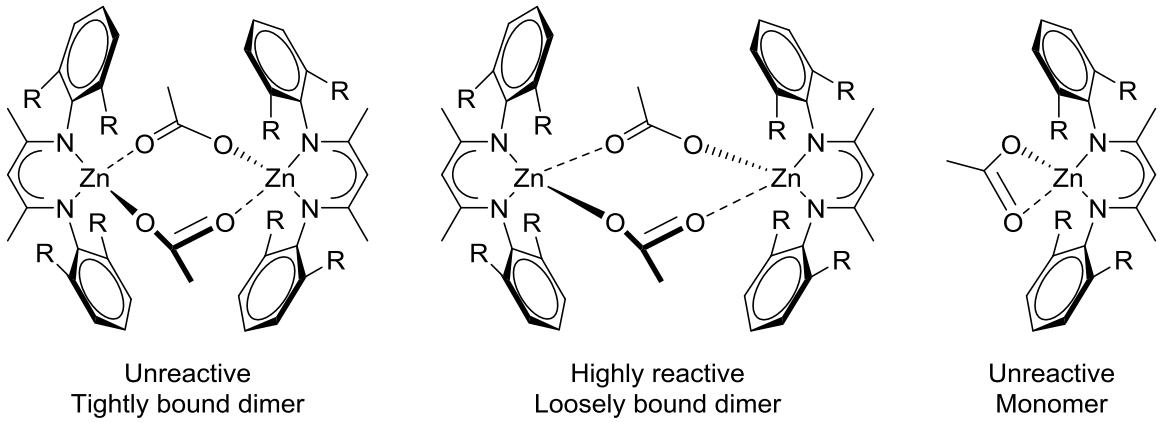


Figure 1.9 – General reactivity of β-diiminate complexes.[109]

Rate studies revealed these complexes to be zero order in CO_2 and first order in cyclohexene oxide, with the order in zinc varying from 1.0 to 1.8 under a range of temperatures and steric environments.[109] This provides evidence for an intermolecular dinuclear active site, although there is also the possibility for a minor contribution from a mononuclear mechanism.

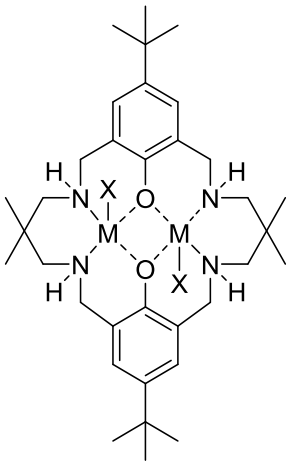
Building on these mechanistic studies, a tethered dinuclear zinc BDI system was reported by Rieger and co-workers (**D8**).[111] Under highly optimised conditions, this catalyst shows the highest turn-over-frequencies for CHO/CO_2 copolymerisation to date, although polycarbonate selectivity is limited to 88 % [155 000 h^{-1}, 100 °C, 0.013 mol%, 30 bar, 5 M CHO in toluene]. The activity and selectivity of this catalyst system varies significantly based on ligand substituents, and shows poor reactivity towards PO/CO_2 copolymerisation.[111-114]

1.3.5. Macrocyclic catalysts

Williams and co-workers reported a macrocyclic di-zinc catalyst (**[$LZn_2(OAc)_2$]**) which showed good activity in the copolymerisation of CHO at low pressures of CO_2

[18 h^{-1}, 80 °C, 0.1 mol%, 1 bar, CHO neat] (Figure 1.10).[115] This di-zinc catalyst was air stable and polymerisations were successful in standard glassware. An open ligand analogue was prepared but was inactive towards copolymerisation.[115]

A range of metals, and co-ligands have been explored, with the di-cobalt analogue (**[$LCo_2(OAc)_2$]**) showing excellent activity under atmospheric pressures [172 h^{-1}, 80 °C, 0.1 mol% 1 bar, CHO neat][116-118] The di-magnesium analogue (**[$LMg_2(OAc)_2$]**), displays even higher activity under optimised conditions [5400 h^{-1}, 125 °C, 0.003 mol%, 10 bar, CHO neat].[11] Trimetallic zinc and cobalt acetate complexes, with the same macrocyclic ligand, show reduced activity in comparison to their dinuclear analogues, perhaps due to increased steric hindrance.[117,118]



X = OAc
M = Mg; **[$LMg_2(OAc)_2$]**
M = Zn; **[$LZn_2(OAc)_2$]**
M = Co; **[$LCo_2(OAc)_2$]**

Figure 1.10 – Bimetallic macrocyclic complexes active under atmospheric pressure of CO_2.

Kinetic studies have shown the di-zinc catalyst to be first order with respect to epoxide and catalyst, and zero order in CO_2 pressure.[119] This strongly suggests the rate determining step is the ring-opening of the epoxide, with fast CO_2 incorporation. This was followed up with a detailed computational study, showing that the lowest energy pathway probably involves the growing polymer chain undergoing a

'shuttling' between the two metal centres, held in close proximity by the macrocyclic ligand (Figure 1.11).[120]

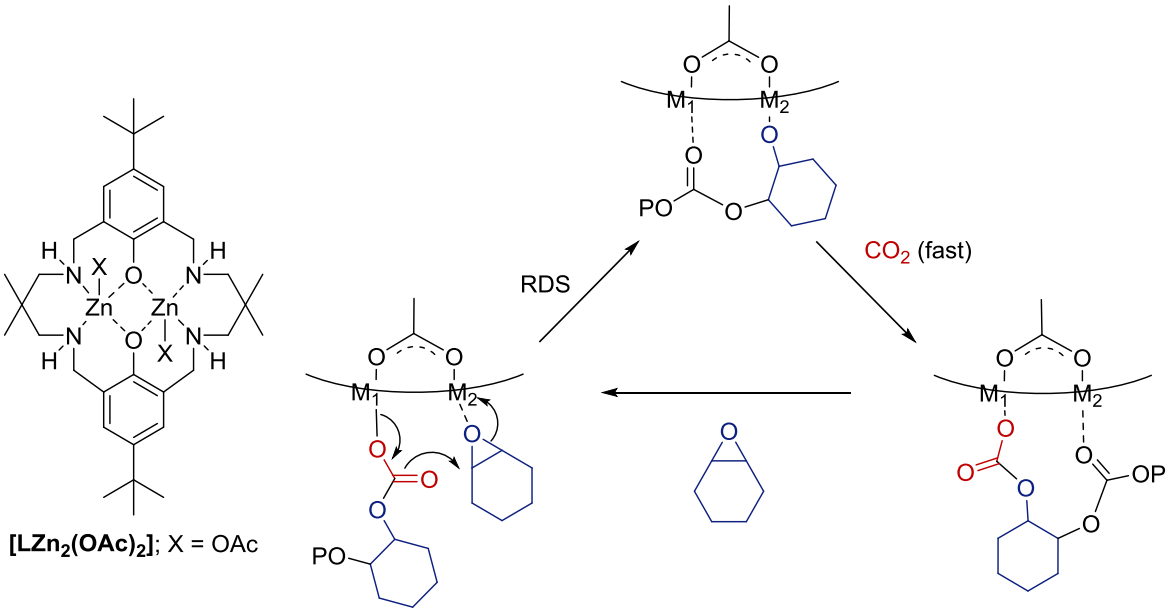


Figure 1.11 – Proposed 'chain-shuttling' mechanism for catalyst ***[LZn₂(OAc)₂]****.*[120] *The ligand scaffold is depicted as a curved line and the growing polymer chain denoted as 'P', for clarity.*

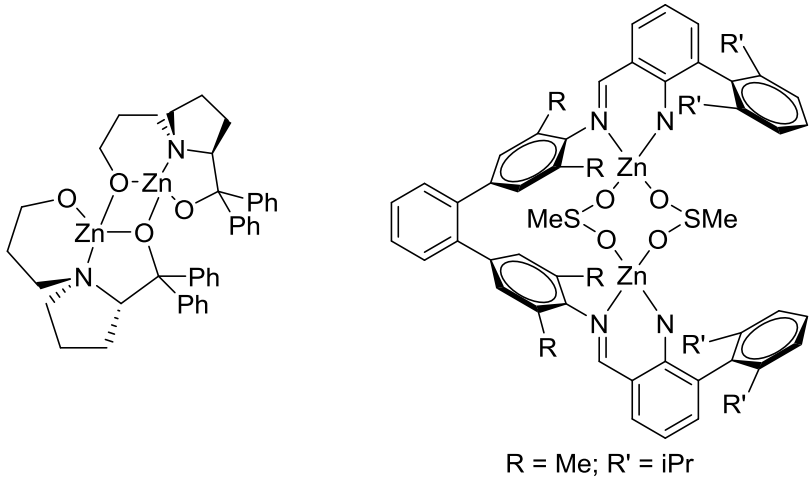
These computational studies looked at the reactivity of a homodinuclear catalyst (**[LZn₂(OAc)₂]**), suggesting the two metal centres have distinctive roles throughout catalysis. Here, in the rate determining step, one metal centre binds the epoxide whilst the other metal delivers the nucleophilic carbonate, transferring the polymer chain to the epoxide-bound metal (Figure 1.11).[120] The insertion of CO_2 is rapid and again results in a transfer of the growing polymer chain, reforming the carbonate on the original metal centre. The polymer chain is shown to switch coordinate site, between the two metal centres, with each sequential monomer insertion.

The carboxylate co-ligands play an important role in this catalysis; one co-ligand initiates the copolymerisation through ring-opening of the epoxide, whilst the other remains coordinated through a bidentate bridge and mediates copolymerisation.[120] It was shown in this study that the choice of co-ligand had an effect on the activity of copolymerisation.[120]

The two metals in the chain shuttling mechanism have different requirements for catalysis. Epoxide coordination would be accelerated by increasing the Lewis acidity or electrophilicity of the metals centres, whilst the nucleophilicity of the attacking carbonate would be increased by labile metal-carbonate bonds. It can be hypothesised that each metal could be tuned to increase the efficiency of the catalytic cycle. It was subsequently shown that magnesium-zinc heterodinuclear complexes were indeed faster than their homodinuclear analogues, *vide infra*.[121,122]

1.3.6. Other dinucleating ligands

Recently Meyer and co-workers described the synthesis of a proline-derived dinuclear zinc catalyst (**E**) which showed high activities for CHO/CO_2 copolymerisation [149 h^{-1}, 80 °C, 0.1 mol%, 1 bar, CHO neat] (Figure 1.12).[123] This catalyst produces isotactically-enriched PCHC, with > 99 % carbonate linkages, and > 98 % polymer selectivity.



E **F**

*Figure 1.12 – A proline-derived dinuclear zinc catalyst (**E**)[123] and an acyclic bis(anilido-aldimine) complex (**F**)[124], active for CHO/CO_2 copolymerisation.*

Lee and co-workers have prepared a range of acyclic bis(anilido-aldimine) complexes (**F**) which show high activities to CHO/CO_2 copolymerisation [312 h^{-1}, 80 °C, 0.02 mol%, 12 bar, CHO neat] (Figure 1.12).[124] Interestingly the macrocyclic

analogues to these complexes show negligible activity for copolymerisation. The activity is sensitive to the *N*-aryl *ortho*-substituents and the fluorination of the aromatic rings significantly increases the TOF values.[124,125] Zinc bis(anilido-aldimine) complexes undergo a bimetallic propagation through an intramolecular dinuclear active site.[124]

Ding has prepared a series of di-zinc and di-magnesium complexes based on Trost phenolate ligands.[126,127] These catalysts show poor activity for CHO/CO_2 copolymerisation under 1 atm pressure of CO_2 but have extremely high selectivities for carbonate formation (> 99 %) [0.4 h^{-1}, 80 °C, 5 mol%, 1 bar, CHO 1 M in toluene].[127] An intramolecular dinuclear active site was speculatively proposed for these catalysts, although no kinetic studies were carried out.[126,127] Blocking or removing the phenolate motif of these catalysts renders them inactive to copolymerisation and the activity was shown to be independent of CO_2 pressure.[127]

1.3.7. Main group catalysis

Zhang *et al*. (2016) showed that BEt_3 activated an epoxide (CHO or PO) and copolymerisation with CO_2 occurred in the presence of an onium chloride or onium alkoxide co-catalyst.[128] Poly(propylene carbonate) and poly(cyclohexene carbonate) were formed in 83 and 99 % selectivity, respectively. The copolymerisations gave high TOFs of 600 h^{-1} for CHO/CO_2 (80 °C) and 49 h^{-1} for PO/CO_2 (60 °C) copolymerisation [0.03 mol%, 10 bar, CHO 7.5 M in THF].

Similar reagents (BEt_3 with a Lewis base = amidine, guanidine or quaternary onium salts) were employed by Darensbourg and co-workers for ROCOP of PO and carbonyl sulphide (COS).[129] A perfectly alternating copolymer with 99 % head-to-tail regioselectivity was produced [199 h^{-1}, 25 °C, 0.1 mol%, PO 4.7 M in THF].[129]

1.3.8. Heteronuclear catalysts

Very few examples of well-defined heteronuclear catalysts for CO_2/epoxide copolymerisation are present in the literature.

Williams and co-workers synthesised a mixture containing a di-zinc (**[$LZn_2(OAc)_2$]**), di-magnesium (**[$LMg_2(OAc)_2$]**) and heterodinuclear magnesium-zinc catalyst (**[$LZnMg(OAc)_2$]**) (Figure 1.13).[121] This system showed increased activity of the heterodinuclear mixture, compared to the homodinuclear counterparts. [121]

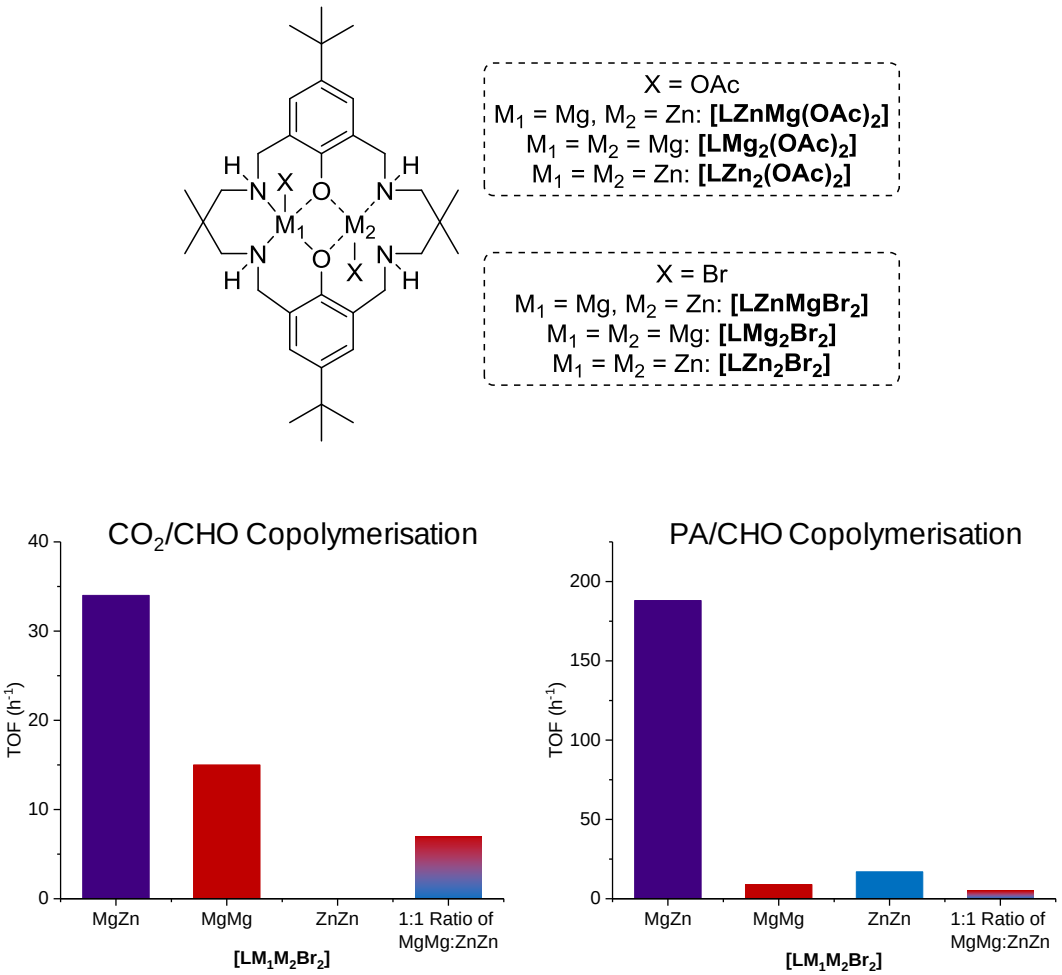


Figure 1.13 – Structure and activity comparison for heterodinuclear and homodinuclear catalysts, based on a phenolic macrocycle, in the copolymerisation of CHO/CO_2 and CHO/PA.[122]

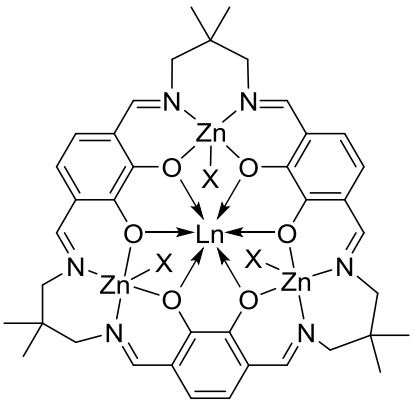
The first pure heterodinuclear catalyst (**[$LZnMgBr_2$]**), active for epoxide/CO_2 copolymerisation, was reported in 2015, showing good activity and selectivity for CHO/CO_2 copolymerisation [34 h^{-1}, 80 °C, 0.1 mol%, 1 bar, CHO neat] (Figure 1.13).[122]

This magnesium-zinc catalyst was synthesised from the macrocyclic ligand by sequential addition of diethyl zinc and magnesium bromide. It shows significantly enhanced activities for the copolymerisation of CHO with CO_2, as well as in polyester formation through the copolymerisation of CHO with PA, compared to the homodinuclear analogues (**[LZn_2Br_2]** and **[LMg_2Br_2]**) (Figure 1.13).[122]

No increase in activity was observed for a 1:1 mixture of the two homodinuclear analogues, suggesting no significant metal scrambling occurs under the polymerisation conditions and that the observed rate enhancement is due to metal cooperativity within the macrocyclic framework.[122]

Rare earth metal-zinc heterotrinuclear catalysts were reported in 2016, by Qin *et al*., which show excellent CO_2 incorporation but low activity [7 h^{-1}, 70 °C, 0.1 mol%, 1 bar].[130] However, the catalyst structures were not well defined and included no testing to conclude the system remained trimetallic under catalytic conditions.

More recently, in 2018, a new family of heterometallic rare earth metal-zinc tris(salen) catalysts (**G**) was developed by Nagae *et al*., which were active for CO_2/CHO copolymerisation [370 h^{-1}, 100 °C, 0.05 mol%, 10 bar] (Figure 1.14).[131]



X = OAc

G

Figure 1.14 – A heterometallic catalyst, active for CO_2/CHO copolymerisation, based on a macrocyclic tris(salen) ligand, with zinc and rare earth metals.[131]

1.3.9. Summary

A range of metals (Al^{3+}, Cr^{3+}, $Co^{3+/2+}$, Zn^{2+}, Mg^{2+}) show activity towards epoxide/CO_2 copolymerisation, with varying ligand structures (Table 1.3 and Table 1.4).

The highest activities for CO_2 copolymerisation are observed with **D8** (CHO) and **C2** (PO), however, the ligand structures are complicated and highly optimised, with long and difficult catalyst syntheses.[103,111] Therefore, some of the most desirable catalysts in the field are salen-derived catalysts (**B4**-**8**) as they yield high activities whilst being quick and relatively cheap to make.[90,91] These salen catalysts typically maintain good selectivity for polycarbonate linkages (**B4** 99 % for PCHC), where other active catalysts perform less well (**D8** 88 % for PCHC). Salen catalysts are frequently employed in the field and some are now commercially available, but require costly co-catalyst.

Table 1.3 – Selected catalysts for the copolymerisation of CHO/CO_2 at elevated pressures.

Catalyst	Co-cat.	Temp. (°C)	ρCO_2 (bar)	Cat. Loading (mol%)	[CHO] (M)	TOF (h^{-1})	Selectivity (%)
D1	-	50	7	0.1	Neat	247	96
B3	[PPN]N_3	60	34	0.04	Neat	405	99
B4	[PPN]Cl	80	35	0.04	Neat	1153	99
F	-	80	12	0.02	Neat	312	94
BEt_3	[PPN]Cl	80	10	0.03	7.5	600	99
D8	-	100	30	0.013	5	155000	88
G	-	100	10	0.05	Neat	370	99

The copolymerisation of PO and CO_2 remains challenging as activities are typically much lower than with CHO (Table 1.4). Achieving high PPC selectivity is difficult as polypropylene linkages and cyclic carbonate form readily. There are therefore far fewer catalysts active for this copolymerisation and they tend to require low temperatures but high pressures of CO_2, which is less compatible with process scale-up.

Table 1.4 – Selected catalysts for the copolymerisation of PO/CO_2.

Catalyst	Co-cat.	Temp. (°C)	ρCO_2 (bar)	Cat. Loading (mol%)	[PO] (M)	TOF (h^{-1})	Selectivity (%)
A3	[PPN]Cl	25	50	0.7	10	3	98
B7	-	25	55	0.2	Neat	71	99
C1	-	25	14	0.05	Neat	253	99
A6	[PPN]Cl	30	30	0.05	Neat	103	90
B2	[PPN]Cl	60	34	0.05	Neat	192	93
BEt_3	$[NBu_4]Cl$	60	10	0.03	7.5	49	83
C2	-	80	20	0.004	Neat	26000	99

To implement epoxide/CO_2 copolymerisation in the production of polyols using existing infrastructure, catalysts are preferred that operate under similar conditions to current production methods. These polyether plants typically operate under < 10 bar pressure, and hence there remains the need to further investigate catalysts which are highly active under these low pressures.

There are several examples of catalysts in the literature which show activity towards CHO/CO_2 copolymerisation, under only 1 bar pressure of CO_2 (Table 1.5). The highest activities are seen with cobalt-derived catalysts (**C3** and **[$LCo_2(OAc)_2$]**), however highly coloured crude polymers are produced.[52,118] It is, therefore, preferential to move towards zinc or magnesium based catalysts, which have also shown promising activities and high selectivities (**E** and **[$LZnMgBr_2$]**).

Table 1.5 – Selected catalysts active under 1 bar pressure of CO_2 for the copolymerisation in neat CHO.

Catalyst	Temp. (°C)	Cat. Loading (mol%)	TOF (h^{-1})	Selectivity (%)
C3	50	0.02	263	99
[$LCo_2(OAc)_2$]	80	0.1	172	99
[$LZn_2(OAc)_2$]	80	0.1	18	96
[$LMg_2(OAc)_2$]	80	0.1	35	99
[$LZnMgBr_2$]	80	0.1	34	99
E	80	0.1	149	98

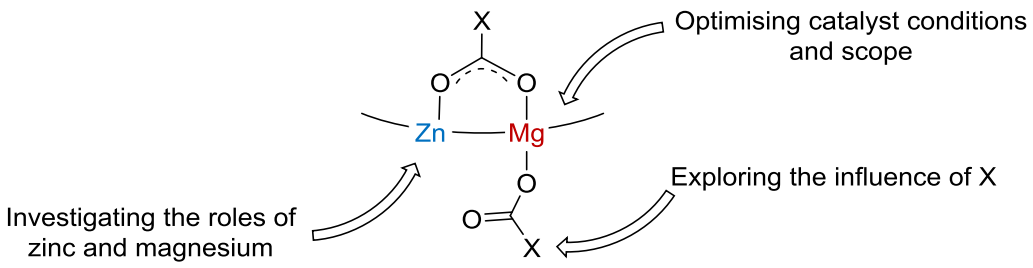
Even the most highly active catalysts will have to compete with the simplicity of some double metal cyanide (DMC) heterogenous catalysts, when considering the cost and

time required to make them at scale. It is therefore unsurprising that DMC catalysts are already being utilised in industry, forming polycarbonate linkages in polyethercarbonate polyols at low pressures (< 10 bar), despite higher levels of polyether formation.[74,75]

1.4. Project Aims

This thesis aims to:

1. Synthesise heterodinuclear Zn-Mg catalysts, with a range of carboxylate co-ligands, active for epoxide copolymerisations with CO_2 and anhydrides.
2. Investigate whether the synergic activity of Zn-Mg catalysts may be increased with different co-ligands, and consider their influence on initiation and propagation rates.
3. Optimise conditions and monomer scope for the most highly active and selective catalysts. Desirable catalysts should be active under atmospheric pressure of CO_2, give high (> 99 %) polycarbonate or polyester linkages at elevated temperatures, and show well controlled polymerisations yielding narrowly dispersed molar masses.
4. Define the rate law for a heterodinuclear Zn-Mg catalyst, in both CHO/CO_2 and CHO/PA copolymerisation.
5. Explore whether the hypothesised chain shuttling mechanism is an appropriate model for heterodinuclear Zn-Mg catalysts.
6. Rationalise the observed increase in activity for heterodinuclear Zn-Mg catalysts, in comparison to their homodinuclear analogues.



1.5. References

(1) Law, K. L.; Morét-Ferguson, S.; Maximenko, N. A.; Proskurowski, G.; Peacock, E. E.; Hafner, J.; Reddy, C. M. *Science* **2010**, *329*, 1185.
(2) Jambeck, J. R.; Geyer, R.; Wilcox, C.; Siegler, T. R.; Perryman, M.; Andrady, A.; Narayan, R.; Law, K. L. *Science* **2015**, *347*, 768.
(3) Zhu, Y.; Romain, C.; Williams, C. K. *Nature* **2016**, *540*, 354.
(4) Poland, S. J.; Darensbourg, D. J. *Green Chem.* **2017**, *19*, 4990.
(5) Zhang, X.; Fevre, M.; Jones, G. O.; Waymouth, R. M. *Chem. Rev.* **2018**, *118*, 839.
(6) van der Ploeg, F. *J. Econ. Lit.* **2011**, *49*, 366.
(7) Winnacker, M.; Rieger, B. *ChemSusChem* **2015**, *8*, 2455.
(8) Stempfle, F.; Ortmann, P.; Mecking, S. *Chem. Rev.* **2016**, *116*, 4597.
(9) Chen, G.-Q.; Patel, M. K. *Chem. Rev.* **2012**, *112*, 2082.
(10) Galbis, J. A.; García-Martín, M. d. G.; de Paz, M. V.; Galbis, E. *Chem. Rev.* **2016**, *116*, 1600.
(11) Chapman, A. C.; Keyworth, C.; Kember, M. R.; Lennox, A. J. J.; Williams, C. K. *ACS Catal.* **2015**, 1581.
(12) von der Assen, N.; Bardow, A. *Green Chem.* **2014**, *16*, 3272.
(13) Okada, M. *Prog. Polym. Sci.* **2002**, *27*, 87.
(14) Kember, M. R.; Buchard, A.; Williams, C. K. *Chem. Commun.* **2011**, *47*, 141.
(15) Klaus, S.; Lehenmeier, M. W.; Anderson, C. E.; Rieger, B. *Coord. Chem. Rev.* **2011**, *255*, 1460.
(16) Lu, X.-B.; Darensbourg, D. J. *Chem. Soc. Rev.* **2012**, *41*, 1462.
(17) Qin, Y.; Wang, X. *Biotechnol. J.* **2010**, *5*, 1164.
(18) Mikkelsen, M.; Jorgensen, M.; Krebs, F. C. *Energy Environ. Sci.* **2010**, *3*, 43.
(19) Geyer, R.; Jambeck, J. R.; Law, K. L. In *Science Advances* 2017; Vol. 3.
(20) Díaz, A.; Katsarava, R.; Puiggalí, J. *Int. J. Mol. Sci.* **2014**, *15*, 7064.
(21) Yokoyama, A.; Yokozawa, T. *Macromolecules* **2007**, *40*, 4093.
(22) Williams, C. K. *Chem. Soc. Rev.* **2007**, *36*, 1576.
(23) Stanford, M. J.; Dove, A. P. *Chem. Soc. Rev.* **2010**, *39*, 486.
(24) Dechy-Cabaret, O.; Martin-Vaca, B.; Bourissou, D. *Chem. Rev.* **2004**, *104*, 6147.
(25) Auras, R.; Harte, B.; Selke, S. *Macromol. Biosci.* **2004**, *4*, 835.
(26) Park, S.-B.; Lih, E.; Park, K.-S.; Joung, Y. K.; Han, D. K. *Prog. Polym. Sci.* **2017**, *68*, 77.
(27) Kim, M. S.; Kim, J. H.; Min, B. H.; Chun, H. J.; Han, D. K.; Lee, H. B. *Polym. Rev.* **2011**, *51*, 23.
(28) Thomas, C. M.; Lutz, J.-F. *Angew. Chem. Int. Ed.* **2011**, *50*, 9244.
(29) Hillmyer, M. A.; Tolman, W. B. *Acc. Chem. Res.* **2014**, *47*, 2390.
(30) Peña Carrodeguas, L.; Martín, C.; Kleij, A. W. *Macromolecules* **2017**, *50*, 5337.
(31) Han, B.; Zhang, L.; Yang, M.; Liu, B.; Dong, X.; Theato, P. *Macromolecules* **2016**, *49*, 6232.
(32) Huijser, S.; Hosseini Nejad, E.; Sablong, R.; de Jong, C.; Koning, C. E.; Duchateau, R. *Macromolecules* **2011**, *44*, 1132.
(33) DiCiccio, A. M.; Coates, G. W. *J. Am. Chem. Soc.* **2011**, *133*, 10724.
(34) Aida, T.; Inoue, S. *J. Am. Chem. Soc.* **1985**, *107*, 1358.
(35) Aida, T.; Sanuki, K.; Inoue, S. *Macromolecules* **1985**, *18*, 1049.
(36) Bernard, A.; Chatterjee, C.; Chisholm, M. H. *Polymer* **2013**, *54*, 2639.
(37) Jeske, R. C.; DiCiccio, A. M.; Coates, G. W. *J. Am. Chem. Soc.* **2007**, *129*, 11330.

(38) DiCiccio, A. M.; Longo, J. M.; Rodríguez-Calero, G. G.; Coates, G. W. *J. Am. Chem. Soc.* **2016**, *138*, 7107.
(39) Li, J.; Liu, Y.; Ren, W.-M.; Lu, X.-B. *J. Am. Chem. Soc.* **2016**, *138*, 11493.
(40) Sanford, M. J.; Peña Carrodeguas, L.; Van Zee, N. J.; Kleij, A. W.; Coates, G. W. *Macromolecules* **2016**, *49*, 6394.
(41) Isnard, F.; Lamberti, M.; Pellecchia, C.; Mazzeo, M. *ChemCatChem* **2017**, *9*, 2972.
(42) Langanke, J.; Wolf, A.; Hofmann, J.; Bohm, K.; Subhani, M. A.; Muller, T. E.; Leitner, W.; Gurtler, C. *Green Chem.* **2014**, *16*, 1865.
(43) Lee, S. H.; Cyriac, A.; Jeon, J. Y.; Lee, B. Y. *Polym. Chem.* **2012**, *3*, 1215.
(44) Longo, J. M.; Sanford, M. J.; Coates, G. W. *Chem. Rev.* **2016**, *116*, 15167.
(45) Darensbourg, D. J.; Wilson, S. J. *Green Chem.* **2012**, *14*, 2665.
(46) Paul, S.; Zhu, Y.; Romain, C.; Brooks, R.; Saini, P. K.; Williams, C. K. *Chem. Commun.* **2015**, *51*, 6459.
(47) Trott, G.; Saini, P. K.; Williams, C. K. *Phil. Trans. R. Soc. A* **2016**, *374*.
(48) Darensbourg, D. J.; Wilson, S. J. *Macromolecules* **2013**, *46*, 5929.
(49) Darensbourg, D. J.; Tsai, F.-T. *Macromolecules* **2014**, *47*, 3806.
(50) Darensbourg, D. J.; Wilson, S. J. *J. Am. Chem. Soc.* **2011**, *133*, 18610.
(51) Liu, Y.; Wang, M.; Ren, W.-M.; He, K.-K.; Xu, Y.-C.; Liu, J.; Lu, X.-B. *Macromolecules* **2014**, *47*, 1269.
(52) Ren, W.-M.; Zhang, X.; Liu, Y.; Li, J.-F.; Wang, H.; Lu, X.-B. *Macromolecules* **2010**, *43*, 1396.
(53) Koning, C.; Wildeson, J.; Parton, R.; Plum, B.; Steeman, P.; Darensbourg, D. J. *Polymer* **2001**, *42*, 3995.
(54) Si, G.; Zhang, L.; Han, B.; Duan, Z.; Li, B.; Dong, J.; Li, X.; Liu, B. *Polym. Chem.* **2015**, *6*, 6372.
(55) Darensbourg, D. J.; Poland, R. R.; Escobedo, C. *Macromolecules* **2012**, *45*, 2242.
(56) Van Zee, N. J.; Coates, G. W. *Angew. Chem. Int. Ed.* **2015**, *54*, 2665.
(57) Zhu, Y.; Radlauer, M. R.; Schneiderman, D. K.; Shaffer, M. S. P.; Hillmyer, M. A.; Williams, C. K. *Macromolecules* **2018**, 10.1021/acs.macromol.7b02690.
(58) Inoue, S.; Koinuma, H.; Tsuruta, T. *J. Polym. Sci., Part B: Polym. Lett.* **1969**, *7*, 287.
(59) Kember, M. R.; Williams, C. K. *J. Am. Chem. Soc.* **2012**, *134*, 15676.
(60) Nakano, K.; Nakamura, M.; Nozaki, K. *Macromolecules* **2009**, *42*, 6972.
(61) Sugimoto, H.; Ohtsuka, H.; Inoue, S. *J. Polym. Sci., Part A: Polym. Chem.* **2005**, *43*, 4172.
(62) Nakano, K.; Kamada, T.; Nozaki, K. *Angew. Chem. Int. Ed.* **2006**, *45*, 7274.
(63) Zhu, Y.; Romain, C.; Poirier, V.; Williams, C. K. *Macromolecules* **2015**, *48*, 2407.
(64) Zhu, Y.; Romain, C.; Williams, C. K. *J. Am. Chem. Soc.* **2015**, *137*, 12179.
(65) Wu, G.-P.; Darensbourg, D. J. *Macromolecules* **2016**, *49*, 807.
(66) Romain, C.; Garden, J. A.; Trott, G.; Buchard, A.; White, A. J. P.; Williams, C. K. *Chem. Eur. J.* **2017**, *23*, 7367.
(67) Hirano, T.; Inoue, S.; Tsuruta, T. *Makromol. Chem.* **1976**, *177*, 3237.
(68) Hirano, T.; Inoue, S.; Tsuruta, T. *Makromol. Chem.* **1975**, *176*, 1913.
(69) Eberhardt, R.; Allmendinger, M.; Zintl, M.; Troll, C.; Luinstra, G. A.; Rieger, B. *Macromol. Chem. Phys.* **2004**, *205*, 42.
(70) Kim, J. S.; Ree, M.; Lee, S. W.; Oh, W.; Baek, S.; Lee, B.; Shin, T. J.; Kim, K. J.; Kim, B.; Luning, J. *J. Catal.* **2003**, *218*, 386.
(71) Ree, M.; Bae, J. Y.; Jung, J. H.; Shin, T. J. *J. Polym. Sci., Part A: Polym. Chem.* **1999**, *37*, 1863.

(72) Chen, S.; Qi, G.-R.; Hua, Z.-J.; Yan, H.-Q. *J. Polym. Sci., Part A: Polym. Chem.* **2004**, *42*, 5284.
(73) Hwang, Y.; Kim, H.; Ree, M. *Macromol. Symp.* **2005**, *224*, 227.
(74) McDaniel, K. G.; Covestro LLC: Patent, 2015.
(75) Hofmann, J.; Gürtler, C.; Grasser, S.; Wolf, A.; Covestro Deutschland AG: Patent, 2016.
(76) Aida, T.; Inoue, S. *J. Am. Chem. Soc.* **1983**, *105*, 1304.
(77) Sugimoto, H.; Kuroda, K. *Macromolecules* **2008**, *41*, 312.
(78) Qin, Y.; Wang, X.; Zhang, S.; Zhao, X.; Wang, F. *J. Polym. Sci., Part A: Polym. Chem.* **2008**, *46*, 5959.
(79) Chatterjee, C.; Chisholm, M. H. *Inorg. Chem.* **2011**, *50*, 4481.
(80) Chen, P.; Chisholm, M. H.; Gallucci, J. C.; Zhang, X.; Zhou, Z. *Inorg. Chem.* **2005**, *44*, 2588.
(81) Chisholm, M. H.; Zhou, Z. *J. Am. Chem. Soc.* **2004**, *126*, 11030.
(82) Anderson, C. E.; Vagin, S. I.; Xia, W.; Jin, H.; Rieger, B. *Macromolecules* **2012**, *45*, 6840.
(83) Darensbourg, D. J. *Chem. Rev.* **2007**, *107*, 2388.
(84) Darensbourg, D. J.; Yarbrough, J. C. *J. Am. Chem. Soc.* **2002**, *124*, 6335.
(85) Ren, W.-M.; Liu, Z.-W.; Wen, Y.-Q.; Zhang, R.; Lu, X.-B. *J. Am. Chem. Soc.* **2009**, *131*, 11509.
(86) Luinstra, G. A.; Haas, G. R.; Molnar, F.; Bernhart, V.; Eberhardt, R.; Rieger, B. *Chem. Eur. J.* **2005**, *11*, 6298.
(87) Darensbourg, D. J.; Mackiewicz, R. M.; Phelps, A. L.; Billodeaux, D. R. *Acc. Chem. Res.* **2004**, *37*, 836.
(88) Darensbourg, D. J.; Phelps, A. L. *Inorg. Chem.* **2005**, *44*, 4622.
(89) Darensbourg, D. J.; Ulusoy, M.; Karroonnirum, O.; Poland, R. R.; Reibenspies, J. H.; Çetinkaya, B. *Macromolecules* **2009**, *42*, 6992.
(90) Darensbourg, D. J.; Mackiewicz, R. M.; Billodeaux, D. R. *Organometallics* **2005**, *24*, 144.
(91) Qin, Z.; Thomas, C. M.; Lee, S.; Coates, G. W. *Angew. Chem. Int. Ed.* **2003**, *42*, 5484.
(92) Cohen, C. T.; Chu, T.; Coates, G. W. *J. Am. Chem. Soc.* **2005**, *127*, 10869.
(93) Lu, X.-B.; Wang, Y. *Angew. Chem. Int. Ed.* **2004**, *43*, 3574.
(94) Niu, Y.; Zhang, W.; Pang, X.; Chen, X.; Zhuang, X.; Jing, X. *J. Polym. Sci., Part A: Polym. Chem.* **2007**, *45*, 5050.
(95) Lu, X.-B.; Shi, L.; Wang, Y.-M.; Zhang, R.; Zhang, Y.-J.; Peng, X.-J.; Zhang, Z.-C.; Li, B. *J. Am. Chem. Soc.* **2006**, *128*, 1664.
(96) Darensbourg, D. J.; Mackiewicz, R. M.; Rodgers, J. L.; Phelps, A. L. *Inorg. Chem.* **2004**, *43*, 1831.
(97) Li, B.; Wu, G.-P.; Ren, W.-M.; Wang, Y.-M.; Rao, D.-Y.; Lu, X.-B. *J. Polym. Sci., Part A: Polym. Chem.* **2008**, *46*, 6102.
(98) Wu, G.-P.; Wei, S.-H.; Ren, W.-M.; Lu, X.-B.; Li, B.; Zu, Y.-P.; Darensbourg, D. J. *Energy Environ. Sci.* **2011**, *4*, 5084.
(99) Darensbourg, D. J.; Bottarelli, P.; Andreatta, J. R. *Macromolecules* **2007**, *40*, 7727.
(100) Paddock, R. L.; Nguyen, S. T. *J. Am. Chem. Soc.* **2001**, *123*, 11498.
(101) Noh, E. K.; Na, S. J.; Sujith, S.; Kim, S. W.; Lee, B. Y. *J. Am. Chem. Soc.* **2007**, *129*, 8082.
(102) Na, S. J.; S., S.; Cyriac, A.; Kim, B. E.; Yoo, J.; Kang, Y. K.; Han, S. J.; Lee, C.; Lee, B. Y. *Inorg. Chem.* **2009**, *48*, 10455.

(103) S, S.; Min, J. K.; Seong, J. E.; Na, S. J.; Lee, B. Y. *Angew. Chem. Int. Ed.* **2008**, *47*, 7306.
(104) Nakano, K.; Hashimoto, S.; Nozaki, K. *Chem. Sci.* **2010**, *1*, 369.
(105) Klaus, S.; Vagin, S. I.; Lehenmeier, M. W.; Deglmann, P.; Brym, A. K.; Rieger, B. *Macromolecules* **2011**, *44*, 9508.
(106) Cheng, M.; Lobkovsky, E. B.; Coates, G. W. *J. Am. Chem. Soc.* **1998**, *120*, 11018.
(107) Cheng, M.; Moore, D. R.; Reczek, J. J.; Chamberlain, B. M.; Lobkovsky, E. B.; Coates, G. W. *J. Am. Chem. Soc.* **2001**, *123*, 8738.
(108) Ellis, W. C.; Jung, Y.; Mulzer, M.; Di Girolamo, R.; Lobkovsky, E. B.; Coates, G. W. *Chem. Sci.* **2014**, *5*, 4004.
(109) Moore, D. R.; Cheng, M.; Lobkovsky, E. B.; Coates, G. W. *J. Am. Chem. Soc.* **2003**, *125*, 11911.
(110) Moore, D. R.; Cheng, M.; Lobkovsky, E. B.; Coates, G. W. *Angew. Chem. Int. Ed.* **2002**, *41*, 2599.
(111) Kissling, S.; Lehenmeier, M. W.; Altenbuchner, P. T.; Kronast, A.; Reiter, M.; Deglmann, P.; Seemann, U. B.; Rieger, B. *Chem. Commun.* **2015**, *51*, 4579.
(112) Kissling, S.; Altenbuchner, P. T.; Lehenmeier, M. W.; Herdtweck, E.; Deglmann, P.; Seemann, U. B.; Rieger, B. *Chem. Eur. J.* **2015**, *21*, 8148.
(113) Lehenmeier, M. W.; Kissling, S.; Altenbuchner, P. T.; Bruckmeier, C.; Deglmann, P.; Brym, A.-K.; Rieger, B. *Angew. Chem. Int. Ed.* **2013**, *52*, 9821.
(114) Reiter, M.; Vagin, S.; Kronast, A.; Jandl, C.; Rieger, B. *Chem. Sci.* **2017**, *8*, 1876.
(115) Kember, M. R.; Knight, P. D.; Reung, P. T. R.; Williams, C. K. *Angew. Chem. Int. Ed.* **2009**, *48*, 931.
(116) Kember, M. R.; Jutz, F.; Buchard, A.; White, A. J. P.; Williams, C. K. *Chem. Sci.* **2012**, *3*, 1245.
(117) Kember, M. R.; White, A. J. P.; Williams, C. K. *Inorg. Chem.* **2009**, *48*, 9535.
(118) Kember, M. R.; White, A. J. P.; Williams, C. K. *Macromolecules* **2010**, *43*, 2291.
(119) Jutz, F.; Buchard, A.; Kember, M. R.; Fredrickson, S. B.; Williams, C. K. *J. Am. Chem. Soc.* **2011**, *133*, 17395.
(120) Buchard, A.; Jutz, F.; Kember, M. R.; White, A. J. P.; Rzepa, H. S.; Williams, C. K. *Macromolecules* **2012**, *45*, 6781.
(121) Saini, P. K.; Romain, C.; Williams, C. K. *Chem. Commun.* **2014**, *50*, 4164.
(122) Garden, J. A.; Saini, P. K.; Williams, C. K. *J. Am. Chem. Soc.* **2015**, *137*, 15078.
(123) Schütze, M.; Dechert, S.; Meyer, F. *Chem. Eur. J.* **2017**, *23*, 16472.
(124) Lee, B. Y.; Kwon, H. Y.; Lee, S. Y.; Na, S. J.; Han, S.-i.; Yun, H.; Lee, H.; Park, Y.-W. *J. Am. Chem. Soc.* **2005**, *127*, 3031.
(125) Bok, T.; Yun, H.; Lee, B. Y. *Inorg. Chem.* **2006**, *45*, 4228.
(126) Xiao, Y.; Wang, Z.; Ding, K. *Macromolecules* **2006**, *39*, 128.
(127) Xiao, Y.; Wang, Z.; Ding, K. *Chem. Eur. J.* **2005**, *11*, 3668.
(128) Zhang, D.; Boopathi, S. K.; Hadjichristidis, N.; Gnanou, Y.; Feng, X. *J. Am. Chem. Soc.* **2016**, *138*, 11117.
(129) Yang, J.-L.; Wu, H.-L.; Li, Y.; Zhang, X.-H.; Darensbourg, D. J. *Angew. Chem. Int. Ed.* **2017**, *56*, 5774.
(130) Qin, J.; Xu, B.; Zhang, Y.; Yuan, D.; Yao, Y. *Green Chem.* **2016**, *18*, 4270.
(131) Nagae, H.; Aoki, R.; Akutagawa, S.-N.; Kleemann, J.; Tagawa, R.; Schindler, T.; Choi, G.; Spaniol, T. P.; Tsurugi, H.; Okuda, J.; Mashima, K. *Angew. Chem. Int. Ed.* **2018**, *57*, 2492.

Chapter 2

Methodology

This chapter describes the key techniques and analytical methods used in this thesis, focussing on data collection and analysis of complexes and polymer compounds. The techniques include NMR spectroscopy, mass spectrometry, size exclusion chromatography and differential scanning calorimetry. A discussion on kinetic and computational methods applied in the thesis is also detailed.

2.1. NMR Spectroscopy

Throughout this thesis one and two dimensional multinuclear (^{1}H and ^{13}C) NMR spectroscopy was routinely used to characterise new compounds.

2.1.1. Characterisation of polymers

^{1}H NMR spectroscopy was used to determine the conversion and selectivity of the polymerisation reactions from the relative integrals of the polymer, monomer and side-products. The chemical shifts used in the copolymerisations of CO_2 and CHO are shown in Table 2.1.[1]

Table 2.1 – ^{1}H NMR chemical shifts for the reactant and products of CHO/CO_2 copolymerisation, in $CDCl_3$.

Component	CHO	PCHC Backbone	PCHC End Group	PCHC End Group	Cyclic Carbonate	Polyether
Chemical shift (ppm)	3.05	4.6	4.35	3.50	3.95	3.45

The polymerisation conversion was calculated from the relative integrals of products against monomers (Equation 2.1). Carbonate selectivity was determined by comparison of the integrals relating to polycarbonate and cyclic carbonate against polyether resonances (Equation 2.2). Polymer selectivity was calculated through the relative integrals of all polymer resonances against cyclic by-products (Equation 2.3).

$$Conv.(\%) = 100 \times \frac{\int H_{polycarbonate} + \int H_{cyclic\ carbonate} + \int H_{polyether}}{\int H_{polycarbonate} + \int H_{cyclic\ carbonate} + \int H_{polyether} + \int H_{CHO}}$$

Equation 2.1 – General method to calculate conversion for the copolymerisation of CO_2 and epoxides.

$$CO_2\ (\%) = 100 \times \frac{\int H_{polycarbonate} + \int H_{cyclic\ carbonate}}{\int H_{polycarbonate} + \int H_{cyclic\ carbonate} + \int H_{polyether}}$$

Equation 2.2 – General method to calculate selectivity towards CO_2 linkages for the copolymerisation of CO_2 and epoxides.

$$Polymer\ (\%) = 100 \times \frac{\int H_{polycarbonate} + \int H_{polyether}}{\int H_{polycarbonate} + \int H_{cyclic\ carbonate} + \int H_{polyether}}$$

Equation 2.3 – General method to calculate selectivity towards polymer linkages for the copolymerisation of CO_2 and epoxides.

The desired product for the copolymerisation is polycarbonate and its selectivity was calculated by comparing the relative integrals of the polycarbonate signals against all other products (Equation 2.4).

$$Polycarbonate\ (\%) = 100 \times \frac{\int H_{polycarbonate}}{\int H_{polycarbonate} + \int H_{cyclic\ carbonate} + \int H_{polyether}}$$

Equation 2.4 – General method to calculate selectivity towards polycarbonate linkages for the copolymerisation of CO_2 and epoxides.

For example, comparing the integrals from the ^{1}H NMR spectrum of a crude sample from the copolymerisation of CHO and CO_2, the conversion and selectivity can be determined (Figure 2.1).

$$\int H_{CHO} = \int H_a = 0.6167$$

$$\int H_{polycarbonate} = \int H_b + \int H_c + \int H_d = 0.3690 + 0.0066 + 0.0072 = 0.3828$$

$$\int H_{cyclic\ carbonate} = 0.0005$$

$$\int H_{polyether} = 0$$

$$Conv.\ (\%) = 100 \times \frac{0.3828 + 0.0005 + 0}{0.3828 + 0.0005 + 0.6167} = 38\ \%$$

$$CO_2(\%) = 100 \times \frac{0.3828 + 0.0005}{0.3828 + 0.0005 + 0} = 100\ \%$$

$$Polymer\ (\%) = 100 \times \frac{0.3828 + 0}{0.3828 + 0.0005 + 0} = 100\ \%$$

$$Polycarbonate\ (\%) = 100 \times \frac{0.3828}{0.3828 + 0.0005 + 0} = 100\ \%$$

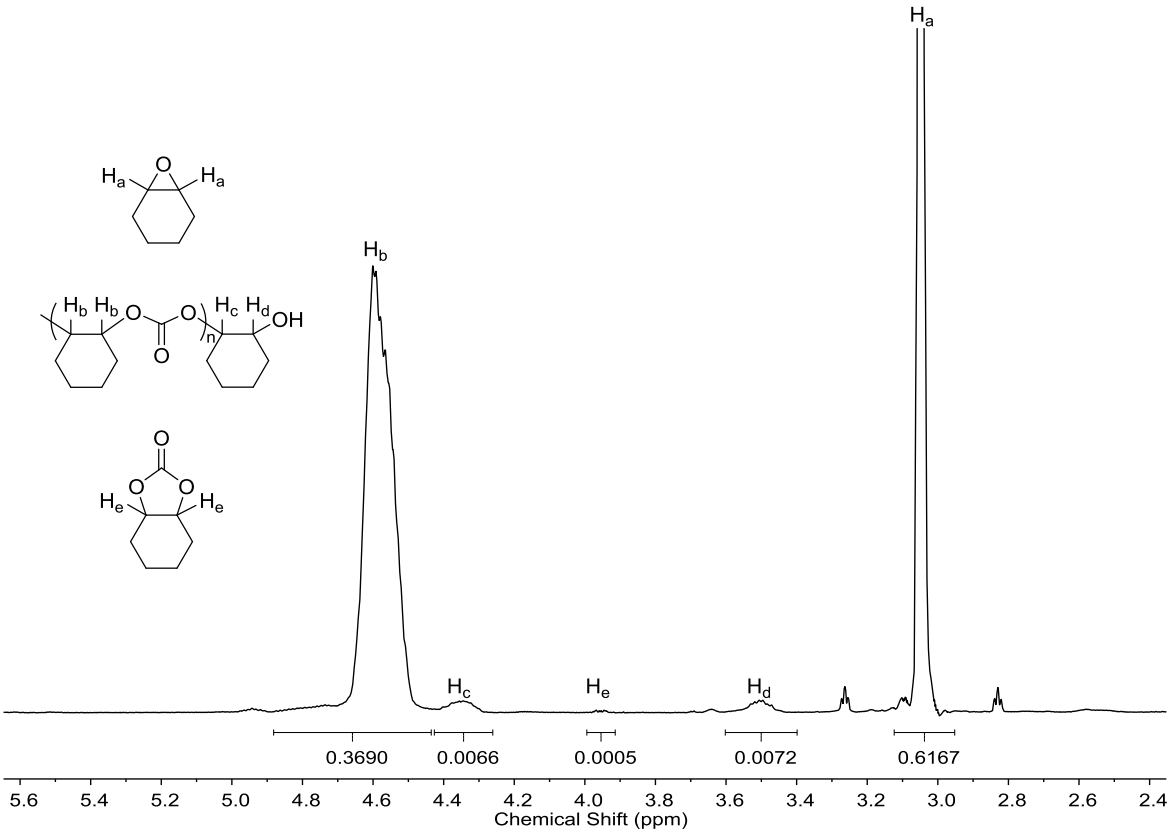


Figure 2.1 – Example of a ^{1}H NMR spectrum of a crude reaction mixture for the copolymerisation of CO_2 with CHO, in $CDCl_3$.

The turnover number (TON) of a catalytic reaction is the number of moles of monomer units each mole of catalyst has converted. This is calculated by multiplying the conversion by the catalyst loading, with the example continued for a molar ratio of 1:1000 for catalyst:CHO (sometimes described as 0.1mol%) (Equation 2.5).

$$TON = \frac{Conv.(\%)}{100} \times (catalyst\ loading) = \frac{38.3}{100} \times 1000 = 383$$

Equation 2.5 – Calculation used to find TON.

Activity is typically calculated by working out the catalyst turnover frequency (TOF), defined by the turnover number per unit time (Equation 2.6).

$$TOF = \frac{TON}{time} = \frac{383}{6} = 64\ h^{-1}$$

Equation 2.6 – Calculation used to find TOF.

Polyester conversion and selectivity is calculated in an analogous way using the chemical shifts shown in Table 2.2. It should be noted that the PA aromatic resonances are equivalent to 4 protons (H_b Figure 2.2) whereas the combined polyester backbone resonances, at 4.98 ppm, are equivalent to 2 protons (H_c + H_d, Figure 2.2). This is taken into consideration when calculating conversion.

Table 2.2 – ^1H NMR chemical shifts for the reactant and products of CHO/PA copolymerisation, in $CDCl_3$.[2]

Component	CHO	PA	PE Backbone	PE End Group	PE End Group	Polyether
Chemical shift (ppm)	3.05	7.83	4.98	4.72	3.39	3.45

$$\int H_{PA} = \int H_b = 0.7723$$

$$\int H_{polyester} = \int H_c + \int H_d + \int H_f + \int H_g = 0.2073 + 0.0111 + 0.0093 = 0.2277$$

$$\int H_{polyether} = 0$$

$$Conv.(\%) = 100 \times \frac{0.2277 + 0}{0.2277 + 0 + \left(\frac{0.7723}{2}\right)} = 37.1\ \%$$

$$Polyester\ (\%) = 100 \times \frac{2277}{0.2277 + 0} = 100\ \%$$

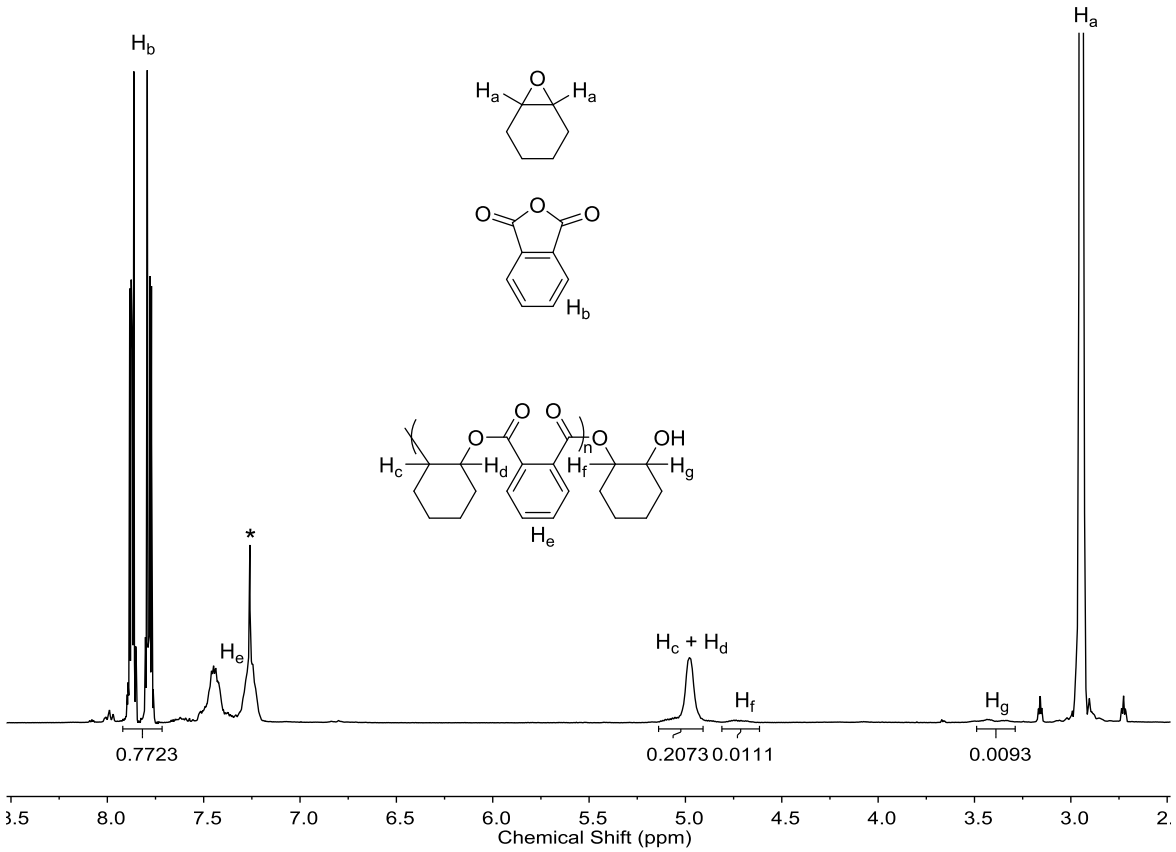


Figure 2.2 – Example of a ^{1}H NMR spectrum of a crude reaction mixture for the copolymerisation of PA with CHO, in $CDCl_3$.

2.1.2. Two dimensional (2D) NMR characterisation techniques

Multinuclear 2D NMR spectroscopy was used to aid full assignment of the ^{1}H and $^{13}C\{^{1}H\}$ spectra, typically using COSY (^{1}H-^{1}H, multiple bond coupling), HSQC (^{1}H-^{13}C, 1 bond coupling) and HMBC (^{1}H-^{13}C, multiple bond coupling) NMR experiments. ^{1}H-^{1}H Rotating Frame Overhauser Effect Spectroscopy (ROESY) was used to determine which protons were close in space or in chemical/conformational exchange.

2.1.3. Diffusion ordered NMR spectroscopy (DOSY)

DOSY NMR spectroscopy is a 2D solution state experiment which separates different NMR resonances based on their diffusion coefficient, which depends upon hydrodynamic radius. DOSY NMR spectroscopy gives valuable information on the possible aggregation states of complexes in solution. Quantitative comparisons of the diffusion gradient to the hydrodynamic radius of a complex are subject to

assumptions.[3] Therefore the data obtained is used here to provide evidence on monomer/dimer formation in solution only.

The signal decay is measured after a series of pulsed field gradient experiments, with the rate of attenuation relating to the diffusion coefficient. Once the diffusion coefficient has been measured, the hydrodynamic radius and molecular weight can be approximated.

The diffusion coefficient (D) is directly inversely proportional to the molecular hydrodynamic radius (r), by the Stokes-Einstein equation (Equation 2.7). Assuming high dilution and that the molecule is spherical, this results in a logarithmic correlation between the diffusion coefficient and molecular weight (MW) (Equations 2.8).

$$D = \frac{k_B T}{6\pi\eta r}$$

Equation 2.7 – Stokes-Einstein equation where D is the diffusion coefficient, k_B the Boltzmann constant, T the temperature, η the solvent viscosity, and r the hydrodynamic radius.

$$D = A(MW)^{\alpha}$$
$$\log(D) = \log(A) + \alpha\log(MW)$$

Equations 2.8 – The relationship between diffusion coefficient and molecular weight, where A and α are intrinsic constants of the solvent.

A linear calibration plot was obtained by measuring the diffusion coefficients of standard compounds, which is then used to estimate molecular weight of the sample. The calibration plots used in this thesis were derived previously for a similar complex, in d_8-THF, and gave α = -0.5626 and log(A) = -7.505.[4]

The calibration plot, along with the measured diffusion coefficient, was used to determine the molecular weight, using the example shown in Figure 2.3.

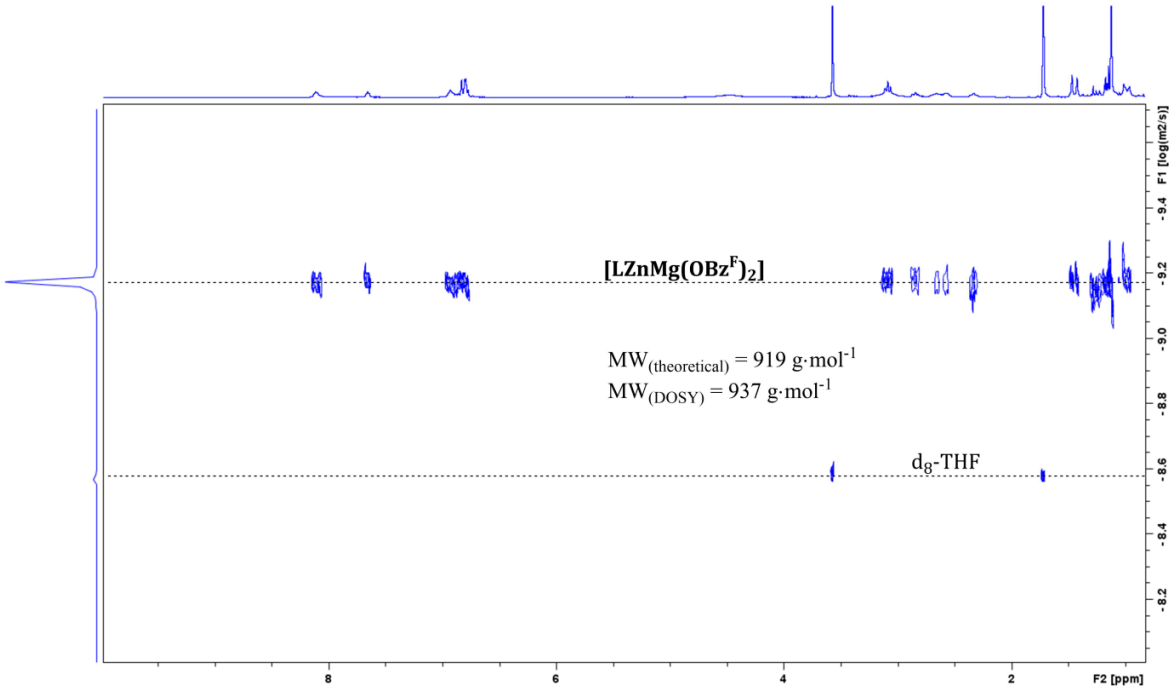


Figure 2.3 – Example of a DOSY spectrum analysed in this thesis.

$$\log(D) = -9.177$$

$$\frac{-9.177 - (-7.505)}{-0.5626} = \log(MW)$$

$$MW = 10^{\left(\frac{7.505-9.177}{-0.5626}\right)} = 937\ g \cdot mol^{-1}$$

Equations 2.9 – Calculation of approximate molecular weight from diffusion coefficient.

The calculated molecular weight (937 g·mol^{-1}) is in close (2 %) agreement of the theoretical molecular weight (919 g·mol^{-1}) of a non-aggregated species.

2.2. Mass Spectrometry

Mass spectrometry applies ionisation to form ions (or fragmented ions), which separate, in an electromagnetic field, based on mass to charge (m/z) ratio. The main ionisation method utilised in this thesis was Matrix Assisted Laser Desorption/Ionisation Time of Flight (MALDI-ToF) Mass Spectrometry. In the experiment, the sample was uniformly mixed with an appropriate matrix (e.g. dithranol) and additive (KTFA), in a 1:1:1 ratio, before the measurement takes place.

The matrix absorbs ultraviolet light, heating rapidly, to cause vaporisation of a very small amount of the matrix and sample, which expands in the instrument vacuum. Charged ions of different charge densities are generated and a potential difference applied across the sample. The velocity of each ion differs according to their charge density, with lighter and more highly charged ions reaching the detector faster. It is a relatively soft ionisation technique used for polymeric samples and metal complexes (600 Da < MW < 10 000 Da).

Typically homogeneous polymers show a series of equally spaced peaks in the MALDI-TOF spectrum due to the range of chain lengths and, therefore, varying molecular weight (Figure 2.4). The difference between two signals should correlate with the repeat unit mass for peaks in a particular distribution. Different distributions may arise due to alternative polymer end-groups and counter ions.

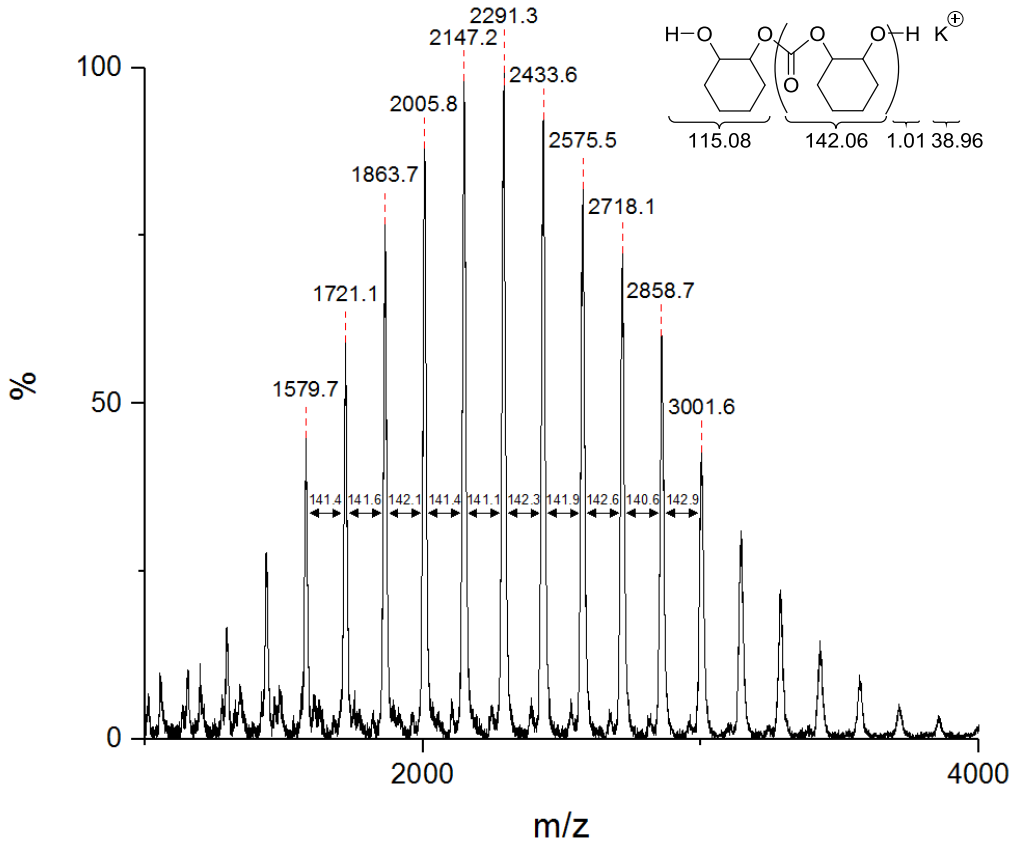


Figure 2.4 – Example of a MALDI-ToF spectrum obtained for an α,ω-hydroxyl end-capped polycarbonate sample.

2.3. Size Exclusion Chromatography (SEC)

SEC, or Gel Permeation Chromatography (GPC) is used to determine the molar mass (M_n) and distribution of polymers ($Đ$). It does not determine absolute molar mass, but can be calibrated against known standards (in this case polystyrene).

A sample of polymer in solution (THF in this work) is passed through a column packed with highly cross-linked polystyrene-divinylbenzene copolymer as the matrix. Polymer samples with a larger hydrodynamic radius are excluded from more pores in the column, and so pass through the column faster than smaller molecules. Smaller molecules are able to permeate pores of smaller volumes and so are retained in the column longer. This results in the polymer samples being separated into fractions and the retention time is measured by a detector at the end of the column. The obtained chart of elution volume against intensity provides details on molar mass distributions, from the number of peaks observed, and their dispersity from the peak width.

Molar mass can be estimated by comparing the elution time against known standards, as there is a linear correlation between hydrodynamic radius and retention time.[5] Polystyrene is usually used as a standard due to the relative ease in which monodispersed fractions can be obtained for calibration. By calibrating to polystyrene it is assumed the polymer sample being measured will interact with the column in a similar way and not interact with the solvent. Although there are limitations in using GPC analysis to determine M_n, it is widely applied in this field. Therefore, the relative molar mass compared to polystyrene are reported in this thesis.

The mollar mass can be defined as per Equations 2.10 (where N_i is the number of molecules of mass M_i, and $w_i = N_i M_i$). The distribution of polymers can be measured by the dispersity ($Đ$), where a completely monodispersed sample would have $Đ = 1$.

$$Number\ average\ molar\ mass = M_n = \frac{\sum N_i M_i}{\sum N_i}$$

$$Weight\ average\ molar\ mass = M_w = \frac{\sum w_i M_i}{\sum w_i}$$

$$Dispersity = Đ = \frac{M_w}{M_n}$$

Equations 2.10 – Definition of molar mass parameters and polydispersity.

2.4. Thermogravimetric Analysis

Thermogravimetric analysis (TGA) is a technique used to monitor the mass of a sample as a function of temperature (or time). The sample is held in a pan which accurately measures the weight whilst the instrument heats or cools the system, in a controlled environment.

In this thesis, a nitrogen atmosphere was maintained and the programme held at 50 °C for 30 minutes before the heating cycle began. The sample was heated at a rate of 5.0 °C·min^{-1} up to 500 °C and the change in sample weight measured. The degradation temperature is defined here as the temperature at which 5 % weight loss has been achieved.

2.5. Differential Scanning Calorimetry

Differential scanning calorimetry (DSC) is a technique which probes the thermal transitions of a material. This was carried out by increasing or decreasing the sample and reference pan temperature at the same rate, and measuring the difference in heat

capacity of the two pans from the amount of energy required to maintain the heating cycle.

The glass transition (T_g) of a material occurs when it changes from the glassy state to a rubbery state. Polymers have a higher heat capacity above the T_g than they do at lower temperatures, therefore, the heat flow will increase as the sample undergoes a glass transition on a heating cycle. This phenomenon is reversible and should be replicated in several heating/cooling cycles. The T_g occurs over a temperature range and is defined here at the midpoint of the slope.

2.6. Kinetic methods

2.6.1. Polymerisation kinetics

For the catalyses here, two monomers are applied (A and B); the rate equation is defined as the product of a rate constant and the concentration of all reagents/catalytic species, raised to defined orders (Equation 2.11).

$$Rate = v = k_p[catalyst]^x[A]^y[\mathrm{B}]^z$$

Equation 2.11 – General rate equation for a catalytic reaction of reactants A and B.

It is assumed that the concentration of the catalyst does not change throughout the course of the reaction, as defined by the nature of a catalytic species and these catalysts were shown to be stable in solvent under polymerisation temperatures. The isolation method assumes that all other reactants are in large excess, except for the reactant being studied, and therefore their concentration also remains constant throughout the course of the reaction. These constants can then be grouped into the observed rate constant, giving a pseudo-order rate law. For example, when it is

assumed that the concentration of B is in excess, the equation used to determine the order in A is shown below (Equation 2.12).

$$v = k_{obs}[A]^{y} \text{ (where } k_{obs} = k_p[cat]^{x}[\mathrm{B}]^{z})$$

Equation 2.12 – Isolation of rate orders to determine the order in A, y.

Assuming that the rate of reaction is determined by the rate of consumption of [A] by time, Equation 2.12 can be rewritten to form a differential equation (Equation 2.13).

$$-\frac{d[A]}{dt} = k_{obs}[A]^{\mathrm{y}}$$

Equation 2.13 – Differential equation to determine the order in A.

By solving this equation for several integer orders, the following relationships are obtained:

$$y = 0; \qquad -\frac{d[A]}{dt} = k_{obs}; \qquad [A] = [A]_0 - k_{obs}t$$

Equation 2.14 – Differential and integrated relationship for a zero order reaction.

$$y = 1; \qquad -\frac{d[A]}{dt} = k_{obs}[A]; \qquad ln[A] = ln[A]_0 - k_{obs}t$$

Equation 2.15 – Differential and integrated relationship for a first order reaction.

$$y = 2; \qquad -\frac{d[A]}{2dt} = k_{obs}[A]^2; \qquad \frac{1}{[A]} = \frac{1}{[A]_0} + 2k_{obs}t$$

Equation 2.16 – Differential and integrated relationship for a second order reaction, where $[A]_0$ is defined as the initial concentration of A.

A series of experiments comparing the initial rate of reaction (0-20 % conversion) can be measured against concentrations of A, to determine the reaction order. Alternatively, the integrated relationships can be compared if the reaction can be monitored to high (> 80 %) conversions.

2.6.2. Monitoring copolymerisation reactions

The rate of change of a monomer was determined through monitoring the reaction progress by *in situ* ATR-IR spectroscopy, where the relative changes in absorbance was measured for several frequencies, assigned to the polymer formation (Figure 2.5). Typically an IR spectrum was recorded every minute over the course of the reaction. The change in absorbance was normalised and correlated to conversion using an aliquot removed at the end of the experiment to determine conversion by ^{1}H NMR spectroscopy.

The initiation period is defined here as the time before any increase in intensity in the polymer bands. For example, in Figure 2.5 the initiation time is 52 minutes.

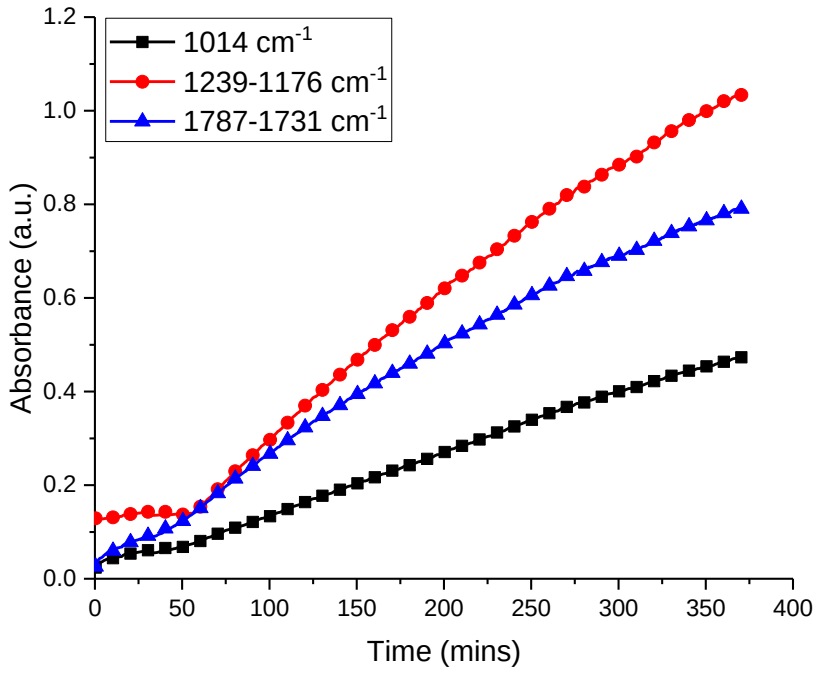


Figure 2.5 – Representative in situ ATR-IR plot showing the change in absorbance vs. time for three vibrational modes corresponding to poly(cyclohexene carbonate) formation during the CHO/CO_2 copolymerisation. For clarity, only every 20th data point is shown.

The absorbance at 1239-1176 cm^{-1} was used to monitor poly(cyclohexene carbonate) formation and its absorbance was correlated to monomer conversion. It is assumed that an increase in polycarbonate absorption is directly proportional to a decrease in

CHO conversion as quantitative carbonate formation was observed. The absorption intensity was first normalised to zero (I_0) at T_0 (where T_0 = 52 minutes in Figure 2.5). The reaction was stopped at T_f and the conversion of CHO to PCHC was calculated using ^{1}H NMR spectroscopy. The final conversion ($\%_f$ = 41 % in this example) was then used to assign the normalised intensity to CHO conversion, and, therefore, directly to [CHO] (Equations 2.17).

$$\%\ CHO\ conversion = \%_{CHO} = I \times \left(\frac{\%_f}{I_f}\right)$$

$$[CHO] = \left(1 - \frac{\%_{CHO}}{100}\right) \times [CHO]_0$$

Equations 2.17 – Calculations for determining [CHO] at a given normalised absorbance intensity.

Once the concentration of CHO at a given time has been derived, the data was fit according to the integrated form of Equation 2.15, to give the rate constant (k_{obs}) as the gradient of the line (Figure 2.6).

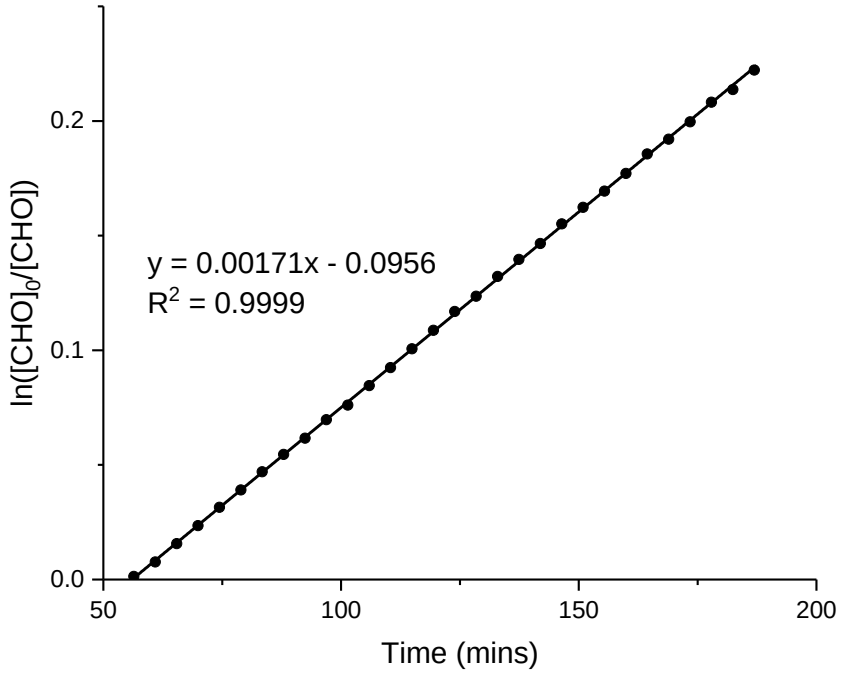


Figure 2.6 – Plot of ln([CHO]$_0$/[CHO]) vs time for CHO/CO_2 copolymerisation. The gradient of the graph represents k_{obs}, assuming a first order dependence on epoxide. For clarity, only every 9th data point is shown.

2.6.3. Treatment of errors

Errors in polymerisation runs were minimised by using stock solutions when the required mass to measure was below 12 mg. All data sets being compared were run using the same volume of solvent, in the same size and type of glassware, with identical stirrer bars and stirring rates. The time between mixing reagents and starting the experiment was also kept approximately constant and minimised. The 5 vacuum/CO_2 refill cycles were conducted at approximately the same rate and the oil bath was allowed to equilibrate for at least 30 minutes before the experiment was started. Aliquots for ^{1}H NMR spectroscopy were taken immediately after the reaction had been removed from the oil bath to minimise errors in conversion.

All R^2 values quoted in this thesis for linear fits are quoted as a coefficient of determination (COD), with a value of 1 indicating no variation in the data being fit, obtained from OriginLab software analysis. Values of 0.98 and above are considered acceptable fits for this work. Where repeat polymerisations were conducted the error is expressed as a percentage from the coefficient of variation (C_v) and calculated as per Equations 2.18.

$$C_v = \frac{\sigma}{\mu} = \frac{standard\ deviation}{mean}$$

$$\mu = \frac{\sum n_i}{N}$$

$$\sigma^2 = \frac{\sum[(n_i - \mu)^2]}{\mu}$$

Equations 2.18 – Calculations to determine C_v, where n_i is the individual data point, N is the total number of data points, μ is the mean and σ is the standard deviation.

2.7. Computational Methods

To explore the potential energy surface for the copolymerisation reaction, the Gaussian 09W, Revision D.01 package was used. When choosing a theoretical method, considerations of a solvent correction (and the ability to allow ionic intermediates to exist), geometry optimisation and transition state location must be adequately accounted for. The method must also allow for the inclusion of a dispersion energy correction, as this mediates the energy change as the polymer chain grows.

Previously, the 6-31G(d) basis set and ωB97XD functional, along with self-consistent-reaction-cavity continuum solvation model, was found to best model a CHO/CO_2 ROCOP using **[$LZn_2(OAc)_2$]**.[6] This protocol sufficiently fulfilled the requirements and predicted energies that were in line with, or better than, other methods compared to experimental data.[6,7] Dichloromethane was used in the solvation model and a temperature of 353.15 K was implemented in the calculations to better simulate the polymerisation conditions (neat epoxide, 80 °C).

All transition states yielded precisely one imaginary vibrational mode in the normal coordinate analysis. This vibrational mode corresponded to the intended reaction pathway to the product, from the reactive state. In one case an intrinsic reaction coordinate (IRC) calculation was carried out to confirm the identity of the reactants/product.

2.8. References

(1) Kember, M. R.; Knight, P. D.; Reung, P. T. R.; Williams, C. K. *Angew. Chem. Int. Ed.* **2009**, *48*, 931.
(2) Saini, P. K.; Romain, C.; Zhu, Y.; Williams, C. K. *Polym. Chem.* **2014**, *5*, 6068.
(3) Cohen, Y.; Avram, L.; Frish, L. *Angew. Chem. Int. Ed.* **2005**, *44*, 520.
(4) Garden, J. A.; Saini, P. K.; Williams, C. K. *J. Am. Chem. Soc.* **2015**, *137*, 15078.
(5) Nicholson, J. W. *The Chemistry of Polymers*; 5th ed.; Royal Society of Chemistry, 2017.
(6) Buchard, A.; Jutz, F.; Kember, M. R.; White, A. J. P.; Rzepa, H. S.; Williams, C. K. *Macromolecules* **2012**, *45*, 6781.
(7) Lehenmeier, M. W.; Bruckmeier, C.; Klaus, S.; Dengler, J. E.; Deglmann, P.; Ott, A.-K.; Rieger, B. *Chem. Eur. J.* **2011**, *17*, 8858.

Chapter 3

Synthesis and Structural Studies of Magnesium and Zinc Heterodinuclear Complexes

This chapter describes the synthesis and characterisation of a series of heterodinuclear Mg/Zn catalysts, based on a macrocyclic diphenoxy tetraamine ligand, with a series of carboxylate co-ligands. Their structure in solution and the solid phase is explored through NMR spectroscopic studies and X-ray crystallography.

3.1. Introduction

3.1.1. Previous synthesis of a heterodinuclear catalyst

The synthesis of pure heterodinuclear catalysts, with a symmetrical macrocycle, has previously proven challenging where initial investigations into the synthesis of complex **[LZnMg(OAc)$_2$]** gave mixtures of the heterodinuclear and homodinuclear species (Figure 3.1).[1]

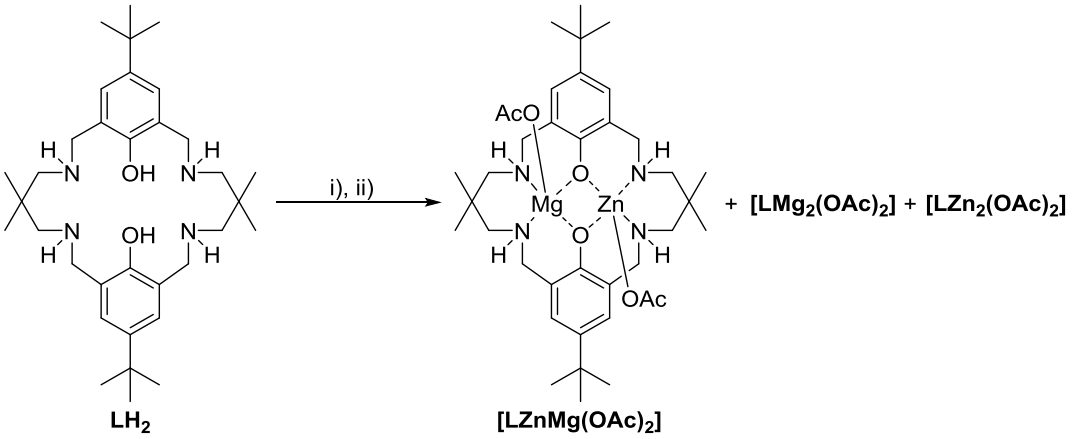


*Figure 3.1 – Previous attempt to synthesise the heterodinuclear catalyst **[LZnMg(OAc)$_2$]**, resulting in a mixture of **[LMg$_2$(OAc)$_2$]**, **[LZn$_2$(OAc)$_2$]** and **[LZnMg(OAc)$_2$]**. i) 1 eq. Et$_2$Zn, THF, –40 °C to 25 °C, 2 h; ii) 1 eq. Mg(OAc)$_2$, THF, 25 °C, 16 h.[1]*

By altering the reaction conditions and using $MgBr_2$ to deliver the second metal centre, a pure and characterisable heterodinuclear catalyst, **[LZnMgBr$_2$]**, was obtained (Figure 3.2).[2] This catalyst is monomeric in d_8-THF solution and stable up to 80 °C for 24 h.

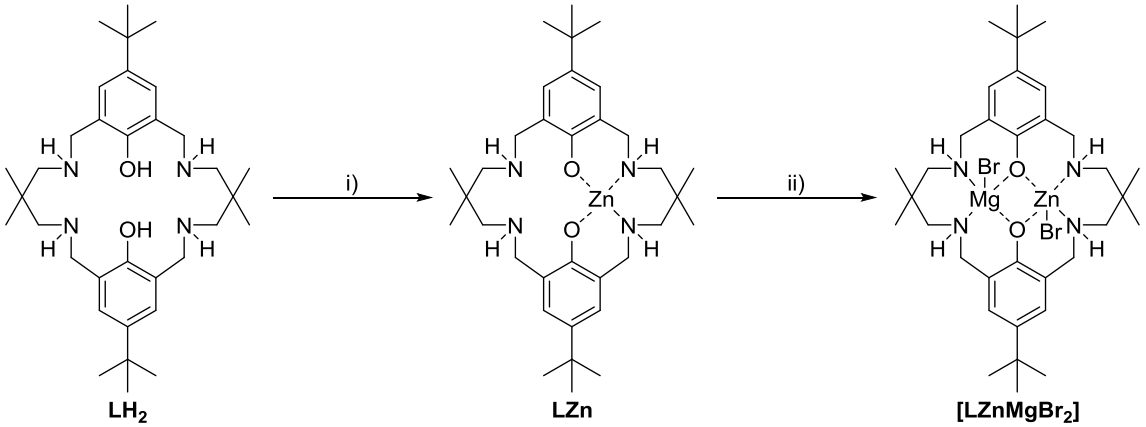


*Figure 3.2 – The first synthesis of a pure heterodinuclear complex, **[LZnMgBr$_2$]**, with the macrocyclic scaffold, **LH$_2$**. i) 1 eq. Et$_2$Zn, THF, 25 °C, 24 h; ii) 1 eq. MgBr$_2$, pyridine, THF, –78 °C to 25 °C, 1 h.*[2]

Catalyst **[LZnMgBr$_2$]**, featuring bromide co-ligands, show initiation periods of over 2 hours (at 80 °C) for the copolymerisation of CO_2 and epoxides.[2] This extended initiation period has also been observed in other catalyst systems.[3,4] Other carboxylate based co-ligands (such as acetate in complexes **[LZn$_2$(OAc)$_2$]** and **[LMg$_2$(OAc)$_2$]**) have been utilised in conjunction with this macrocycle to enhance catalyst performance.[5,6] Several detailed studies on the mechanism for the copolymerisation of CO_2 with epoxides have been carried out, for a variety of different catalysts.[7-9]

3.1.2. Aims of this chapter

It is the aim of this work to synthesise a family of catalysts which combine the rate enhancing features of heterodinuclear catalysts with more efficient co-ligands, based on carboxylate ligands. This was attempted through the reaction of complex **[LZnMgBr$_2$]** with a range of potassium carboxylate salts.

A series of *para*-substituted benzoates were chosen as target catalysts to assess whether the electronic character of the co-ligand would influence the rate, selectivity or control of copolymerisations. Benzoates were chosen with a range of inductively and mesomerically electron withdrawing or donating substituents.

3.2. Synthesis of [LZnMgBr$_2$]

The literature synthesis of the heterodinuclear complex **[LZnMgBr$_2$]** involved the isolation of the reactive intermediate **[LZn]**, before reaction with $MgBr_2$, at high dilution with strongly electron donating solvents, such as pyridine (Figure 3.2).[2] Removal of the pyridine, due to its high boiling point and strong donor characteristics, required at least 6 azeotropes with toluene and drying under vacuum for a prolonged period. The highly dilute (6 mM) conditions meant that the reaction was difficult to scale and errors in stoichiometries were likely to be high. High dilution also meant that any residual water in the solvents led to decomposition of **[LZn]**.

An alternative synthesis was developed to avoid isolation of **[LZn]**, the use of pyridine solvent, and allow more concentrated conditions. Neat THF was used where the water content was confirmed to be ≤ 3 ppm by Karl Fischer titration. The reaction was carried out on a 1.8 mmol scale, using only 40 mL of THF solvent, therefore affording a 7-fold increase in concentration. The drop wise addition of $MgBr_2$ was maintained and carried out at −78 °C, as before. These alterations to the synthesis produced the heterodinuclear complex in 90-95 % selectivity over the homodinuclear analogues (Figure 3.3). It is proposed that the low levels of homodinuclear species are due to stoichiometry errors. THF solvent was easily removed under vacuum and complex **[LZnMgBr$_2$]** was isolated in less than 24 hours from the starting free ligand, a significant (> 4 times) reduction from the previous 4 day synthesis.

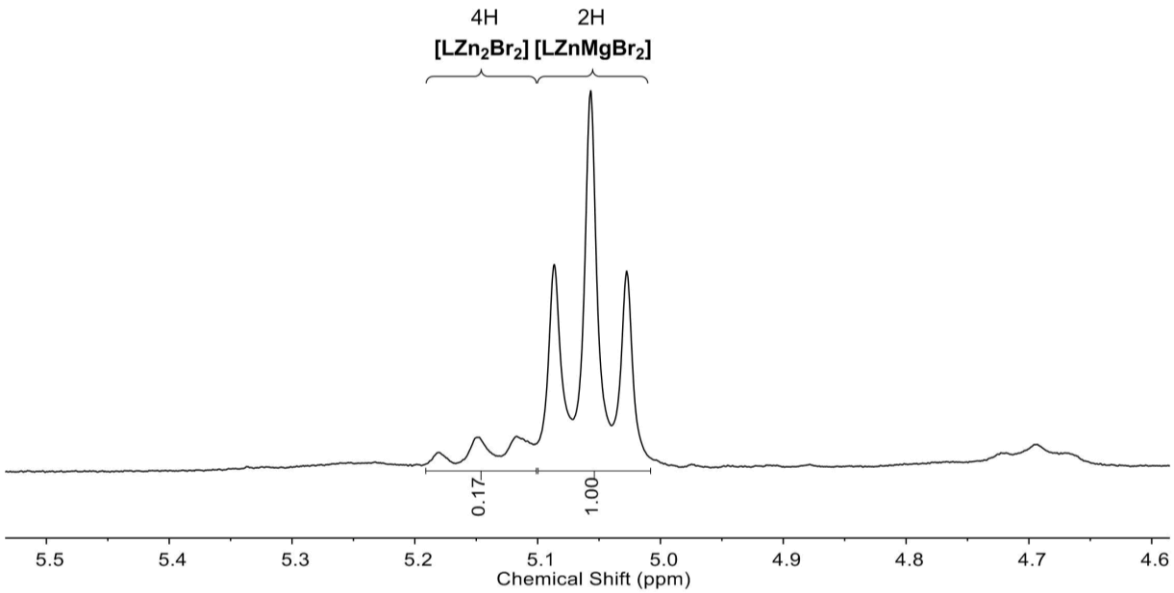


Figure 3.3 – Representative comparison of heterodinuclear content by ^{1}H NMR spectroscopy, showing a sample of ***[LZnMgBr$_2$]*** *with 92 % heterodinuclear content.*

This synthesis has proved highly reproducible and complex **[LZnMgBr$_2$]** can also be used *in situ*, without isolation, for further reactions (*vide infra*). This procedure should significantly increase yields of new catalysts.

3.3. Synthesis of Heterodinuclear Catalysts

3.3.1. General synthesis of complexes [LZnMgX$_2$]

Catalyst **[LZnMgBr$_2$]** was reacted *in situ* with a series of potassium salts in THF solvent, at room temperature, to form the desired catalysts. To improve yields, the metathesis reactions were stirred overnight before purification. The insoluble KBr by-product was removed by centrifugation and filtration. The THF solvent was removed *in vacuo* to yield the crude reaction mixture, with further purification described below. All catalysts were characterised by ^{1}H and ^{13}C NMR spectroscopy, with their structure being confirmed by 2D NMR spectroscopy, mass spectrometry and elemental analysis.

3.3.2. Benzoate derivatives

The unsubstituted potassium benzoate (KOBz) was commercially available, however, all other potassium salts were synthesised either through reaction of the benzoic acid with KH or KHMDS in THF, (at 0 °C) under argon or, more commonly with KO^{t}Bu, in EtOH, at room temperature in air using an adapted literature procedure.[10] All potassium benzoate salts were characterised by ^{1}H and ^{13}C{^{1}H} NMR spectroscopy and elemental analysis before use.

Complex **[LZnMgBr$_2$]** was formed *in situ* from **LH$_2$** and then reacted with the selected potassium benzoate to yield complexes **[LZnMg(OBz^R)$_2$]** (Figure 3.4). All complexes were soluble in THF solvent and after filtration, to remove the KBr by-product, the solutions were concentrated and then dissolved in DCM solvent. The solution was stirred for 1 h before a second filtration was carried out to remove any residual insoluble KBr. The complexes were then dried and azeotroped with pentane to aid solvent removal.

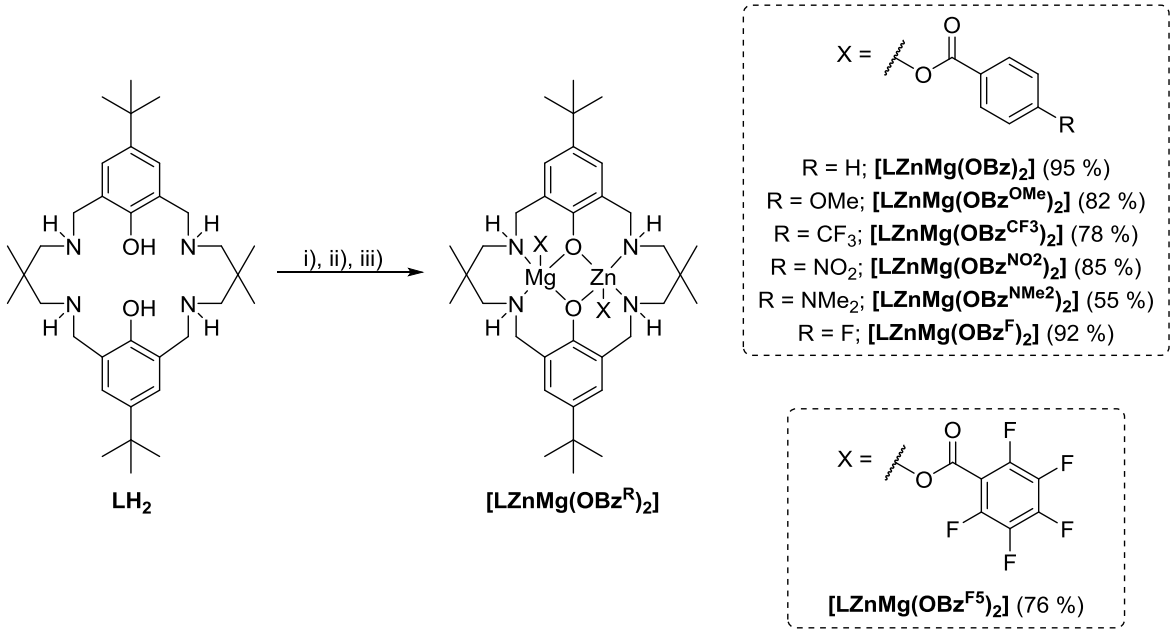


Figure 3.4 – The synthesis of a series of heterodinuclear catalysts based on benzoate co-ligands. Reagents: i) ZnEt$_2$, THF, RT, 16 h; ii) MgBr$_2$, THF, -78 °C → RT, 1 h; iii) KX, THF, RT, 16 h. Yields given in parentheses.

The metathesis reactions are judged as successful by comparison of the ^{1}H NMR spectra. For example, comparing the spectra of **[LZnMgBr$_2$]** with complex **[LZnMg(OBz^{CF3})$_2$]**, all chemical shifts are significantly altered, most notably in the methylene region (Figure 3.5).

All complexes were obtained as powders in 55 – 95 % yield and were pure by elemental analysis.

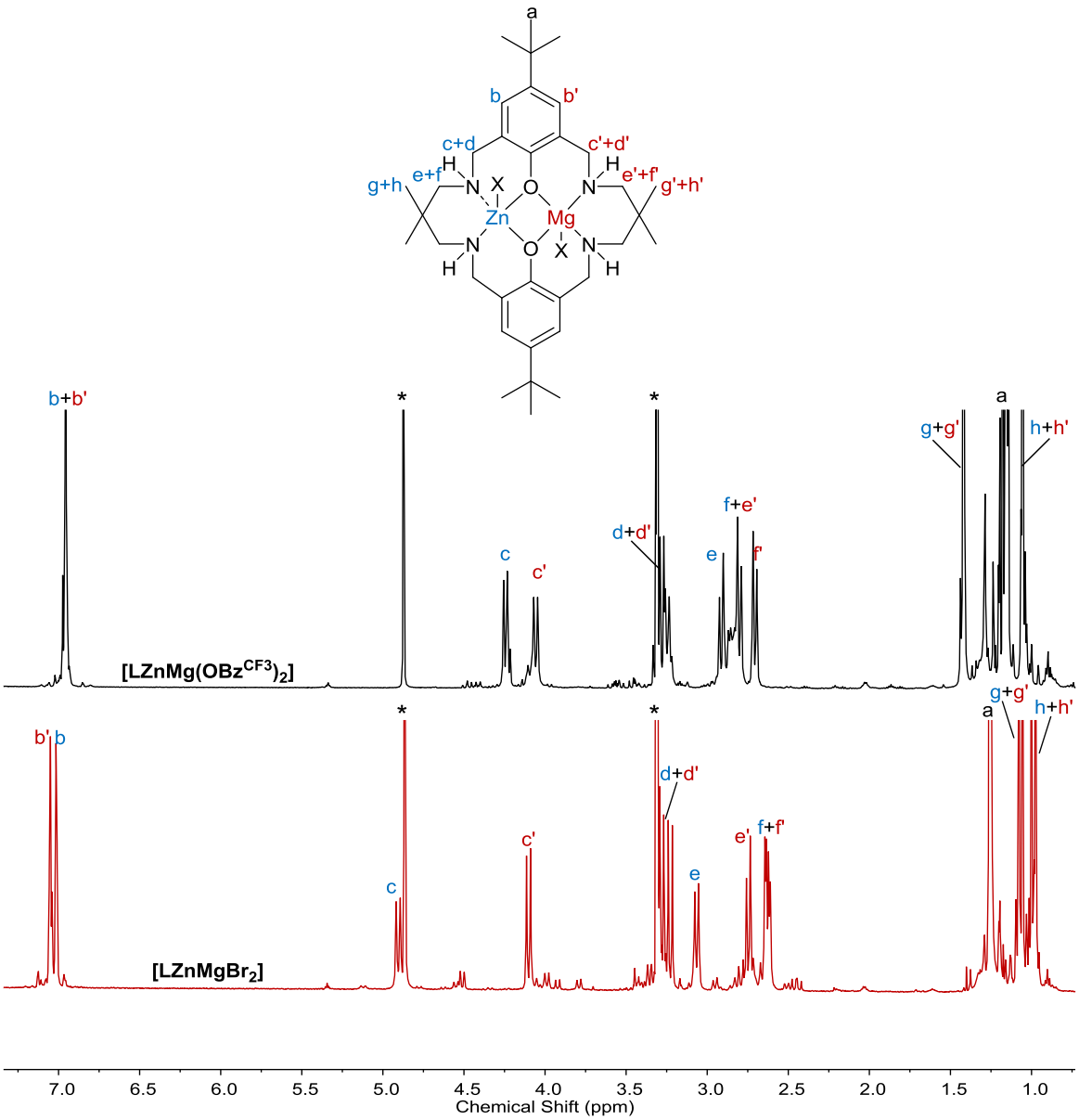


*Figure 3.5 – Comparative ^{1}H NMR spectra in d_4-methanol of complex **[LZnMgBr$_2$]**, before salt metathesis (bottom), and **[LZnMg(OBz^{CF3})$_2$]**, after salt metathesis (top). Co-ligand resonances are omitted for clarity. Deuterated solvent and water residue marked with an *.*

3.3.3. Acetate derivatives

Due to previously observed high activities with the acetate co-ligand in the homodinuclear analogues, this family of co-ligands was also targeted. Difficulties in its synthesis through direct mono-metalation routes had previously been observed.[1] However the synthesis of complex **[LZnMg(OAc)$_2$]** was successfully achieved through the metathesis of complex **[LZnMgBr$_2$]** with commercially available potassium acetate (KOAc) (Figure 3.6).

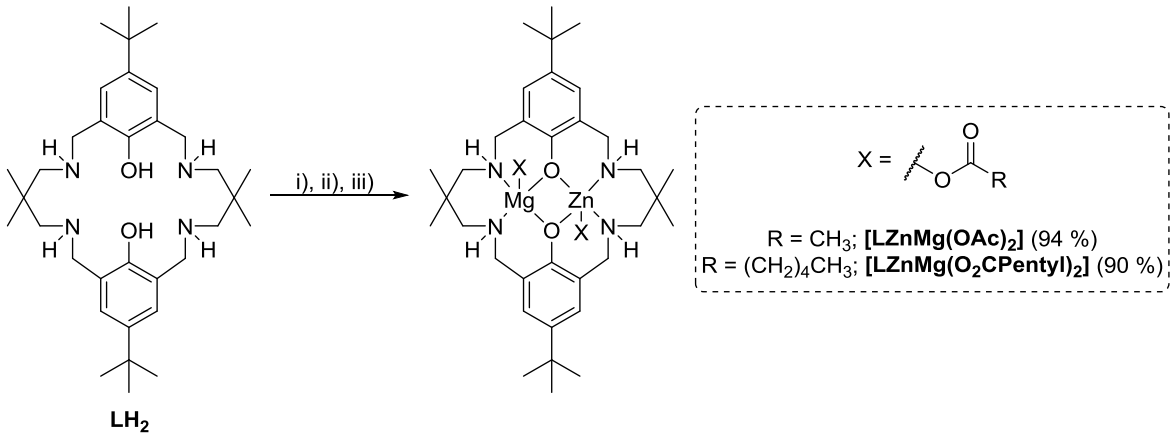


Figure 3.6 – The synthesis of heterodinuclear catalysts based on acetate co-ligands. Reagents: i) $ZnEt_2$, THF, RT, 16 h; ii) $MgBr_2$, THF, -78 °C → RT, 1 h; iii) KX, THF, RT, 16 h.

After forming **[LZnMg(OAc)$_2$]** *in situ* and isolating the THF solution from the solid KBr, only a small amount (~20 %) of the catalyst was isolated. Upon washing the initial solid with DCM solvent and filtering again, a further crop of **[LZnMg(OAc)$_2$]** was obtained. These two portions were combined, stirred in DCM and any solid residues filtered off. After drying and sequential pentane azeotropes, the final product was obtained in 94 % yield as a white powder.

In contrast, the complex formed with hexanoate co-ligands, **[LZnMg(O$_2$CPentyl)$_2$]**, showed extremely high solubility, even in pentane. The complex was therefore extracted from pentane, with any solid residues removed by filtration, and dried in

vacuo. Due to the similarity in the hydrophobic chains of the hexanoate co-ligands and the pentane solvent, a thick oily solution was obtained initially which required increased drying time to remove the solvent. This catalyst has not passed elemental analysis after several attempts at the synthesis and purification. Crystallisation or precipitation was extremely difficult due to its high solubility. As a result, this catalyst has not been extensively studied in polymerisation catalysis.

3.4. NMR Spectroscopy Studies

3.4.1. Role of solvent

Complexes with this macrocyclic ligand have previously been difficult to characterise by NMR spectroscopy, often requiring high temperatures to sharpen broad resonances in d_2-TCE.[11] This is hypothesised to be due to the highly flexible ligand backbone having many different conformations which are energetically similar, as supported by computational studies.[12] The fluxionality of these ligand conformations often leads to broadened resonances.

Co-ligands which can form a bidentate bridge, such as acetates and benzoates, have the additional fluxionality of the oxygen centres binding κ_1 or κ_2. It was therefore not surprising that initial studies in d_8-THF for the carboxylate derivatives revealed complicated and unassignable ^{1}H NMR spectra. However, the ^{1}H NMR for complex **[LZnMg(OBz)$_2$]** in d_8-THF exhibits the ligand aromatic signals as a doublet of doublets which couple in the COSY NMR spectrum ($^4J_{H-H}$ = 3 Hz) (Figure 3.7). This is proof of heterodinuclear character as the two sides of the aromatic rings on the ligand are clearly inequivalent, due to the presence of the two different metals, but the coupling shows they are part of the same complex. A mixture of homodinuclear analogues would result in two aromatic singlets, with no coupling between them.

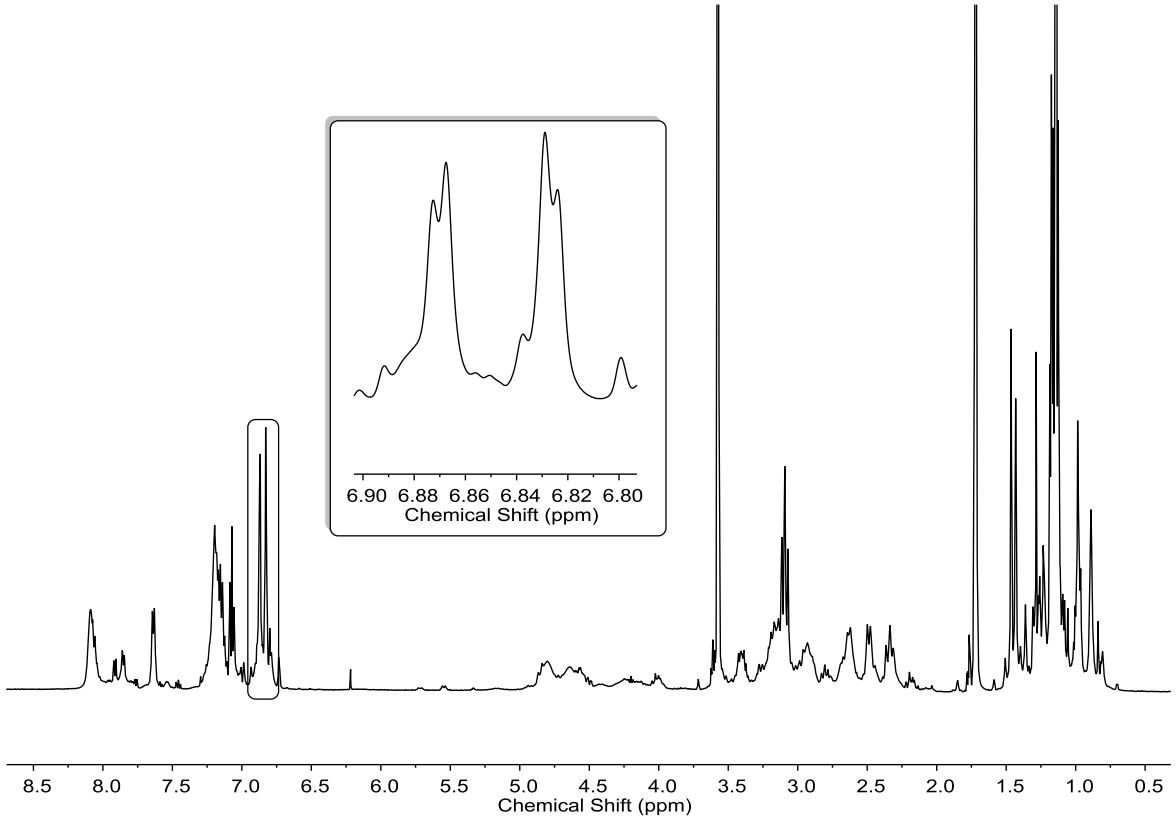


*Figure 3.7 – ^{1}H NMR spectrum for complex **[LZnMg(OBz)$_2$]**, in d$_8$-THF solvent at 298 K, zoomed in on the ligand aromatic region.*

The ^{1}H NMR spectrum in d$_8$-THF, of complex **[LZnMg(OBz^{OMe})$_2$]**, remains unchanged when the NMR sample was heated overnight at 80 °C, in a sealed Young's tap NMR tube, showing thermal stability under simulated polymerisation conditions.

Although d$_8$-THF generated complicated spectra, analysis in d$_4$-methanol yielded sharp ^{1}H NMR spectra which could be fully assigned. All ligand signals for complexes **[LZnMg(OBz^{R})$_2$]** show similar chemical shifts in the ^{1}H and ^{13}C NMR spectra, with the co-ligand signals varying significantly, as expected. The representative ^{1}H NMR spectrum of complex **[LZnMg(OBz^{CF3})$_2$]** shows the chemical inequivalence of the ligand methyl, benzylic and methylene protons (Figure 3.8).

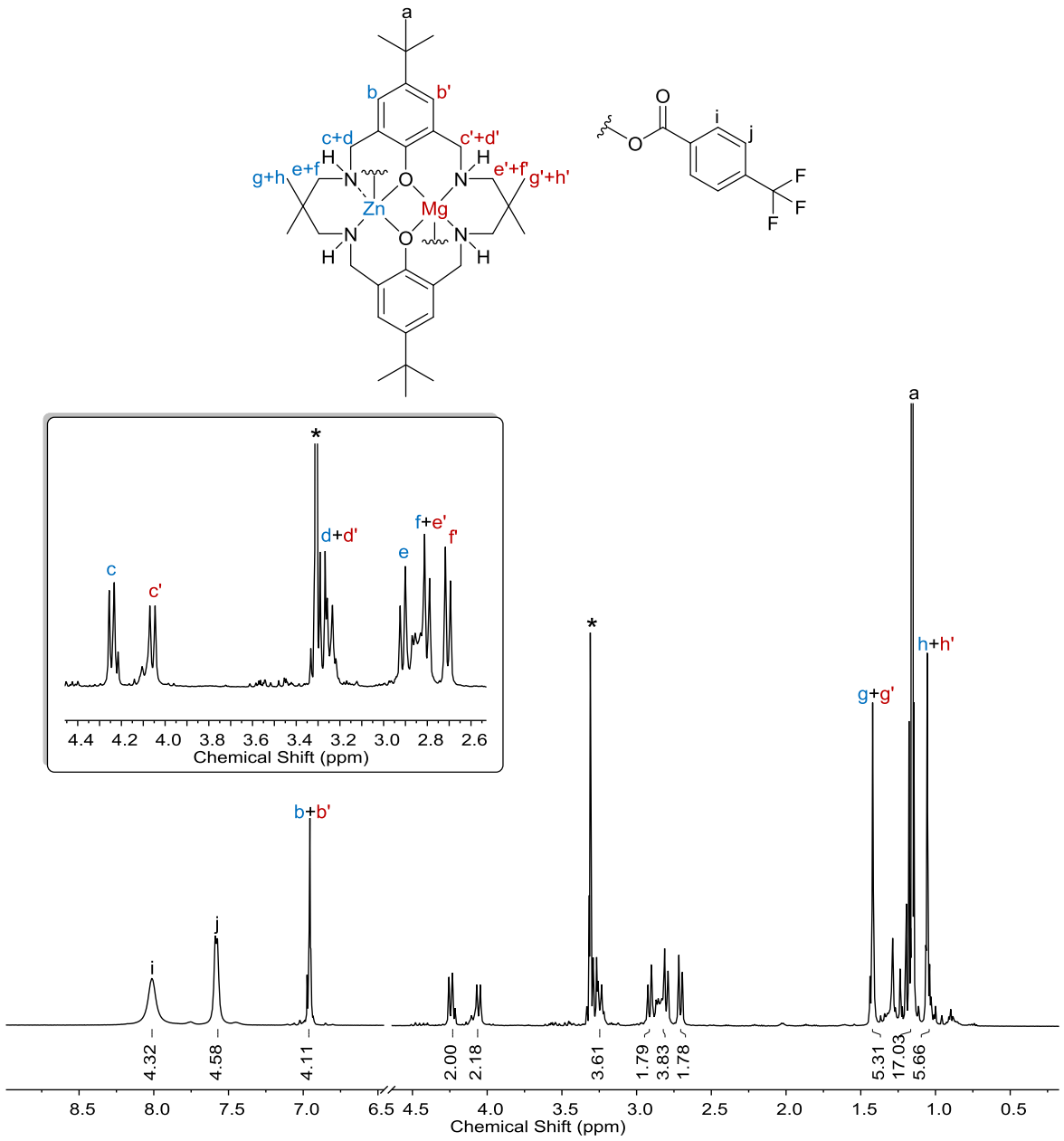


Figure 3.8 – ^{1}H NMR spectrum of ***[LZnMg(OBz^{CF3})$_2$]*** *in d_4-methanol. Deuterated solvent residue marked with an *.*

As well as observing different resonances for the two sides of the complex (e.g. c vs c', Figure 3.8) as defined by the zinc and magnesium centres, the methylene and benzylic protons are diastereotopic due to coordination of the nitrogen atoms (e.g. c vs d, Figure 3.8). This results in two different chemical shifts being observed for protons c+d, and they couple in the COSY NMR spectrum. The $^{1}H/^{13}C$ HSQC NMR spectrum confirms that protons c and d are located on the same carbon atom, but a

different one to that which c' and d' are bonded to. Similarly the methyl groups on the diamine backbone are also diastereotopic and so protons g and h give rise to two different chemical shifts. In d_4-methanol, the N–H signals are not observed, likely due to rapid solvent exchange, however, absorbances are present in the IR spectra which correspond to N–H stretches and bends (Section 3.5). It is hypothesised that the spectrum is sharp and defined in d_4-methanol as it binds to the metal centre and prevents ligand fluxionality. The benzoate co-ligands (i and j, Figure 3.8) are broad with a major and minor population.

To explore the dissimilar ^{1}H NMR spectra obtained in different solvents, a small amount of protic MeOH was added to a sample of **[LZnMg(OBz^{OMe})$_2$]** in d_8-THF. Upon this addition, the ^{1}H NMR spectrum changed dramatically (Figure 3.9). This is most apparent in the aromatic region (6 – 8 ppm) where the spectrum sharpens to give 4 clearly defined environments, relating to the benzoate co-ligands. It should be noted that one of these resonances coincides with the signals from the ligand backbone. After removing all solvents under high vacuum, the sample was redissolved in d_8-THF and the ^{1}H NMR spectrum was almost identical to the original sample. The binding of MeOH is therefore suggested to be reversible and induces a significant change in the complex fluxionality even when present in low quantities.

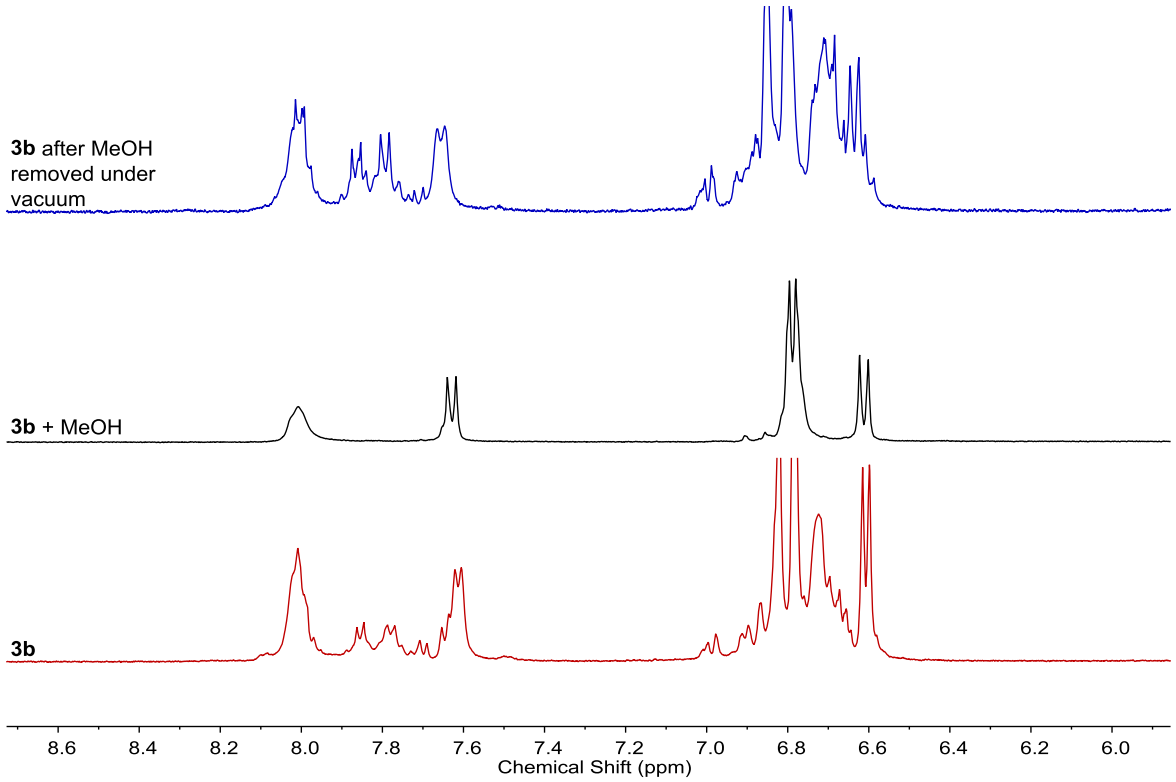


Figure 3.9 – ^{1}H NMR spectrum of complex ***[LZnMg(OBz^{OMe})$_2$]*** *in d_8-THF before (bottom) and after (middle) the addition of protic MeOH, as well as after all solvents have been removed (top).*

Looking more closely at the proposed ligand conformations in different solvents, when the catalyst is in state A (Figure 3.10), the ligand can undergo a conformational inversion, resulting in another chemically equivalent state, A'. If this process is on a similar timescale to the NMR timescale then broad signals would be observed as the different benzoate (e.g. a and a', Figure 3.10) and ligand environments are not fully resolved, hence the complicated spectrum for **[LZnMg(OBz^{OMe})$_2$]** in d_8-THF is observed. The ligand is displayed here in a 'bowl'-shape which has previously been observed as the lowest energy conformation.[12] However, it should also be noted that other conformations are possible, such as an 'S'-shape, and intermediates between these stages may be giving rise to the broadened and complicated ligand resonances.

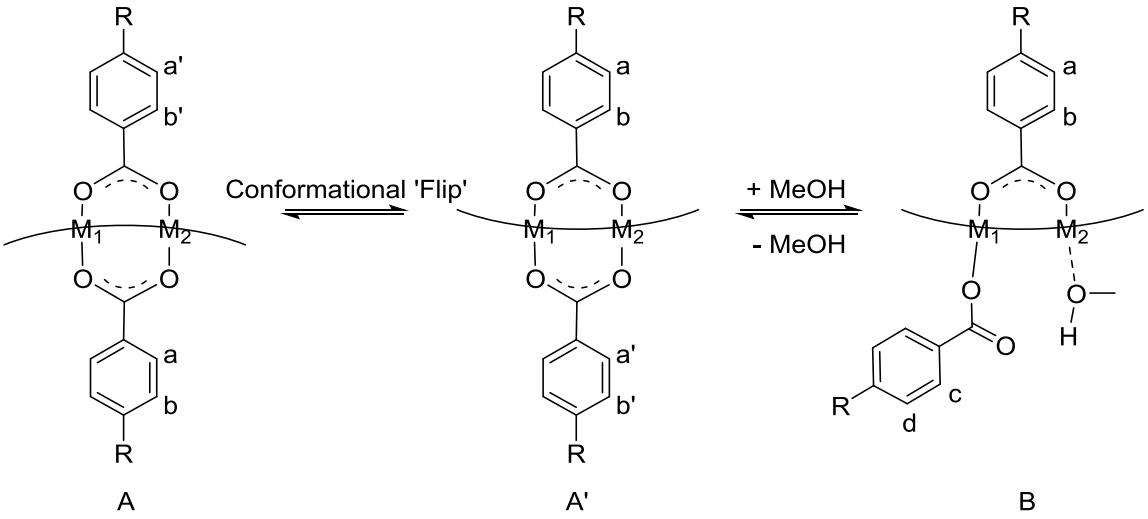


Figure 3.10 – Representation of possible equilibria in the presence of a binding donor, in this case MeOH. The ligand is represented as a curved line, depicting the 'bowl'-shaped conformation most commonly observed for this ligand scaffold.

The ^{1}H NMR spectrum obtained when MeOH is present, could be consistent with both co-ligands on the catalyst occupying 2 distinctive environments. This could be achieved by one co-ligand remaining κ_2 whilst the other is forced to adopt a κ_1 binding mode, due to the strong binding of an equivalent of MeOH (B, Figure 3.10). This renders all four benzoate environments chemically inequivalent. It is postulated that, due to the binding of a donor atom, one face of the catalyst is now significantly more sterically hindered than the other, forcing the ligand to remain in one conformation, with the convex 'open' face accommodating the extra steric bulk (B, Figure 3.10). Once the MeOH has been removed, there is no longer a strong enough donor present to favour one conformation, switching back to the equilibrium of state A-A' and therefore regenerating a very similar spectrum to that of the compound before MeOH addition. The binding mode of B is also observed in the solid state (section 3.7) and both bridging and terminal modes are observed by infrared spectroscopy (see discussions in section 3.5).

3.4.2. Variable temperature ^{1}H NMR study

The ^{1}H NMR spectrum of **[LZnMg(OBz^{CF3})$_2$]** in d$_4$-methanol, at room temperature, shows several broad resonances in the aromatic region, appearing as a shoulder to the benzoate protons (Figure 3.8). It was established that these were not due to impurities, but most likely due to an equilibrium similar to the one described above. The ROESY NMR of this complex shows that the assigned benzoate resonance at 7.99 ppm (i, Figure 3.8) is in exchange with the shoulder at 7.76 ppm (Figure 3.11). Similarly, the other benzoate resonance at 7.56 ppm (j, Figure 3.8) is shown to be in exchange with the shoulder at 7.45 ppm. A variable temperature NMR study was conducted to investigate the equilibrium (Figure 3.12).

As the temperature is decreased, the population of the shoulder resonances increases, becoming sharp and well defined, with an appearance similar to the spectrum of **[LZnMg(OBz^{OMe})$_2$]** with added MeOH (middle spectrum, Figure 3.9). This could be consistent with complex **[LZnMg(OBz^{CF3})$_2$]** corresponding to state B at 200 K or, where an equivalent of methanol is bound (Figure 3.10).

It is hypothesised that at room temperature, there is a small population of state B observed as a shoulder, which is in equilibrium with the unbound state, A, hence the presence of exchange peaks in the ROESY NMR spectrum (Figure 3.11).

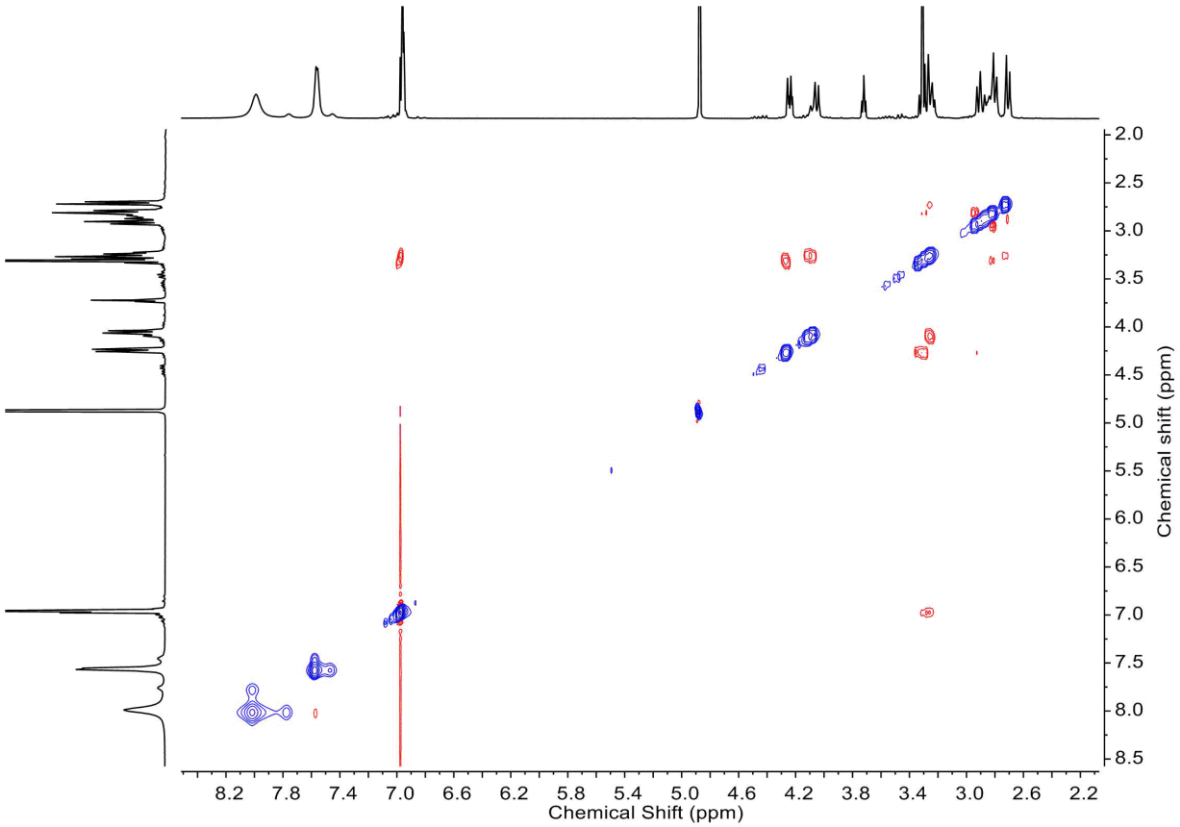


Figure 3.11 – ROESY NMR of ***[LZnMg(OBz^{CF3})$_2$]*** *in d_4-methanol at room temperature.*

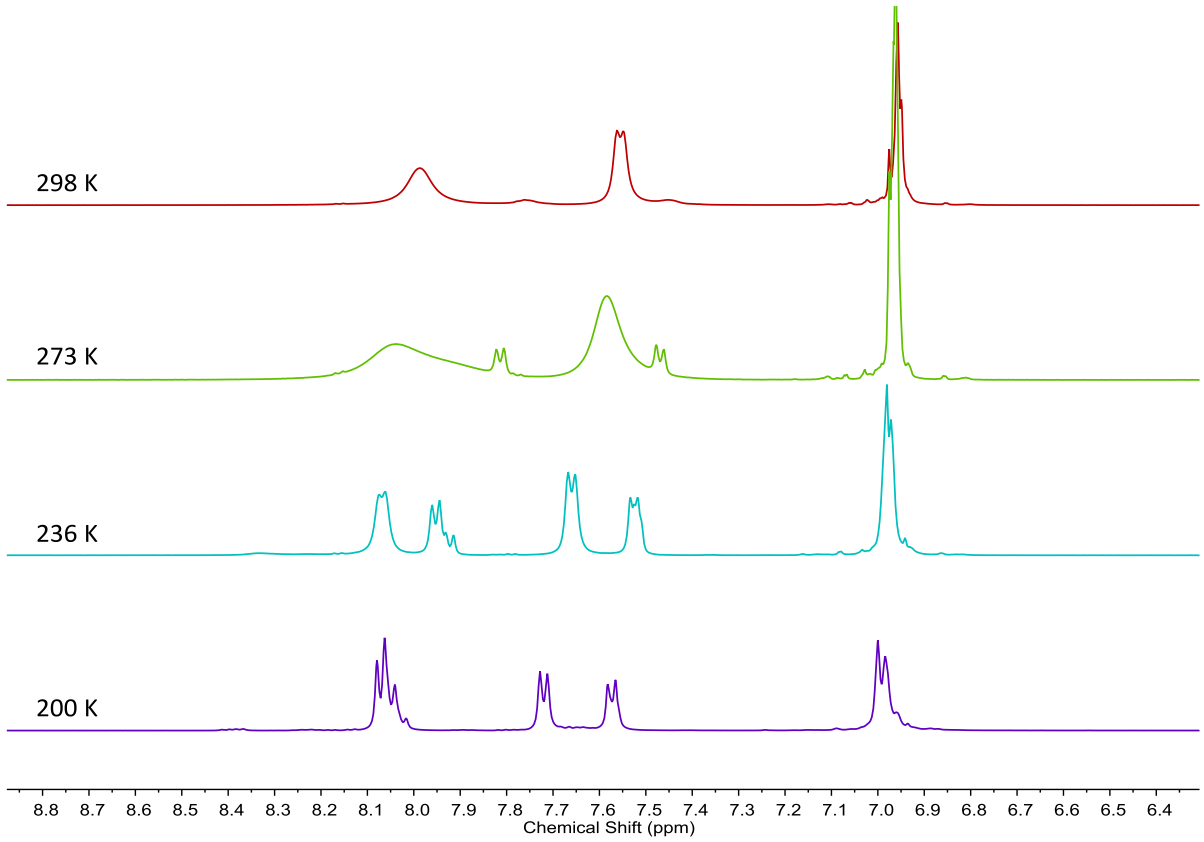


Figure 3.12 – Variable temperature ^{1}H NMR spectra of complex ***[LZnMg(OBz^{CF3})$_2$]*** *in d_4-methanol, showing the aromatic region.*

3.4.3. DOSY NMR studies

DOSY NMR studies were carried out in d_8-THF for complexes **[LZnMg(OBz^R)$_2$]** and **[LZnMg(OAc)$_2$]**, with d_8-THF selected to mimic the neat epoxide used in polymerisations. Diffusion coefficients were calibrated according to previous studies and used to estimate molecular weight (Appendix A, Figure A.1-A.8).[2] The data suggests all complexes are mononuclear under these conditions (Figure 3.13).

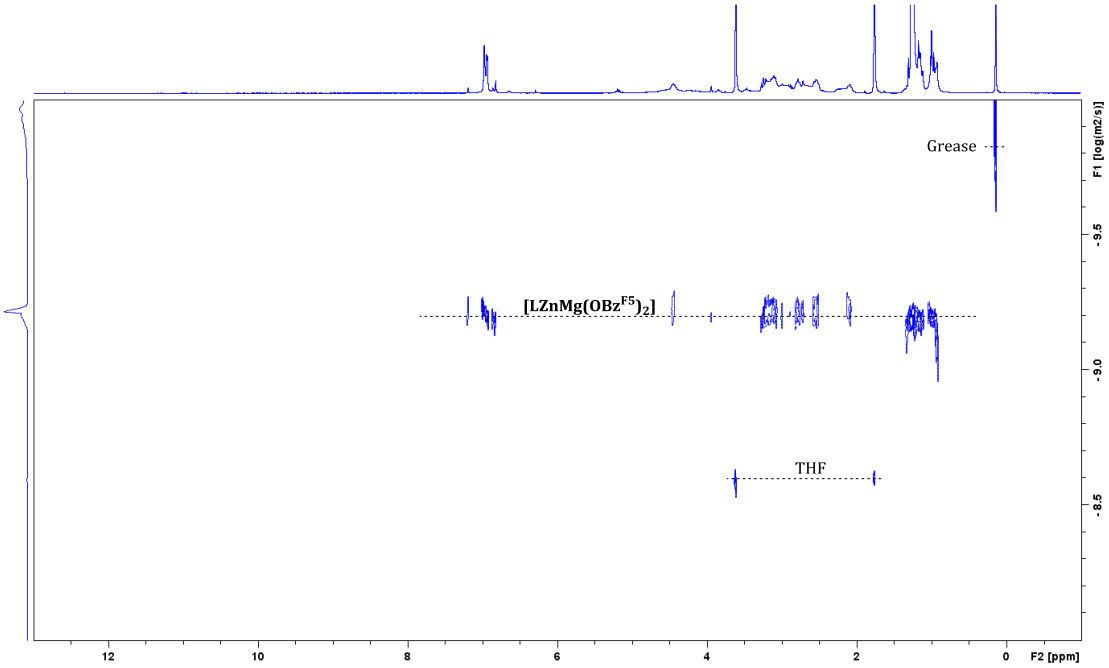


*Figure 3.13 – DOSY NMR spectrum of complex **[LZnMg(OBz^{F5})$_2$]** in d_8-THF.*

*Through comparison of the diffusion coefficient observed for **[LZnMg(OBz^{F5})$_2$]**, to a calibration plot of known standards in d_8-THF solution,[2] a predicted molecular weight of 1104 g·mol^{-1} was obtained, in very close (4 %) agreement with that of a monomeric species (1063 g·mol^{-1}).*

3.4.4. Air stability tests

All complexes were synthesised under anaerobic and anhydrous conditions. Nonetheless, it is important to assess their air stability and so a solution of complex **[LZnMg(OBz^{CF3})$_2$]** was exposed to air for several days. The solid remained colourless and the ^{1}H NMR spectrum showed that no discernible decomposition had occurred (Figure 3.14).

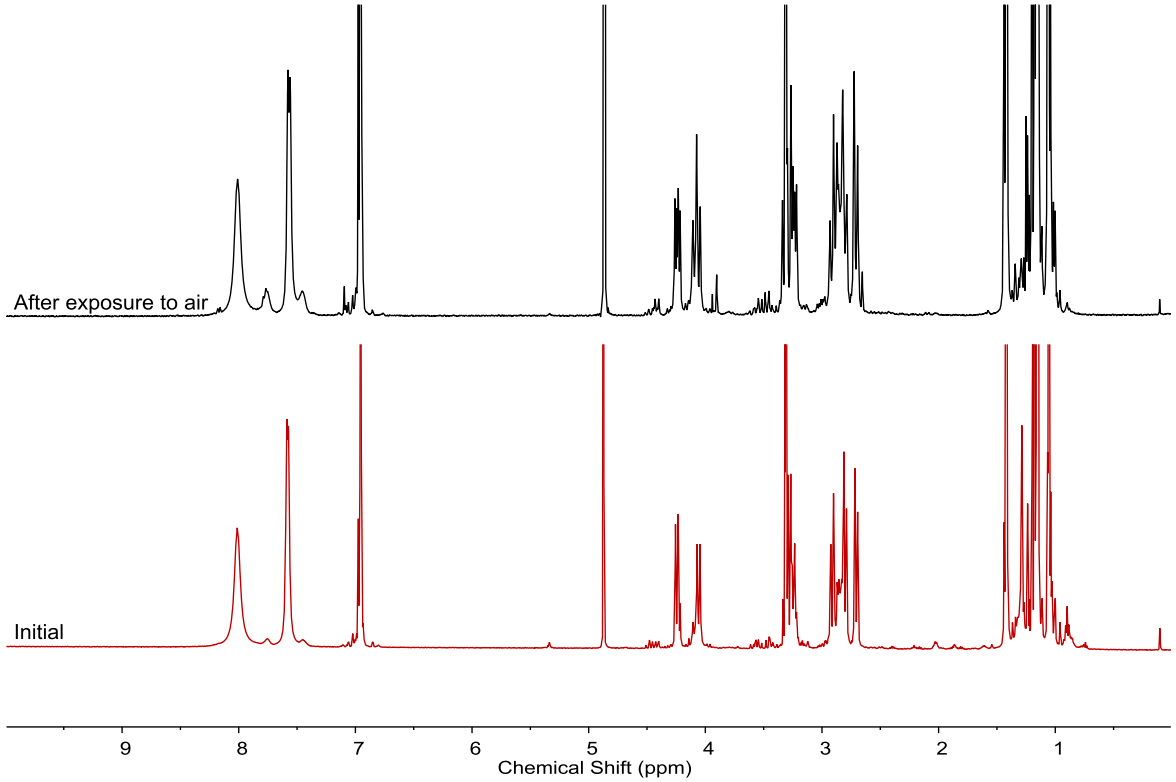


Figure 3.14 – ^{1}H NMR spectra for ***[LZnMg(OBz^{CF3})$_2$]*** *in d_4-methanol before and after exposure to air overnight.*

This is an important observation for the potential use of these complexes as catalysts – removing the need for their storage under inert atmospheres. Their use as catalysts under aerobic conditions is also explored in Chapter 4.

3.5. IR Spectroscopy

Infrared spectra were conducted in the solid phase in air, having been exposed for minimal time. All spectra (**[LZnMg(OBz^R)$_2$]** and **[LZnMg(OAc)$_2$]**) showed a distinctive N–H stretching peak at 3302 cm^{-1}, which was also present in the free ligand (Figure 3.15). These diagnostic stretching frequencies confirm the presence of the N–H groups in the complexes, which were not seen in the corresponding ^{1}H NMR spectra, probably due to deuterium exchange with d_4-methanol.

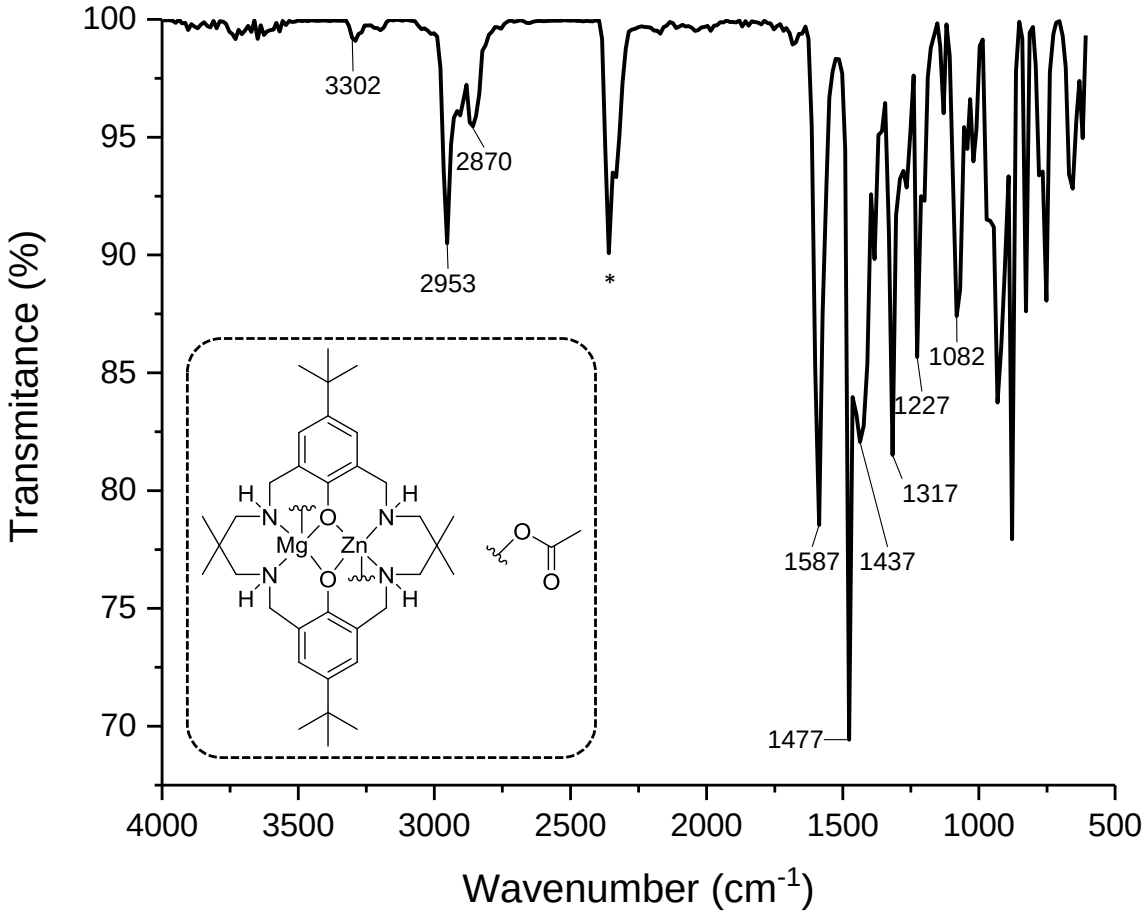


*Figure 3.15 – Infrared spectrum of **[LZnMg(OAc)$_2$]** taken in air from a powdered sample. Assignment: 3302 N–H (s), 2953 and 2870 C–H (s), 1587 C=O (asymmetric stretch, bridging carboxylate), 1477 C_{ar}–C_{ar} (s), 1437 (symmetric stretch, bridging carboxylate), 1227 C–N (s), 1082 C–O (s, ligand). CO_2 stretching frequencies observed due to background air and marked with a *.*

The asymmetric carboxylate stretching frequencies give a clear indication of binding mode.[13,14] Peaks between 1260 and 1590 cm^{-1} were assigned to a bridging (κ_2) carboxylate, whereas peaks between 1600 and 1630 cm^{-1} were assigned to a terminal (κ_1) carboxylate. In many complexes both binding modes were present however, no clear correlation between electronic structure of the co-ligand and their observed carboxylate binding mode or frequency could be seen.

3.6. Mass Spectrometry

The MALDI-ToF spectra of all complexes were obtained and the **[LZnMgX]$^+$** fragment was observed in all cases (Figure 3.16). It is presumed that the other co-ligand is cleaved in the ionisation process to form the positively charged ion. Minor populations of the

corresponding **[LZn$_2$X]$^+$** and **[LMg$_2$X]$^+$** ions were observed, possibly due to metal scrambling upon ionisation. As MALDI mass spectrometry is not a quantitative technique, this method cannot be used to assess the purity of the sample.

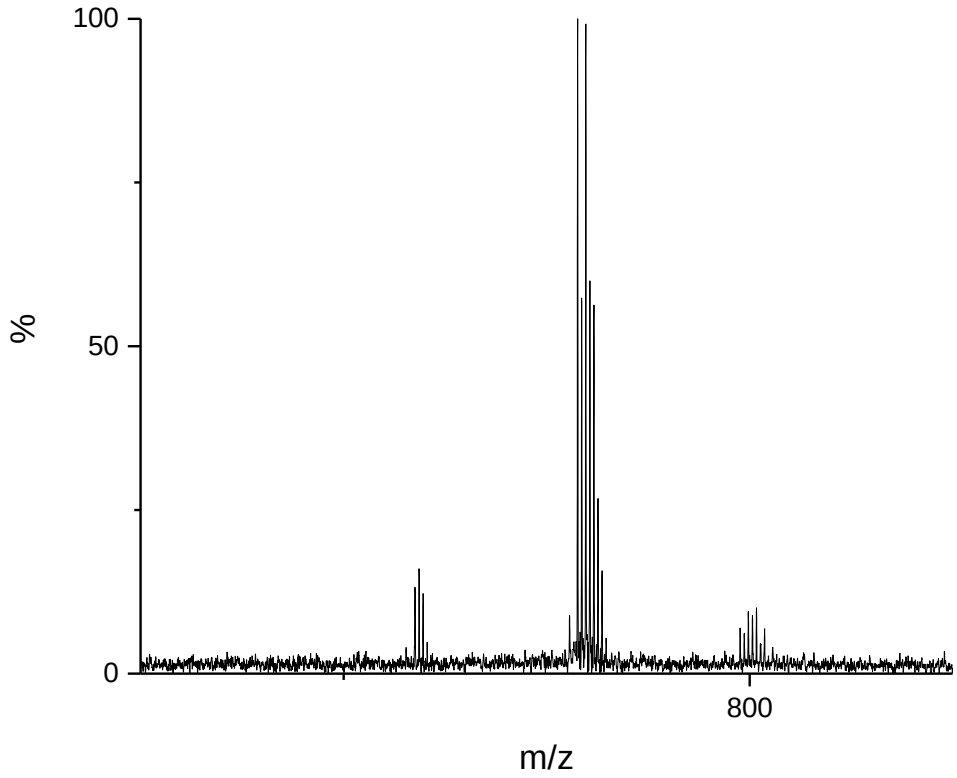


*Figure 3.16 – MALDI-ToF spectrum of **[LZnMg(OBz)$_2$]**, displaying an m/z peak of 759.4 assigned to **[LZnMg(OBz)]$^+$**.*

3.7. Crystallography

As expected from the high solubility in a range of solvents, and the flexibility of the macrocycle, these catalysts have proved very challenging to crystallise. A range of solvent systems and methods (layering, vapour diffusion, cooling) were investigated with little success.

However, it was found that crystals suitable for single crystal X-ray crystallography were obtained for catalysts **[LZnMg(O$_2$CPentyl)$_2$]** and **[LZnMg(OBz^{CF3})$_2$]**, after standing in methanol solvent for several days (Figure 3.17). Complex **[LZnMg(O$_2$CPentyl)$_2$]** crystallised with one molecule of MeOH coordinated to a

metal centre, with a further two MeOH molecules in the lattice. Complex **[LZnMg(OBz^{CF3})$_2$]** also crystallised with a coordinated molecule of MeOH.

The two different metal centres could not be distinguished in either case, due to substitutional disorder in Mg and Zn. Due to the disorder, meaningful bond length data cannot be extracted; however, the structures provide useful confirmation of connectivity.

Both structures show the ligand in a "bowl" conformation, with one equivalent of MeOH bound to a metal, one monodentate carboxylate co-ligand bound to the other metal, and the remaining carboxylate co-ligand displaying bidentate binding. Both metals have approximate octahedral geometry in the two structures.

The coordination of methanol solvent can be seen as a model for epoxide binding throughout the course of the polymerisation reactions. It is the current working hypothesis that CHO would bind in a similar regime to the MeOH in the crystal structure for **[LZnMg(O$_2$CPentyl)$_2$]** (Figure 3.17, a). This binding would render the methine carbon of CHO more electrophilic and therefore ring-opening would occur through the nucleophilic attack from the carboxylate oxygen. This is shown to be well placed in the crystal structure for **[LZnMg(O$_2$CPentyl)$_2$]** and strongly resembles the structures proposed in previous computational studies.[12]

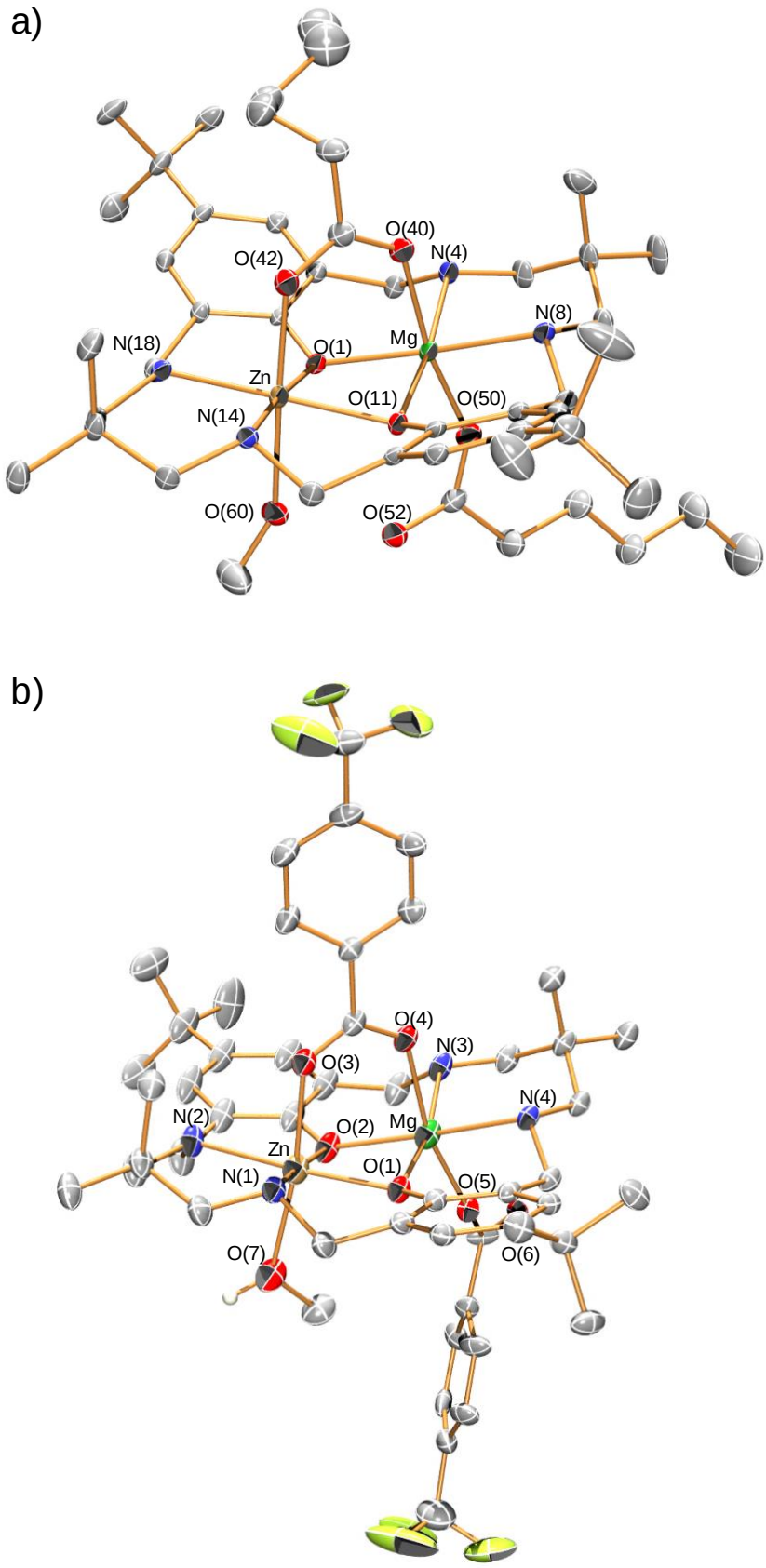


Figure 3.17 – ORTEP representation of a) ***[LZnMg(O$_2$CPentyl)$_2$]***·*MeOH and b)* ***[LZnMg(OBz^{CF3})$_2$]***·*MeOH. Both structures show substitutional disorder (a – 65:35; b – 59:41) of the Mg and Zn centres, with the major distribution shown here. Ellipsoids drawn at 50% probability, hydrogens and disorder omitted for clarity. Green = Magnesium, Bronze = Zinc, Blue = Nitrogen, Scarlet = Oxygen, Grey = Carbon, Fluorine = Yellow. Appendix B, Table B.1-B.3.*

As binding of MeOH is hypothesised to reduce the fluxionality of the system, aiding both NMR spectroscopic studies and the formation of crystals, other donors such as CHO, THF and DMAP were explored. The addition of DMAP, in THF, led to immediate precipitation as an insoluble powder. Due to the high solubility of these complexes in CHO and THF, no crystals were formed at high concentrations, low temperatures, or through the addition of antisolvents.

3.8. Conclusions and Future Work

This chapter has described the synthesis of 9 previously inaccessible heterodinuclear complexes and their characterisation. These complexes are based on a symmetrical macrocyclic framework coordinated to zinc and magnesium, with substituted benzoate or acetate co-ligands. The salt metathesis reaction shows promise for the synthesis of other heterodinuclear complexes as it is quick and reliable whilst giving acceptable to good yields (55 – 95 %).

The NMR spectroscopic studies of these complexes have been challenging but through the exploration of different solvents and temperatures, information was gleaned on the behaviour of these complexes in solution. The proven ability to bind small oxygenated molecules at the metal centres, along with the clear ligand flexibility, may be beneficial for the target ROCOP catalysis. The complexes in d_8-THF solution are mononuclear which suggests they will not form aggregates during the polymerisation.

Work remains on the synthesis of catalysts with other co-ligand manifolds. Co-ligands which cannot initiate the ring-opening of an epoxide but are highly reactive to proton

sources (e.g. aryls, alkyls, amides) are of particular interest due to their potential as pre-catalysts in the formation of telechelic polymers.

3.9. References

(1) Saini, P. K.; Romain, C.; Williams, C. K. *Chem. Commun.* **2014**, *50*, 4164.
(2) Garden, J. A.; Saini, P. K.; Williams, C. K. *J. Am. Chem. Soc.* **2015**, *137*, 15078.
(3) Rao, D.-Y.; Li, B.; Zhang, R.; Wang, H.; Lu, X.-B. *Inorg. Chem.* **2009**, *48*, 2830.
(4) Darensbourg, D. J.; Moncada, A. I. *Inorg. Chem.* **2008**, *47*, 10000.
(5) Ph.D Thesis of Prabhjot Kaur Saini, Imperial College London, 2015
(6) Kember, M. R.; Williams, C. K. *J. Am. Chem. Soc.* **2012**, *134*, 15676.
(7) Wu, G.-P.; Darensbourg, D. J. *Macromolecules* **2016**, *49*, 807.
(8) Kissling, S.; Altenbuchner, P. T.; Lehenmeier, M. W.; Herdtweck, E.; Deglmann, P.; Seemann, U. B.; Rieger, B. *Chem. Eur. J.* **2015**, *21*, 8148.
(9) Darensbourg, D. J.; Yeung, A. D. *Polym. Chem.* **2015**, *6*, 1103.
(10) Gooßen, L. J.; Rodríguez, N.; Lange, P. P.; Linder, C. *Angew. Chem. Int. Ed.* **2010**, *49*, 1111.
(11) Kember, M. R.; Knight, P. D.; Reung, P. T. R.; Williams, C. K. *Angew. Chem. Int. Ed.* **2009**, *48*, 931.
(12) Buchard, A.; Jutz, F.; Kember, M. R.; White, A. J. P.; Rzepa, H. S.; Williams, C. K. *Macromolecules* **2012**, *45*, 6781.
(13) Zeleňák, V.; Vargová, Z.; Györyová, K. *Spectrochim. Acta A* **2007**, *66*, 262.
(14) Nakamoto, K. *Applications in Coordination Chemistry: Infrared and Raman Spectra of Inorganic and Coordination Compounds*; John Wiley & Sons, Inc.: 2008.

Chapter 4

Heterodinuclear Catalysts for Copolymerisations

The activity and selectivity of catalysts **[LZnMg(OBz^{R})$_2$]** and **[LZnMg(OAc)$_2$]** are tested in the copolymerisation of CHO and CO_2 at both atmospheric (1 bar) and elevated (20 bar) pressures. Excellent activity and selectivity are observed at low pressures and higher (120 °C) temperatures, with narrow polydispersities observed over a range of molar masses. The effect of chain transfer agents and aerobic conditions is also studied, yielding telechelic polymers in well-controlled polymerisations. A range of epoxides are successfully copolymerised with CO_2; notably, with the formation of poly(propylene carbonate) as well as the formation of high molar mass poly(cyclopentene carbonate).

The copolymerisation of PA and CHO with these catalysts gives good activity and high polyester selectivity. A range of anhydrides, containing 5 to 7-membered rings, are shown to undergo ring-opening to form polyesters with a range of functionalities.

4.1. Introduction

4.1.1. Epoxide copolymerisations

The motivation behind these syntheses of polycarbonates was detailed in Chapter 1. The synthesis of poly(cyclohexene carbonate) (PCHC), from CO_2 and cyclohexene oxide (CHO) has been widely explored as a means to test new catalysts (Figure 4.1).[1-4] The polyester derived from phthalic anhydride (PA) and CHO, poly(cyclohexene phthalate) (PCHPE), is also frequently studied as a benchmark system (Figure 4.1).[5,6]

PCHPE polyesters are a potentially interesting polymer due to its high (146 °C) T_g (M_n = 13 000 g·mol^{-1}).[7] This makes them interesting candidates for use as rigid polymers or hard blocks in thermoplastic elastomers, which have previously focussed on PLA blocks (T_g = 60 °C).[8] A very recent report demonstrated amorphous multiblock polyesters, based on PCHPE and poly(ε-decalactone), which phase separated with T_g values of -45 and 100 °C.[9] This material behaved as a thermoplastic elastomer, from -20 to 100 °C, with a high elongation at break (2450 %). Shape memory character was also observed at other compositions.[9]

Once activity is known using CHO, PA and CO_2 monomers, a range of other ROCOP catalyses can be investigated using other epoxides and anhydrides.[2,10-13]

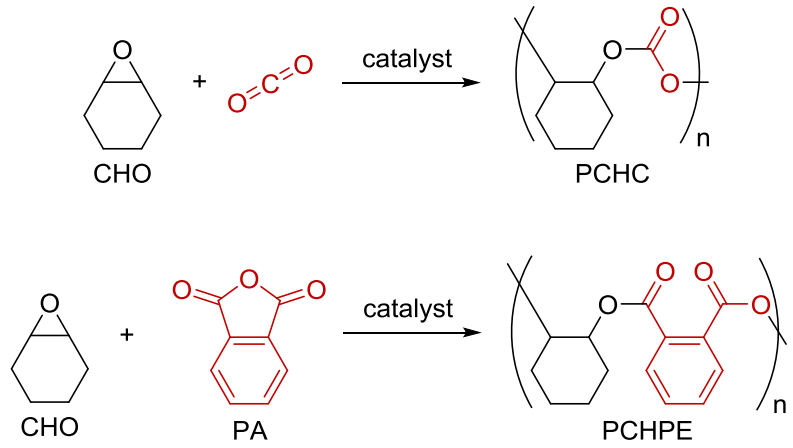


Figure 4.1 – Epoxide copolymerisations focussed on within this work. (top) The copolymerisation of CO_2 with CHO to yield poly(cyclohexene carbonate). (bottom) The copolymerisation of phthalic anhydride with CHO to yield poly(cyclohexene phthalate).

4.1.2. Chapter aims

The activity, selectivity and control of catalysts **[LZnMg(OBz^{R})$_2$]** and **[LZnMg(OAc)$_2$]** in several ROCOP reactions are assessed and compared to other literature catalysts. Differences in the rate of the polymerisations for the co-ligand series are studied and analysed. It is desirable to have catalysts which are highly active under atmospheric pressures of CO_2, and maintain polycarbonate or polyester selectivity even at high (> 100 °C) temperatures.

The potential to apply a range of epoxides and anhydrides, with various functionalities, will be tested with these catalysts, with a view to incorporate rigid rings, through anhydrides such as PA or diphenic anhydride (DPA), to synthesise high T_g materials. The installation of internal or external double bonds through the application of vinyl cyclohexene oxide (vCHO) or cyclohexadiene oxide (CHD) would enable access to materials which have the potential for post-modification, altering their materials properties or enabling their use in biomedical applications.[14,15]

4.2. Low Pressure CO_2/CHO Copolymerisations

4.2.1. Activity under 1 bar pressure of CO_2

A series of reactions were carried out at 1 bar pressure of CO_2, with a probe fitted to monitor the copolymerisation by *in situ* ATR-IR spectroscopy (Table 4.1). This allowed the initiation time (i.e. the time before an increase in polymer absorbances was observed) to be recorded, as well the initial rate. The initiation time will provide a distorted value of the TOFs, a standard measure of activity in the literature. *In situ* ATR-IR spectroscopy provides a straightforward way to monitor the reaction and extract the initial rate by analysing the formation of polymer up to 20 % conversion.

Table 4.1 – CHO/CO_2 ROCOP Data for Catalysts ***[LZnMgBr$_2$]***, ***[LZnMg(OAc)$_2$]*** *and* ***[LZnMg(OBz^R)$_2$]*** *Under 1 bar Pressure of CO_2 at 80 °C.*[a]

Cat.	Time (h)	TOF (h^{-1})[b]	TON	CO_2 (%)	Polym. (%)	Initiation (min)	k_{obs} (x 10^{-5} s^{-1})[c]	M_n [$Đ$][d]
[LZnMgBr$_2$]	6	78	247	> 99	> 99	160	3.0[e]	3100 [1.18]
[LZnMg(OAc)$_2$]	6	98	438	> 99	> 99	50	3.1	12700 [1.04] 5100 [1.16]
[LZnMg(OBz)$_2$]	6	87	407	> 99	> 99	50	2.8	13300 [1.03] 6400 [1.06]
[LZnMg(OBz^{OMe})$_2$]	3	108	252	> 99	> 99	40	3.5	8700 [1.04] 3500 [1.18]
[LZnMg(OBz^{CF3})$_2$]	6	89	383	> 99	> 99	30	2.8	10500 [1.03] 4700 [1.13]
[LZnMg(OBz^{NO2})$_2$]	3	124	307	> 99	> 99	20	3.8	10300 [1.02] 4800 [1.08]
[LZnMg(OBz^{NMe2})$_2$]	3	101	258	> 99	> 99	27	3.3	10000 [1.04] 4200 [1.14]
[LZnMg(OBz^F)$_2$]	6	83	437	> 99	> 99	45	3.4	19000 [1.03] 8000 [1.18]
[LZnMg(OBz^{F5})$_2$]	6	43	199	> 99	> 99	80	1.4	2800 [1.23]

a) Reactions were carried out using in situ ATR-IR spectroscopy. Reactions were run using a catalyst:CHO molar ratio of 1:1,000 under 1 bar pressure of CO_2. Appendix D, Figure D.1-D.18. b) TOF = number of moles of CHO consumed per mole of catalyst per hour, calculated from 0-20 % conversion, excluding the initiation period. c) Initial rate calculated assuming first order dependence of CHO on reaction rate, using data from 0-20 % conversion. d) Bimodal distribution reported individually. e) Calculated from 10-20 % due to slow initiation.

These catalysts show good activity for the copolymerisation of cyclohexene oxide (CHO) and CO_2, even under low pressures of CO_2 and 80 °C (Table 4.1). They give both high rates (TOF) and excellent selectivity (> 99 %) for poly(cyclohexene carbonate). Notably, catalysts **[LZnMg(OBz^{OMe})$_2$]**, **[LZnMg(OBz^{NO2})$_2$]** and

[LZnMg(OBz^{NMe2})$_2$] displayed the fastest rates (for CHO/CO_2 copolymerisation at 1 bar) observed for any zinc or magnesium catalysts coordinated by this ligand, with turn over frequencies of up to 124 h^{-1} (Table 4.1).[16-20] These values are also close to those achieved by using cobalt acetate catalysts at 80 °C (172 and 159 h^{-1}).[21] This increase in activity, compared to catalyst **[LZnMgBr$_2$]** (TOF of 78 h^{-1}), clearly demonstrates the potential to mediate the rate through change of the co-ligand.

The initial rate analysis from 0-20 % conversion, allows comparison by determination of the k_{obs} values (Table 4.1). As expected, catalyst **[LZnMgBr$_2$]** shows a long initiation time (160 minutes) in comparison to the acetate and benzoate catalysts at (20 – 80 minutes). This is consistent with carboxylates in general being faster initiators. Thus the choice of co-ligand has a substantial effect on the rate of initiation – by changing bromide (**[LZnMgBr$_2$]**) for a nitro-substituted benzoate (**[LZnMg(OBz^{NO2})$_2$]**), the initiation time was decreased by more than 8 times (160 vs 20 minutes).

The rate of propagation remains rather similar for the series of *para*-substituted benzoates and is discussed later.

The catalyst activity was increased by running the reactions at 120 °C (Table 4.2), whilst maintaining excellent selectivity for poly(cyclohexane carbonate) (PCHC). It was straightforward to remove the minor cyclic carbonate by-product in purification of the polymer, which was achieved using a series of precipitations from THF into pentane. This high level of selectivity, at 120 °C, was particularly pleasing as **[LZn$_2$(OAc)$_2$]** only shows 94 % selectivity for PCHC at 100 °C.[19] It is well known that

other catalysts also show increased cyclic carbonate formation at higher temperatures, often well below 100 °C.[22,23]

Table 4.2 – CHO/CO_2 ROCOP Data for Selected Catalysts Under 1 bar Pressure of CO_2 at 120 °C.[a]

Cat.	Time (h)	TOF ± 4 % (h^{-1})[b]	TON	CO_2 (%)	Polym. (%)	Initiation (min)	k_{obs} (x 10^{-5} s^{-1})[c]	M_n [$Đ$]
[LZnMg(OBz^{OMe})$_2$]	1	435	377	> 99	96	8	16.6	12300 [1.04] 5300 [1.13]
[LZnMg(OBz^{CF3})$_2$]	1	466	419	> 99	93	6	17.5	14500 [1.06] 5900 [1.15]
[LZnMg(OBz^{NMe2})$_2$]	0.75	645	430	> 99	> 99	5	28.4	21800 [1.04] 9100 [1.15]

a) Reactions were carried out using in situ ATR-IR spectroscopy. Reactions were run using a catalyst:CHO molar ratio of 1:1,000 under 1 bar pressure of CO_2. Appendix D, Figure D.19-D.24. b) TOF = number of moles of CHO consumed per mole of catalyst per hour, calculated from 0-20 % conversion, excluding the initiation period. c) Initial rate calculated assuming first order dependence of CHO on reaction rate, using data from 0-20 % conversion.

It should be noted that catalyst **[LZnMg(OBz^{NO2})$_2$]** appeared to show some discolouration, which may indicate decomposition, during copolymerisation at 120 °C. Therefore, this catalyst was not investigated further.

4.2.2. Activity discussion

These turn over frequencies for CHO/CO_2 copolymerisation are amongst the highest reported values at 1 bar pressure for any catalyst system, particularly whilst maintaining high selectivity for both carbonate and polymer linkages (Table 4.3).[20,22,24,25] There are several catalysts in the field which have shown good (150-270 h^{-1}) activity at 80 °C, with Lu's tethered salen (**C3**) being the most active.[26] **[LZnMg(OBz^{NO2})$_2$]** shows an acceptable TOF of 124 h^{-1} in comparison to these active catalysts.

Although the highly active catalyst (**D8**), reported by Rieger and co-workers, shows a higher TOF of 939 h^{-1} at 100 °C, the selectivity for PCHC was very poor (47 %).[24] Therefore at 1 bar pressure of CO_2, **[LZnMg(OBz^{NMe2})$_2$]** can access the highest activities in the field for a catalyst which is still highly (> 99 %) selective for PCHC formation.

Table 4.3 – Comparison of highly active catalysts under 1 bar pressure of CO_2 for the copolymerisation in neat CHO.

Catalyst	Temp. (°C)	Cat. Loading (mol%)	TOF (h^{-1})	Selectivity (%)
C3	50	0.02	263	99
E	80	0.1	149	98
[LCo$_2$(OAc)$_2$]	80	0.1	172	99
[LZn$_2$(OAc)$_2$]	100	0.1	25	94
D8	100	0.03	939	47
[LZnMg(OBz^{NO2})$_2$]	80	0.1	124	99
[LZnMg(OBz^{NMe2})$_2$]	120	0.1	654	99

4.2.3. Effect of chain transfer agents

A bimodal molar mass distribution was observed in the SEC analysis from the copolymerisation in CHO, due to the presence of chains initiated by co-ligand and from 1,2-cyclohexenediol, as described earlier (section 1.2.2).[21,27-30] The presence of benzoate end groups was confirmed in the MALDI-ToF spectra for these samples (Figure 4.2, a), demonstrating that the co-ligands can initiate. Monomodal molar mass distributions were obtained by the addition of 10 equivalents of chain transfer agents (Figure 4.2, b).

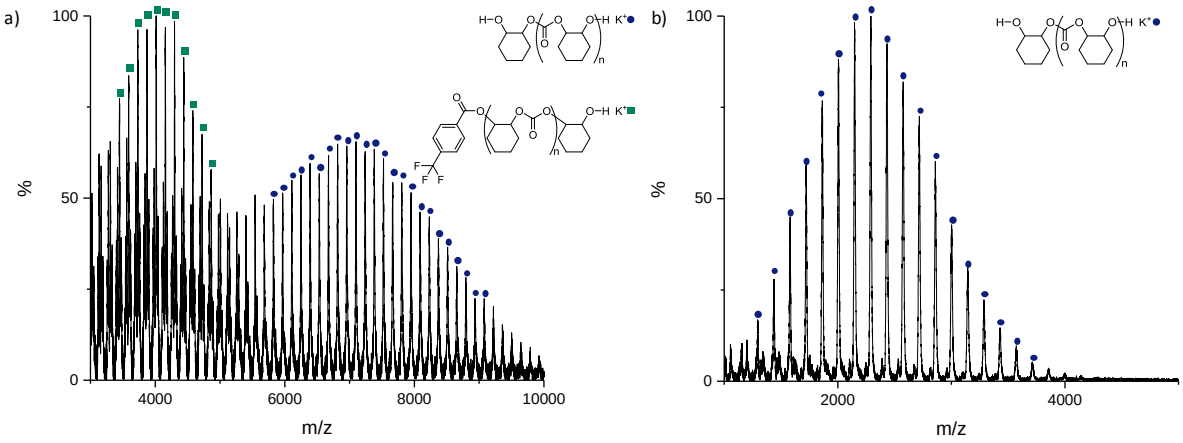


*Figure 4.2 – MALDI-ToF mass spectrum of poly(cyclohexene carbonate) formed from catalyst **[LZnMg(OBz^{CF3})$_2$]** (0.1 mol%): a) showing a bimodal distribution due to the presence of ions originating from polymers containing benzoate end groups or hydroxyl end groups; b) with 10 equivalents of added CHD, showing a monomodal distribution due to the presence of ions originating from polymers containing hydroxyl end groups.*

Catalyst **[LZnMg(OBz^{CF3})$_2$]** was used to test the tolerance to 10 equivalents of chain transfer agents (Table 4.4). When 10 equivalents of water were added, a decrease in activity was observed but the copolymerisations maintained complete selectivity for PCHC and the activity remained reasonable. The addition of 10 equivalents of CHD did not substantially reduce the rate. The copolymerisations resulted in the production of monomodal, low molar mass polyols.

Table 4.4 – CHO/CO_2 ROCOP Data for Chain Transfer Agents with catalyst ***[LZnMg(OBz^{CF3})$_2$]***.[a]

CTA (eq.)	CO_2 (%)	Polymer (%)	TON	TOF (h^{-1})	M_n [Đ]
None	> 99	> 99	634	106	7000 [1.04] 3400 [1.07]
H_2O (10)	> 99	> 99	274	46	600 [1.14]
CHD (10)	> 99	> 99	440	73	1700 [1.10]

a) *Reactions were run using a catalyst:CHO molar ratio of 1:1,000 at 80 °C under 1 bar pressure of CO_2 for 6 hours in a Schlenk.*

A linear relationship was observed between conversion and molar mass with all polymers showing narrow polydispersities. This indicates that CO_2/CHO ROCOP with these catalysts is well controlled (Figure 4.3). This, combined with the production of colourless crude polymers, make these catalysts attractive for industrial production of polyols for polyurethanes.

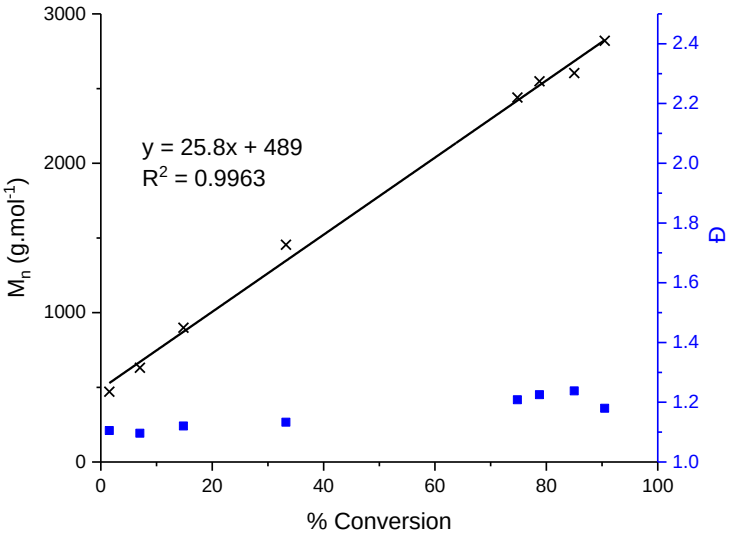


Figure 4.3 – Plot of the polycarbonate M_n (black crosses) and M_w/M_n (blue squares) versus CHO conversion. Reaction conditions: ***[LZnMg(OBz^{OMe})$_2$]****/CHO/CHD = 1/1000/10, 80 °C, 5M in toluene (Appendix C, Figure C.36-C.43).*

4.2.4. Catalysis under aerobic conditions

To test the aerobic stability of these catalysts, a solution of catalyst **[LZnMg(OBz^{OMe})$_2$]** in 1000 equivalents of CHO was stirred in air for 1 hour. This solution was then flushed with CO_2, without the application of vacuum, and heated to 80 °C for 6 hours, whilst stirring. The catalyst maintained its high activity and selectivity for PCHC formation with > 99 % polycarbonate linkages (Table 4.5). The activity (93 h^{-1}) is similar to that displayed by the same catalyst using ATR-IR spectroscopy (84 h^{-1}, including initiation time).

*Table 4.5 – CHO/CO_2 ROCOP Data under Aerobic Conditions for catalyst **[LZnMg(OBz^{OMe})$_2$]**.[a]*

CO_2 (%)	Polymer (%)	TON	TOF (h^{-1})	M_n [$Đ$]
> 99	> 99	559	93	2900 [1.13]

a) Reaction was run using a catalyst:CHO molar ratio of 1:1,000 at 80 °C under 1 bar pressure of CO_2 for 6 hours. Catalyst and CHO were stirred in air for 1 h at 25 °C before purging the system with CO_2 and heating to 80 °C.

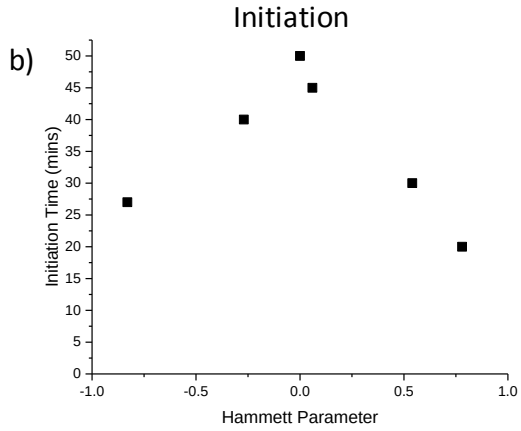
The ability to carry out these polymerisations, with nearly identical activity or selectivity, without the need to store the catalysts and load the reaction vessels under anaerobic conditions, could be useful for future uses at larger scale.

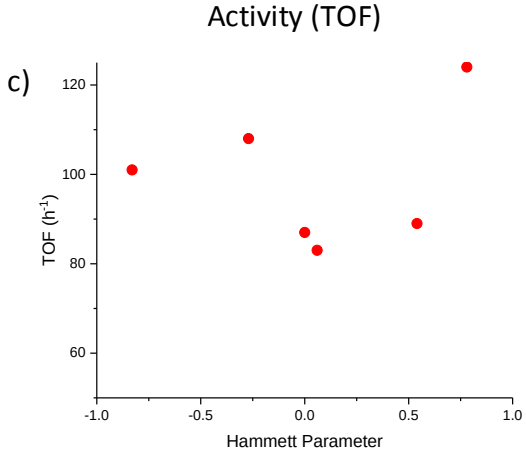
4.2.5. Effect of co-ligand

The electronic effects of the co-ligands can be compared to the Hammett parameters for this series of benzoates (Figure 4.4). Using the unsubstituted benzoate as a point of comparison, catalysts **[LZnMg(OBz^{OMe})$_2$]** and **[LZnMg(OBz^{NMe2})$_2$]** have increased electron donating capacity. Catalyst **[LZnMg(OBz^{NO2})$_2$]** is strongly mesomerically electron withdrawing and **[LZnMg(OBz^{CF3})$_2$]** inductively withdrawing. Catalyst **[LZnMg(OBz^{F})$_2$]** is mesomerically electron donating but inductively withdrawing and so the overall electronic properties are very similar to catalyst **[LZnMg(OBz)$_2$]**.

a)

Catalyst *para*-substituent	Hammett Parameter
H	0
OMe	-0.27
CF_3	0.54
NO_2	0.78
NMe_2	-0.83
F	0.06





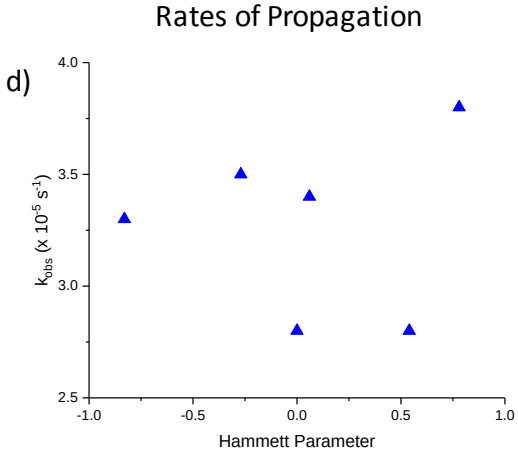


Figure 4.4 – Comparison of Activities vs Hammett Parameters for catalysts ***[LZnMg(OBz^R)$_2$]*** *in the copolymerisation of CO_2/CHO at 1:1000 catalyst:CHO loading at 80 °C. a) Table of catalysts with their corresponding Hammett Parameter for the corresponding benzoic acid;[31] b) Time taken for polymer formation to start, observed by in situ ATR-IR spectroscopy; c) Turn over frequency based on conversion by ^{1}H NMR spectroscopy at a given time; d) Rate constant calculated for the first 20 % conversion.*

Comparing the data collected using *in situ* ATR-IR spectroscopy against Hammett parameter, a halving of initiation time is observed by either strongly electron donating (NMe_2) groups, or strongly electron withdrawing (NO_2) groups (Figure 4.4, b). However, when looking at overall rate parameters (TOF or k_{obs}), there is no obvious correlation between electronic substituent factors and rate (Figure 4.4, c and d).

All reactions were carried out under identical conditions, stirring rates, heating rates and scale, as well as being homogeneous solutions. The difference in initiation time is,

therefore, proposed to relate to the catalyst structure, rather than any physical differences between experiments.

To rationalise the observations, there are two competing factors to consider in the initiation and rate determining steps of this reaction: epoxide binding and carbonate attack. A more Lewis acidic metal centre would be expected to bind the epoxide more strongly, resulting in a more electrophilic carbon centre at the epoxide. However, increasing the Lewis acidity of the other metal, in the dinuclear catalyst, may strengthen the M–O_2CR bond, increasing the barrier to epoxide ring-opening. These two competing considerations make predicting catalytic activity challenging, and so comparing only the Hammett parameters with activity (TOF or k_{obs}) does not give an obvious correlation (Figure 4.4).

An alternative comparison could be drawn from the stretching frequencies observed in the IR spectra, for the benzoate carboxylate moieties. The previously described co-ligand electronic factors would determine the distribution of electron density across the carboxylate, and therefore the stretching frequency. A terminal carboxylate stretching frequency was observed for all *para*-substituted benzoate co-ligands; these are compared in Figure 4.5.

There appears to be a very weak negative correlation between initiation time and carboxylate stretching frequency (Figure 4.5, b). No clear correlation was observed between the co-ligand stretching frequency with either activity (TOF) or the rate of propagation (Figure 4.5, c and d). The lack of correlation is perhaps expected here as the co-ligand is suggested to not be strongly involved in the rate determining step.

a)

Catalyst *para*-substituent	Carboxylate Frequency (cm^{-1})
H	1603
OMe	1597
CF_3	1618
NO_2	1626
NMe_2	1612
F	1610

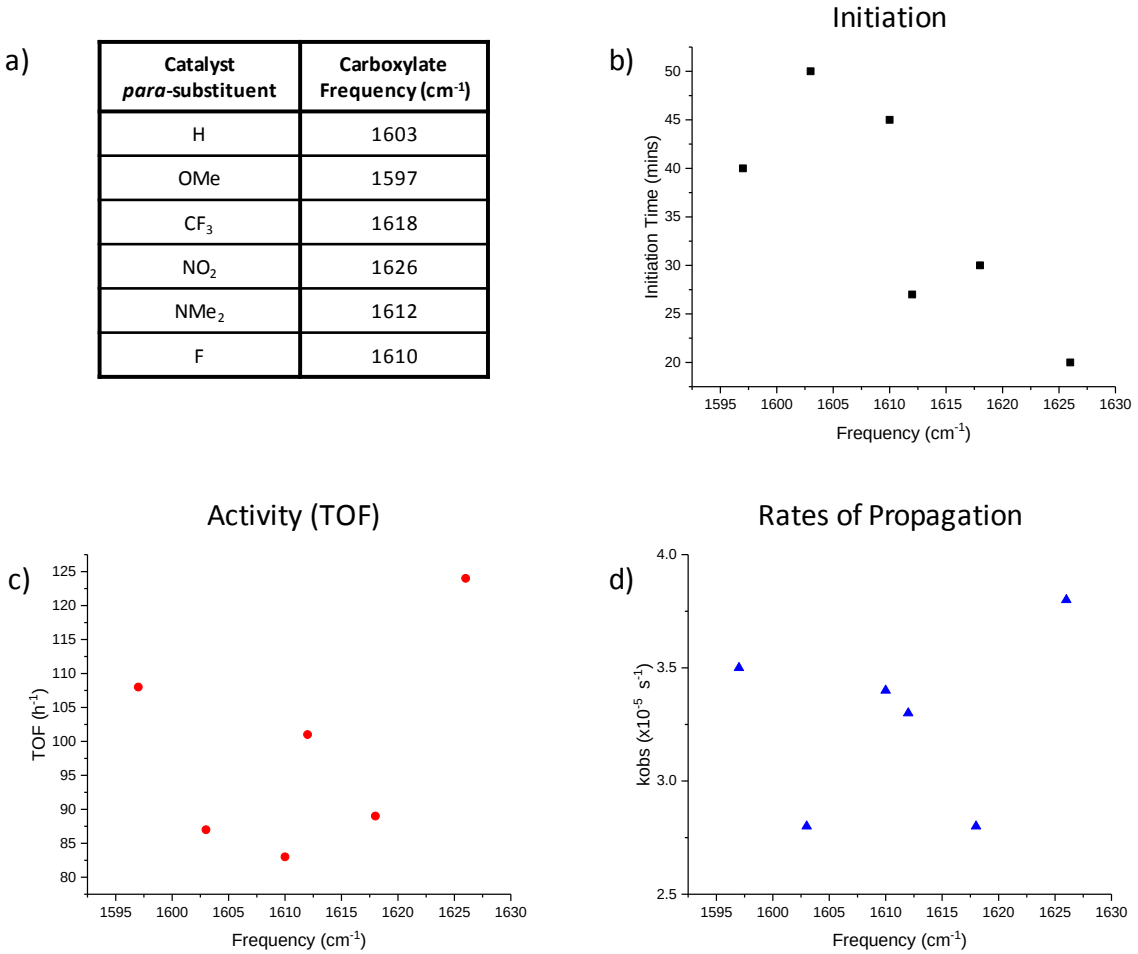


Figure 4.5 - Comparison of activities vs terminal carboxylate stretching frequency for catalysts ***[LZnMg(OBz^R)$_2$]*** *in the copolymerisation of CO_2/CHO at 1:1000 catalyst:CHO loading at 80 °C. a) Table of catalysts with their corresponding terminal carboxylate stretching frequency; b) Time taken for polymer formation to start, observed by in situ ATR-IR spectroscopy; c) Turn over frequency based on conversion by ^{1}H NMR spectroscopy at a given time; d) Rate constant calculated for the first 20 % conversion.*

As the carboxylate co-ligand is directly involved in the initiation step, by nucleophilic ring-opening of an epoxide, it is expected that a more nucleophilic carboxylate would display a shorter initiation time. The weak negative correlation implies benzoates with stronger stretching frequencies (i.e. where the benzoate *para*-substituent is a -NO_2, -CF_3 or -NMe_2 group), show shorter initiation (below 30 minutes).

Crudely, electron withdrawing groups have been found to increase the stretching frequency of benzoate derivatives, due to an increase in bond order of the carboxylate group.[32] This suggests that the nucleophilic oxygen lone pairs are less available when the stretching frequency of the carboxylate increases. Clearly this

does not explain the weak negative correlation observed with initiation time, suggesting that the rate of initiation cannot be simply explained by the nucleophilicity of the carboxylate.

4.3. High Pressure CO_2/CHO Copolymerisations

4.3.1. Activity

Table 4.6 - CHO/CO_2 ROCOP Data for Catalyst ***[LZnMg(OBz^{CF3})$_2$]*** *Under 20 bar Pressure of CO_2.*[a]

Catalyst (mol%)	Temp (°C)	Time (h)	PCHC Selectivity (%)	TON	TOF (h–1)	Mn [Đ]
0.01	80	4	> 99	732	183	1900 [1.16]
0.01	120	0.5	> 99	4415	8830	44400 [1.04] 21200 [1.05]
0.005	120	4	> 99	5435	1359	54400 [1.04] 26600 [1.04]

a) Reactions were carried out in a Parr high pressure vessel with an impeller at 20 bar.

When carrying out the copolymerisation of CHO and CO_2 in a Parr reactor, at 1:10,000 catalyst to CHO loading and 120 °C, catalyst **[LZnMg(OBz^{CF3})$_2$]** showed a very high turnover frequency of 8830 h^{-1}, without any compromise in selectivity (Table 4.6). Catalyst **[LZnMg(OBz^{CF3})$_2$]** is tolerant to low loadings (20,000) which results in high molar mass PCHC.

4.3.2. Discussion

The activities displayed by **[LZnMg(OBz^{CF3})$_2$]** in a Parr reactor are amongst the highest TOF values obtained for CHO/CO_2 copolymerisation (Table 4.7). Although this is not as fast as the best literature catalyst (**D8**), it demonstrates superior selectivity for PCHC (> 99 vs 88 %).[24] At 80 °C **[LZnMg(OBz^{CF3})$_2$]** is an order of magnitude slower than the fastest salen catalyst (**B4**) at this temperature, however, operating industrial plants at a lower temperature is undesirable due to product viscosity. This further demonstrates the potential of these catalysts to be useful in the production of polycarbonates from CO_2.

Table 4.7 – Selected catalysts for the copolymerisation of CHO/CO_2 at elevated pressures.

Catalyst	Cocat.	Temp. (°C)	ρCO_2 (bar)	Cat. Loading (mol%)	[CHO] (M)	TOF (h^{-1})	Selectivity (%)
B3	[PPN]N_3	60	34	0.04	Neat	405	99
B4	[PPN]Cl	80	35	0.04	Neat	1153	99
D8	-	100	30	0.013	5	155000	88
G	-	100	10	0.05	Neat	370	99

4.4. Alternative Epoxides

4.4.1. Activity scope

Since this series of catalysts shows excellent activity and selectivity in the copolymerisation of CHO and CO_2, a range of other epoxides were tested. It was envisaged that due to the generally increased activities, previously inaccessible polymer structures could be accessed using these catalysts. The scope of epoxides assessed is shown in Figure 4.6.

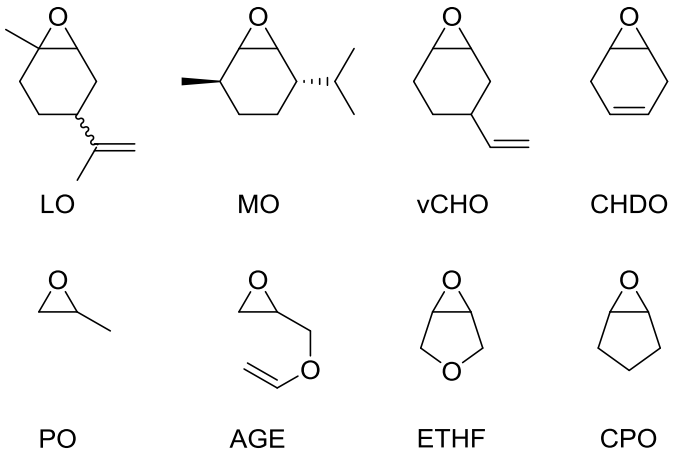


Figure 4.6 – Range of epoxides tested for the copolymerisation with CO_2.

The terpene-derived, renewable epoxide limonene oxide (LO) remained inactive towards any ring-opening reactions under high temperature and pressure of CO_2 (Table 4.8). This is perhaps unsurprising given its previously observed stability with a range of catalysts, indeed very few catalysts have been reported with this monomer.[13,33,34] This is likely due to the sterically highly disfavoured tertiary alkoxide propagating species.

Menthene oxide (MO) is another plant-derived renewable monomer which has been under explored in copolymerisation.[35] Encouragingly, this epoxide was active to the copolymerisation with CO_2 at only 80 °C and 1 bar pressure. Very little polyether was observed, and only relatively small amounts of cyclic carbonate were formed after the initial stages of polymerisation. Although activity was significantly reduced compared to CHO, it is a promising result as conditions could be optimised in future work with increasing temperatures and pressures to achieve higher rates and conversions.

Table 4.8 – Epoxide/CO_2 ROCOP Data for Catalyst ***[LZnMg(OBz^{OMe})$_2$]*** *with a range of epoxides.*[a]

Epoxide	ρCO_2 (bar)	Temp. (°C)	Catalyst (mol%)	Time (h)	CO_2 (%)	Polym. (%)	TON	M_n [Đ]
LO	20	120	0.01	72	0	0	0	-
MO	1	80	0.1	6	97	86	28	800 [1.13]
MO	1	80	0.1	24	99	94	256	3000 [1.20]
vCHO	1	80	0.1	6	> 99	> 99	428	31000 [1.04] 12200 [1.19]
CHDO	1	80	0.1	6	> 99	74	6	2400 [1.27]
PO	20	60	0.01	72	98	26	593	4000 [1.20] 1200 [1.20]
AGE	1	80	0.1	6	> 99	0	105	-
AGE	1	80	0.1	24	> 99	0	269	-
ETHF	1	80	0.1	6	> 99	93	83	1100 [1.64]
ETHF	1	80	0.1	24	> 99	98	289	1300 [1.76]

a) *Reactions at 1 bar pressure of CO_2 were carried out in a Schlenk with magnetic stirring. Reactions at 20 bar were carried out in a Parr high pressure vessel with an impeller.*

Other cyclohexene-based epoxides were tested to investigate the ability to install additional functionality into the polymer backbone. Vinyl CHO (vCHO) was tested as it can undergo thiol-ene click post-modification to access various new polycarbonate and graft polymers.[14,15,36-40] ROCOP using vCHO and CO_2 showed high activity (71 h^{-1}), with complete polycarbonate selectivity at 80 °C and 1 bar pressure. The poly(vinyl cyclohexene carbonate) contains an external double bond per repeat unit; these

alkenes can be reacted with thiols to install different functionality to the polymer (Figure 4.7).[14,15,37]

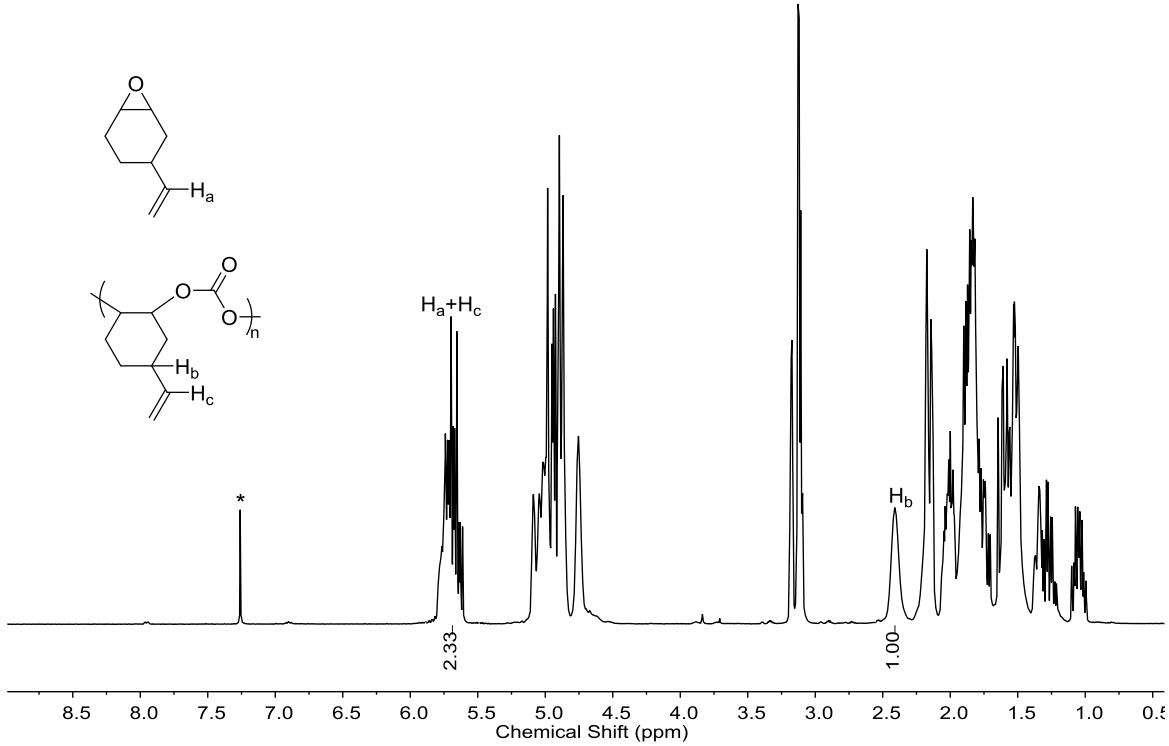


*Figure 4.7 – ^{1}H NMR spectrum of the crude reaction mixture for the copolymerisation of vCHO and CO_2, in $CDCl_3$, used to calculate the TON for the copolymerisation. $CDCl_3$ residual solvent signal marked with *.*

The copolymerisation with cyclohexadiene oxide (CHDO) was significantly slower than with vCHO, showing only low activity after 6 hours. Nonetheless, the reaction did show complete selectivity for carbonate linkages, but a significant amount of cyclic carbonate (26 %) was formed.

Poly(propylene carbonate) (PPC) is desirable to prepare soft-block polyols for polyurethane production, i.e. in flexible foam applications.[41-46] The main challenge in PO/CO_2 ROCOP is selectivity for polycarbonate formation, as polyether linkages and cyclic propylene carbonate are frequently observed in high percentages. With **[LZnMg(OBz^{OMe})$_2$]**, even at very low loadings (0.01 mol%), extremely high levels of carbonate selectivity (98 %) were observed, but yielded only 26 % polymer selectivity. However the formation of a small amount of PPC is still a promising

finding, compared to **[LZn$_2$(OAc)$_2$]** and **[LMg$_2$(OAc)$_2$]** which were inactive. Future research should investigate lower reaction temperatures to try to increase polymer selectivity.

Allyl glycidyl ether (AGE) was an attractive monomer due to its extra functionality and high boiling point (154 °C vs 34 °C for PO). Although catalyst **[LZnMg(OBz^{OMe})$_2$]** could ring-open the epoxide, only the cyclic carbonate product was formed at 1 bar CO_2 (80 °C). This may be due to high temperatures favouring the cyclic product, so the reaction at lower temperatures should be tested to investigate whether any polycarbonate linkages can be formed.

Cyclopentene-derived epoxides showed slow rates but the copolymerisation of 3,4-epoxytetrahydrofuran (ETHF) with CO_2 was remarkably selective (> 99 %) for polycarbonate linkages. The polymer is of interest due to the presence of an ether functionality in each repeat unit (Figure 4.8). The polymer has significantly reduced solubility compared to other polycarbonates and after removal of the excess epoxide from the crude polymerisation mixture, the polymer was totally insoluble in DCM, $CHCl_3$ and DMF, with poor solubility in THF and EtOAc.

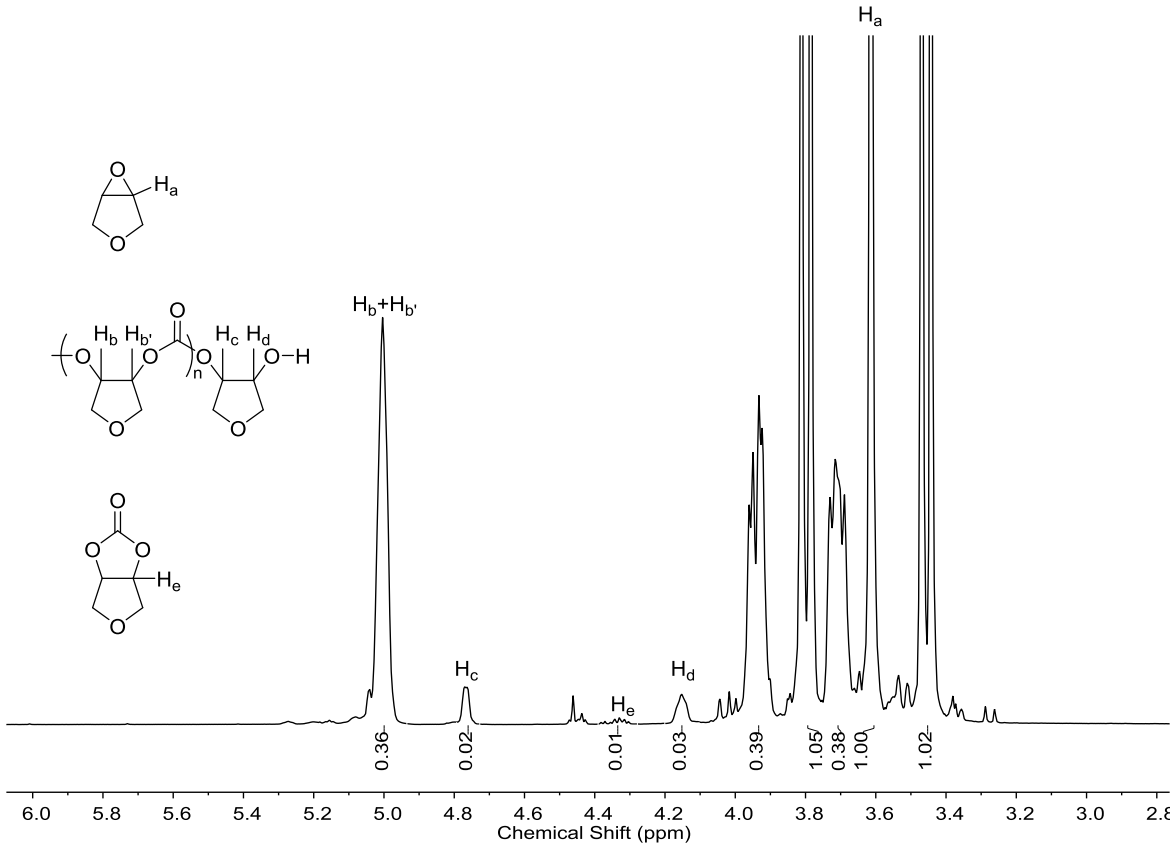


Figure 4.8 – ^{1}H NMR spectrum of the crude reaction mixture for the copolymerisation of ETHF and CO_2, in $CDCl_3$ used to calculate the TON and selectivity for the copolymerisation.

The copolymerisation with cyclopentene oxide (CPO) and CO_2 to form poly(cyclopentene carbonate) (PCPC) was successful (Table 4.9). No cyclic carbonate or polyether resonances were observed in the crude ^{1}H NMR spectrum (Figure 4.9). Reactions conducted in a Parr reaction vessel, charged to 20 bar CO_2 pressure, yielded turnover frequencies of 76 h^{-1} and enabled the formation of high molar mass PCPC (> 41 000 g·mol^{-1}). PCPC with molar mass above 30 000 g·mol^{-1} are yet to be reported, and therefore this material is of interest for thermo-mechanical studies.[47-51]

The observed activity is lower than previously reported values of 108 h^{-1} (at 70 °C)[48] and 199 h^{-1} (at 25 °C)[52], but significantly lower catalyst loadings were required (0.1 vs 0.01 mol%). Under 1 bar CO_2 pressure, Lu and co-workers observed a TOF of 42 h^{-1} which increased to 647 h^{-1} upon increasing temperature and pressure, with an enantiopure cobalt catalyst.[53] Coates and co-workers have shown that CPO can be

incorporated into isotactic (86 % ee) block copolymers.[54] Darensbourg has previously shown that poly(cyclopentene carbonate) is able to undergo depolymerisation to reform the epoxide, an interesting proposition for use in recyclable materials.[55,56]

Table 4.9 – CPO/CO_2 ROCOP Data for Catalyst ***[LZnMg(OBz^{OMe})$_2$]*** *at 80 °C.*[a]

Pressure (bar)	Catalyst (mol%)	Time (h)	CO_2 (%)	Polymer (%)	TON[d]	TOF (h^{-1})	M_n [Đ]
1	0.1	6	> 99	> 99	179	30	10200 [1.04] 4500 [1.13]
1	0.1	24	> 99	> 99	520	22	17600 [1.05] 5600 [1.36]
20	0.01	24	> 99	> 99	1825	76	41800 [1.03] 15100 [1.25]

a) Reactions at 1 bar pressure of CO_2 were carried out in a Schlenk with magnetic stirring. Reactions at 20 bar were carried out in a Parr high pressure vessel with an impeller.

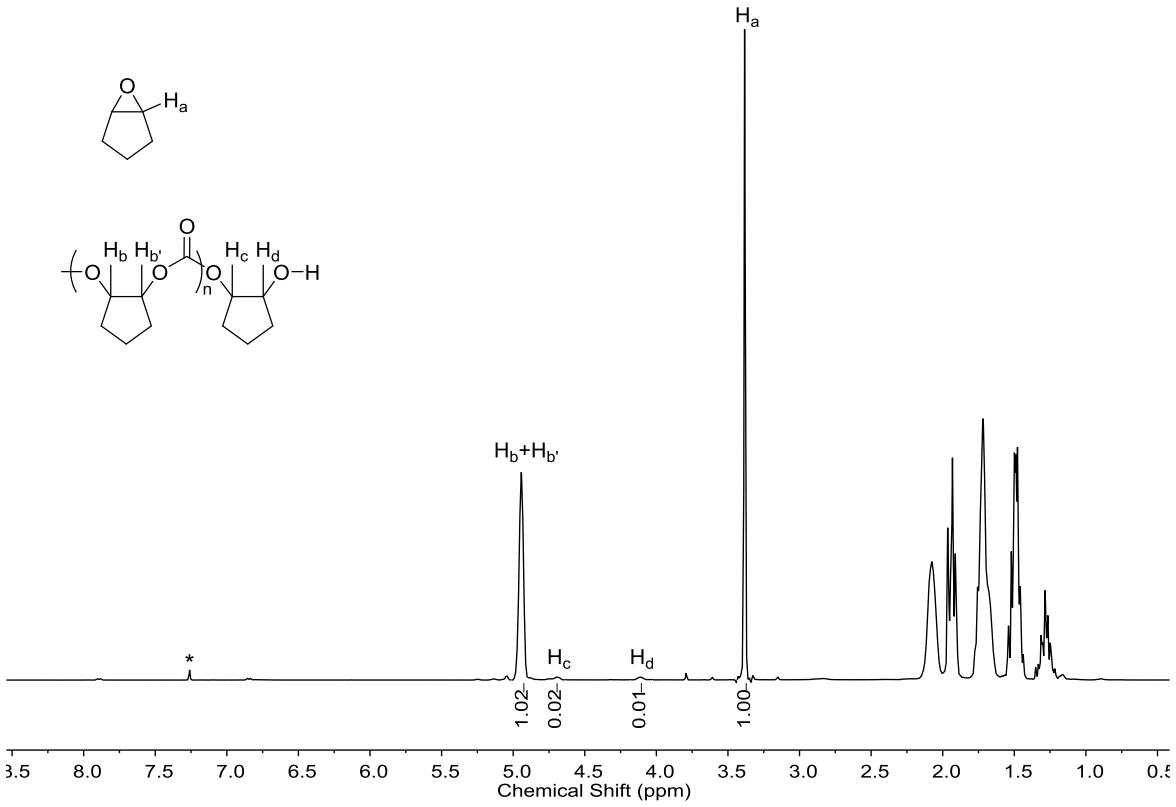


*Figure 4.9 – ^{1}H NMR spectrum of the crude reaction mixture for the copolymerisation of CPO and CO_2 in $CDCl_3$ at 298 K, used to calculate the TON and selectivity for the copolymerisation. $CDCl_3$ residual solvent signal marked with *.*

4.4.2. Polymer properties

A PCPC sample of molar mass ~42 000 g·mol^{-1}, was purified through silica and precipitated from DCM into methanol. This polymer was found to have a degradation

temperature of 122 °C in the thermal gravimetric analysis (Figure 4.10, a). A glass transition was observed at 66 °C (second heating cycle) (Figure 4.10, b). As expected, a lower molar mass sample (~18 000 g·mol^{-1}) displayed a lower T_g at 43 °C, with a degradation temperature (5 %) of 110 °C. An increase in T_g with molar mass is consistent with theory, however, the observed T_g is significantly lower than the 85 °C reported by Darensbourg and co-workers, for a 27 000 g·mol^{-1} PCPC polymer.[48]

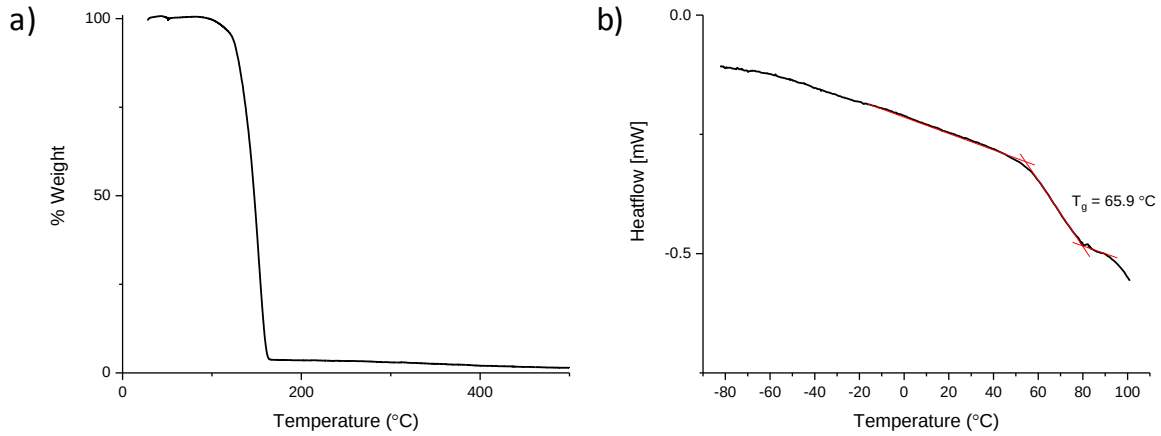


Figure 4.10 – a) Thermal Gravimetric Analysis for a sample of PCPC; b) Second heating cycle for the Differential Scanning Calorimetry plot, showing a glass transition temperature of 65.9 °C.

4.5. PA/CHO Copolymerisations

Catalysts were also tested in the copolymerisation of CHO with phthalic anhydride (PA) to form polyesters (Table 4.10). These catalysts are also efficient in the synthesis of poly(1,2-cyclohexylene-1,2-phthalate) with complete selectivity for polyester enchainment maintained for all catalysts. High turnover frequencies of up to 289 h^{-1} were obtained.

Table 4.10 – CHO/PA ROCOP Data for ***[LZnMgBr$_2$]*** *and* ***[LZnMg(OBz^R)$_2$]***.[a]

Catalyst	Polyester Selectivity (%)	TOF (h^{-1})	k_{obs} ($x10^{-3}$ Ms^{-1})	Initiation (min)[b]
[LZnMgBr$_2$]	> 99	274	1.26	5.1
[LZnMg(OBz)$_2$]	> 99	245	1.03	2.9
[LZnMg(OBz^{OMe})$_2$]	> 99	281	1.08	4.6
[LZnMg(OBz^{CF3})$_2$]	> 99	123	0.61	5.6
[LZnMg(OBz^{NO2})$_2$]	> 99	289	1.16	2.0
[LZnMg(OBz^{F5})$_2$]	> 99	62	0.42	8.5

a) Reactions were conducted with a catalyst:PA:CHO molar ratio of 1:100:800 at 100 ° C in a series of PTFE capped vials which were stopped at various times. b) Calculated assuming reaction is zero order in PA by plotting [PA] vs time. Appendix E, Figure E.1-E.6.

These catalysts are the most active zinc or magnesium catalysts for PA/CHO copolymerisation. An asymmetric dizinc salen catalyst showed similarly high activity and selectivity (> 99 %) [198 h^{-1}, 100 °C, 0.13 mol%, neat CHO].[57] Previous homodinuclear complexes with this macrocyclic ligand were found to have lower turnover frequencies of 97 h^{-1} (**[LMg$_2$(OAc)$_2$]**) and 24 h^{-1} (**[LZn$_2$(OAc)$_2$]**) [100 °C, 0.13 mol%, neat CHO].[58] Other dinuclear and mononuclear zinc iminophenolate catalysts have been reported for this copolymerisation but had low activities of 3 h^{-1}.[59]

With other metals, several chromium salophen catalysts, with a [PPN]Cl co-catalyst, have reported moderate to high activities, albeit with higher catalyst loadings and temperatures [50 – 250 h^{-1}, 110 °C, 0.4 mol%, neat CHO].[60-62] The use of an enantiopure bimetallic aluminium complex enabled access to extremely high turnover frequencies to yield enantiomerically enriched polyesters [750 h^{-1}, 50 °C, 0.1 mol%, neat CHO].[62]

Catalysts **[LZnMg(OBz^{OMe})$_2$]** and **[LZnMg(OBz^{NO2})$_2$]** are, therefore, shown to be among the most highly active catalysts reported. Good control was evident from a

linear increase in molar mass with conversion, and the polymers displaying narrow dispersity (Figure 4.11).

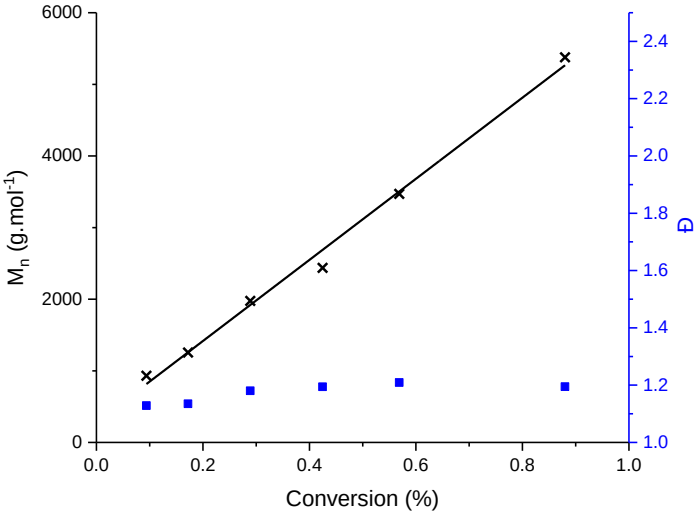


Figure 4.11 – Plot of the polyester M_n (black crosses) and M_w/M_n (blue squares) versus PA conversion for ***[LZnMg(OBz^{OMe})$_2$]*** *(Appendix C, Figure C.44-C.49.).*

Catalysts **[LZnMg(OBz^{R})$_2$]** were monitored by *in situ* ATR-IR spectroscopy to calculate the observed rate constant. When comparing this with the Hammett parameters for substituted benzoates, a greater variation was seen than that observed for CO_2/CHO copolymerisation (Figure 4.12). There is also no clear trend in activity against the electronic features of the co-ligand, again indicating a complex interplay of factors on the rate limiting step, or possible changes to the rate determining step depending on co-ligand.

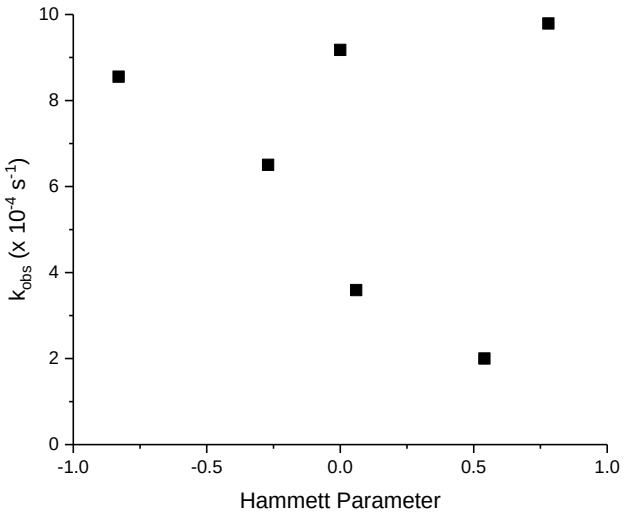


Figure 4.12 – Comparison of activities vs Hammett Parameters for catalysts ***[LZnMg(OBz^{R})$_2$]*** *in the copolymerisation of PA/CHO. Reactions were carried out using in situ ATR-IR spectroscopy, using a catalyst:PA:CHO molar ratio of 1:100:800 at 100 °C. Rate calculated assuming zero order dependence of PA on reaction rate, using data from 40-90 % conversion. Appendix D, Figure D.25-D.36.*

4.6. Alternative Anhydrides

Catalyst **[LZnMg(OBz^{OMe})$_2$]** was tested in the copolymerisation of CHO with other 5, 6 and 7-membered anhydrides displaying a range of functionalities (Figure 4.13).

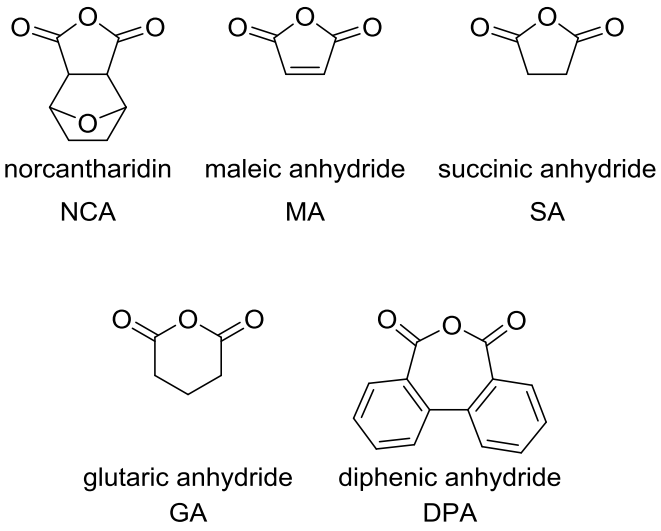


Figure 4.13 – Range of anhydrides tested for the copolymerisation with CHO.

Catalyst **[LZnMg(OBz^{OMe})$_2$]** was generally highly selective for polyester formation and showed good activity for a range of different anhydrides (Table 4.11). Three 5-membered ring anhydrides were tested, including norcantharidin (NCA), maleic anhydride (MA) and succinic anhydride (SA). All these anhydrides were

copolymerised more slowly than the equivalent reaction with PA under analogous conditions. The copolymerisations of CHO with NCA or SA were both highly selective for polyester linkages, however, the rate of reaction with SA was very low. Both reactions showed bimodal molar mass distributions with the polyester derived from NCA displaying very narrow polydispersities. The copolymerisation of CHO and MA yielded a polymer with broad dispersity with a high ether linkage content – a problem known to the field.[63] This reaction was run at 45 °C to minimise the possible cross-linking side-reactions, but it seems these may be partly responsible for the broad dispersity values.

Table 4.11 – CHO/anhydride ROCOP Data for Catalyst ***[LZnMg(OBz^{OMe})$_2$]*** *with a range of anhydrides.*[a]

Anhydride	Temp. (°C)	Time (h)	Polyester (%)	TON	TOF (h^{-1})	M_n [$Đ$]
NCA	100	1	> 99	44	44	4100 [1.02] 1100 [1.05]
NCA	100	2	> 99	89	44	8000 [1.05] 3500 [1.09]
MA	45	22	14	24	1	26100 [1.92]
SA	100	30	> 99	93	3	4000 [1.20] 1200 [1.20]
GA	100	1	> 99	22	22	2000 [1.08]
DPA	100	1	> 99	80	80	15900 [1.07] 6720 [1.07]

a) Reactions were conducted with a catalyst:anhydride:CHO molar ratio of 1:100:800 in PTFE capped vials.

The copolymerisation of the 6-membered glutaric anhydride, GA, showed moderate activity, with narrow dispersity polymers. Copolymerisation of CHO with the 7-membered diphenic anhydride gave high molar mass polyesters with narrow dispersities and showed good activity (TOF = 80 h^{-1}).

These initial studies show that catalyst **[LZnMg(OBz^{OMe})$_2$]** can ring-open a range of cyclic anhydrides, with varying ring size. This catalyst also enables a range of functionality to be installed in the polyester chains, whilst accessing high molar mass polymers.

4.7. Conclusions and Future Work

A series of heterodinuclear catalysts were tested in copolymerisation reactions with a range of epoxides and CO_2 or anhydrides. They were highly active under low pressure for the copolymerisation of CO_2 and CHO. These catalysts were amongst the most active catalysts for this system at 1 bar CO_2, whilst achieving superior selectivity to other catalyst systems. These heterodinuclear catalysts also operate without the need for high catalyst loadings, expensive co-catalysts or elevated pressures. The catalysts are air-stable and result in colourless products.

A range of monomer feedstocks were explored, focussing on renewable epoxides or substituted monomers enabling functionalised polymer production. Some polycarbonate was formed in the copolymerisation of PO and CO_2 – a promising step to a desirable material. Good activities and selectivities were also observed for 5-membered ring epoxides, notably with CPO. The formation of polymers with internal or external double bonds was explored for future use in post-modification.

The copolymerisation of CHO and PA was shown to be well controlled with good activities and excellent polyester selectivity. The ROCOP of CHO with a range of anhydrides was extended and shows that this new catalyst class has potential to yield a variety of polyesters with high selectivity and acceptable activities.

No clear conclusions could be drawn from comparing the catalyst activity with electronic structure of the co-ligands. This suggests the macrocyclic ligand and metal combination are mostly responsible for the high activity and altering the electronic substitution of the benzoate gives an only a minor effect. However, there are clear advantages to exploring different classes of co-ligands, with large increases in

turnover frequency observed when moving from a bromide to benzoate, due to shortened initiation times.

As these catalysts are highly active to the ring-opening copolymerisation of both epoxide/CO_2 and epoxide/anhydrides, their use in terpolymerisations and switch catalysis in recommended.[30,64,65] In the first instance it is important to establish activity for lactone ROP. Future work should also focus on exploiting the high activity to prepare a range of polymers including with variable compositions, chain lengths and structures.

4.8. References

(1) Kember, M. R.; Buchard, A.; Williams, C. K. *Chem. Commun.* **2011**, *47*, 141.
(2) Poland, S. J.; Darensbourg, D. J. *Green Chem.* **2017**, *19*, 4990.
(3) Darensbourg, D. J.; Wilson, S. J. *Green Chem.* **2012**, *14*, 2665.
(4) Trott, G.; Saini, P. K.; Williams, C. K. *Phil. Trans. R. Soc. A* **2016**, *374*.
(5) Paul, S.; Zhu, Y.; Romain, C.; Brooks, R.; Saini, P. K.; Williams, C. K. *Chem. Commun.* **2015**, *51*, 6459.
(6) Longo, J. M.; Sanford, M. J.; Coates, G. W. *Chem. Rev.* **2016**, *116*, 15167.
(7) Si, G.; Zhang, L.; Han, B.; Duan, Z.; Li, B.; Dong, J.; Li, X.; Liu, B. *Polym. Chem.* **2015**, *6*, 6372.
(8) Watts, A.; Kurokawa, N.; Hillmyer, M. A. *Biomacromolecules* **2017**, *18*, 1845.
(9) Zhu, Y.; Radlauer, M. R.; Schneiderman, D. K.; Shaffer, M. S. P.; Hillmyer, M. A.; Williams, C. K. *Macromolecules* **2018**, 10.1021/acs.macromol.7b02690.
(10) Reiter, M.; Vagin, S.; Kronast, A.; Jandl, C.; Rieger, B. *Chem. Sci.* **2017**, *8*, 1876.
(11) Saini, P. K.; Fiorani, G.; Mathers, R. T.; Williams, C. K. *Chem. Eur. J.* **2017**, *23*, 4260.
(12) Sanford, M. J.; Peña Carrodeguas, L.; Van Zee, N. J.; Kleij, A. W.; Coates, G. W. *Macromolecules* **2016**, *49*, 6394.
(13) Peña Carrodeguas, L.; Martín, C.; Kleij, A. W. *Macromolecules* **2017**, *50*, 5337.
(14) Uysal, B. B.; Gunay, U. S.; Hizal, G.; Tunca, U. *J. Polym. Sci., Part A: Polym. Chem.* **2014**, *52*, 1581.
(15) Darensbourg, D. J.; Wang, Y. *Polym. Chem.* **2015**, *6*, 1768.
(16) Garden, J. A.; Saini, P. K.; Williams, C. K. *J. Am. Chem. Soc.* **2015**, *137*, 15078.
(17) Saini, P. K.; Romain, C.; Williams, C. K. *Chem. Commun.* **2014**, *50*, 4164.
(18) Kember, M. R.; White, A. J. P.; Williams, C. K. *Inorg. Chem.* **2009**, *48*, 9535.
(19) Kember, M. R.; Knight, P. D.; Reung, P. T. R.; Williams, C. K. *Angew. Chem. Int. Ed.* **2009**, *48*, 931.
(20) Kember, M. R.; Williams, C. K. *J. Am. Chem. Soc.* **2012**, *134*, 15676.
(21) Kember, M. R.; White, A. J. P.; Williams, C. K. *Macromolecules* **2010**, *43*, 2291.
(22) Xiao, Y.; Wang, Z.; Ding, K. *Macromolecules* **2006**, *39*, 128.

(23) Darensbourg, D. J.; Yarbrough, J. C.; Ortiz, C.; Fang, C. C. *J. Am. Chem. Soc.* **2003**, *125*, 7586.
(24) Kissling, S.; Lehenmeier, M. W.; Altenbuchner, P. T.; Kronast, A.; Reiter, M.; Deglmann, P.; Seemann, U. B.; Rieger, B. *Chem. Commun.* **2015**, *51*, 4579.
(25) Xiao, Y.; Wang, Z.; Ding, K. *Chem. Eur. J.* **2005**, *11*, 3668.
(26) Ren, W.-M.; Zhang, X.; Liu, Y.; Li, J.-F.; Wang, H.; Lu, X.-B. *Macromolecules* **2010**, *43*, 1396.
(27) Wu, G.-P.; Darensbourg, D. J. *Macromolecules* **2016**, *49*, 807.
(28) van Meerendonk, W. J.; Duchateau, R.; Koning, C. E.; Gruter, G.-J. M. *Macromolecules* **2005**, *38*, 7306.
(29) Zhu, Y.; Romain, C.; Poirier, V.; Williams, C. K. *Macromolecules* **2015**, *48*, 2407.
(30) Zhu, Y.; Romain, C.; Williams, C. K. *J. Am. Chem. Soc.* **2015**, *137*, 12179.
(31) Hansch, C.; Leo, A.; Taft, R. W. *Chem. Rev.* **1991**, *91*, 165.
(32) Nummert, V.; Travnikova, O.; Vahur, S.; Leito, I.; Piirsalu, M.; Mäemets, V.; Koppel, I.; Koppel, I. A. *J. Phys. Org. Chem.* **2006**, *19*, 654.
(33) Byrne, C. M.; Allen, S. D.; Lobkovsky, E. B.; Coates, G. W. *J. Am. Chem. Soc.* **2004**, *126*, 11404.
(34) Hauenstein, O.; Reiter, M.; Agarwal, S.; Rieger, B.; Greiner, A. *Green Chem.* **2016**, *18*, 760.
(35) Hauenstein, O.; Agarwal, S.; Greiner, A. *Nat. Commun.* **2016**, *7*, 11862.
(36) Zhang, J.-F.; Ren, W.-M.; Sun, X.-K.; Meng, Y.; Du, B.-Y.; Zhang, X.-H. *Macromolecules* **2011**, *44*, 9882.
(37) Guillaume, C.; Ajellal, N.; Carpentier, J.-F.; Guillaume, S. M. *J. Polym. Sci., Part A: Polym. Chem.* **2011**, *49*, 907.
(38) Hoyle, C. E.; Lowe, A. B.; Bowman, C. N. *Chem. Soc. Rev.* **2010**, *39*, 1355.
(39) Golas, P. L.; Matyjaszewski, K. *Chem. Soc. Rev.* **2010**, *39*, 1338.
(40) Blasco, E.; Sims, M. B.; Goldmann, A. S.; Sumerlin, B. S.; Barner-Kowollik, C. *Macromolecules* **2017**, *50*, 5215.
(41) Cohen, C. T.; Chu, T.; Coates, G. W. *J. Am. Chem. Soc.* **2005**, *127*, 10869.
(42) Nakano, K.; Kamada, T.; Nozaki, K. *Angew. Chem. Int. Ed.* **2006**, *45*, 7274.
(43) Lu, X.-B.; Liang, B.; Zhang, Y.-J.; Tian, Y.-Z.; Wang, Y.-M.; Bai, C.-X.; Wang, H.; Zhang, R. *J. Am. Chem. Soc.* **2004**, *126*, 3732.
(44) Noh, E. K.; Na, S. J.; Sujith, S.; Kim, S. W.; Lee, B. Y. *J. Am. Chem. Soc.* **2007**, *129*, 8082.
(45) Vagin, S. I.; Reichardt, R.; Klaus, S.; Rieger, B. *J. Am. Chem. Soc.* **2010**, *132*, 14367.
(46) Nakano, K.; Hashimoto, S.; Nakamura, M.; Kamada, T.; Nozaki, K. *Angew. Chem. Int. Ed.* **2011**, *50*, 4868.
(47) Liu, Y.; Ren, W. M.; He, K. K.; Lu, X. B. *Nat. Commun.* **2014**, *5*.
(48) Darensbourg, D. J.; Chung, W.-C.; Wilson, S. J. *ACS Catal.* **2013**, *3*, 3050.
(49) Huang, L.-S.; Tsai, C.-Y.; Chuang, H.-J.; Ko, B.-T. *Inorg. Chem.* **2017**, *56*, 6141.
(50) Liu, Y.; Ren, W.-M.; Wang, M.; Liu, C.; Lu, X.-B. *Angew. Chem. Int. Ed.* **2015**, *54*, 2241.
(51) Hua, Y.-Z.; Yang, X.-C.; Liu, M.-M.; Song, X.; Wang, M.-C.; Chang, J.-B. *Macromolecules* **2015**, *48*, 1651.
(52) Liu, Y.; Ren, W.-M.; He, K.-K.; Lu, X.-B. *Nat. Commun.* **2014**, *5*, 5687.
(53) Liu, Y.; Ren, W.-M.; Liu, J.; Lu, X.-B. *Angew. Chem. Int. Ed.* **2013**, *52*, 11594.
(54) Ellis, W. C.; Jung, Y.; Mulzer, M.; Di Girolamo, R.; Lobkovsky, E. B.; Coates, G. W. *Chem. Sci.* **2014**, *5*, 4004.

(55) Darensbourg, D. J.; Wei, S.-H.; Yeung, A. D.; Ellis, W. C. *Macromolecules* **2013**, *46*, 5850.
(56) Darensbourg, D. J.; Yeung, A. D.; Wei, S.-H. *Green Chem.* **2013**, *15*, 1578.
(57) Thevenon, A.; Garden, J. A.; White, A. J. P.; Williams, C. K. *Inorg. Chem.* **2015**, *54*, 11906.
(58) Saini, P. K.; Romain, C.; Zhu, Y.; Williams, C. K. *Polym. Chem.* **2014**, *5*, 6068.
(59) Yu, C.-Y.; Chuang, H.-J.; Ko, B.-T. *Catal. Sci. Technol.* **2016**, *6*, 1779.
(60) Hosseini Nejad, E.; van Melis, C. G. W.; Vermeer, T. J.; Koning, C. E.; Duchateau, R. *Macromolecules* **2012**, *45*, 1770.
(61) Huijser, S.; Hosseini Nejad, E.; Sablong, R.; de Jong, C.; Koning, C. E.; Duchateau, R. *Macromolecules* **2011**, *44*, 1132.
(62) Li, J.; Liu, Y.; Ren, W.-M.; Lu, X.-B. *J. Am. Chem. Soc.* **2016**, *138*, 11493.
(63) Shi, Q.; Yang, X.; Zhang, X.; Li, X.; Yang, J.; Lü, X. *Inorg. Chem. Commun.* **2016**, *73*, 4.
(64) Romain, C.; Williams, C. K. *Angew. Chem. Int. Ed.* **2014**, *53*, 1607.
(65) Romain, C.; Zhu, Y.; Dingwall, P.; Paul, S.; Rzepa, H. S.; Buchard, A.; Williams, C. K. *J. Am. Chem. Soc.* **2016**, *138*, 4120.

Chapter 5

Mechanistic Investigations of a Heterodinuclear Catalyst in Copolymerisation Reactions

This chapter describes the kinetic investigations undertaken to derive the rate equation for a heterodinuclear catalyst (**[LZnMgBr$_2$]**) in the copolymerisation reactions of CO_2/CHO and PA/CHO. The copolymerisation of CO_2/CHO was found to be first order with respect to **[LZnMgBr$_2$]** and CHO, with a likely zero order dependence on CO_2 pressure. A computational study into the propagation step for different metal combinations is also detailed. The copolymerisation of PA/CHO has a zero order dependence on PA concentration and studies suggest a probable first order dependence on the concentration of **[LZnMgBr$_2$]** and CHO, although further investigation is recommended.

5.1. Introduction

5.1.1. Previous investigations into related systems

Homodinuclear zinc and magnesium catalysts with acetate co-ligands (**[LZn$_2$(OAc)$_2$]** and **[LMg$_2$(OAc)$_2$]**) were found to follow the rate equation for the copolymerisation of CO_2/CHO:[1-3]

Equation 5.1 $$rate = k_p[catalyst]^1[CHO]^1\rho CO_2{}^0$$

A bimetallic mechanism is hypothesised for this class of catalysts where the ring-opening of a single molecule of CHO, by one equivalent of the dinuclear catalyst, is the rate determining step. This system does not have a pressure dependence on CO_2.

This mechanism shows some similarities to other mono- and bimetallic catalysts in the field, which operate under dinuclear mechanisms, where two metal centres are proposed to act cooperatively in the copolymerisation.[4-7]

5.1.2. Aims of the chapter

Mechanistic details of the heterodinuclear catalyst system are investigated through kinetic studies to elucidate the rate law for complex **[LZnMgBr$_2$]** in both CO_2/CHO and PA/CHO copolymerisation. A computational study explores the cooperative propagation step for CHO/CO_2 copolymerisation applying different combinations of zinc and magnesium centres.

5.2. Rate Equation for CO_2/CHO Copolymerisation

5.2.1. Order in epoxide

The formation of polycarbonate over time was monitored under dilute (5 M) conditions in toluene at 80 °C. A semi-logarithmic plot of $\ln([CHO]_0/[CHO])$ against time displays linearity, suggesting a first order dependence on the concentration of CHO (Figure 5.1).

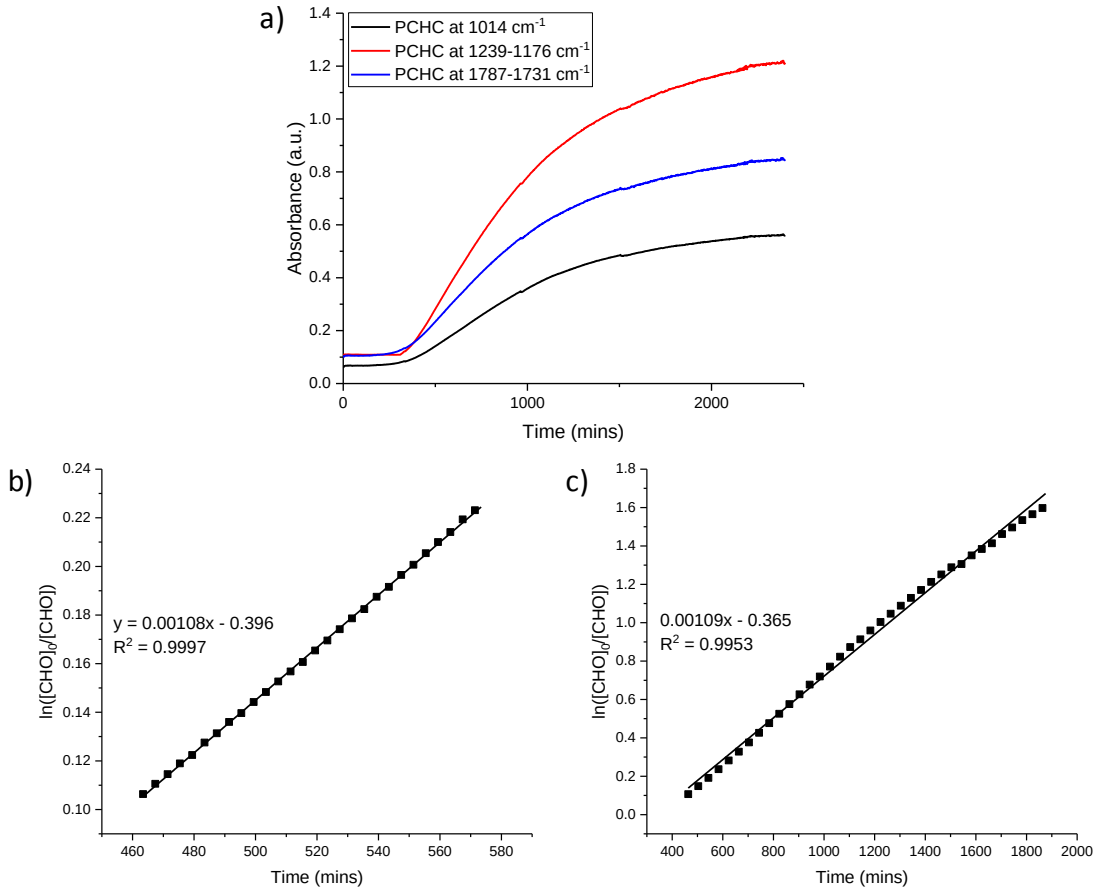


*Figure 5.1 – a) ATR-IR spectroscopic trace of the copolymerisation of CHO and CO_2. Reaction conditions: [**[LZnMgBr$_2$]**] = 5 mM and $[CHO]_0$ = 5 M in toluene, 80 °C, 1 bar pressure of CO_2. b) Plot of $\ln([CHO_0/[CHO])$ vs time for 10 to 20 % conversion of CHO. For clarity, every 2nd data point is shown. c) Plot of $\ln([CHO_0/[CHO])$ vs time for 10 to 80 % conversion of CHO. For clarity, every 20th data point is shown.*

A conversion of 80+ % was achieved under dilute conditions and therefore allowed the utilisation of an integrated rate law method; however, reaction rates are obviously slower than the corresponding reaction run in neat epoxide. There is good

agreement for the integrated first order fit when comparing 10-20 % against 10-80 % conversion for the same polymerisation run (Figure 5.1). Under dilute conditions, this suggests evaluating the data from 10-20 % conversion, also gives a meaningful result for the whole polymerisation.

5.2.2. Order in catalyst

The catalyst order of **[LZnMgBr$_2$]** in the copolymerisation of CO_2 and CHO was obtained through the initial rates method in neat epoxide. The initial rate of reaction, for a series of catalyst concentrations, was measured by *in situ* ATR-IR spectroscopy at 1 bar CO_2 pressure. Catalyst **[LZnMgBr$_2$]** displayed a typically slow initiation period from 0-10 % conversion of epoxide. Therefore, the conversion period from 10-20 % was used to calculate the initial rate of reaction.

All initial rate reactions were run in triplicate and a plot of rate against catalyst concentration shows that a first order fit is acceptable (Figure 5.2, a). To confirm this observation, a plot of ln(rate) against ln(concentration) was best fit with a slope of 0.7 (Figure 5.2, b). Applying zero and second order fits to the original data resulted in less satisfactory correlations.

The coefficient of variation ranges from 7 to 22 % for different catalyst concentrations and so clearly there are significant errors in the data (Appendix D, Table D.1). This could be an inherent problem with the method for monitoring reaction progress, although all reagent batches, stirring rates and reaction vessel sizes were kept constant to minimise error. Further repeats, and a larger range of catalyst concentrations, are recommended to confirm the apparent first order fit.

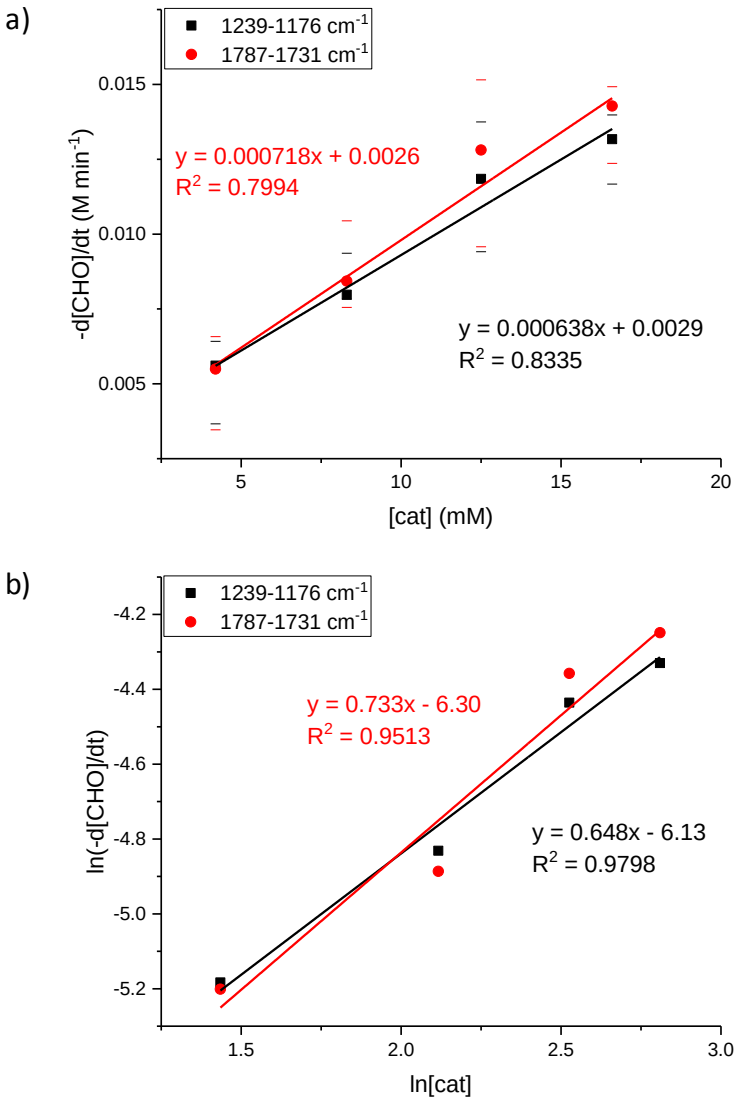


Figure 5.2 – Plots to determine the order in ***[LZnMgBr$_2$]****. Reaction conditions: [CHO] = 8.24 M in DEC, 80 °C, 1 bar pressure CO$_2$. a) Initial rate of reaction (10-20 % CHO conversion) against catalyst concentration. b) A ln(initial rate) against ln(catalyst concentration) plot of the median data points measured. Appendix D, Figure D.37-D.48.*

5.2.3. Order in CO_2

A series of reactions at 4-50 bar CO_2 pressure were carried out in a stainless steel reactor equipped with an impeller, at 120 °C. All reactions were stopped at 5 h to allow comparative point kinetics. The activity of the catalyst was assessed by calculating turnover frequency from CHO conversion (determined by ^{1}H NMR spectroscopy). Over the range 10-50 bar there is no particular correlation between pressure and activity, suggesting a zero order dependence on CO_2 pressure (Figure

5.3). The activity observed at 4 bar is lower than expected, but this may be attributed to the rapid consumption of a significant relative pressure of CO_2 during the course of the polymerisation. The only way to test this would be to attempt to run a system with regular pressurisation of the reaction vessel, although this is currently unachievable with the reactor set up. The reaction was run in triplicate at 10 bar and in duplicate at 4 bar; these repeat experiments show excellent agreement with an error of 7 and 2 %, respectively.

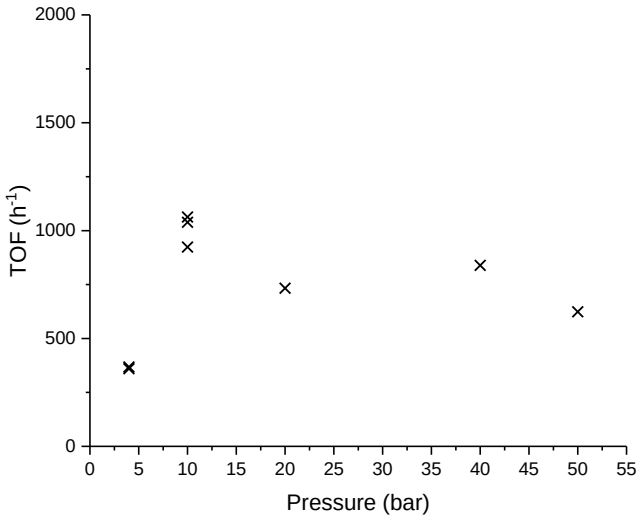


*Figure 5.3 – Plot of activity (TOF) against pressure for catalyst **[LZnMgBr$_2$]**. Reaction conditions: 120 °C, 5 h, 1:10,000 catalyst:CHO. Value at 50 bar from Garden et al.[8]*

It is worth noting that the data are point kinetic measurements, which has been used previously in the field to ascertain the order in CO_2.[6] An alternative would be to determine the rate of reaction through monitoring the reaction through aliquots or using *in situ* ATR-IR spectroscopy. These options are being explored for future studies.

5.2.4. Discussion

Based on the results obtained in the kinetic analysis, it is suggested that the rate equation for the heterodinuclear catalyst **[LZnMgBr$_2$]** also follows Equation 5.1. It is

clear that the polymerisation is first order in epoxide and the point kinetic measurements strongly suggest a zero order dependence on CO_2 pressure. These findings are consistent with other kinetic studies in the field which show copolymerisation to be zero order in CO_2 and first order in CHO.[5]

An initial rate treatment of the data for determining catalyst concentration implied a first order dependence on catalyst concentration. Upon further analysis it seems that the data collected could be consistent with a non-integer dependence on catalyst concentration. However, an order of < 1 for catalyst concentration seems chemically unlikely based on the observed first and zero orders for CHO and CO_2, respectively. The data strongly suggests that it is unlikely that more than one catalyst species is present in the rate determining step.

Other catalysts in the field have shown non-integer orders in catalyst but these have typically been greater than 1, due to cooperation between catalyst centres or bifunctional mechanisms.[5,7,9,10] From the data collected, it seems unlikely that more than 1 equivalent of **[LZnMgBr$_2$]**is present in the rate determining step.

Other heterodinuclear catalysts, which display shorter definitive initiation times (e.g. **[LZnMg(OBz^{NMe2})$_2$]**), will be studied to confirm the rate law for other co-ligand systems, in future work.

The suggested rate equation is consistent with previous studies on homodinuclear analogues based on this macrocyclic ligand.[2,3] It therefore seems reasonable to assume that these heterodinuclear catalysts operate under a similar mechanism to **[LZn$_2$(OAc)$_2$]**, where the rate determining step is the ring-opening of the epoxide by a single catalyst unit, with rapid insertion of CO_2. As no clear differences are apparent

in the rate equation, it seems reasonable to assume the chain-shuttling mechanism may also be a viable model for this system. This ideal mechanism is further explored computationally in the following section.

5.3. Computational studies for CO_2/CHO Copolymerisation

5.3.1. Calculated reaction pathways for a heterodinuclear catalyst

The propagation pathway for different catalysts, all containing zinc or/and magnesium, has been explored computationally. The pathway for catalyst **[$LZn_2(OAc)_2$]** has previously been detailed by Buchard *et al*. and was recalculated here at 353.15 K (black pathway, Figure 5.4).[1] The energy levels for the propagation pathway of the dinuclear magnesium catalyst, **[$LMg_2(OAc)_2$]**, were also calculated (blue pathway, Figure 5.4). Due to the inherent asymmetry of the proposed chain-shuttling mechanism, the calculations for the heterodinuclear catalyst, **[$LZnMg(OAc)_2$]**, were conducted for both possible metal iterations: one where the magnesium centre is binding the epoxide, with the zinc alkoxide undergoing CO_2 insertion (green pathway, Figure 5.4), and the other where zinc is binding epoxide and magnesium alkoxide inserts a CO_2 molecule (red pathway, Figure 5.4).

DFT calculations were performed using Gaussian 09W and applied the ωB97XD density functional and 6-31G(d) basis set, in accordance with previous studies where various functionals were compared.[1] The self-consistent-reaction-cavity continuum solvation model was used, with dichloromethane solvent, to model solvation in cyclohexene oxide. The output files from the previous study by Buchard *et al*. were used in this work.[1]

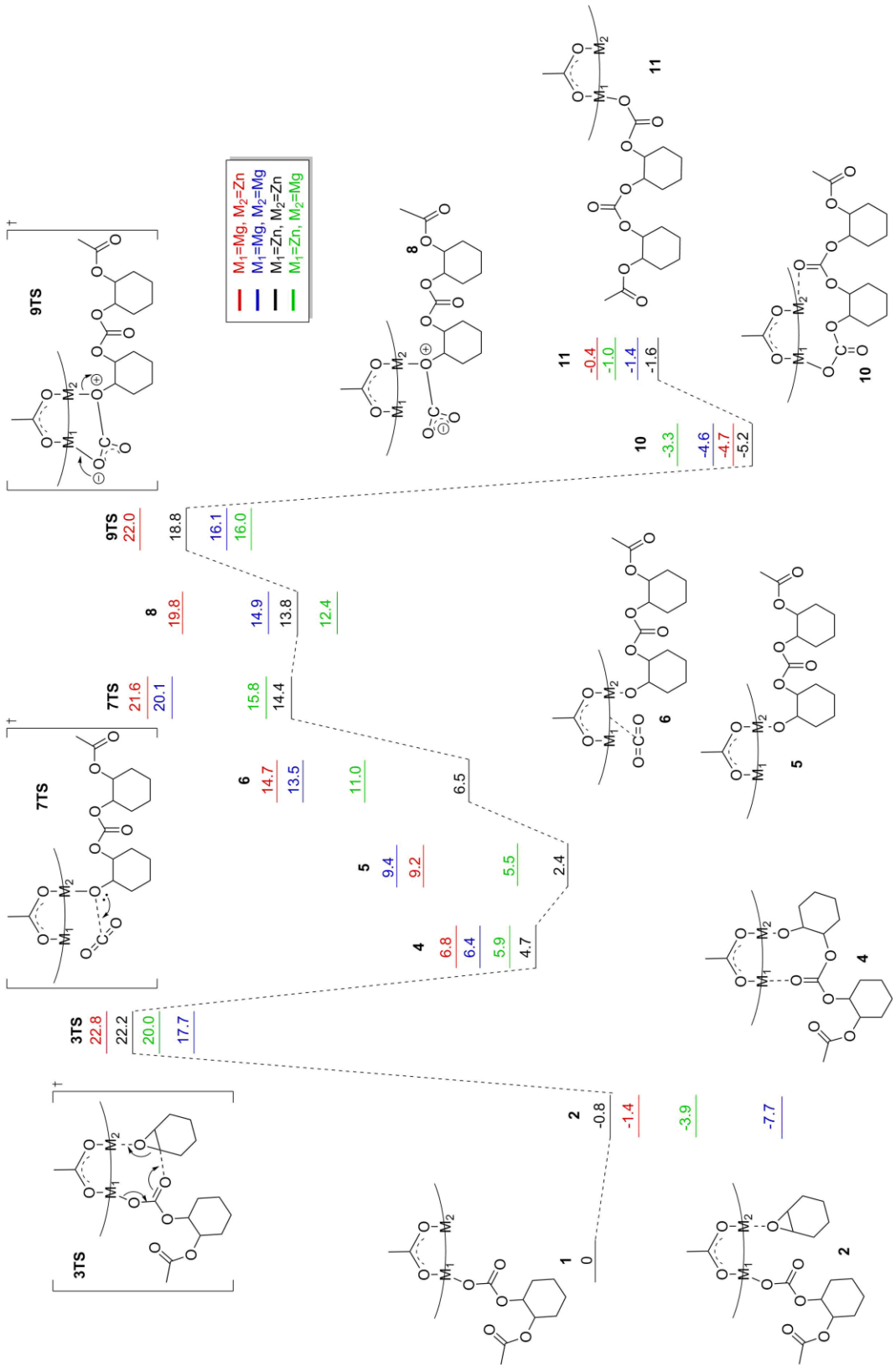


Figure 5.4 – Graphical representation of the propagation pathway for the possible combinations of zinc and magnesium, within a dinuclear framework, with acetate co-ligands. DFT protocol: wb97xd/6-31G(d)/cpcm=DCM/Temp=353.15 K (solvent modelled using the polarizable conductor calculation model SCRF=CPCM). The ancillary ligand structure is omitted for clarity.

All transition states were characterized by normal coordinate analysis revealing precisely one imaginary mode corresponding to the intended reaction. The transition state for epoxide ring-opening, ***3TS***, for **[LMg$_2$(OAc)$_2$]** was then augmented by an intrinsic reaction coordinate (IRC) calculation, which also confirmed the identity of the pathway (Appendix F, Figure F.1). As the transition state (***3TS***) for **[LMg$_2$(OAc)$_2$]** showed no change in pathway by IRC calculation, it was assumed that the analogous transition states for all metal iterations led to the observed products. The calculations were run at 353.15 K to better model the standard polymerisation reaction conditions (80 °C).

Intermediate ***1*** represents the start of the propagation cycle, i.e. after the acetate co-ligand has inserted one molecule of CHO and CO_2 in the initiation step. The energy of this intermediate (with the addition of free CHO and CO_2) is used to calculate the relative energies shown for all other intermediates, in each of the four pathways. M_1 is defined by the starting metal-carbonate bond in intermediate ***1***. M_2 is then defined by the binding of a CHO molecule in intermediate ***2***.

The rate determining step for all metal combinations is found here to be the ring-opening of the epoxide to form the transition state ***3TS***. After epoxide ring-opening, a metal alkoxide is formed on M_2, with M_1 coordinating to a carbonyl on the propagating species. This coordination must be broken to insert CO_2, hence the formation of intermediate ***5***.

CO_2 insertion is achieved by a series of processes where CO_2 is weakly coordinated before a zwitterionic intermediate is formed, resulting in the reformation of a metal-carboxylate on M_1 in intermediate ***10***. Intermediate ***11*** is the final calculation

shown, and the start of the second propagation cycle, in an analogous conformation to intermediate ***1*** where the propagating chain is non-coordinating and the catalyst primed for epoxide binding.

5.3.2. Discussion

No obvious qualitative differences were observed in the mechanism for the reported pathway of catalyst **[LZn$_2$(OAc)$_2$]**, compared to those calculated here for catalysts **[LZnMg(OAc)$_2$]** and **[LMg$_2$(OAc)$_2$]**. The computationally derived rate determining step is the ring-opening of the epoxide in all cases, with smaller transition energies for the insertion of CO_2. This is consistent with the rate equation derived experimentally for all catalysts **[LZnMgBr$_2$]**, **[LMg$_2$(OAc)$_2$]** and **[LZn$_2$(OAc)$_2$]**. Analogous intermediates and transition states for **[LZnMg(OAc)$_2$]** and **[LMg$_2$(OAc)$_2$]** were observed for all stages of the propagation pathway previously found for **[LZn$_2$(OAc)$_2$]**, suggesting that the mechanism for the heterodinuclear catalysts most likely operate under the same chain-shuttling mechanism.

The calculations suggest that epoxide binding (***2-1***, Figure 5.4) is energetically most favourable when M_2 is a magnesium centre (blue and green). The energy barrier for CO_2 insertion appears lower (***7TS-4***, Figure 5.4) when M_1 is a zinc centre (black and green). This would imply that a catalyst combining these two features (i.e. **[LZnMg(OAc)$_2$]** in the green regime), would have a significantly lower activation energy for the copolymerisation. However, the important step, which defines the rate of reaction, is the rate determining step to form ***3TS***. The energy barrier to form this (***3TS-2***, Figure 5.4) is similar for all four combinations. For catalyst **[LZnMg(OAc)$_2$]** $\Delta G^{\dagger}_{3TS}$ is equal to +24.2 (red) or +23.9 (green) kcal·mol^{-1}. Catalyst **[LMg$_2$(OAc)$_2$]** has a $\Delta G^{\dagger}_{3TS}$ of +25.4 and **[LZn$_2$(OAc)$_2$]** a $\Delta G^{\dagger}_{3TS}$ of +23.0 kcal·mol^{-1}. These energy

differences are likely to be within error of the calculations and so meaningful comparisons are unable to be drawn reliably. They also do not follow the rate order observed by experiment (**[LZnMg(OAc)$_2$]** > **[LMg$_2$(OAc)$_2$]** > **[LZn$_2$(OAc)$_2$]**).

These calculations demonstrate the conflicting electronic factors present in rationalising catalytic activity, and therefore catalyst design. Although increasing the Lewis acidity of the metal centre (through metal choice or ligand properties) may increase the strength of epoxide binding, this may also strengthen the metal carboxylate bond that must be broken in the rate determining step. These two competing electronic effects, along with a coordination geometry preference of the metals and solvation effects, are just a few of the factors which must be considered when rationalising catalytic cycles. Due to the complexity of most catalytic pathways, it is rarely the case that the catalytic cycle can be easily rationalised using only a small number of molecular features.

5.4. Rate Equation for PA/CHO

5.4.1. Determining the rate equation for PA/CHO copolymerisation

The rate equation for the copolymerisation of PA and CHO with **[LZnMgBr$_2$]** was explored by analysis of:

Equation 5.2 $$rate = k_p[PA]^x\ [catalyst]^y[CHO]^z$$

The isolation method was utilised and the reaction progress monitored by *in situ* ATR-IR spectroscopy.

5.4.2. Order in PA

The rate of formation of the polyester absorption bands was monitored by *in situ* ATR-IR spectroscopy. Catalyst concentration is assumed to remain constant throughout and [CHO] was in excess such that the rate of polyester formation is equivalent to the rate of PA consumption. As before, an initial polymerisation period (0-10 % conversion) was removed to eliminate any initiation effects from the bromide co-ligand. As viscosity remains low enough to be negligible over the course of the reaction, the entire reaction profile can be utilised. Plotting the concentration of PA over time, between 10 and 99 % conversion, shows a linear decrease (Figure 5.5). This strongly implies a zero order dependence on the rate of reaction with changing PA concentration.

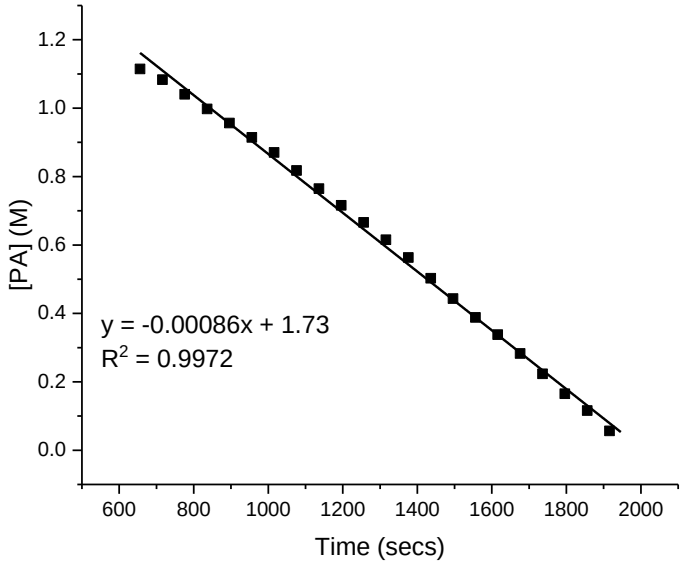


Figure 5.5 – Plot to show a zero order decay from 10 – 99 % consumption of PA. Reactions conditions: ***[LZnMgBr$_2$]****:PA:CHO 1:100:800, 100 °C. For clarity, every 2nd data point is shown.*

5.4.3. Order in catalyst

The order in catalyst can be isolated as the order in PA was determined to be zero, and the concentration of CHO can be kept approximately constant through running the polymerisation at large excess. A plot of reaction rate against catalyst

concentration yields a straight line and a plot of ln(rate) against ln[cat] plot has a gradient approximately equal to 1, suggesting a first order dependence (Figure 5.6).

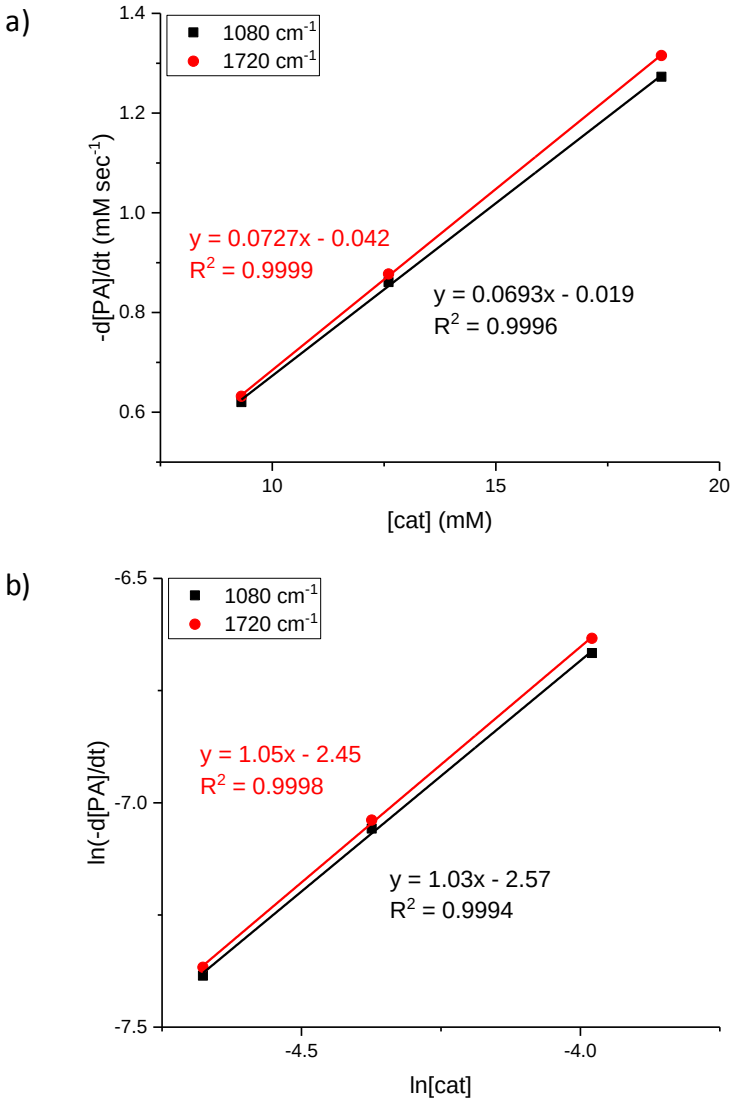


Figure 5.6 – Plots to determine the order in ***[LZnMgBr$_2$]*** *through ATR-IR spectroscopy. Reaction conditions: [PA]$_0$ = 1.24 M, 100 °C. a) Rate of reaction (10-99 % PA conversion) against catalyst concentration. b) A ln(rate) against ln(catalyst concentration) plot. Appendix D, Figure D.49-D.51.*

Having only three measurements for initial rate analysis would normally not give reliable results. Therefore, this analysis can be further validated by implementing Reaction Progress Kinetic Analysis (RPKA), with the removal of the initiation period (0-10 %).[11,12] In this method the time coordinate is normalised through multiplication by the [cat]^x, where x is equal to the order to be fit. As the concentration of catalyst does not change throughout the course of a catalytic

reaction, the time axis is therefore normalised by catalyst concentration. The advantages of this method are that the entire reaction profile can be utilised and very few runs at different concentrations are required to obtain meaningful comparisons. A series of fits have been tested for different catalyst orders (Figure 5.7). This allows a direct comparison between reactions of different catalytic loadings, through fitting to different orders.

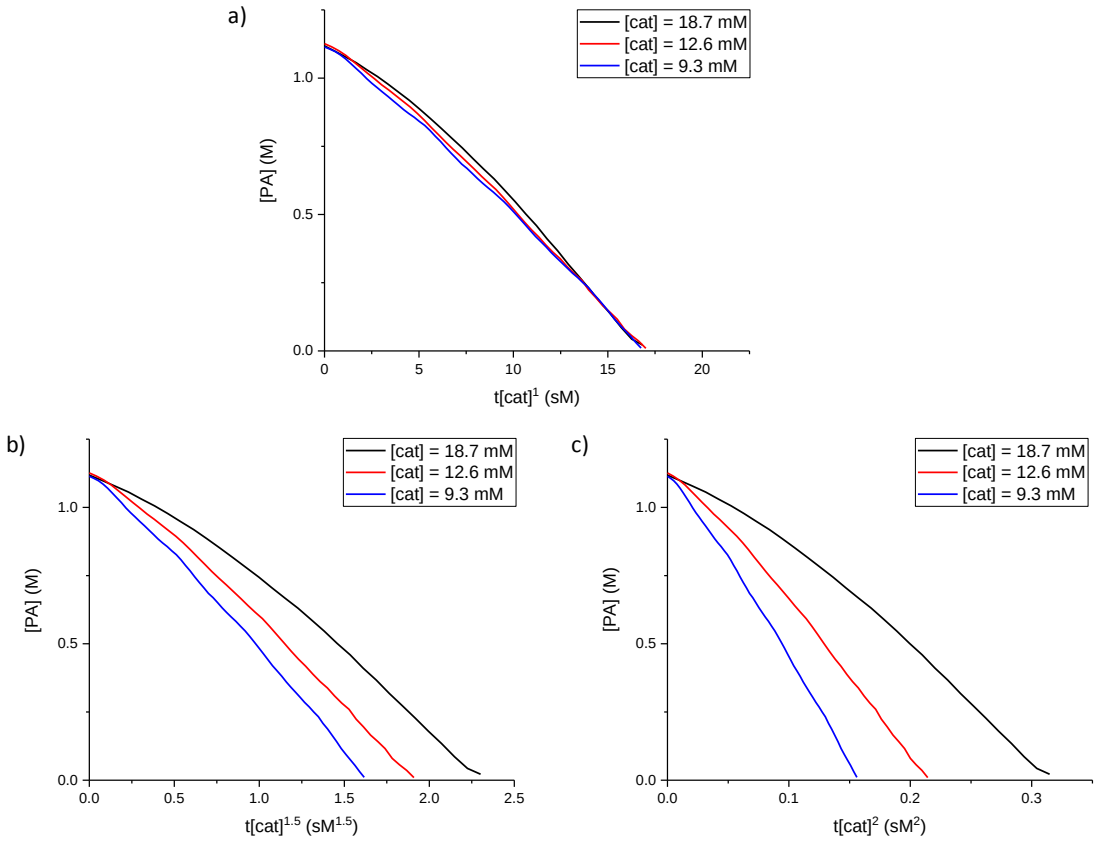


*Figure 5.7 – Comparative plots for a series of fits for the order in **[LZnMgBr$_2$]** for the copolymerisation of PA and CHO. Data obtained through in situ ATR-IR spectroscopy. Reaction conditions: [PA]$_0$ = 1.24 M, 100 °C. Fits shown for [cat]^x where x = 1(a), 1.5(b) and 2(c).*

Qualitatively, the best fit for the three catalyst concentrations appears from the t[cat]^1 axis, suggesting a first order dependency in catalyst concentration. This can be verified further through statistical analysis of the x-axis values at 99 % conversion (i.e. when dispersion would be greatest) (Table 5.1). The relative standard deviation (or coefficient of variation, C_v) clearly shows that a first order dependence is the best fit for this data.

Table 5.1 – Comparison of the coefficient of variation, calculated from the values of t[cat]^x at 99 % PA conversion, to determine the reaction order in catalyst for the copolymerisation of PA and CHO.

Data Fit	[cat] (mM)			Standard Deviation (σ)	Coefficient of Variation (C_v)
	18.7	12.6	9.3		
t[cat]^1	19.635	17.010	16.758	1.593	0.090
t[cat]$^{1.5}$	2.685	1.909	1.617	0.552	0.267
t[cat]^2	0.367	0.214	0.156	0.109	0.444

5.4.4. Order in epoxide

Comparing the initial rates of polymerisation for a range of CHO concentrations (200 to 800 equivalents, in toluene solvent) yields a straight line plot, suggesting a first order relationship of CHO in the copolymerisation with PA (Figure 5.8). This method was used by Tolman and co-workers, amongst others, in an epoxide/anhydride copolymerisation kinetic study.[13] The epoxide was also kept in excess here, to further ensure that the assumption of zero order PA dependence was valid. Tolman and co-workers compared polymerisation using initial rates (0-20 % conversion) to extract the rate constant.[13] For this work using **[LZnMgBr$_2$]**, an initiation period of 0-10 % PA conversion was removed, as previously implemented, and the reaction also monitored to 20 % anhydride conversion.

A ln(rate) against ln[CHO] plot shows a linear relationship with a gradient of ~0.7. This finding suggests a possible order of < 1 in CHO. Although this is close to 1, further investigation is recommended.

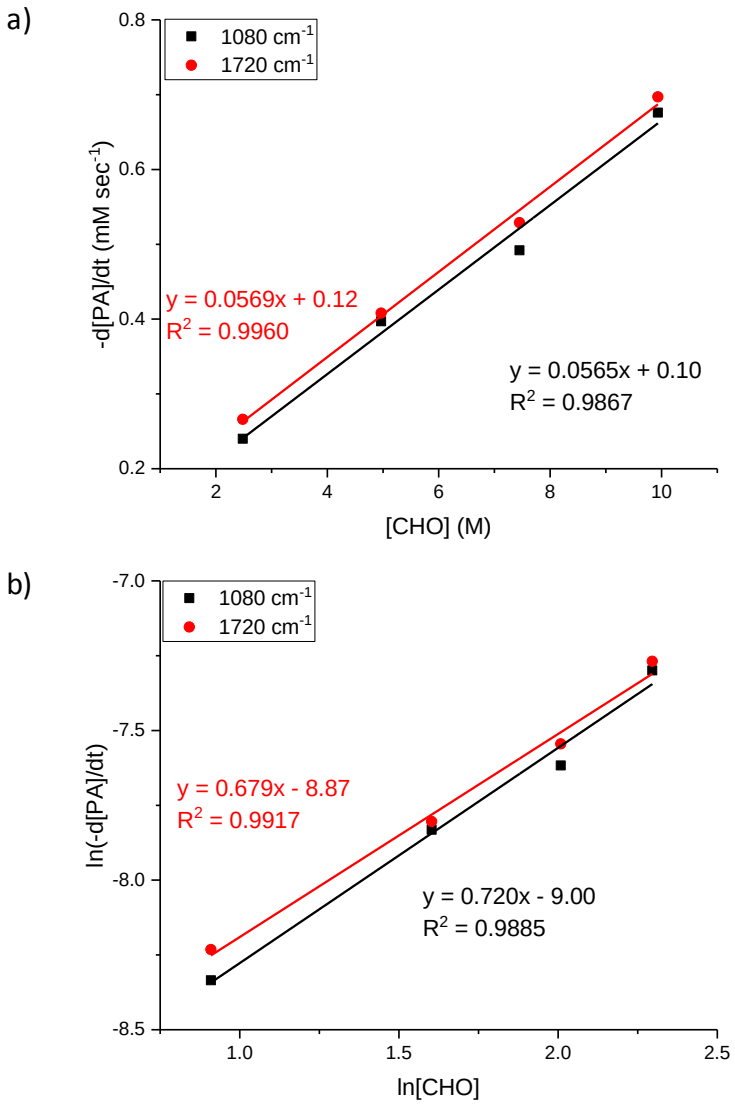


Figure 5.8 – Plots to determine the order in CHO through ATR-IR spectroscopy. Reaction conditions: ***[LZnMgBr$_2$]*** *= 12.6 mM, [PA]$_0$ = 1.24 M, toluene, 100 °C. a) Rate of reaction (10-20 % PA conversion) against catalyst concentration. b) A ln(rate) against ln(catalyst concentration) plot. Appendix D, Figure D.52-D.55.*

5.4.5. Discussion

From the preliminary rate studies into the copolymerisation of PA and CHO with the heterodinuclear catalyst **[LZnMgBr$_2$]**, the rate equation is likely to take the form of:

Equation 5.3 $$rate = k_p[PA]^0[\mathbf{LZnMgBr_2}]^1[CHO]^1$$

The data obtained clearly shows a zero order dependence on the concentration of PA. The correlation with a first order dependence on catalyst concentration was strong for the two different methods of analysis. The order in CHO is tentatively assigned as

first order as there is a linear relationship between rate of polymerisation and CHO concentration. However, further investigation is recommended as the ln(rate) against ln[CHO] plot suggested an order of < 1. This would make little chemical sense based on our current understanding of possible mechanistic pathways, but will be explored.

It seems likely that the rate determining step involves the epoxide and **[LZnMgBr$_2$]** and that the insertion of PA would then be rapid and not rate-limiting. This epoxide ring-opening rate determining step and rapid PA insertion is consistent with observations from a variety of other catalytic systems for anhydride/epoxide copolymerisation.[13-15]

5.5. Conclusions

The rate equation was derived for a heterodinuclear complex in the copolymerisation of CO_2/CHO and PA/CHO. **[LZnMgBr$_2$]** and CHO are found to be approximately first order, with a zero order dependence on CO_2 pressure, in the copolymerisation of CHO and CO_2. For CHO/PA copolymerisation, the order in **[LZnMgBr$_2$]** and CHO are suggested to be first order, with a clear zero order dependence on PA. Several kinetic analysis methods were used to validate the results.

Further work is needed to confirm the order in catalyst and CO_2 for CO_2/CHO copolymerisation, as well as the order in CHO for PA/CHO copolymerisation. This should be made easier through the study of other heterodinuclear catalysts, now accessible through this work, that do not have slow initiation. Catalysts with benzoate co-ligands (such as catalyst **[LZnMg(OBz^{NMe2})$_2$]**) could be ideal candidates for this study. The utilisation of *in situ* ATR-IR spectroscopy for a high pressure system would also facilitate these kinetic studies and is recommended in future.

A computational study, building on previous results, revealed a reaction pathway for catalysts **[LZnMg(OAc)$_2$]**, **[LMg$_2$(OAc)$_2$]** and **[LZn$_2$(OAc)$_2$]** which was analogous to a previous study.[1] Differences in reactivity between the homodinuclear and heterodinuclear catalysts could not be rationalised through this computational work. However, the rate determining step was again shown to be the ring-opening of the epoxide by the catalyst, in a cooperative dinuclear mechanism.

It seems reasonable to infer that the chain-shuttling mechanism for the copolymerisation of CO_2 and CHO, proposed for the zinc acetate homodinuclear catalyst **[LZn$_2$(OAc)$_2$]**, is an appropriate model for the heterodinuclear catalyst **[LZnMgBr$_2$]**. This suggests the rate enhancement observed for the heterodinuclear catalysts, in comparison to their homodinuclear analogues, does not originate from an alternative mechanism.

5.6. References

(1) Buchard, A.; Jutz, F.; Kember, M. R.; White, A. J. P.; Rzepa, H. S.; Williams, C. K. *Macromolecules* **2012**, *45*, 6781.
(2) Jutz, F.; Buchard, A.; Kember, M. R.; Fredrickson, S. B.; Williams, C. K. *J. Am. Chem. Soc.* **2011**, *133*, 17395.
(3) Ph.D Thesis of Prabhjot Kaur Saini *Imperial College London* **2015**.
(4) Nakano, K.; Hashimoto, S.; Nozaki, K. *Chem. Sci.* **2010**.
(5) Moore, D. R.; Cheng, M.; Lobkovsky, E. B.; Coates, G. W. *J. Am. Chem. Soc.* **2003**, *125*, 11911.
(6) Xiao, Y.; Wang, Z.; Ding, K. *Macromolecules* **2006**, *39*, 128.
(7) Klaus, S.; Vagin, S. I.; Lehenmeier, M. W.; Deglmann, P.; Brym, A. K.; Riegert, B. *Macromolecules* **2011**, *44*, 9508.
(8) Garden, J. A.; Saini, P. K.; Williams, C. K. *J. Am. Chem. Soc.* **2015**, *137*, 15078.
(9) Lehenmeier, M. W.; Bruckmeier, C.; Klaus, S.; Dengler, J. E.; Deglmann, P.; Ott, A.-K.; Rieger, B. *Chem. Eur. J.* **2011**, *17*, 8858.
(10) Liu, J.; Ren, W.-M.; Liu, Y.; Lu, X.-B. *Macromolecules* **2013**, *46*, 1343.
(11) Blackmond, D. G. *Angew. Chem. Int. Ed.* **2005**, *44*, 4302.
(12) Burés, J. *Angew. Chem. Int. Ed.* **2016**, *55*, 2028.
(13) Fieser, M. E.; Sanford, M. J.; Mitchell, L. A.; Dunbar, C. R.; Mandal, M.; Van Zee, N. J.; Urness, D. M.; Cramer, C. J.; Coates, G. W.; Tolman, W. B. *J. Am. Chem. Soc.* **2017**, *139*, 15222.
(14) Jeske, R. C.; Rowley, J. M.; Coates, G. W. *Angew. Chem. Int. Ed.* **2008**, *47*, 6041.
(15) Saini, P. K.; Romain, C.; Zhu, Y.; Williams, C. K. *Polym. Chem.* **2014**, *5*, 6068.

Chapter 6

Conclusions and Outlook

6.1. Conclusions

This thesis has described the successful synthesis of a new class of heterodinuclear catalysts coordinated by the same symmetric macrocycle and a range of carboxylate co-ligands. The catalysts show high activity in epoxide copolymerisation reactions, without compromising on selectivity or stability under high temperatures or aerobic conditions. A synthetic procedure was developed which capitalises on a simple co-ligand metathesis reaction to access a series of new catalysts. This method could be a useful step in the future preparation of catalysts which show even higher activity. The salt metathesis route produced catalysts which were significantly more active than the precursor dibromide catalyst, most notably through decreasing the initiation time of the reaction.

This work demonstrates the use of *in situ* ATR-IR spectroscopy to provide a detailed analysis of copolymerisation reaction progress. The current literature standard method of calculating activity, based on turnover frequency calculated from a single time point, gives only limited information compared to this determination of rate constant. Indeed, a comparison of turnover frequency, from a single point kinetic measurement, against calculated rate constant highlights the advantages of continual reaction assessment for comparing catalyst systems.

It was shown that the catalyst initiation times varied significantly, even when using a series of benzoate co-ligands. The correlation between initiation time and catalyst structure is not simple and requires further investigation to fully uncover the factors responsible, but **[LZnMg(OBz^{NO2})$_2$]** displayed an initiation time 8 times shorter than **[LZnMgBr$_2$]** [80 °C, 1 bar]. Propagation rates also varied depending on the co-ligand, although only by a maximum factor of 3. It is, therefore, valid to target future efforts

in catalyst design towards optimisation of the co-ligand class, rather than fine-tuning the electronic features of a particular co-ligand, as was the focus here.

The new heterodinuclear catalysts were active for the copolymerisations with various epoxides, of varying ring strain, including cyclopentene oxide and vinyl cyclohexene oxide, with limited formation of ether linkages. In terms of renewably derived epoxides, there was no reaction with limonene oxide; however, the catalysts were active for the selective copolymerisation of menthene oxide and cyclohexadiene oxide with CO_2, providing a means to access biorenewable polymers. The catalysts showed low activity for propylene oxide/CO_2 ROCOP; this result should be followed up as the lack of polyether formation is rather unusual.

Mechanistic investigations into the copolymerisation of CO_2 and cyclohexene oxide with heterodinuclear catalysts gave the same rate equation as an analogous homodinuclear catalyst.[1] This study could be extended in future to include a second heterodinuclear catalyst, showing a shorter initiation time, to improve the quality of the data. The rate equation for the copolymerisation of phthalic anhydride and cyclohexene oxide was also investigated and showed a first order dependence on catalyst and epoxide, with a zero order dependence on anhydride. However, additional investigations are needed to confirm the reaction order in epoxide.

A computational study using density functional theory, based on previous publications, explored the effects of the zinc and magnesium centres on the relative energy barriers in the propagation cycle. A slight preference for the magnesium centre to bind the epoxide, and a possible lower barrier to CO_2 insertion at the zinc centre, was observed. However, the differences in the energy barrier for the rate

determining step (ring-opening of an epoxide by a metal carbonate) were negligible and probably within experimental error. Competing electronic and steric factors affect the relative energy of intermediates and transition states, complicating any explanation and, therefore, prediction of experimental trends in catalytic cycles.

The mechanistic studies supported the hypothesis that heterodinuclear catalysts could operate by a chain shuttling mechanism. However, the origins of the experimentally observed rate enhancement, compared to their homodinuclear analogues, still remains rather unclear.

In summary, this thesis presents eight new pure heterodinuclear complexes which show some of the highest rates in the low pressure copolymerisation of CO_2 with epoxides.

6.2. Outlook

6.2.1. Formations of polyols for polyurethanes

Currently the major application for low molar mass polycarbonates, produced from the copolymerisation of epoxides with CO_2, is in the production of polycarbonate polyols for polyurethane (PU) synthesis.[2] The incorporation of CO_2 into the polyols lowers the greenhouse gas emissions associated with polymer production by up to 19 %, compared to polyether derivatives, by reducing the amount of petrochemically-derived epoxides required.[3]

Such polyols benefit from the high levels of polymerisation control, which allow access to monomodal polyols with narrow dispersity. Since telechelic hydroxyl terminated polyols are essential, therefore, further efforts to control the end group

are warranted. One attraction of these catalysts is the facility to use them with excess diol which leads to selective polyol formation.

Multifunctional initiators, such as triols, allow routes to branched polyol structures and can increase the number of hydroxyl groups per gram of polyol produced.[4,5] A higher polyol hydroxyl number leads to greater crosslinking when reacted with isocyanates, producing more rigid polyurethanes with improved thermal properties.

The utilisation of poly(propylene carbonate) polyols have also shown to be promising routes to waterborne and flame-retardant polyurethanes.[6,7]

6.2.2. Production of block copolymers

As the catalysts described in this thesis are active towards a range of monomers, they should be explored in the production of block copolymers through application of switch catalysis. This is where a single catalyst switches between both ROCOP and ROP processes in a one-pot reaction, forming block copolymers.[8-10] Block copolymers are of particular interest for the production of elastomeric materials, where a central soft block (e.g. a long-chain aliphatic polyester) and outer hard blocks (e.g. semi-aromatic polyesters or rigid polycarbonates) can be tuned to show phase separation.[11]

The ROP of lactones should therefore be investigated and applied with epoxide/CO_2 or epoxide/anhydride ROCOP. These mixed monomer feedstocks have been used previously to access different polymer architectures.[12]

This process also requires monomodal molar mass distributions and so, when using the catalysts described here, an excess of chain transfer agents is required to form the desired telechelic polymers. These catalysts currently show promise in the formation

of known B-A-B blocks, with ε-caprolactone ROP and CHO/CO_2 ROCOP, at significantly faster rates (Figure 6.1). The monomer scope still needs to be explored, for example by using lactide in ROP or installing double bonds in ROCOP, to form a wider range of polymer architectures with the possibility to later apply post functionalisation methods.

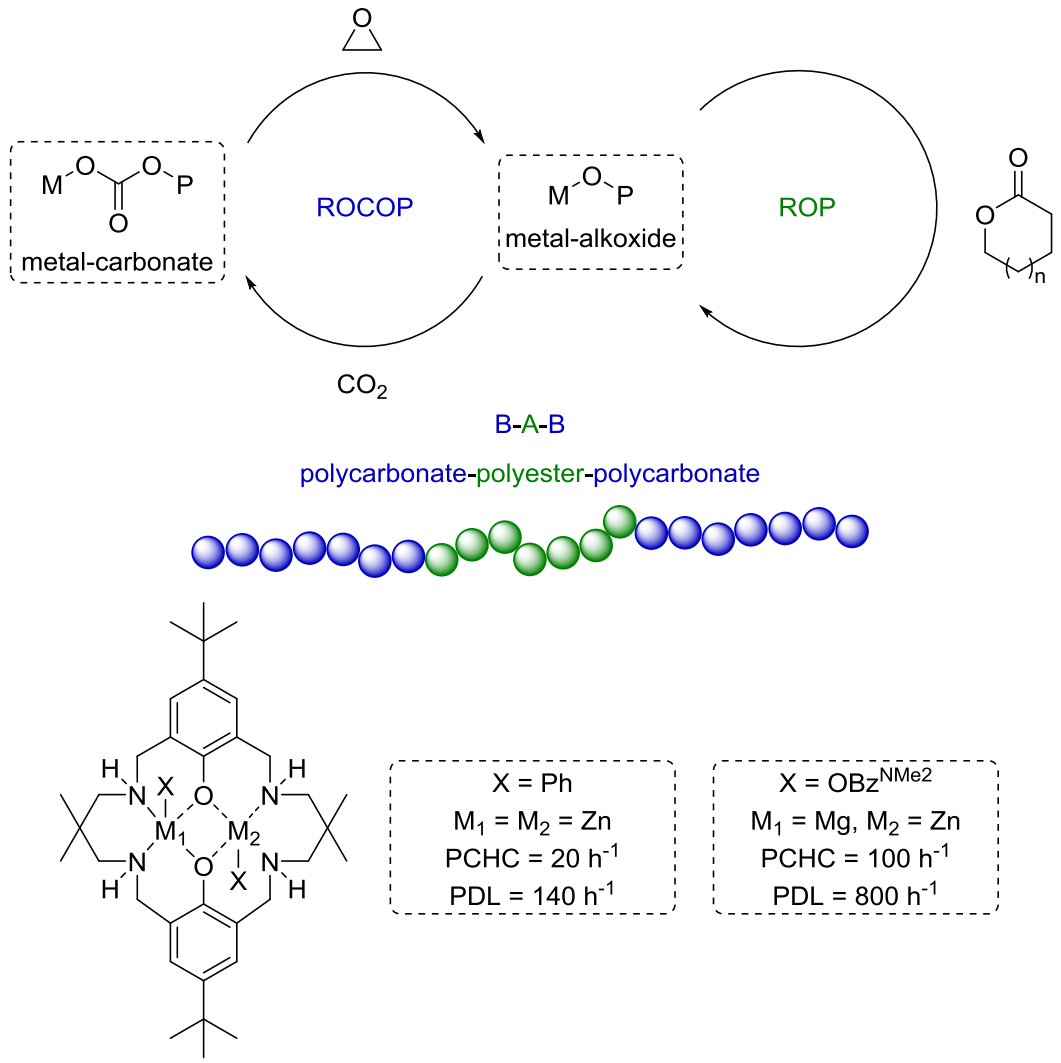


Figure 6.1 – General formation of block copolymers from ROP/ROCOP 'switch' catalysis (top). Comparative activities of catalysts, applied previously ***[LZn$_2$Ph$_2$]*** *and from this work* ***[LZnMg(OBz^{NMe2})$_2$]****, for the ROP of ε-DL at 100 °C and ROCOP of CHO and CO_2 at 80 °C.*

6.2.3. Catalyst modifications

The ligand applied in this thesis has been established in epoxide/CO_2 ROCOP for almost a decade, and as such several aspects of the corresponding catalysts have been explored.[13-17] Different metals from across the periodic table have been coordinated,

with cobalt showing high rates.[16] Heterodinuclear catalysts based on magnesium and zinc have shown superior performances to their homodinuclear analogues.[18,19] This work has now demonstrated that co-ligand choice can further enhance catalyst performance, albeit within a limited range.

Initial studies have been conducted to produce catalysts which contain highly reactive, non-initiating co-ligands, such as phenyl, alkyl, and amine ($N(SiMe_3)_3$) groups. These co-ligands will react by protonolysis with diols to form metal alkoxides either *in situ* or for isolation.[20] The metal alkoxides are able to initiate polymerisation and form telechelic polyols.[20] Initial studies suggest that phenyl reagents are too basic and a side reaction involving N–H deprotonation occurs. Other less basic co-ligands, such as pentafluorophenyl, are targeted.

Other features of the catalyst system are less easily modified but alterations to the ligand were also explored. Previous investigations showed that the macrocycle was more active than its open analogue, and that the amine functionality was essential for superior activity.[13] As the ability to operate catalysts at atmospheric pressures of CO_2 is still rare in the literature, this particular macrocycle clearly plays an important role in controlling catalysis, but as yet this is not fully understood. Work, carried out by the author, to modify the ligand was undertaken and is briefly highlighted here as another future avenue for catalyst development.

6.2.3.1. Thiol-derived macrocycle

A thio-phenolate analogue of the macrocyclic ligand was targeted to investigate the influence of the bridging anionic group on intermetallic distance and electronic communication ($\mathbf{L^1H_2}$, Figure 6.2).[21,22]

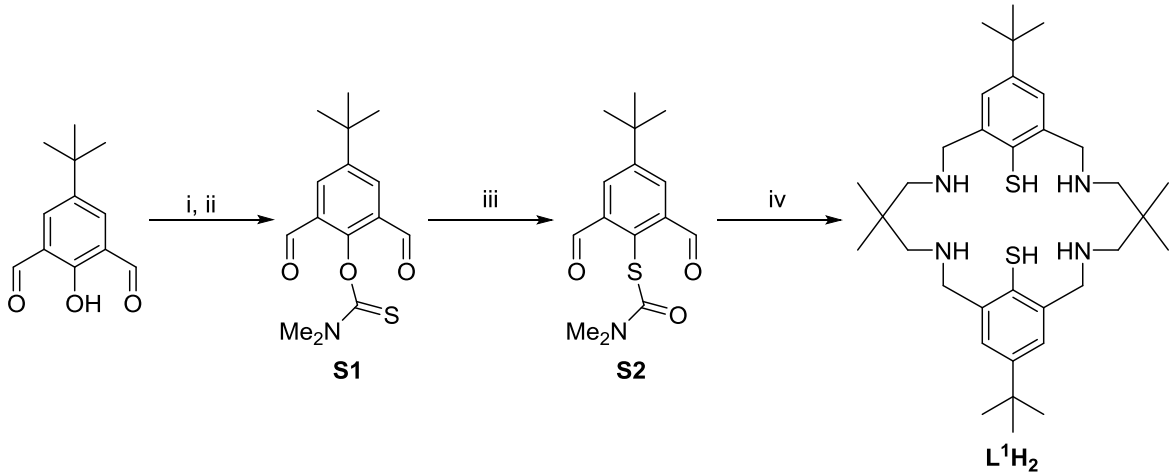


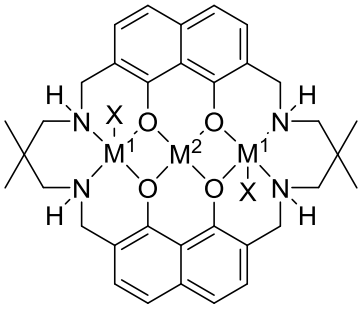
Figure 6.2 – Attempted synthesis of ***L¹H₂****: i) 2 eq DABCO, DMF, 35 °C, 15 min; ii) 1.5 eq dimethylthiocarbamoyl chloride, 35 °C, 16 h; iii) $BF_3{\cdot}OEt_2$, toluene, 85 °C, 16 h; iv) templation trials and reduction.*

Synthetic routes, based on previous methods, were tested and precursor **S2** was prepared in good overall yield (73 %), after several optimisations.[21] The ligand synthesis, by a metal templation step, was attempted for the *para*-methyl substituted phenolate analogue with different metal salts, e.g. NaOH and $Zn(OAc)_2$. However, ^1H NMR spectroscopy studies were inconclusive due to poor solubility and broad resonances observed in d_4-methanol, d_8-THF and d_3-MeCN. It was, therefore, difficult to distinguish between complex formation and polymer by-products. It seems that the *para*-phenolate tertiary butyl groups are essential for solubility, as other derivatives become almost completely insoluble upon macrocyclic formation. Future work should focus on using **S2** as a precursor, and investigate other templating agents and conditions, by increasing dilution or decreasing temperature.

The synthesis of ligand $\mathbf{L^1H_2}$ is targeted for the future to allow subsequent complexation and thereby enable investigation into the importance of the S–M bond in comparison to the phenolic O–M analogue in copolymerisation.

6.2.3.2. Extended naphthalene-derived macrocycle

Since heterodinuclear catalysts have proven to be efficient, a series of trimetallic catalysts are targeted, accessed by extension of the ligand framework (Figure 6.3).



$[L^2M^1_2M^2X_2]$

Figure 6.3 – Proposed catalyst structure for a trimetallic ligand.

This ligand would allow three metal centres to be coordinated within the plane of the ligand. The corresponding catalysts could enable investigation of metal cooperativity and differentiation of roles in catalysis; for example, the central metal (M^2) can only serve as a Lewis acid and cannot obviously initiate, whilst the M^1 metals provide sites for initiation and chain growth.

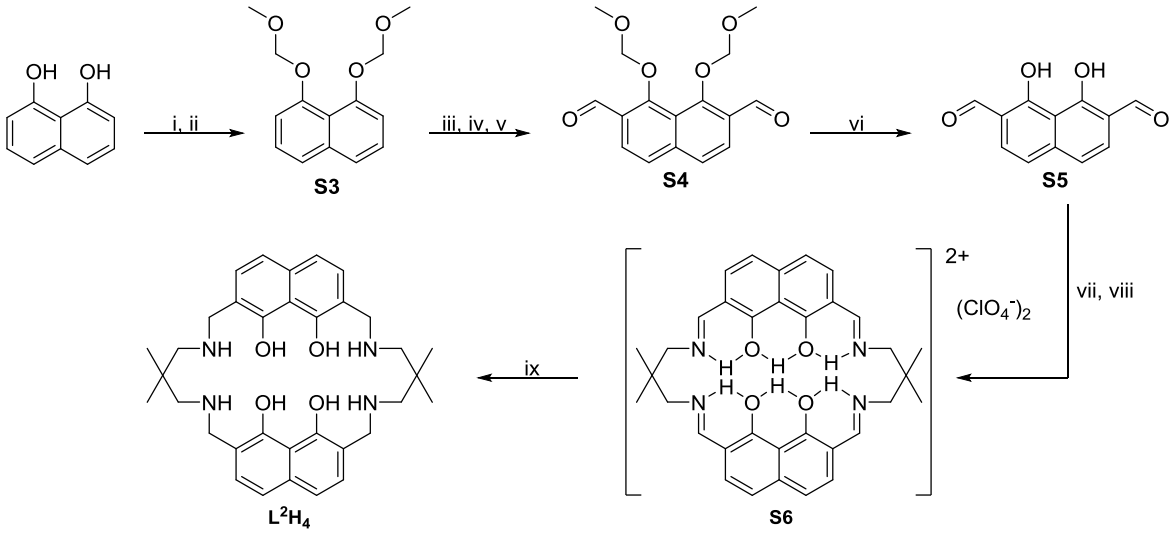


Figure 6.4 – Proposed synthesis of ***L²H₂****: i) 2.2 eq NaH, DMF, 0 °C; ii) 2 eq MOMCl, Et_2O, RT, 16 h; iii) 3 eq ^{n}BuLi, 3 eq TMEDA, Et_2O, 0 °C, 8 h; iv) 6 eq DMF, 0 °C, 1 h; v) HCl (dilute); vi) HCl–^{i}PrOH, DCM, 0 °C, 24 h; vii) 4 eq $NaClO_4$, 2 eq AcOH, MeOH; viii) 1 eq 2,2-dimethyl-1,3-propanediamine, MeOH, RT, 24; ix) 26 eq $NaBH_4$, MeOH, 0 °C → RT.*

S3 can be made on an 8 g scale with 71 % yield. However, the synthesis of precursor **S4** is lengthy and particularly low yielding (41 %).[23,24] The deprotection step to form

S5 is reproducibly achieved in 94 % yield. The proton templation step to form **S6** was successful, although a mixture of polymer and macrocycle was produced. The macrocycle was sparingly soluble in MeOH and therefore could be recrystallised to form the pure product, albeit only 85 mg.

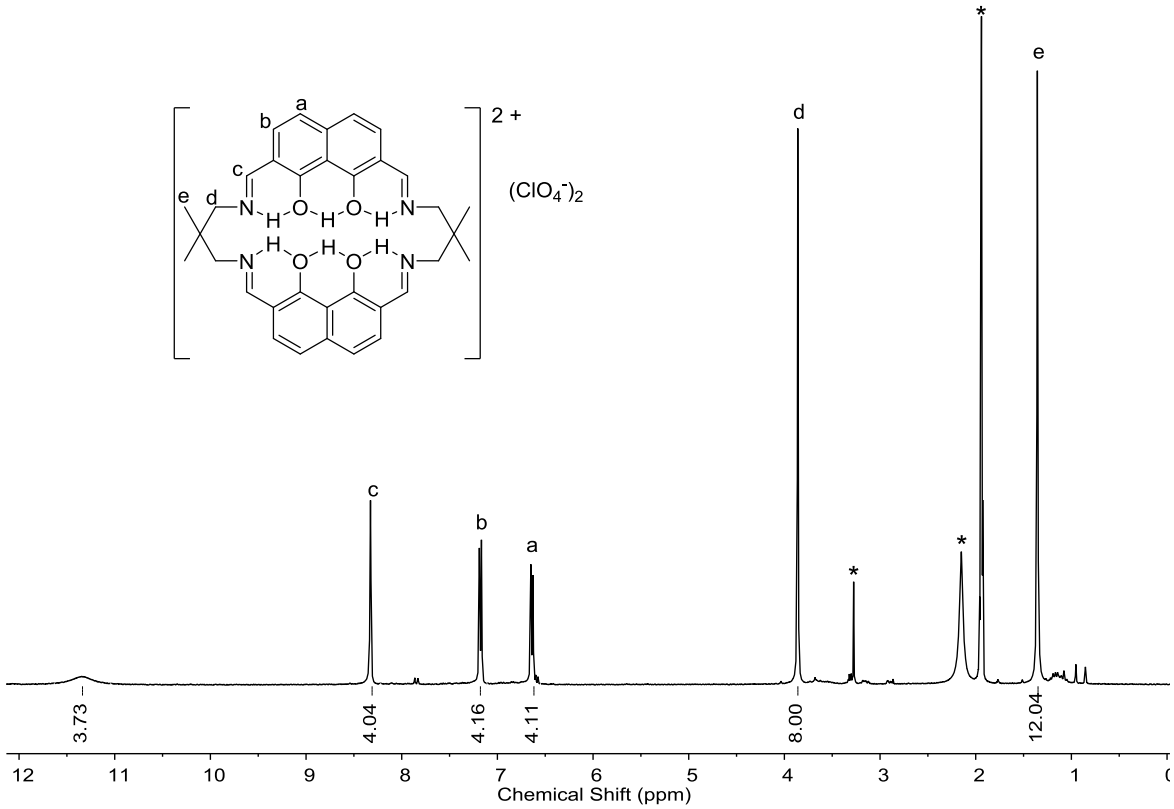


*Figure 6.5 – ^{1}H NMR spectrum of **S6** in d_3-MeCN, with residual solvent signals and MeOH solvent are labelled with *.*

The reduction of **S6** could only be carried out on a < 100 mg scale, due to low yields in previous steps. This was carried out with a $NaBH_4$ reduction, and a colour change of deep red to yellow was observed, suggesting reduction has been at least partially successful. However, the product could not be isolated from the boron salts due to the low quantities of materials produced. Although the synthesis of the ligand appears feasible, the formation of pure $\mathbf{L^2H_2}$ is yet to be confirmed and characterised. Initial tests suggest it also has low solubility in a range of solvents, such as MeOH, water, DMSO and EtOAc. Modifications, to install alkyl groups onto the aromatic ring, are therefore most likely required to improve yields.

6.2.4. Overview

To improve the commercial viability of the copolymerisation of CO_2 and epoxides, cheap and highly active catalysts are needed. Catalysts able to form poly(propylene carbonate) and other poly(alkylene carbonates) are desirable as these epoxides are already manufactured and used at scale in polyurethane applications. To further improve sustainability, biorenewable epoxides are worth further investigation, particularly these which are by-products of, or are present in, agricultural or industrial waste streams.

It is essential to try to better understand the underlying mechanisms of the copolymerisation reactions to improve catalyst design. Therefore further studies are required to confirm the rate law by collecting more data points and utilising *in situ* ATR-IR spectroscopy, at a range of CO_2 pressures. This work has also demonstrated the importance of initiation in catalysis and should thus be studied through NMR spectroscopy and IR spectroscopy to better understand the first coordination/insertion step. It may also be important to extract the activation energy of the heterodinuclear systems through Eyring analysis, and compare these between catalysts.

A final consideration is that catalysts that are straightforward to make and air stable are likely top targets for future commercial value. The field of CO_2/epoxide copolymerisation is continually moving forward in its performances, and has recently begun commercialisation by several companies, such as Novomer (acquired by Saudi Aramco), Repsol, Covestro and Econic Technologies.[25-28]

6.3. References

(1) Jutz, F.; Buchard, A.; Kember, M. R.; Fredrickson, S. B.; Williams, C. K. *J. Am. Chem. Soc.* **2011**, *133*, 17395.
(2) Langanke, J.; Wolf, A.; Hofmann, J.; Bohm, K.; Subhani, M. A.; Muller, T. E.; Leitner, W.; Gurtler, C. *Green Chem.* **2014**, *16*, 1865.
(3) Assen, N. v. d.; Bardow, A. *Green Chem.* **2014**, *16*, 3272.
(4) Scharfenberg, M.; Hofmann, S.; Preis, J.; Hilf, J.; Frey, H. *Macromolecules* **2017**, *50*, 6088.
(5) Hilf, J.; Schulze, P.; Seiwert, J.; Frey, H. *Macromol. Rapid Commun.* **2014**, *35*, 198.
(6) Wang, J.; Zhang, H.; Miao, Y.; Qiao, L.; Wang, X.; Wang, F. *Green Chem.* **2016**, *18*, 524.
(7) Cyriac, A.; Lee, S. H.; Varghese, J. K.; Park, J. H.; Jeon, J. Y.; Kim, S. J.; Lee, B. Y. *Green Chem.* **2011**, *13*, 3469.
(8) Romain, C.; Williams, C. K. *Angew. Chem. Int. Ed.* **2014**, *53*, 1607.
(9) Zhu, Y.; Romain, C.; Williams, C. K. *J. Am. Chem. Soc.* **2015**, *137*, 12179.
(10) Stößer, T.; Chen, T. T. D.; Zhu, Y.; Williams, C. K. *Phil. Trans. R. Soc. A* **2018**, *376*.
(11) Zhu, Y.; Radlauer, M. R.; Schneiderman, D. K.; Shaffer, M. S. P.; Hillmyer, M. A.; Williams, C. K. *Macromolecules* **2018**.
(12) Romain, C.; Zhu, Y.; Dingwall, P.; Paul, S.; Rzepa, H. S.; Buchard, A.; Williams, C. K. *J. Am. Chem. Soc.* **2016**, *138*, 4120.
(13) Kember, M. R.; Knight, P. D.; Reung, P. T. R.; Williams, C. K. *Angew. Chem. Int. Ed.* **2009**, *48*, 931.
(14) Kember, M. R.; Williams, C. K. *J. Am. Chem. Soc.* **2012**, *134*, 15676.
(15) Kember, M. R.; White, A. J. P.; Williams, C. K. *Inorg. Chem.* **2009**, *48*, 9535.
(16) Kember, M. R.; White, A. J. P.; Williams, C. K. *Macromolecules* **2010**, *43*, 2291.
(17) Buchard, A.; Kember, M. R.; Sandeman, K. G.; Williams, C. K. *Chem. Commun.* **2011**, *47*, 212.
(18) Saini, P. K.; Romain, C.; Williams, C. K. *Chem. Commun.* **2014**, *50*, 4164.
(19) Garden, J. A.; Saini, P. K.; Williams, C. K. *J. Am. Chem. Soc.* **2015**, *137*, 15078.
(20) Romain, C.; Garden, J. A.; Trott, G.; Buchard, A.; White, A. J. P.; Williams, C. K. *Chem. Eur. J.* **2017**, *23*, 7367.
(21) Brooker, S.; Croucher, P. D.; Roxburgh, F. M. *J. Chem. Soc., Dalton Trans.* **1996**, 3031.
(22) Brooker, S.; Croucher, P. D.; Davidson, T. C.; Dunbar, G. S.; Beck, C. U.; Subramanian, S. *Eur. J. Inorg. Chem.* **2000**, 169.
(23) Glaser, T.; Liratzis, I. *Synlett* **2004**, 735.
(24) Salata, M. R.; Marks, T. J. *Macromolecules* **2009**, *42*, 1920.
(25) http://www.saudiaramco.com/en/home/news-media/news/acquires-novomers-polyol-business-downstream-expansion.html. Published Online: 2016 (accessed 28th March 2018).
(26) https://www.britishplastics.co.uk/materials/econic-opens-uks-first-carbon-capture-utilisation-demonstra/. Published Online: 2018 (accessed 28th March 2018).
(27) http://press.covestro.com/news.nsf/id/further-increase-of-polycarbonate-production. Published Online: 2017 (accessed 28th March 2018).
(28) http://www.bioplasticsmagazine.com/en/news/meldungen/20170224-Repsol-starts-up-pilot-plant-to-manufacture-CO2-based-polycarbonate-polyols.php. Published Online: 2017 (accessed 28th March 2018).

Chapter 7

Experimental Procedures and Data

7.1. Materials

7.1.1. General materials

All metal complexes were synthesised under anhydrous conditions, using standard glovebox and Schlenk line techniques. The macrocyclic ligand was synthesised according to literature procedures.[1]

All solvents used in complex synthesis and polymerisation reactions were dried, degassed by at least three freeze-pump-thaw cycles and stored over activated 4 Å molecular sieves under nitrogen. Tetrahydrofuran (THF) was dried by refluxing over sodium and benzophenone. Toluene and dichloromethane were collected from a MB-SPS-800 Solvent Purification System (MBraun). Pyridine and diethyl carbonate were purchased from Sigma Aldrich as anhydrous, with pyridine then being distilled from calcium hydride at atmospheric pressure. All deuterated solvents were obtained as anhydrous (> 99.6 %) from GOSS Scientific, with d_4-methanol being used as received from individual glass ampoules and d_8-THF being degassed and stored over activated molecular sieves before use.

Research grade carbon dioxide (BOC, 99.99 %) was used for all copolymerisation studies and dried through two MicroTorr purifier columns at point of use, with a flow rate below 0.5 slpm (standard litre per minute). All other reagents were obtained from Sigma Aldrich or Strem and were used as received.

7.1.2. Epoxide synthesis and purification

Menthene oxide (synthesised by Dr Giulia Fiorani) and cyclohexadiene oxide (synthesised by Dr Leticia Peña Carrodeguas) were synthesised according to literature methods.[2,3] All other epoxides were purchased from commercial sources.

Cyclohexene oxide was dried over calcium hydride and fractionally distilled under nitrogen at atmospheric pressure. Limonene oxide, menthene oxide and cyclohexadiene oxide were dried over calcium hydride and fractionally distilled under reduced pressure. Propylene oxide was dried over calcium hydride and fractionally distilled, repeating this process a second time. Cyclopentene oxide, 3,4-epoxytetrahydrofuran, 4-vinyl-1-cyclohexene 1,2-epoxide and allyl glycidyl ether were dried over calcium hydride and then a vacuum transfer was carried out before drying with sodium hydride and collecting via vacuum transfer. All epoxides were stored under nitrogen.

7.1.3. Anhydride purification

The synthesis of norcantharidin (NA) was conducted by Dr Giulia Fiorani, from a literature preparation.[4] Phthalic anhydride was dissolved in benzene and filtered, before a crystallisation from chloroform and sublimation at 40 °C.[5] All other anhydrides were sublimed before use and all were stored under a nitrogen atmosphere.

7.2. Instrumentation

In situ ATR-IR measurements were performed on a Mettler-Toledo ReactIR ic.10 spectrometer equipped with a MCT detector and a silver halide DiComp probe.

^{1}H and $^{13}C\{^{1}H\}$ NMR spectra were recorded on Bruker Avance III or Bruker Avance with ^{13}C cryoprobe instruments.

MALDI ToF analysis was performed on Micromass MALDI micro MX spectrometers. Dithranol matrix was used for all catalysts and polymer samples and potassium trifluoroacetate was utilised as an additive for polymer samples.

Thermogravimetric analysis (TGA) was carried out using a Mettler Toledo TGA/DSC 1, under a flow of dry nitrogen with flow rate of 60 $mL \cdot min^{-1}$, from 50–500°C, at a heating rate of $5°C \cdot min^{-1}$.

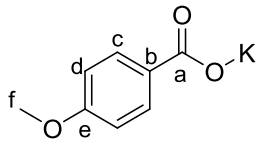
Differential scanning calorimetry (DSC) was performed on a Mettler Toledo DSC 3 Star calorimeter with a flow rate of nitrogen maintained at 80 $mL \cdot min^{-1}$. The sample was heated at rate of 10 $°C \cdot min^{-1}$ to 110 °C. The sample was then held at 110 °C for 1 minute, before starting the cooling cycle, at the same rate, to -90 °C. The heating and cooling cycle was repeated another two times.

The X-ray crystallography for complex **[LZnMg(O_2CPentyl)$_2$]**·MeOH was carried out by Dr Andrew J. P. White at Imperial College London, Department of Chemistry, London, SW7 2AZ. Data was collected using an Agilent Xcalibur PX 3E diffractometer. The crystallographic data for complex **[LZnMg(OBz^{CF3})$_2$]**·MeOH was collected and solved by Dr Christopher B. Durr, at the University of Oxford, using an Oxford Diffraction Supernova diffractometer. Structural solutions were conducted with SHELXT and refinements were carried out using SHELXL-14/2013 programmes.

Elemental analysis was carried out by Mr Stephen Boyer at London Metropolitan University, North Campus, Holloway Road, London N7 7DD.

7.3. Potassium Salt Synthesis

7.3.1. [KOBz^{OMe}]

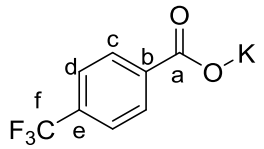


KH (320 mg, 7.98 mmol) was added to a Schlenk before the addition of dry THF (40 mL) and cooled to 0 °C. *p*-Anisic acid (1.24 g, 7.8 mmol) was slowly added via a solid addition tube and stirred for 15 min at 0 °C. The suspension was warmed to room temperature, stirred for 1 h and then the solvent filtered before drying the solid *in vacuo* to give the product as a white powder (1.25 g, 6.5 mmol, 82 % yield).

^{1}H NMR (400 MHz, d$_4$-methanol, δ(ppm)): 7.90 (d, 2H, $^{3}J_{H-H}$ = 9 Hz, c), 6.87 (d, 2H, $^{3}J_{H-H}$ = 9 Hz, d), 4.87 (s, 3H, f). ^{13}C{^{1}H} NMR (100 MHz, d$_4$-methanol, δ(ppm)): 175.4 (a), 163.0 (e), 132.1 (c), 131.5 (b), 113.8 (d), 55.7 (f).

Calc. for $C_8H_7O_3K$: C, 50.51; H, 3.71; Found: C, 50.35; H, 3.90 %.

7.3.2. [KOBz^{CF3}]

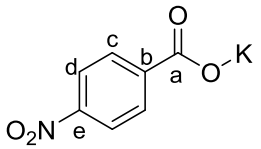


KH (320 mg, 7.98 mmol) was added to a Schlenk before the addition of dry THF (40 mL) and cooled to 0 °C. 4-(Trifluoromethyl)benzoic acid (1.52 g, 7.8 mmol) was slowly added via a solid addition tube and stirred, for 15 min, at 0 °C. The suspension was warmed to room temperature, stirred for 1 h, and then the solvent filtered off before drying the solid *in vacuo* to give the product as a white powder (1.47 g, 6.5 mmol, 81 % yield).

^{1}H NMR (400 MHz, d$_4$-methanol, δ(ppm)): 8.07 (d, 2H, $^{3}J_{H-H}$ = 8 Hz, c), 7.65 (d, 2H, $^{3}J_{H-H}$ = 8 Hz, d). ^{13}C{^{1}H} NMR (100 MHz, d$_4$-methanol, δ(ppm)): 173.6 (a), 143.2 (b), 132.7 (q, $^{2}J_{F-H}$ = 32 Hz, e), 130.7 (c), 125.8 (q, $^{1}J_{F-H}$ = 272 Hz, f), 125.7 (q, $^{3}J_{F-H}$ = 5 Hz, d). ^{19}F{^{1}H} NMR (376 MHz, d$_4$-methanol, δ(ppm)): -64.9 (s).

Calc. for $C_8H_4F_3O_2K$: C, 42.10; H, 1.77; Found: C, 42.02; H, 1.74 %.

7.3.3. [KOBz^{NO2}]^{6}

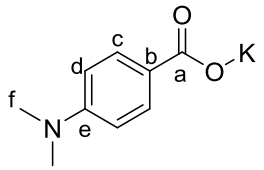


4-Nitrobenzoic acid (3.34 g, 20 mmol) was stirred in a round bottom flask in EtOH (30 mL) with a dropping funnel attached, containing KO^{t}Bu (2.24 g, 20 mmol) dissolved in EtOH (20 mL). This solution was added to the acid, dropwise over 1 hour, at room temperature and stirred for a further hour. The resulting solid was collected by filtration and washed with EtOH (2 x 10 mL) and cold Et$_2$O (10 mL). The product was collected as a white powder and dried *in vacuo* (2.17 g, 10.6 mmol, 53 % yield).

^{1}H NMR (400 MHz, d$_4$-methanol, δ(ppm)): 8.22 (d, 2H, $^{3}J_{H-H}$ = 9 Hz, d), 8.11 (d, 2H, $^{3}J_{H-H}$ = 9 Hz, c). ^{13}C{^{1}H} NMR (100 MHz, d$_4$-methanol, δ(ppm)): 172.5 (a), 150.4 (e), 145.2 (b), 131.2 (c), 123.9 (d).

Calc. for $C_7H_4NO_4K$: C, 40.97; H, 1.96; N, 6.83; Found: C, 41.09; H, 2.04; N, 6.76 %.

7.3.4. [KOBz^{NMe2}]

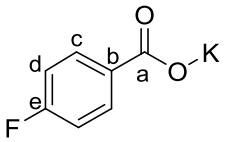


4-(Dimethylamino)benzoic acid (1.32 g, 8.0 mmol) was stirred in THF (40 mL) before the slow addition of $KN(SiMe_3)_2$ (1.59 g, 8.0 mmol). The suspension was stirred for 16 hours at room temperature before removal of the solvent by filtration. The resulting solid was washed with pentane and dried *in vacuo* to give the product as a white powder (1.51 g, 7.4 mmol, 93 % yield).

^{1}H NMR (400 MHz, d_4-methanol, δ(ppm)): 7.83 (d, 2H, $^3J_{H-H}$ = 9 Hz, c), 6.68 (d, 2H, $^3J_{H-H}$ = 9 Hz, d), 2.97 (s, 6H, f). ^{13}C{^{1}H} NMR (100 MHz, d_4-methanol, δ(ppm)): 176.4 (a), 153.7 (e), 131.8 (c), 126.3 (b), 112.3 (d), 40.5 (f).

Calc. for $C_9H_{10}NO_2K$: C, 53.18; H, 4.96; N, 6.89; Found: C, 53.07; H, 5.01; N, 6.86 %.

7.3.5. [KOBz^F]



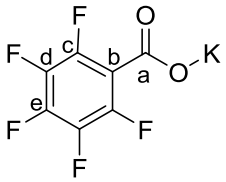
4-Fluorobenzoic acid (2.80 g, 20 mmol) was stirred in a round bottom flask in EtOH (20 mL) with a dropping funnel attached, containing KO^{t}Bu (2.24 g, 20 mmol) dissolved in EtOH (20 mL). This solution was added to the acid dropwise over 1 hour at room temperature and stirred for a further hour. The resulting solid was collected by filtration and washed with EtOH (2 x 10 mL) and cold Et_2O (10 mL). The product was collected as a white powder and dried *in vacuo* (3.25 g, 18.3 mmol, 91 % yield).

^{1}H NMR (400 MHz, d_4-methanol, δ(ppm)): 7.98 (m, 2H, c), 7.05 (m, 2H, d). ^{13}C{^{1}H} NMR (100 MHz, d_4-methanol, δ(ppm)): 174.2 (a), 165.6 (d, $^1J_{C-F}$ = 249 Hz, e), 135.5

(b), 132.6 (d, $^{3}J_{C-F}$ = 9 Hz, c), 115.2 (d, $^{2}J_{C-F}$ = 21 Hz, d). $^{19}F\{^{1}H\}$ NMR (376 MHz, d_4-methanol, δ(ppm)): -113.8.

Calc. for $C_7H_4FO_2K$: C, 47.18; H, 2.26; Found: C, 47.30; H, 2.13 %.

7.3.6. [KOBz^{F5}]^{6}

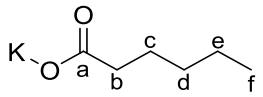


2,3,4,5,6-Pentafluorobenzoic acid (4.24 g, 20 mmol) was stirred in a round bottom flask in EtOH (20 mL) with a dropping funnel attached, containing KO^{t}Bu (2.24 g, 20 mmol) dissolved in EtOH (20 mL). This solution was added to the acid, dropwise over 1 hour, at room temperature and stirred for a further hour. The resulting solid was collected by filtration and washed with EtOH (2 x 10 mL) and cold Et_2O (10 mL). The product was collected as a white powder and dried *in vacuo* (4.32 g, 17.2 mmol, 86 % yield).

$^{19}F\{^{1}H\}$ NMR (376 MHz, d_4-methanol, δ(ppm)): -145.4 (m, 2F, c), -161.0 (t, 1F, $^{3}J_{F-F}$ = 20 Hz, e), -165.4 (m, 2F, d). $^{13}C\{^{1}H\}$ NMR (100 MHz, d_4-methanol, δ(ppm)): 164.3 (a), 144.1 (doublet of multiplets, $^{1}J_{C-F}$ = 245 Hz, c/d), 141.5 (doublet of multiplets, $^{1}J_{C-F}$ = 250 Hz, e), 138.6 (doublet of multiplets, $^{1}J_{C-F}$ = 251 Hz, c/d), 118.4 (triplet of multiplets, $^{2}J_{C-F}$ = 25 Hz, b).

Calc. for $C_7F_5O_2K$: C, 33.61; Found: C, 33.52 %.

7.3.7. [$KO_2CPentyl$]



Hexanoic acid (2.5 mL, 20 mmol) was stirred in a round bottom flask in EtOH (15 mL), with a dropping funnel containing KO^{t}Bu (2.24 g, 20 mmol) dissolved in EtOH (20 mL), attached. This solution was added to the acid dropwise over 1 hour at room temperature, and the reaction was stirred for a further hour. The solution was concentrated and recrystallised from hot EtOH. The resulting crystals were collected, washed with cold EtOH and dried *in vacuo* (1.34 g, 8.7 mmol, 43 % yield).

^{1}H NMR (400 MHz, d_4-methanol, δ(ppm)): 2.14 (t, 2H, $^3J_{H-H}$ = 8 Hz, b), 1.60 (m, 2H, c), 1.33 (m, 4H, d+e), 0.91 (t, 3H, $^3J_{H-H}$ = 7 Hz, f). $^{13}C\{^1H\}$ NMR (100 MHz, d_4-methanol, δ(ppm)): 183.1 (a), 39.3 (b), 33.1 (d), 27.5 (c), 23.6 (e), 14.4 (f).

Calc. for $C_6H_{11}O_2K$: C, 46.72; H, 7.19; Found: C, 46.82; H, 7.23 %.

7.4. Catalyst Synthesis

7.4.1. Synthesis of catalyst [LMgZnBr$_2$]

LH$_2$ (1.0 g, 1.82 mmol) and THF (5 mL) were added to a Schlenk tube, before the addition of a solution of $ZnEt_2$ (224 mg, 1.82 mmol) in THF (5 mL). The reaction mixture was stirred for 16 hours, at room temperature, before the addition of more THF (10 mL). This solution was cooled to -78 °C whilst stirring and then a solution of $MgBr_2$ (334 mg, 1.82 mmol), in THF (20 mL), and was added, dropwise, over 15 min. The reaction mixture was stirred at -78 °C, for 15 min, and then at room temperature, for 30 min, before the solvent was removed. The white powder was dried *in vacuo* overnight to yield the product (1.44 g, 1.80 mmol, 97 %).

^{1}H NMR (400 MHz, d$_4$-methanol, δ(ppm)): 7.05 (m, 2H, b'), 7.01(m, 2H, b), 4.91 (d, 2H, c), 4.10 (d, 2H, c'), 3.28 (d, 2H, d'), 3.23 (d, 2H, d), 3.07 (d, 2H, e), 2.75 (d, 2H, e'), 2.64 (d, 2H, f), 2.62 (d, 2H, f'), 1.25 (s, 18H, a), 1.08 (s, 3H, g), 1.06 (s, 3H, g'), 1.00 (s, 3H, h), 0.98 (s, 3H, h').

^{13}C{^{1}H} NMR (100 MHz, d$_4$-methanol, δ(ppm)): 161.5 (f), 139.1 (c), 129.4 (d'), 129.0 (d), 125.5 (e'), 124.7 (e), 64.0 (h), 63.4 (h'), 58.2 (g), 56.4 (g'), 35.0 (i'), 34.4 (b), 34.3 (i), 32.0 (a), 28.6 (j'), 28.3 (j), 21.6 (k), 21.0 (k').

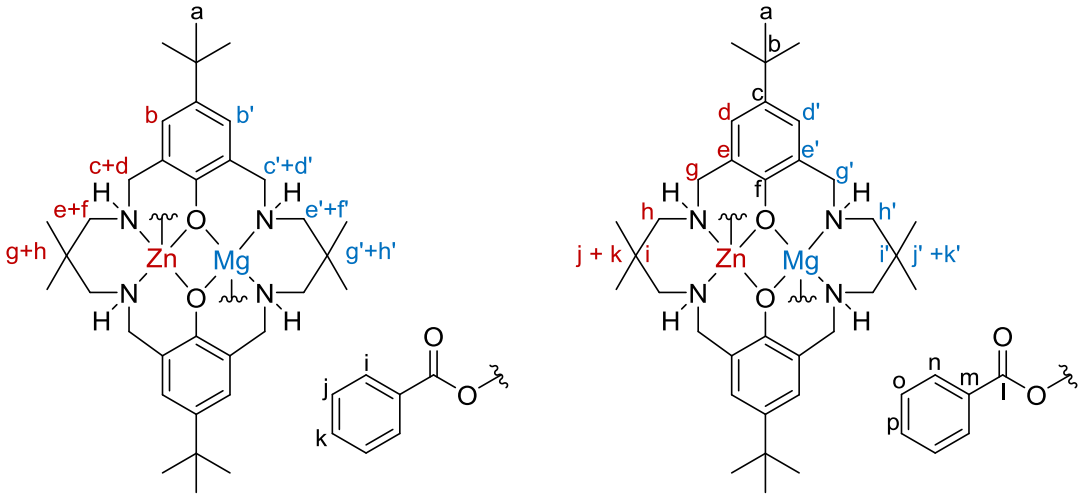
Calc. for $C_{34}H_{54}O_2N_4MgZnBr_2$: C, 51.03; H, 6.80; N, 7.00; Found: C, 51.23; H, 6.84; N, 6.94 %.

7.4.2. General procedure for synthesis of carboxylate-based catalysts

The intermediate complex, **[LMgZnBr$_2$]**, was synthesised as above, on a 0.91 mmol scale, without extensive drying. After complex formation in solution, the solvent was removed, the sample taken into the glovebox and the corresponding KX salt (1.82 mmol) was then added and stirred for 16 hours at room temperature. The resulting solid (KBr) was removed by filtration and the solution concentrated before the addition of DCM (2 mL). The solution was stirred for 1 hour before being filtered again and dried *in vacuo* to give the desired complex.

Where the scale of the reaction was altered, all reagent and solvent quantities were scaled accordingly.

7.4.3. Complex [LMgZn(OBz)$_2$]



Synthesised on a 1.82 mmol scale. Yielded a white powder (1.53 g, 1.73 mmol, 95 %).

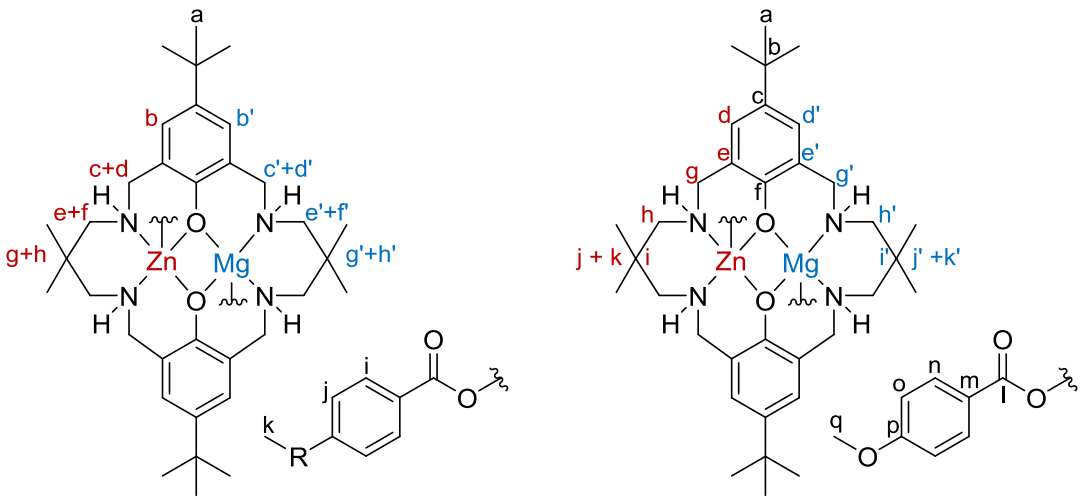
^{1}H NMR (400 MHz, d$_4$-methanol, δ(ppm)): 7.85 (br s, 4H, i), 7.33 (br t, $^3J_{H-H}$ = 6 Hz, 2H, k), 7.26 (br t, $^3J_{H-H}$ = 6 Hz, 4H, j), 6.96 (s, 4H, b+b'), 4.24 (d, $^2J_{H-H}$ = 12 Hz, 2H, c), 4.05 (d, $^2J_{H-H}$ = 12 Hz, 2H, c'), 3.27 (br m, 4H, d+d'), 2.91 (br d, $^2J_{H-H}$ = 11 Hz, 2H, e), 2.86-2.78 (m, 4H, f+e'), 2.71 (br d, $^2J_{H-H}$ = 11 Hz, 2H, f'), 1.43 (m, 6H, g+g'), 1.17 (s, 18H, a), 1.05 (m, 6H, h+h'). ^{13}C{^{1}H} NMR (100 MHz, d$_4$-methanol, δ(ppm)): 174.4 (l), 162.8 (f), 138.1 (c), 131.4 (p), 130.3 (n), 129.2 (d'), 129.1 (m), 129.0 (d), 128.5 (o), 125.3 (e'), 124.6 (e), 64.2 (h), 63.4 (h'), 56.9 (g), 56.2 (g'), 35.4 (i'), 34.9 (i), 34.3 (b), 32.0 (a), 28.9 (j'), 28.8 (j), 21.8 (k'), 21.3 (k).

IR ($\nu_{c=o}$, cm^{-1}, neat): 1603 (a, terminal), 1564 (a, bridging), 1387 (s, terminal).

MS (MALDI-ToF): m/z 758 [LMgZnOBz]$^+$ (100 %)

Calc. for $C_{48}H_{64}O_6N_4MgZn$: C, 65.31; H, 7.31; N, 6.35; Found: C, 65.17; H, 7.43; N, 6.39 %.

7.4.4. Complex [LMgZn(OBz^{OMe})$_2$]



Synthesised on a 1.82 mmol scale. Yielded a white powder (1.40 g, 1.48 mmol, 82 %).

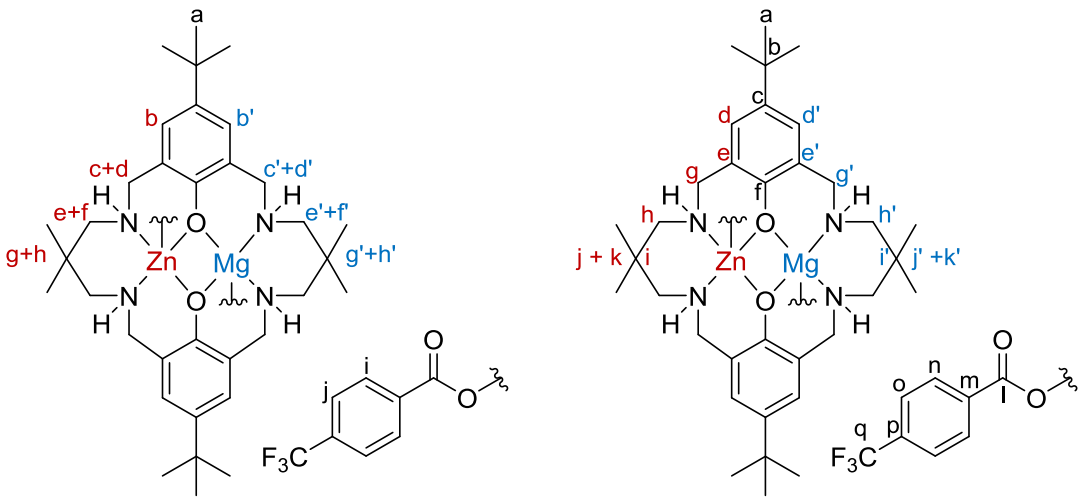
^{1}H NMR (400 MHz, d$_4$-methanol, δ(ppm)): 7.82 (br s, 4H, i), 6.96 (m, 4H, b+b'), 6.79 (br s, 4H, j), 4.23 (m, 2H, c), 4.09-4.02 (m, 2H, c'), 3.76 (s, 6H, k), 3.29-3.20 (m, 4H, d+d'), 2.91-2.87 (br m, 2H, e), 2.86-2.78 (m, 4H, f+e'), 2.70 (br d, 2H, f'), 1.44-1.41 (m, 6H, g+g'), 1.21-1.15 (m, 18H, a), 1.06-1.03 (m, 6H, h+h'). ^{13}C{^{1}H} NMR (100 MHz, d$_4$-methanol, δ(ppm)): 174.5 (l), 163.1 (p), 162.8 (f), 138.1 (c), 132.2 (n), 129.3 (d'), 129.0 (d), 128.1 (m), 125.3 (e'), 124.6 (e), 113.7 (o), 64.3 (h), 63.4 (h'), 56.9 (g), 56.3 (g'), 55.7 (q), 35.4 (i'), 34.8 (i), 34.3 (b), 32.0 (a), 28.9 (j'), 28.8 (j), 21.9 (k'), 21.3 (k).

IR ($\nu_{c=o}$, cm^{-1}, neat): 1597 (a, terminal), 1558 (a, bridging), 1381 (s, terminal).

MS (MALDI-ToF): m/z 790 [LMgZnOBz^{OMe}]$^+$ (100 %)

Calc. for $C_{50}H_{68}O_8N_4MgZn$: C, 63.70; H, 7.27; N, 5.94; Found: C, 63.51; H, 7.18; N, 5.82 %.

7.4.5. Complex [LMgZn(OBz^{CF3})$_2$]



Synthesised on a 0.91 mmol scale. Yielded a white powder (780 mg, 0.71 mmol, 78 %).

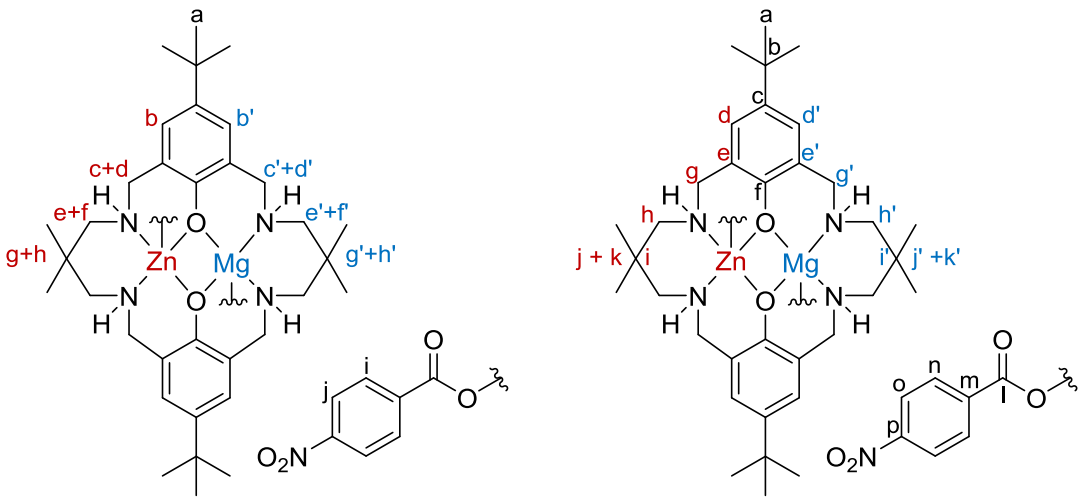
^{1}H NMR (400 MHz, d$_4$-methanol, δ(ppm)): 8.01 (br s, 4H, i), 7.58 (br d, $^{3}J_{H-H}$ = 7 Hz, 4H, j), 6.96 (s, 4H, b+b'), 4.24 (d, $^{2}J_{H-H}$ = 12 Hz, 2H, c), 4.06 (d, $^{2}J_{H-H}$ = 12 Hz, 2H, c'), 3.30 (br d, $^{2}J_{H-H}$ = 12 Hz, 2H, d), 3.22 (br t, $^{2}J_{H-H}$ = 12 Hz, 2H, d'), 2.91 (br d, $^{2}J_{H-H}$ = 12 Hz, 2H, e), 2.86-2.78 (m, 4H, f+e'), 2.71 (br d, $^{2}J_{H-H}$ = 12 Hz, 2H, f'), 1.42 (s, 6H, g+g'), 1.16 (s, 18H, a), 1.06 (s, 6H, h+h'). ^{13}C{^{1}H} NMR (100 MHz, d$_4$-methanol, δ(ppm)): 172.9 (l), 162.8 (f), 138.1 (c), 132.8 (q, $^{2}J_{C-F}$ = 32 Hz, p), 130.8 (n), 129.3 (d'), 129.1 (m), 129.0 (d), 125.7 (q, $^{1}J_{C-F}$ = 270 Hz, q), 125.6 (q, $^{3}J_{C-F}$ = 3 Hz, o), 125.4 (e'), 124.6 (e), 64.2 (h), 63.4 (h'), 56.9 (g), 56.2 (g'), 35.4 (i'), 34.9 (i), 34.3 (b), 32.0 (a), 28.9 (j'), 28.8 (j), 21.8 (k'), 21.4 (k). ^{19}F{^{1}H} NMR (377 MHz, d$_4$-methanol, δ(ppm)): -62.8 (s).

IR ($\nu_{c=o}$, cm^{-1}, neat): 1618 (a, terminal), 1566 (a, bridging), 1391 (s, terminal).

MS (MALDI-ToF): m/z 827 [LMgZnOBz^{CF3}]$^{+}$ (90 %)

Calc. for $C_{50}H_{62}F_6O_6N_4MgZn$: C, 58.95; H, 6.13; N, 5.50; Found: C, 58.77; H, 6.31; N, 5.38 %.

7.4.6. Complex [LMgZn(OBz^{NO2})$_2$]



Synthesised on a 0.91 mmol scale. Yielded an orange powder (753 mg, 0.77 mmol, 85 %).

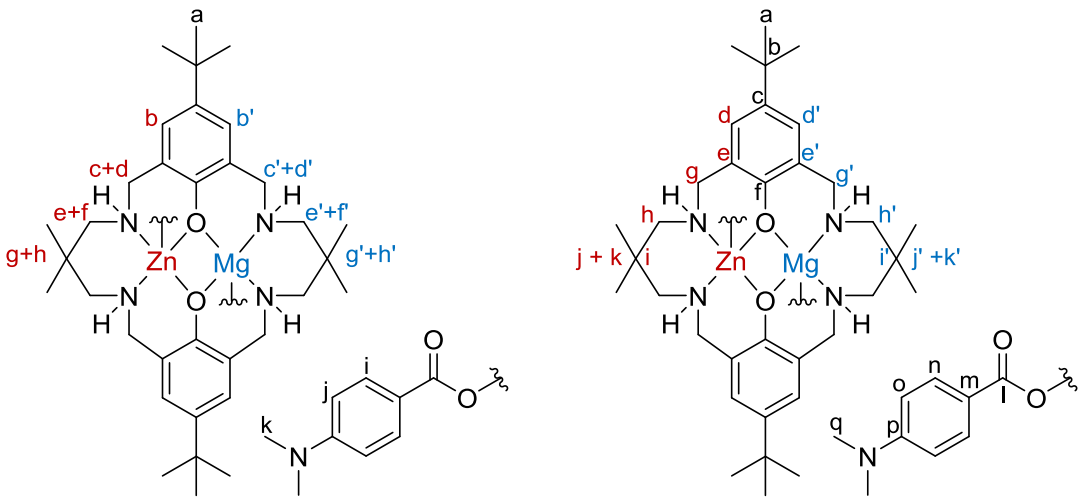
^{1}H NMR (400 MHz, d$_4$-methanol, δ(ppm)): 8.13 (br s, 4H, i), 8.05 (br s, 4H, j), 7.00-6.96 (m, 4H, b+b'), 4.25-4.17 (m, 2H, c), 4.08-4.01 (m, 2H, c'), 3.41-3.36 (m, 2H, d), 3.29-3.24 (m, 2H, d'), 2.98-2.88 (m, 2H, e), 2.86-2.77 (m, 4H, f+e'), 2.73-2.70 (m, 2H, f'), 1.42-1.40 (m, 6H, g+g'), 1.22-1.14 (m, 18H, a), 1.07-1.00 (m, 6H, h+h'). ^{13}C{^{1}H} NMR (100 MHz, d$_4$-methanol, δ(ppm)): 171.9 (l), 162.8 (f), 150.5 (p), 138.6 (m), 138.2 (c), 131.4 (o), 129.4 (d'), 129.2 (d), 125.4 (e'), 124.6 (e), 123.8 (n), 64.2 (h), 63.4 (h'), 56.9 (g), 56.3 (g'), 35.4 (i'), 34.8 (i), 34.3 (b), 32.0 (a), 28.9 (j'), 28.8 (j), 21.9 (k'), 21.4 (k).

IR ($\nu_{c=o}$, cm^{-1}, neat): 1626 (a, terminal), 1587 (a, bridging), 1383 (s, terminal).

MS (MALDI-ToF): m/z 803 [LMgZnOBz^{NO2}]$^{+}$ (100 %)

Calc. for $C_{48}H_{62}O_{10}N_6MgZn$: C, 59.27; H, 6.42; N, 8.64; Found: C, 59.19; H, 6.58; N, 8.49 %.

7.4.7. Complex [LMgZn(OBz^{NMe2})$_2$]



Synthesised on a 0.91 mmol scale. Yielded a white powder (0.484 g, 0.50 mmol, 55 %).

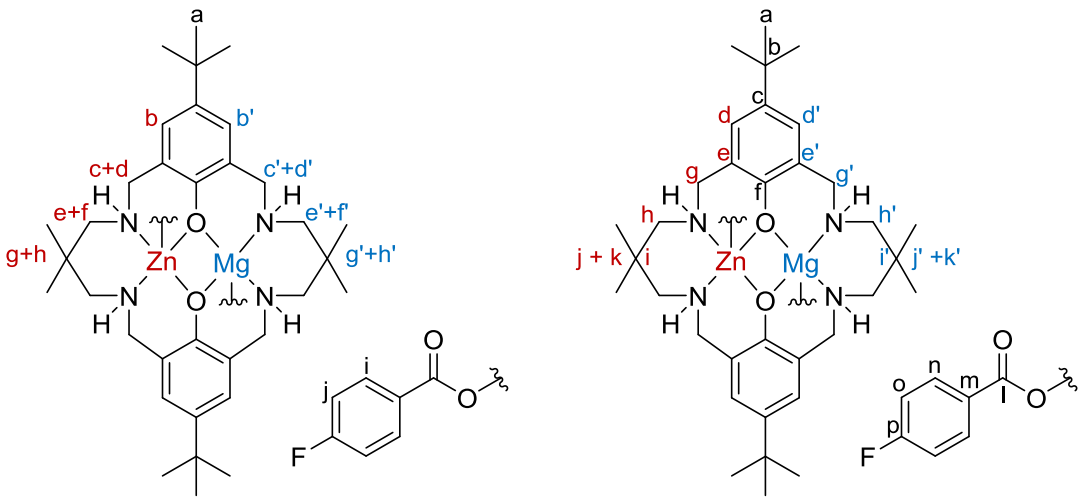
^{1}H NMR (400 MHz, d$_4$-methanol, δ(ppm)): 7.81 (br s, 4H, i), 6.96 (s, 4H, b+b'), 6.63 (br s, 4H, j), 4.22 (d, $^2J_{H-H}$ = 12 Hz, 2H, c), 4.04 (m, 2H, c'), 3.29-3.23 (br m, 4H, d+d'), 2.95 (s, 6H, k), 2.89 (br d, 2H, e), 2.85-2.75 (m, 4H, f+e'), 2.71 (br d, 2H, f'), 1.43 (m, 6H, g+g'), 1.17 (m, 18H, a), 1.05 (m, 6H, h+h'). ^{13}C{^{1}H} NMR (100 MHz, d$_4$-methanol, δ(ppm)): 162.8 (f), 162.6 (l), 153.8 (p), 138.2 (c), 132.0 (n), 129.3 (d'), 129.3 (m), 129.0 (d), 125.3 (e'), 124.7 (e), 111.9 (o), 64.4 (h), 63.4 (h'), 56.9 (g), 56.3 (g'), 40.5 (q), 35.4 (i'), 34.8 (i), 34.3 (b), 32.0 (a), 28.9 (j'), 28.8 (j), 21.8 (k'), 21.3 (k).

IR ($\nu_{c=o}$, cm^{-1}, neat): 1612 (a, terminal), 1377 (s, terminal).

MS (MALDI-ToF): m/z 802.4 [LMgZnOBz^{NMe2}]$^+$ (100 %)

Calc. for $C_{52}H_{74}O6N_6MgZn$: C, 64.46; H, 7.70; N, 8.67; Found: 64.60; H, 7.87; N, 8.39 %.

7.4.8. Complex [LMgZn(OBz^F)$_2$]



Synthesised on a 1.24 mmol scale. Yielded a white powder (1.05 g, 1.14 mmol, 92 %).

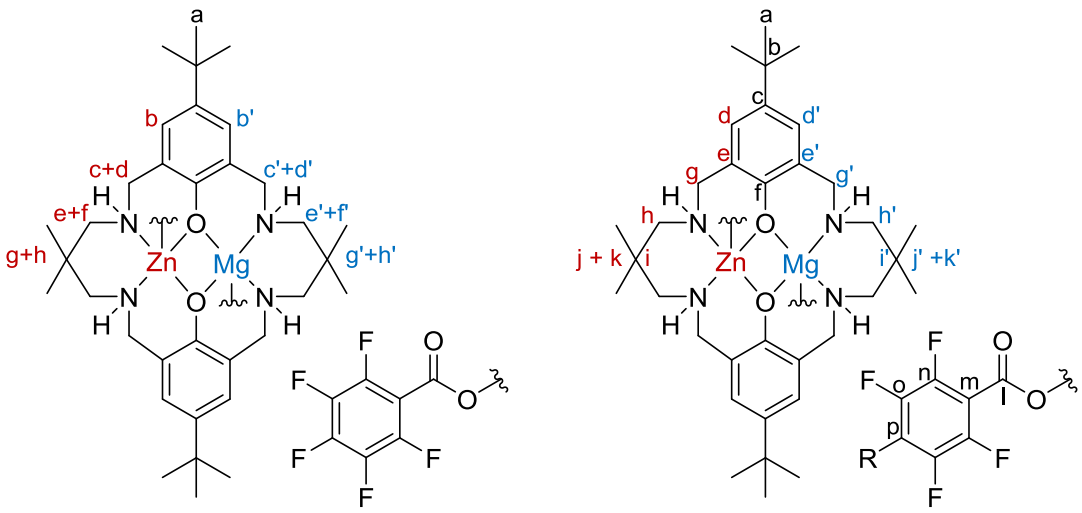
^{1}H NMR (400 MHz, d$_4$-methanol, δ(ppm)): 7.89 (br s, 4H, i), 6.96 (br s, 4H, j), 6.96 (s, 4H, b+b'), 4.24 (d, $^2J_{H-H}$ = 12 Hz, 2H, c), 4.04 (d, $^2J_{H-H}$ = 12 Hz, 2H, c'), 3.27 (br m, 4H, d+d'), 2.91 (m, 2H, e), 2.86-2.78 (m, 4H, f+e'), 2.70 (br d, $^2J_{H-H}$ = 11 Hz, 2H, f'), 1.42 (m, 6H, g+g'), 1.17 (s, 18H, a), 1.05 (m, 6H, h+h'). ^{13}C{^{1}H} NMR (100 MHz, d$_4$-methanol, δ(ppm)): 173.3 (l), 165.7 (d, $^1J_{F-C}$ = 248 Hz) (p) 162.8 (f), 138.0 (c), 132.8 (d, $^3J_{F-C}$ = 9 Hz) (n), 129.3 (d'), 129.1 (m), 129.0 (d), 125.3 (e'), 124.6 (e), 115.2 (d, $^2J_{F-C}$ = 22 Hz) (o), 64.2 (h), 63.4 (h'), 56.9 (g), 56.2 (g'), 35.4 (i'), 34.9 (i), 34.3 (b), 32.0 (a), 28.9 (j'), 28.8 (j), 21.8 (k'), 21.3 (k). ^{19}F{^{1}H} NMR (377 MHz, d$_4$-methanol, δ(ppm)): -113.2.

IR ($\nu_{c=o}$, cm^{-1}, neat): 1610(a, terminal), 1570 (a, bridging), 1391 (s, terminal).

MS (MALDI-ToF): m/z 777.4 [LMgZnOBz^F]$^+$ (100 %)

Calc. for $C_{48}H_{62}O_6N_4F_2MgZn$: C, 62.75; H, 6.80; N, 6.10; Found: C, 60.39; H, 7.12; N, 5.88 %.

7.4.9. Complex [LMgZn(OBz^{F5})$_2$]



Synthesised on a 0.91 mmol scale. Yielded a white powder (739 mg, 0.70 mmol, 76 %).

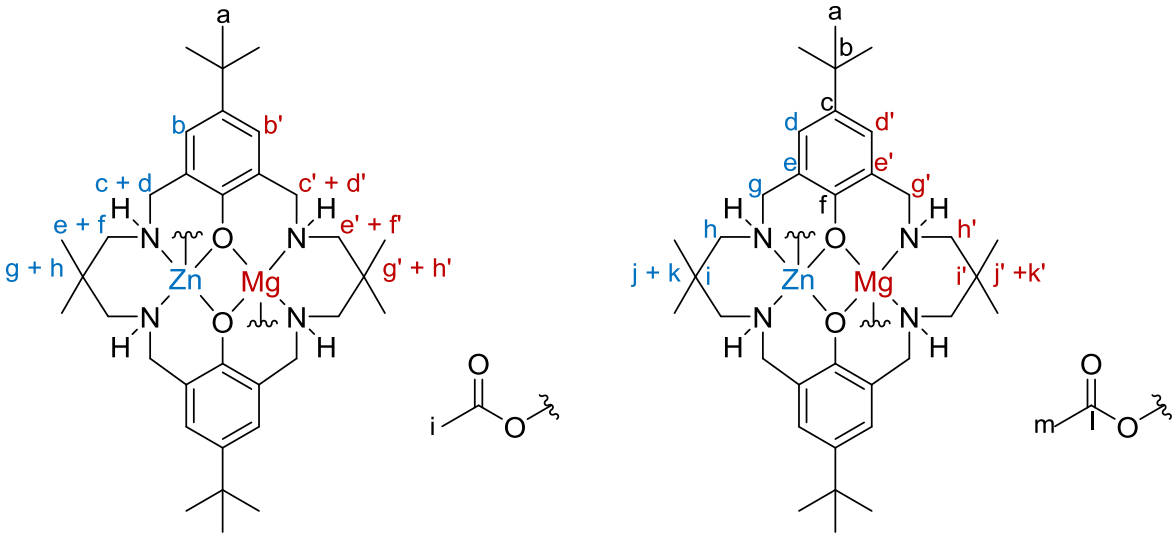
^{1}H NMR (400 MHz, d$_4$-methanol, δ(ppm)): 7.02 (s, 4H, b+b'), 4.25 (m, 2H, c), 4.03 (br m, 2H, c'), 3.27 (br m, 4H d+d'), 2.87 (br m, 2H, e), 2.82-2.73 (m, 4H, f+e'), 2.67 (br m, 2H, f'), 1.23 (m, 18H, a), 1.22 (m, 3H, g), 1.17 (m, 3H, g'), 1.02 (s, 6H, h+h'). ^{13}C{^{1}H} NMR (100 MHz, d$_4$-methanol, δ(ppm)): 164.0 (l), 162.5 (f), 138.8 (c), 129.3 (d'), 129.1 (d), 128.1 (m), 125.3 (e'), 124.5 (e), 64.0 (h), 63.2 (h'), 56.8 (g), 56.0 (g'), 35.2 (i'), 34.7 (i), 34.3 (b), 32.0 (a), 28.7 (j'), 28.6 (j), 21.2 (k'), 21.1 (k). The broad resonances, expected for the pentafluorobenzoate co-ligand (n, o, p), appear in the region 138 – 146 ppm but could not be assigned due to significant C–F coupling. ^{19}F{^{1}H} NMR (377 MHz, d$_4$-methanol, δ(ppm)): -143.7, -144.6, -157.8, -160.1, -165.4, -165.7.

IR ($\nu_{c=o}$, cm^{-1}, neat): 1647 (a, terminal), 1381 (s, terminal).

MS (MALDI-ToF): m/z 848 [LMgZnOBz^{F5}]$^+$ (50 %)

Calc. for $C_{48}H_{54}O_6N_4F_{10}MgZn$: C, 54.25; H, 5.12; N, 5.27; Found: C, 54.13; H, 5.27; N, 5.17 %.

7.4.10. Complex [LMgZn(OAc)$_2$]



Due to reduced solubility in THF, further product was extracted in DCM from the post-metathesis solid and combined with the initial fraction before drying. Synthesised on a 0.91 mmol scale. Yielded a white powder (647 mg, 0.85 mmol, 94 %).

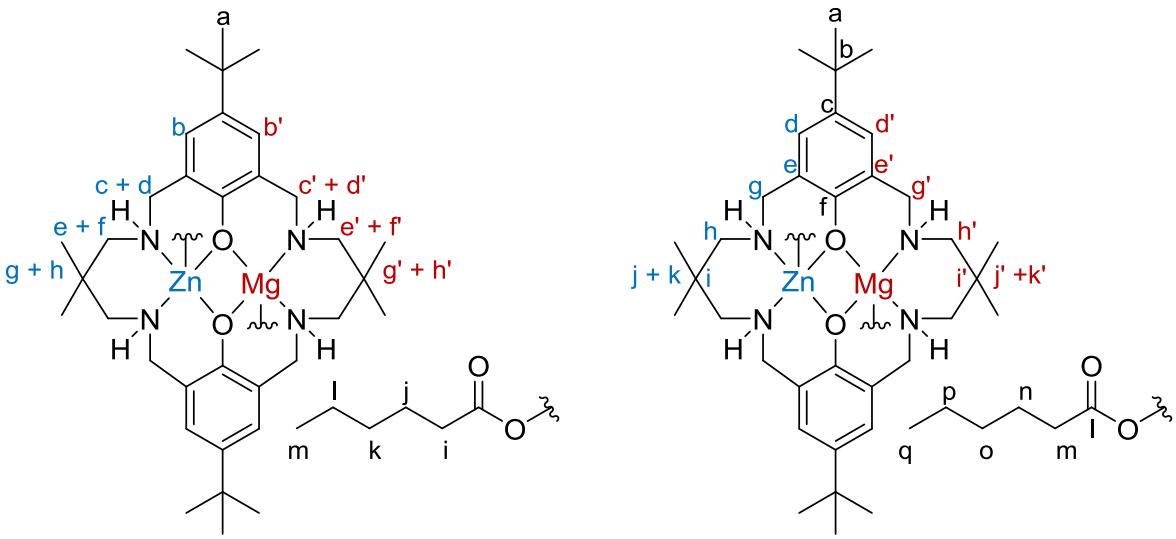
^{1}H NMR (400 MHz, d$_4$-methanol, δ(ppm)): 7.02 (s, 4H, b+b'), 4.22 (m, 2H, c), 3.99 (m, 2H, c'), 3.36-3.21 (m, 4H, d+d'), 2.87-2.79 (m, 2H, e), 2.79-2.68 (m, 4H, f+e'), 2.67-2.62 (m, 2H, f'), 1.70 (br s, 6H, i), 1.26 (m, 18H, a), 1.25-1.23 (m, 6H, g+g'), 1.02-0.98 (m, 6H, h+h'). ^{13}C{^{1}H} NMR (100 MHz, d$_4$-methanol, δ(ppm)): 179.7 (l), 162.6 (f), 138.3 (c), 129.3 (d'), 129.1 (d), 125.4 (e'), 124.7 (e), 64.2 (h), 63.4 (h'), 56.9 (g), 56.1 (g'), 35.3 (i'), 34.7 (i), 34.4 (b), 32.1 (a), 28.9 (j'), 28.7 (j), 24.0 (m), 21.4 (k'), 21.3 (k).

IR ($\nu_{c=o}$, cm^{-1}, neat): 1587 (a, bridging), 1437 (s, bridging).

MS (MALDI-ToF): m/z 697.4 [LMgZnOAc]$^+$ (60 %)

Calc. for $C_{38}H_{60}O_6N_4MgZn$: C, 60.17; H, 7.97; N, 7.39; Found: C, 60.08; H, 8.03; N, 7.27 %.

7.4.11. Complex [LMgZn(O_2CPentyl)$_2$]



Synthesised on a 1.2 mmol scale. Yielded a white powder (900 mg, 1.08 mmol, 90 %).

^{1}H NMR (400 MHz, d$_4$-methanol, δ(ppm)): 7.01 (s, 4H, b+b'), 4.19 (m, 2H, c), 4.00 (m, 2H, c'), 3.26 (d, $^2J_{H-H}$ = 12 Hz, 2H, d'), 3.24 (d, $^2J_{H-H}$ = 12 Hz, 2H, d), 2.86 (m, 2H, e), 2.79-2.73 (m, 4H, f+e'), 2.65 (m, 2H, f'), 2.09-1.82 (m, 4H, i), 1.50-1.35 (m, 4H, j), 1.26 (m, 6H, g+g'), 1.25 (m, 18H, a), 1.25-1.19 (m, 8H, k+l), 1.02 (m, 6H, h+h'), 0.83 (m, 6H, m). ^{13}C{^{1}H} NMR (100 MHz, d$_4$-methanol, δ(ppm)): 182.0 (l), 162.86 (f), 138.2 (c), 129.3 (d'), 129.1 (d), 125.4 (e'), 124.7 (e), 64.1 (h), 63.3 (h'), 56.7 (g), 56.1 (g'), 38.4 (m), 35.3 (i'), 34.7 (i), 34.4 (b), 32.7 (o), 32.1 (a), 28.8 (j'), 28.7 (j), 27.0 (n), 23.5 (p), 21.5 (k'), 21.1 (k), 14.4 (q).

7.5. Copolymerisation of CO_2 and Epoxides

7.5.1. Low pressure CO_2/epoxide copolymerisation

For polymerisations at 1 bar, a solution of catalyst (0.015 mmol) in epoxide (14.9 mmol) was added to a Schlenk tube in the glovebox. This Schlenk tube was then subjected to five rapid vacuum/CO_2 (pressure regulated to 1 bar) cycles, before the reaction was started by heating to 80 °C (unless the temperature was otherwise stated) in an oil bath. Aliquots were taken under a positive pressure of CO_2.

Reactions were quenched by cooling the sample and exposing to air. ^{1}H NMR spectra were taken in air in $CDCl_3$ before the crude product was obtained through removal of volatile CHO under vacuum at the end of the reaction. GPC analysis was carried out on the crude sample. Polycarbonates were purified by dissolution in DCM before passing through a silica plug and precipitating from methanol before TGA or DSC analysis was conducted.

7.5.2. *In situ* ATR-IR monitoring of CO_2/CHO at low pressures

Polymerisations which were carried out in neat epoxide were prepared as above and the atmosphere replaced with CO_2 as described. Under a positive pressure of CO_2, the Schlenk cap was replaced with an adapter fitted with the DiComp probe. The probe and Schlenk were positioned to ensure efficient stirring before placing in the oil bath, at the required temperature, and the monitoring started.

To end the reaction, the programme was stopped and the Schlenk immediate removed from the oil bath, removing the probe and exposing to air. An aliquot was removed for ^{1}H NMR spectroscopy to calculate the overall conversion and selectivity. The collected polymer was purified as before.

The procedure for monitoring diluted reactions is unchanged, except for the volumes used. When carrying out a series of kinetic investigations, the catalyst (0.05-0.2 mol%) was dissolved in CHO (2.5 mL) and diethyl carbonate (DEC) (0.5 mL).

7.5.3. High pressure CO_2/CHO copolymerisation

For polymerisations at elevated pressures, a solution of catalyst (0.01-0.005 mol%) in epoxide (60 mmol) was added to the high pressure reactor, under N_2, in a glovebox. The reactor was secured before removing from the glovebox and then pressurised with CO_2 whilst heating to the desired temperature. The system was closed to further gas pressure for the duration of the polymerisation reaction. Reactions were quenched by cooling, depressurising and opening to air and the polymer samples analysed as before.

7.6. Copolymerisation of Anydrides and CHO

7.6.1. Copolymerisation of PA/CHO

Catalyst and CHO (0.2 mL, from a 12.5 mM solution in CHO, 0.025 mmol of catalyst) were added to a series of PTFE capped vials, each with PA (37 mg, 0.25 mmol) and a stirrer bar under N_2 in the glovebox. Each reaction was started by heating the polymerisation mixture to 100 °C and quenched by opening to air. An aliquot for ^{1}H NMR spectroscopy and GPC analysis was taken, in $CDCl_3$. The crude polymer was purified by addition of MeOH to the solution before the precipitate was filtered, washed with further MeOH and dried under vacuum.

7.6.2. *In situ* ATR-IR monitoring of PA/CHO

To determine the reaction order in catalyst, a Schlenk was charged with catalyst (0.014-0.028 mmol), PA (1.86 mmol) and CHO (1.5 mL, 14.9 mmol). To determine the order in CHO, a Schlenk was charged with catalyst (0.019 mmol), PA (1.86 mmol) and CHO (3.73-14.9 mmol). An appropriate amount of toluene was then added to take the total volume to 1.5 mL.

The Dicomp probe was fitted under a positive pressure of N_2 and the reaction started once the Schlenk was positioned in an oil bath at 100 °C. Once the reaction was complete, a ^{1}H NMR spectra was taken in air in $CDCl_3$ and quenched as before.

7.6.3. Other anhydride/CHO copolymerisations

A stock solution of catalyst in CHO was made (1:800 catalyst:CHO, 12.7 mM) and a portion of this (0.3 mL) was added to the anhydride (0.38 mmol) in a PTFE capped vial with stirrer bar. The vials were then heated at the stated temperature and time, before quenching with MeOH in air.

7.7. References

(1) Kember, M. R.; Knight, P. D.; Reung, P. T. R.; Williams, C. K. *Angew. Chem. Int. Ed.* **2009**, *48*, 931.
(2) Winkler, M.; Romain, C.; Meier, M. A. R.; Williams, C. K. *Green Chem.* **2015**, *17*, 300.
(3) Peña Carrodeguas, L.; Martín, C.; Kleij, A. W. *Macromolecules* **2017**, *50*, 5337.
(4) Zhang, J.; Lawrance, G. A.; Chau, N.; Robinson, P. J.; McCluskey, A. *New J. Chem.* **2008**, *32*, 28.
(5) Zhu, Y.; Romain, C.; Williams, C. K. *J. Am. Chem. Soc.* **2015**, *137*, 12179.
(6) Gooßen, L. J.; Rodríguez, N.; Lange, P. P.; Linder, C. *Angew. Chem. Int. Ed.* **2010**, *49*, 1111.

Appendices

Appendix A: DOSY NMR Spectra

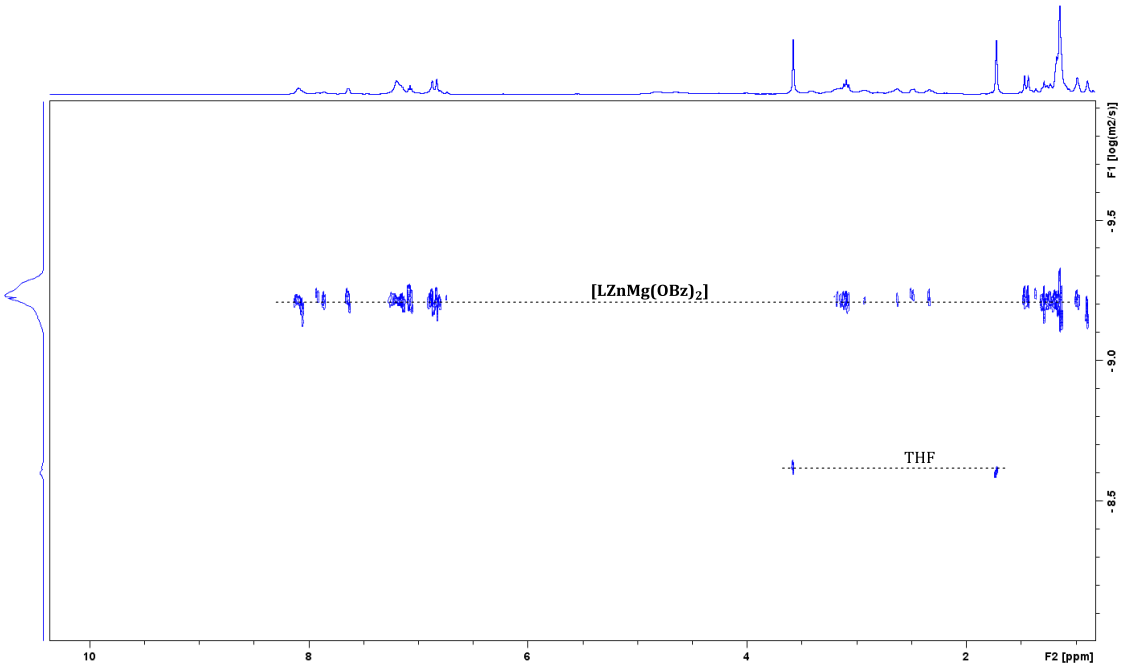


Figure A.1 – DOSY NMR spectrum of complex ***[LZnMg(OBz)$_2$]*** *in d_8-THF.*

Through comparison of the diffusion coefficient observed for ***[LZnMg(OBz)$_2$],*** *to a calibration plot of known standards in d_8-THF solution,[1] a predicted molecular weight of 1077 g·mol^{-1} was obtained, in relatively close (22 %) agreement with that of a monomeric species (883 g·mol^{-1}).*

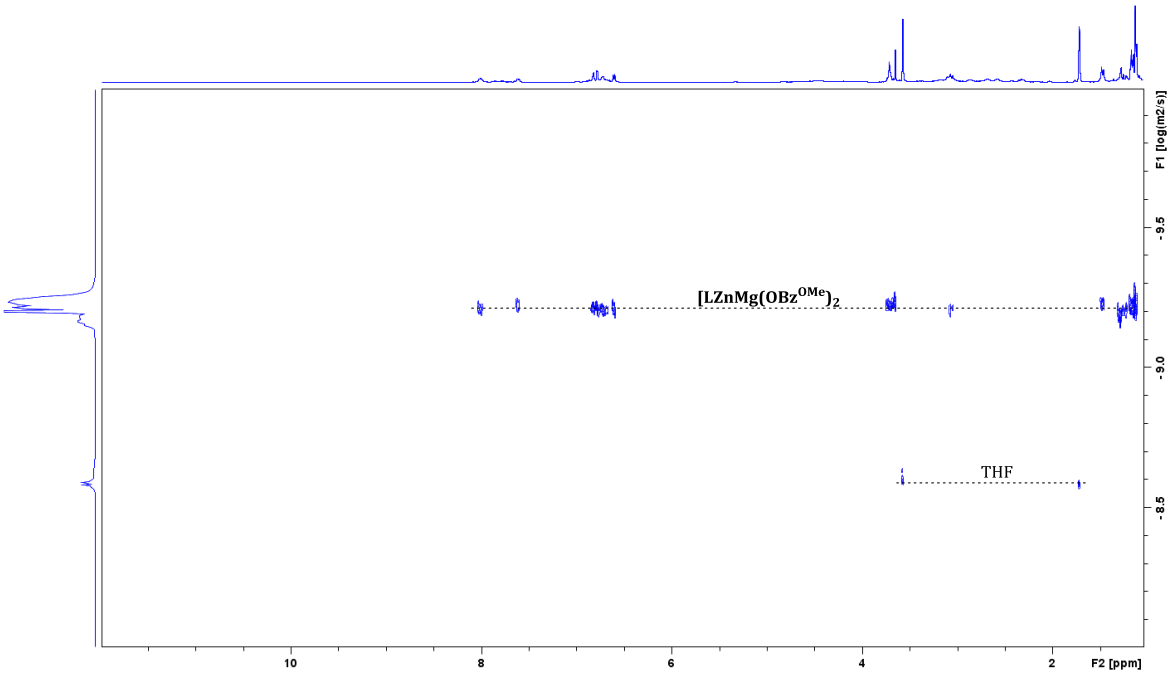


Figure A.2 – DOSY NMR spectrum of complex ***[LZnMg(OBz^{OMe})$_2$]*** *in d_8-THF.*

Through comparison of the diffusion coefficient observed for ***[LZnMg(OBz^{OMe})$_2$],*** *to a calibration plot of known standards in d_8-THF solution,[1] a predicted molecular weight of 1091 g·mol^{-1} was obtained, in relatively close (16 %) agreement with that of a monomeric species (943 g·mol^{-1}).*

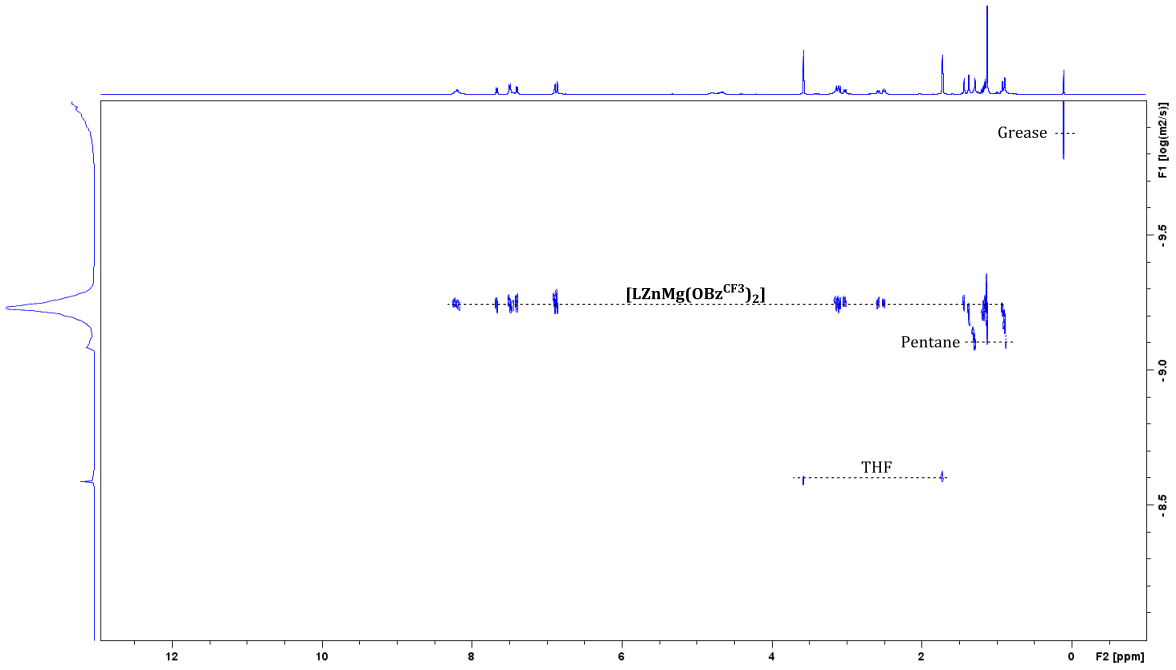


Figure A.3 – DOSY NMR spectrum of complex ***[LZnMg(OBz^{CF3})$_2$]*** *in d_8-THF.*

Through comparison of the diffusion coefficient observed for ***[LZnMg(OBz^{CF3})$_2$],*** *to a calibration plot of known standards in d_8-THF solution,[1] a predicted molecular weight of 1248 g·mol^{-1} was obtained, in relatively close (14 %) agreement with that of a monomeric species (1098 g·mol^{-1}).*

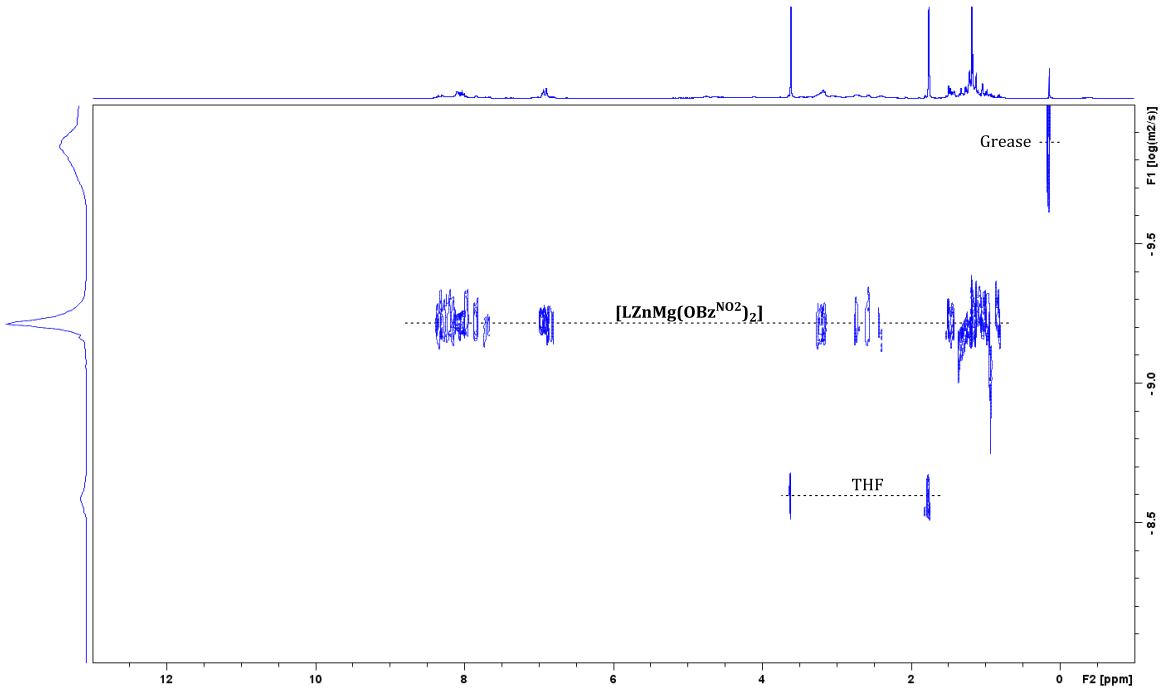


Figure A.4 – DOSY NMR spectrum of complex ***[LZnMg(OBz^{NO2})$_2$]*** *in d_8-THF.*

Through comparison of the diffusion coefficient observed for ***[LZnMg(OBz^{NO2})$_2$],*** *to a calibration plot of known standards in d_8-THF solution,[1] a predicted molecular weight of 1091 g·mol^{-1} was obtained, in close (12 %) agreement with that of a monomeric species (973 g·mol^{-1}).*

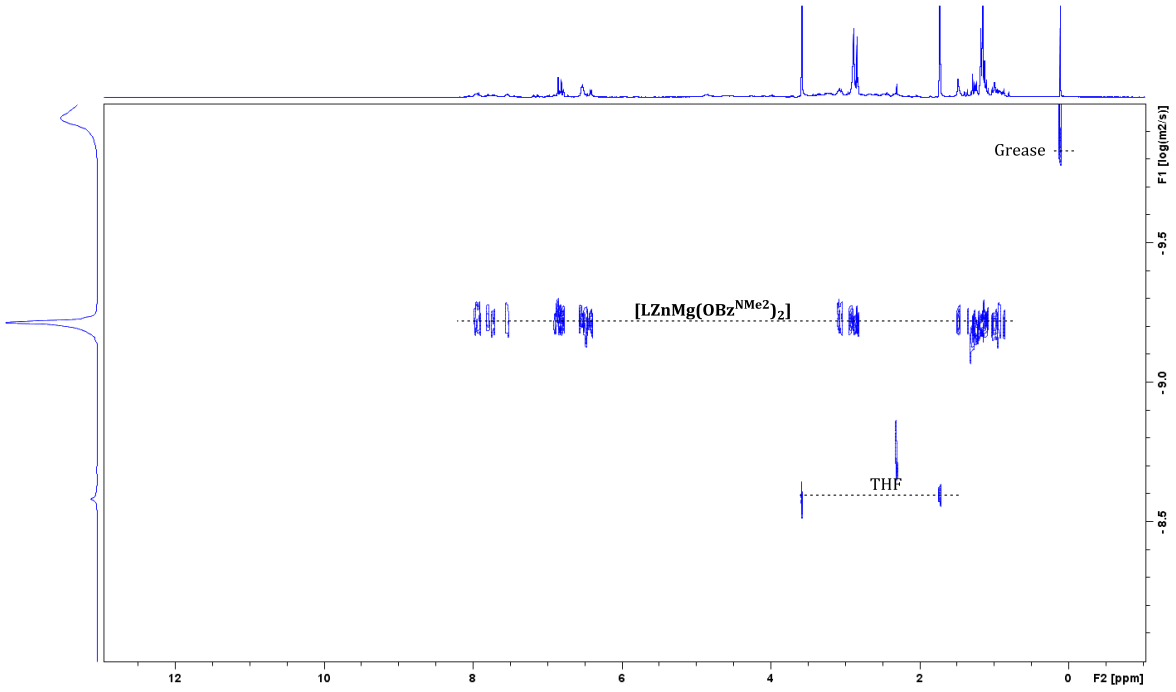


Figure A.5 – DOSY NMR spectrum of complex ***[LZnMg(OBz^{NMe2})$_2$]*** *in d_8-THF.*

Through comparison of the diffusion coefficient observed for ***[LZnMg(OBz^{NMe2})$_2$],*** *to a calibration plot of known standards in d_8-THF solution,[1] a predicted molecular weight of 1104 g·mol^{-1} was obtained, in close (14 %) agreement with that of a monomeric species (969 g·mol^{-1}).*

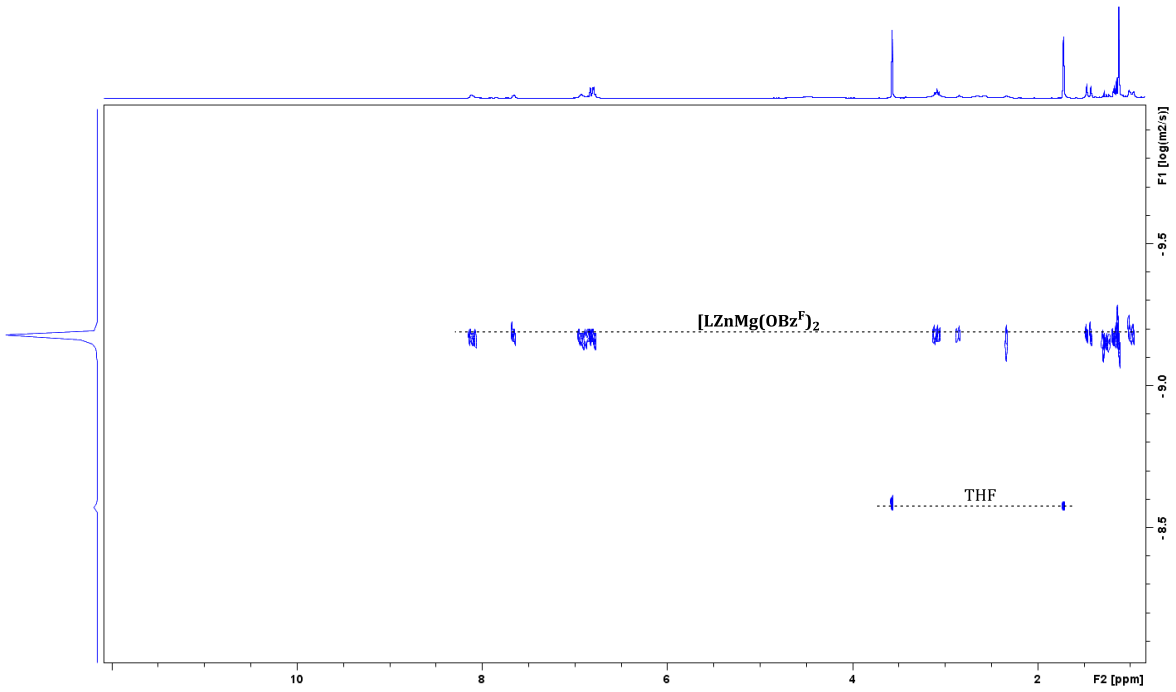


Figure A.6 – DOSY NMR spectrum of complex ***[LZnMg(OBzF)$_2$]*** *in d_8-THF.*

Through comparison of the diffusion coefficient observed for ***[LZnMg(OBz^F)$_2$],*** *to a calibration plot of known standards in d_8-THF solution,[1] a predicted molecular weight of 938 g·mol^{-1} was obtained, in very close (2 %) agreement with that of a monomeric species (919 g·mol^{-1}).*

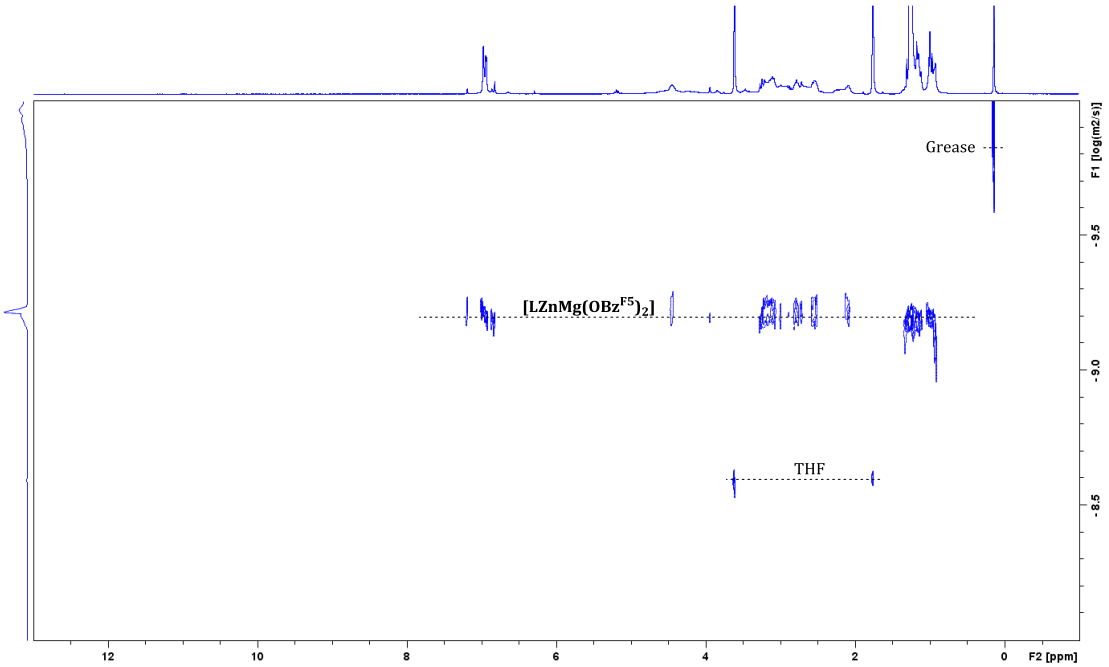


Figure A.7 – DOSY NMR spectrum of complex ***[LZnMg(OBz^{F5})$_2$]*** *in d_8-THF.*

Through comparison of the diffusion coefficient observed for ***[LZnMg(OBz^{F5})$_2$],*** *to a calibration plot of known standards in d_8-THF solution,[1] a predicted molecular weight of 1104 g·mol^{-1} was obtained, in very close (4 %) agreement with that of a monomeric species (1063 g·mol^{-1}).*

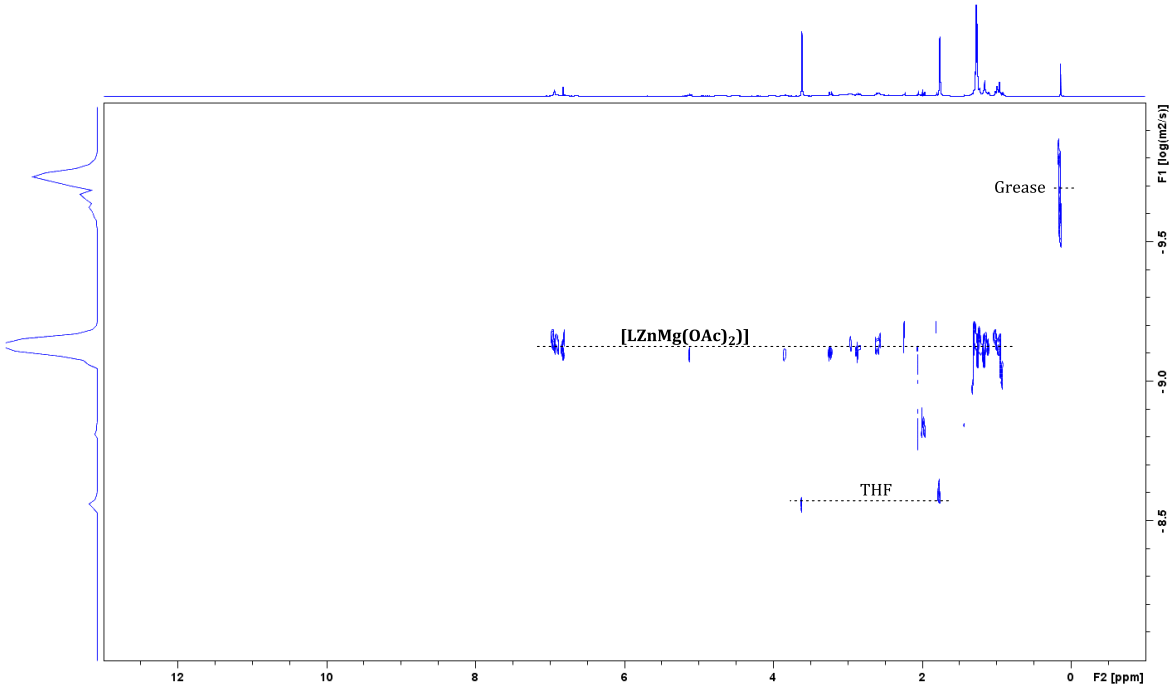


Figure A.8 – DOSY NMR spectrum of complex ***[LZnMg(OAc)$_2$]*** *in d_8-THF.*

Through comparison of the diffusion coefficient observed for ***[LZnMg(OAc)$_2$],*** *to a calibration plot of known standards in d_8-THF solution,[1] a predicted molecular weight of 777 g·mol^{-1} was obtained, in very close (2 %) agreement with that of a monomeric species (759 g·mol^{-1}).*

Appendix B: Crystallographic Data

Table B.1 – Select crystallographic details for complexes ***[LZnMg(O$_2$CPentyl)$_2$]*** *and* ***[LZnMg(OBz^{CF3})$_2$]****.*

Compound	**[LZnMg(O$_2$CPentyl)$_2$]** ·3(MeOH)	**[LZnMg(OBz^{CF3})$_2$]** ·(MeOH)
Chemical formula	$C_{49}H_{88}N_4O_9Mg_{1.07}Zn_{0.93}$	$C_{51}H_{66}F_6MgN_4O_7Zn$
Formula weight	963.83	1050.75
Temp (K)	173(2)	150(2)
Space group	Orthorhombic, $P2_12_12_1$	Monoclinic, $P2_1/c$
a (Å)	14.7254(6)	24.4215(4)
b (Å)	15.2095(8)	13.3468(2)
c (Å)	24.4137(9)	17.1174(3)
α (°)	90	90
β (°)	90	108.971(2)
γ (°)	90	90
V (Å^3)	5467.9(4)	5276.34(16)
Z	4	4
D_{calcd} (Mg/m^3)	1.171	1.323
Crystal size (mm)	0.56 x 0.31 x 0.10	0.250 x 0.250 x 0.150
Theta range for data collection (°)	2.548 to 28.190	3.825 to 76.186
μ (mm^{-1})	(Mo, Kα) 0.482	(Cu, Kα) 1.390
Reflections collected	12785	64409
Unique reflections	9586 [R(int) = 0.0390]	10994 [R(int) = 0.0347]
Data Completeness to [θ]	98.9 % [25.242]	100.0 % [67.684]
Data/restraints/parameters	9586 / 92 / 644	10994 / 299 / 783
R1[a] (%) (all data)	0.0621 (0.0837)	0.0899 (0.0986)
wR2[b] (%)(all data)	0.1503 (0.1726)	0.3080 (0.3295)
Goodness-of-fit on F^2	1.058	1.508
Largest diff. peak and hole (e Å^{-3})	0.824, -0.932	1.322 and -1.790

[a] $R1 = \sum ||F_o|-|F_c|| / \sum |F_o| \times 100$

[b] $wR2 = [\sum w(F_o^2-F_c^2)^2 / \sum (w|F_o|^2)^2]^{1/2} \times 100$

*Table B.2 – Key bond lengths and angles for complex **1d**·3MeOH*

Bond	Bond Length (Å)	Bond	Bond Length (Å)
Mg(1)-O(50)	2.046(4)	Zn(1)-O(42)	2.060(4)
Mg(1)-O(1)	2.069(4)	Zn(1)-O(11)	2.092(4)
Mg(1)-O(11)	2.075(4)	Zn(1)-O(1)	2.104(3)
Mg(1)-O(40)	2.126(4)	Zn(1)-N(14)	2.121(4)
Mg(1)-N(4)	2.159(4)	Zn(1)-N(18)	2.123(4)
Mg(1)-N(8)	2.161(4)	Zn(1)-O(60)	2.219(4)
Mg(1)-Zn(1)	3.0185(12)		
Bond	Bond Angle (°)	Bond	Bond Angle (°)
O(50)-Mg(1)-O(1)	96.28(17)	O(42)-Zn(1)-O(60)	176.15(15)
O(50)-Mg(1)-O(11)	95.29(16)	O(11)-Zn(1)-O(60)	82.97(15)
O(1)-Mg(1)-O(11)	83.93(14)	O(1)-Zn(1)-O(60)	83.88(15)
O(50)-Mg(1)-O(40)	170.50(17)	N(14)-Zn(1)-O(60)	94.14(14)
O(1)-Mg(1)-O(40)	91.10(16)	N(18)-Zn(1)-O(60)	94.27(15)
O(11)-Mg(1)-O(40)	91.42(16)	O(42)-Zn(1)-Mg(1)	81.24(11)
O(50)-Mg(1)-N(4)	90.05(16)	O(11)-Zn(1)-Mg(1)	43.36(10)
O(1)-Mg(1)-N(4)	92.35(15)	O(1)-Zn(1)-Mg(1)	43.21(11)
O(11)-Mg(1)-N(4)	173.79(15)	N(14)-Zn(1)-Mg(1)	132.95(11)
O(40)-Mg(1)-N(4)	83.66(15)	N(18)-Zn(1)-Mg(1)	132.73(12)
O(50)-Mg(1)-N(8)	89.23(16)	O(60)-Zn(1)-Mg(1)	95.43(10)
O(1)-Mg(1)-N(8)	173.82(16)	C(1)-O(1)-Mg(1)	125.4(3)
O(11)-Mg(1)-N(8)	92.78(16)	C(1)-O(1)-Zn(1)	123.1(3)
O(40)-Mg(1)-N(8)	83.73(16)	Mg(1)-O(1)-Zn(1)	92.66(15)
N(4)-Mg(1)-N(8)	90.46(16)	C(3)-N(4)-Mg(1)	108.3(3)
O(50)-Mg(1)-Zn(1)	112.32(13)	C(5)-N(4)-Mg(1)	116.2(3)
O(1)-Mg(1)-Zn(1)	44.13(10)	C(7)-N(8)-Mg(1)	117.4(3)
O(11)-Mg(1)-Zn(1)	43.80(10)	C(9)-N(8)-Mg(1)	107.2(3)
O(40)-Mg(1)-Zn(1)	77.17(11)	C(11)-O(11)-Mg(1)	125.2(3)
N(4)-Mg(1)-Zn(1)	130.85(11)	C(11)-O(11)-Zn(1)	123.5(3)
N(8)-Mg(1)-Zn(1)	130.82(12)	Mg(1)-O(11)-Zn(1)	92.84(15)
O(42)-Zn(1)-O(11)	95.81(16)	C(15)-N(14)-Zn(1)	117.5(3)
O(42)-Zn(1)-O(1)	92.35(16)	C(13)-N(14)-Zn(1)	109.3(3)
O(11)-Zn(1)-O(1)	82.66(14)	C(17)-N(18)-Zn(1)	119.3(3)
O(42)-Zn(1)-N(14)	89.56(15)	C(19)-N(18)-Zn(1)	109.5(3)
O(11)-Zn(1)-N(14)	92.75(15)	C(41)-O(40)-Mg(1)	129.6(4)
O(1)-Zn(1)-N(14)	175.18(15)	C(41)-O(42)-Zn(1)	127.5(4)
O(42)-Zn(1)-N(18)	86.64(16)	C(51)-O(50)-Mg(1)	138.7(4)
O(11)-Zn(1)-N(18)	174.57(16)	C(51)-O(50)-Mg(1)	138.7(4)
O(1)-Zn(1)-N(18)	92.41(15)	C(61)-O(60)-Zn(1)	149.3(5)
N(14)-Zn(1)-N(18)	92.12(16)		

*Table B.3 – Key bond lengths and angles for complex **3c**·MeOH*

Bond	Bond Length (Å)	Bond	Bond Length (Å)
N(1)-Mg(1)	2.123(3)	O(2)-Zn(1)	2.062(2)
N(2)-Mg(1)	2.139(3)	O(2)-Mg(1)	2.065(2)
N(3)-Zn(1)	2.141(3)	O(3)-Mg(1)	2.141(2)
N(4)-Zn(1)	2.140(2)	O(4)-Zn(1)	2.201(2)
O(1)-Mg(1)	2.048(2)	Mg(1)-O(7)	2.182(3)
O(1)-Zn(1)	2.059(2)	Mg(1)-Zn(1)	3.0498(10)
Bond	**Bond Angle (°)**	**Bond**	**Bond Angle (°)**
C(12)-N(1)-Mg(1)	118.8(2)	O(2)-Mg(1)-O(7)	93.69(12)
C(11)-N(1)-Mg(1)	109.1(2)	N(1)-Mg(1)-O(7)	89.26(12)
C(16)-N(2)-Mg(1)	118.2(2)	N(2)-Mg(1)-O(7)	89.25(12)
C(17)-N(2)-Mg(1)	107.9(2)	O(3)-Mg(1)-O(7)	170.97(11)
C(29)-N(3)-Zn(1)	117.85(19)	O(1)-Mg(1)-Zn(1)	42.17(6)
C(28)-N(3)-Zn(1)	108.0(2)	O(2)-Mg(1)-Zn(1)	42.31(7)
C(34)-N(4)-Zn(1)	107.88(17)	N(1)-Mg(1)-Zn(1)	131.09(7)
C(33)-N(4)-Zn(1)	115.24(17)	N(2)-Mg(1)-Zn(1)	130.80(9)
Zn(1)-N(4)-H(4)	108.1	O(3)-Mg(1)-Zn(1)	81.08(6)
C(1)-O(1)-Mg(1)	126.93(18)	O(7)-Mg(1)-Zn(1)	107.71(10)
C(1)-O(1)-Zn(1)	127.65(18)	O(1)-Zn(1)-O(2)	80.82(9)
Mg(1)-O(1)-Zn(1)	95.92(9)	O(1)-Zn(1)-N(4)	91.96(9)
C(23)-O(2)-Zn(1)	127.8(3)	O(2)-Zn(1)-N(4)	170.46(9)
C(23)-O(2)-Mg(1)	126.8(2)	O(1)-Zn(1)-N(3)	168.65(10)
Zn(1)-O(2)-Mg(1)	95.30(9)	O(2)-Zn(1)-N(3)	92.35(11)
C(35)-O(3)-Mg(1)	126.72(19)	N(4)-Zn(1)-N(3)	93.74(10)
C(35)-O(4)-Zn(1)	128.7(2)	O(1)-Zn(1)-O(4)	89.76(9)
O(1)-Mg(1)-O(2)	80.99(9)	O(2)-Zn(1)-O(4)	91.06(9)
O(1)-Mg(1)-N(1)	92.95(9)	N(4)-Zn(1)-O(4)	82.64(9)
O(2)-Mg(1)-N(1)	173.38(10)	N(3)-Zn(1)-O(4)	81.27(10)
O(1)-Mg(1)-N(2)	172.96(11)	O(1)-Zn(1)-Mg(1)	41.91(6)
O(2)-Mg(1)-N(2)	92.25(10)	O(2)-Zn(1)-Mg(1)	42.39(7)
N(1)-Mg(1)-N(2)	93.70(11)	N(4)-Zn(1)-Mg(1)	128.64(7)
O(1)-Mg(1)-O(3)	94.92(9)	N(3)-Zn(1)-Mg(1)	128.33(8)
O(2)-Mg(1)-O(3)	91.57(10)	O(4)-Zn(1)-Mg(1)	77.37(6)
N(1)-Mg(1)-O(3)	86.28(10)	C(50)-O(7)-Mg(1)	116.5(3)
N(2)-Mg(1)-O(3)	83.21(10)	Mg(1)-O(7)-H(7)	121.8
O(1)-Mg(1)-O(7)	93.14(10)		

Appendix C: SEC Analysis Plots

C.1 Data for Table 4.1

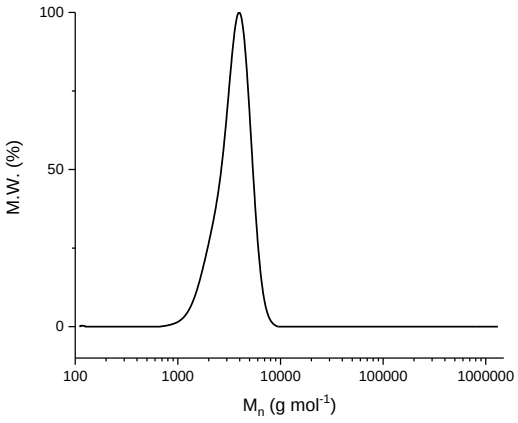


Figure C.1 – SEC plot of M_n for catalyst ***[LZnMgBr$_2$]*** *at 80 °C under 1 bar CO_2 for 6 hours.*

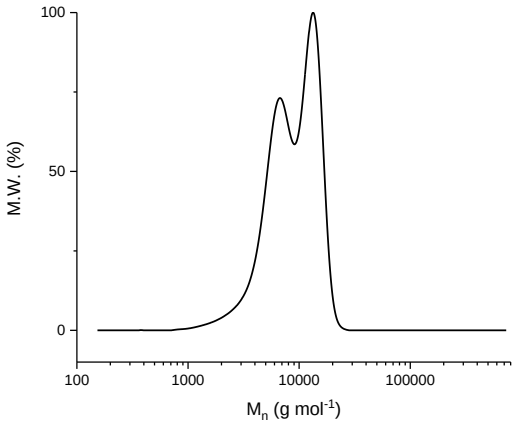


Figure C.2 – SEC plot of M_n for catalyst ***[LZnMg(OAc)$_2$]*** *at 80 °C under 1 bar CO_2 for 6 hours.*

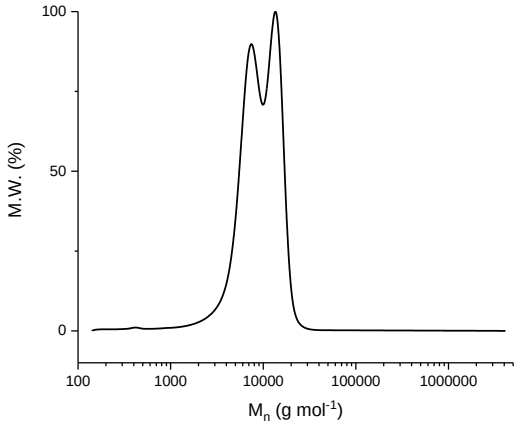


Figure C.3 – SEC plot of M_n for catalyst ***[LZnMg(OBz)$_2$]*** *at 80 °C under 1 bar CO_2 for 6 hours.*

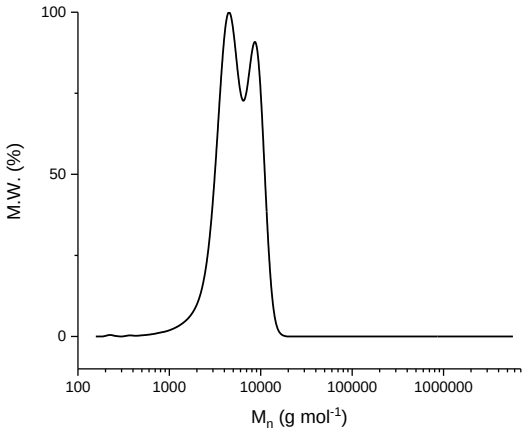


Figure C.4 – SEC plot of M_n for catalyst ***[LZnMg(OBz^{OMe})$_2$]*** *at 80 °C under 1 bar CO_2 for 3 hours.*

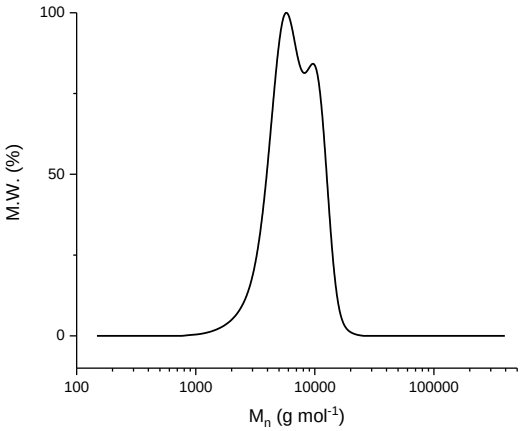


Figure C.5 – SEC plot of M_n for catalyst ***[LZnMg(OBz^{CF3})$_2$]*** *at 80 °C under 1 bar CO_2 for 6 hours.*

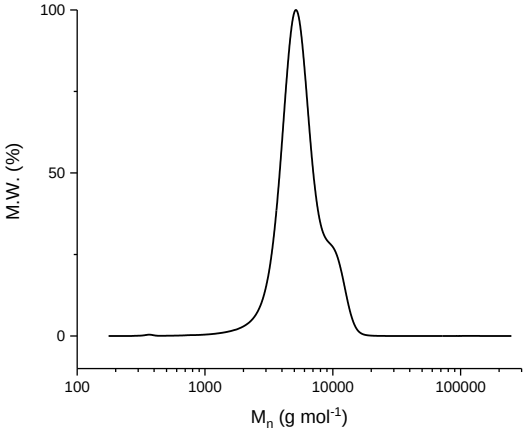


Figure C.6 – SEC plot of M_n for catalyst ***[LZnMg(OBz^{NO2})$_2$]*** *at 80 °C under 1 bar CO_2 for 3 hours.*

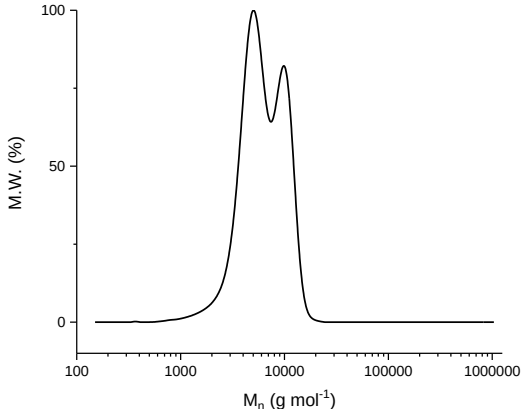


Figure C.7 – SEC plot of M_n for catalyst ***[LZnMg(OBz^{NMe2})$_2$]*** *at 80 °C under 1 bar CO_2 for 3 hours.*

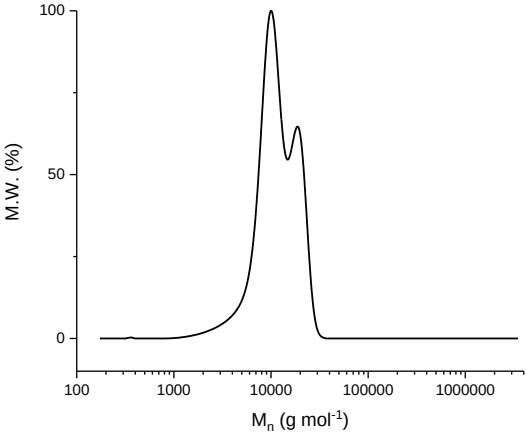


Figure C.8 – SEC plot of M_n for catalyst ***[LZnMg(OBz^{F})$_2$]*** *at 80 °C under 1 bar CO_2 for 6 hours.*

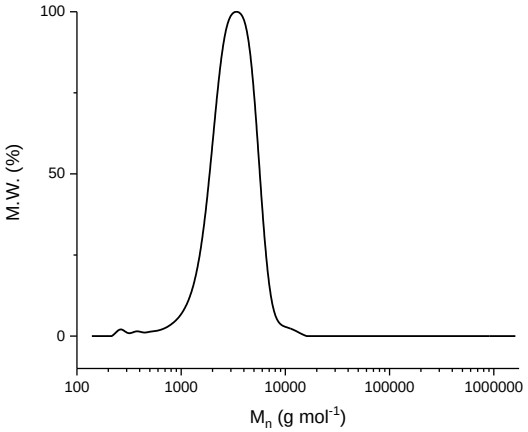


Figure C.9 – SEC plot of M_n for catalyst ***[LZnMg(OBz^{F5})$_2$]*** *at 80 °C under 1 bar CO_2 for 6 hours.*

C.2 Data for Table 4.2

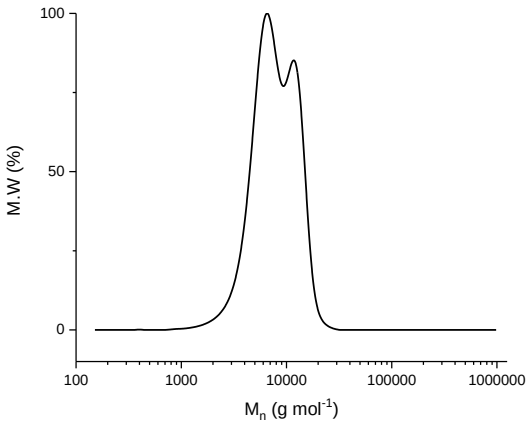


Figure C.10 – SEC plot of M_n for catalyst ***[LZnMg(OBz^{OMe})$_2$]*** *at 120 °C under 1 bar CO_2 for 1 hour.*

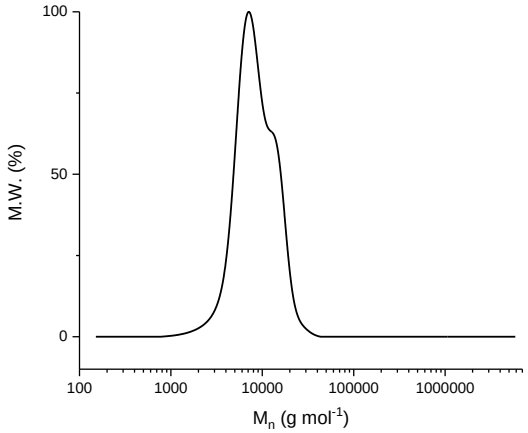


Figure C.11 – SEC plot of M_n for catalyst ***[LZnMg(OBz^{CF3})$_2$]*** *at 120 °C under 1 bar CO_2 for 1 hour.*

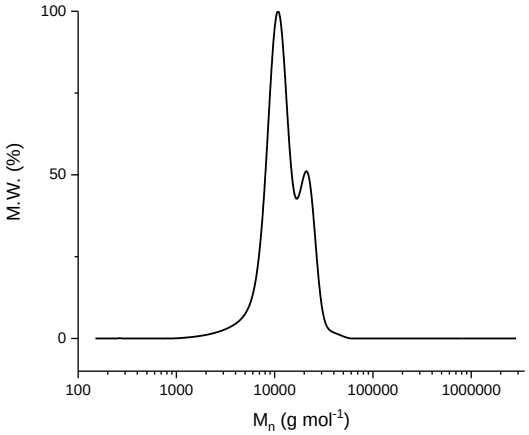


Figure C.12 – SEC plot of M_n for catalyst ***[LZnMg(OBz^{NMe2})$_2$]*** *at 120 °C under 1 bar CO_2 for 1 hour.*

C.3 Data for Table 4.4

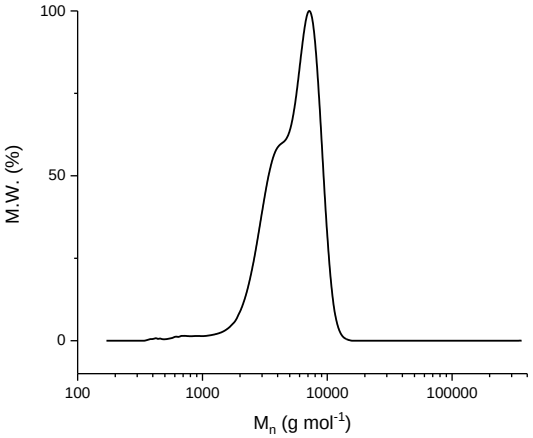


Figure C.13 – SEC plot of M_n for catalyst ***[LZnMg(OBz^{CF3})$_2$]*** *at 80 °C under 1 bar CO_2 for 6 hours with no added chain transfer.*

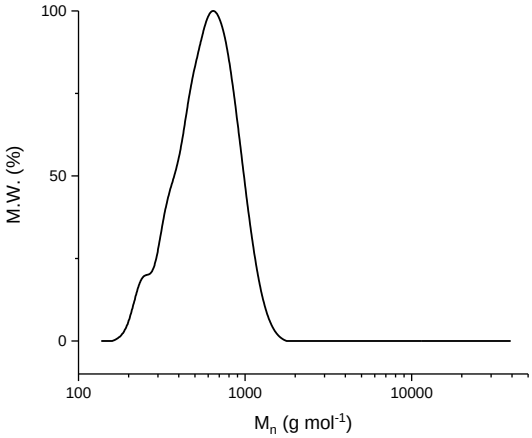


Figure C.14 – SEC plot of M_n for catalyst ***[LZnMg(OBz^{CF3})$_2$]*** *at 80 °C under 1 bar CO_2 for 6 hours with 10 equivalents of H_2O.*

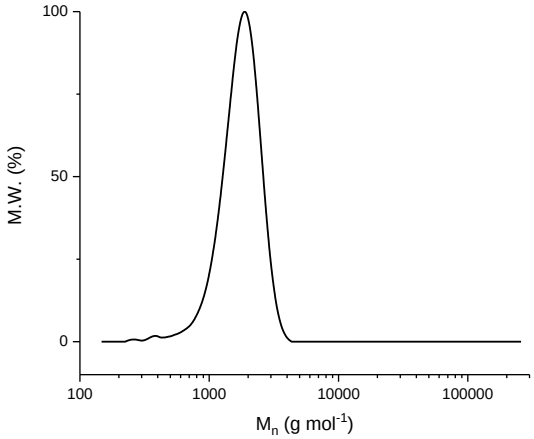


Figure C.15 – SEC plot of M_n for catalyst ***[LZnMg(OBz^{CF3})$_2$]*** *at 80 °C under 1 bar CO_2 for 6 hours with 10 equivalents of CHD.*

C.4 Data for Table 4.5

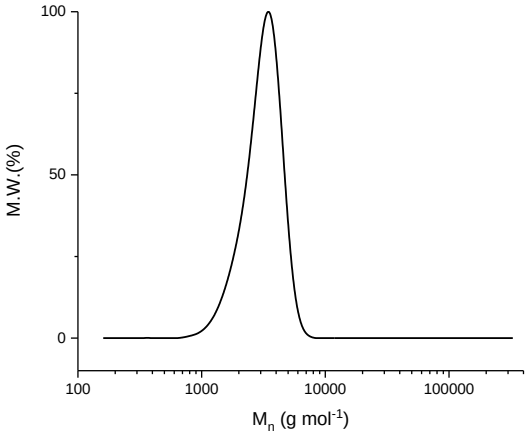


Figure C.16 – SEC plot of M_n for catalyst ***[LZnMg(OBz^{OMe})$_2$]*** *at 80 °C under 1 bar CO_2 for 6 hours with pre-stirring in air for 1 h.*

C.5 Data for Table 4.6

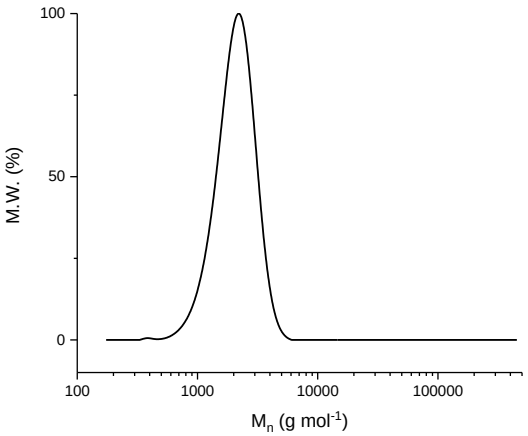


Figure C.17 – SEC plot of M_n for catalyst ***[LZnMg(OBz^{CF3})$_2$]*** *at 80 °C under 20 bar CO_2 for 4 hours at 0.01 mol% catalyst loading.*

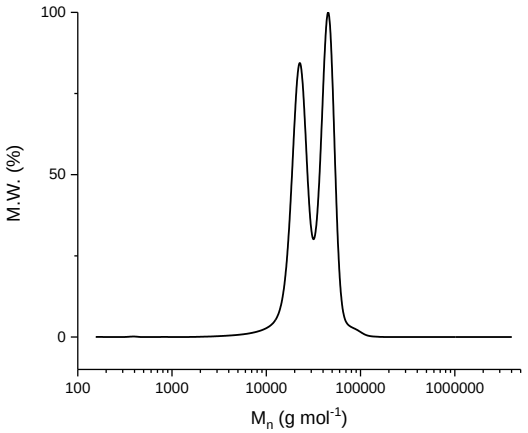


Figure C.18 – SEC plot of M_n for catalyst ***[LZnMg(OBz^{CF3})$_2$]*** *at 120 °C under 20 bar CO_2 for 0.5 hours at 0.01 mol% catalyst loading.*

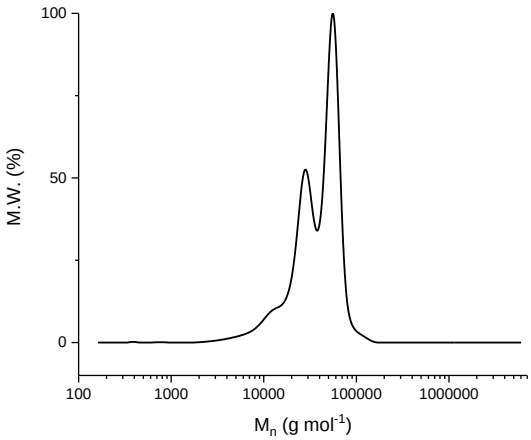


Figure C.19 – SEC plot of M_n for catalyst ***[LZnMg(OBz^{CF3})$_2$]*** *at 120 °C under 20 bar CO_2 for 4 hours at 0.005 mol% catalyst loading.*

C.6 Data for Table 4.8

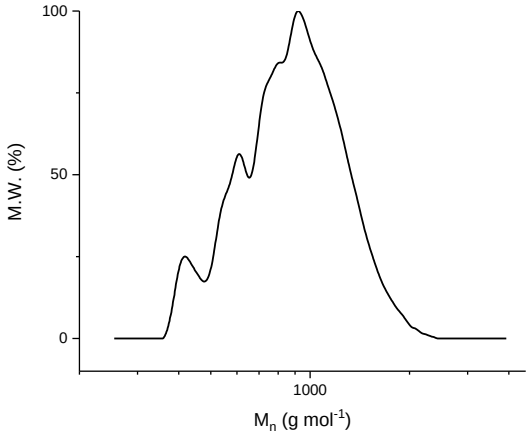


*Figure C.20 – SEC plot of M_n for catalyst **[LZnMg(OBz^{OMe})$_2$]** with MO at 80 °C under 1 bar CO_2 for 6 hours at 0.1 mol% catalyst loading.*

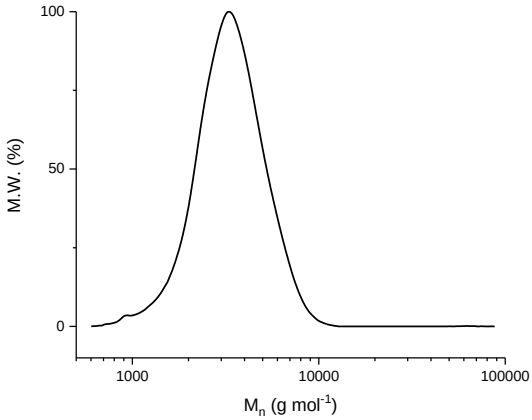


*Figure C.21 – SEC plot of M_n for catalyst **[LZnMg(OBz^{OMe})$_2$]** with MO at 80 °C under 1 bar CO_2 for 24 hours at 0.1 mol% catalyst loading.*

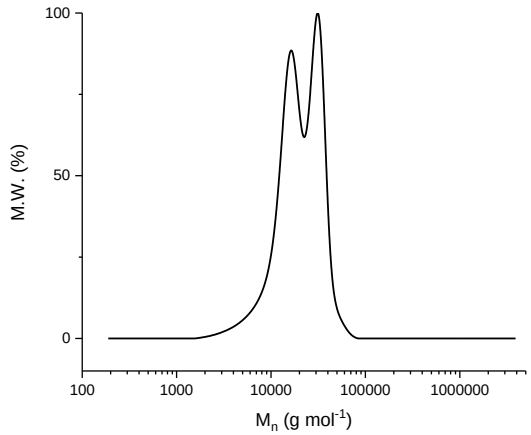


*Figure C.22 – SEC plot of M_n for catalyst **[LZnMg(OBz^{OMe})$_2$]** with vCHO at 80 °C under 1 bar CO_2 for 6 hours at 0.1 mol% catalyst loading.*

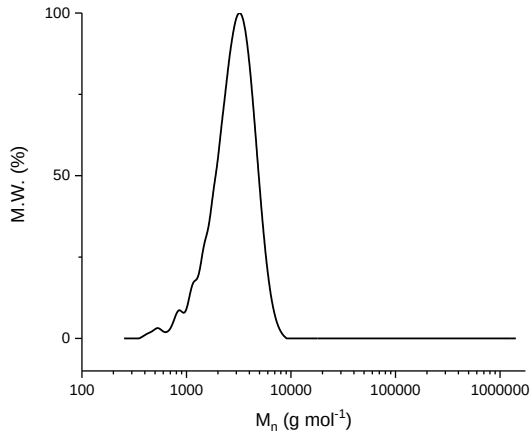


*Figure C.23 – SEC plot of M_n for catalyst **[LZnMg(OBz^{OMe})$_2$]** with CHDO at 80 °C under 1 bar CO_2 for 6 hours at 0.1 mol% catalyst loading.*

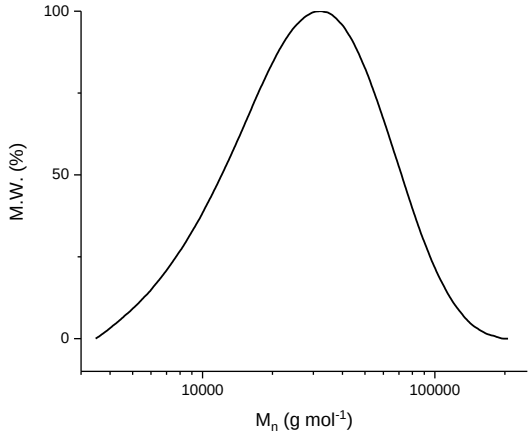


*Figure C.24 – SEC plot of M_n for catalyst **[LZnMg(OBz^{OMe})$_2$]** with PO at 60 °C under 20 bar CO_2 for 72 hours at 0.01 mol% catalyst loading.*

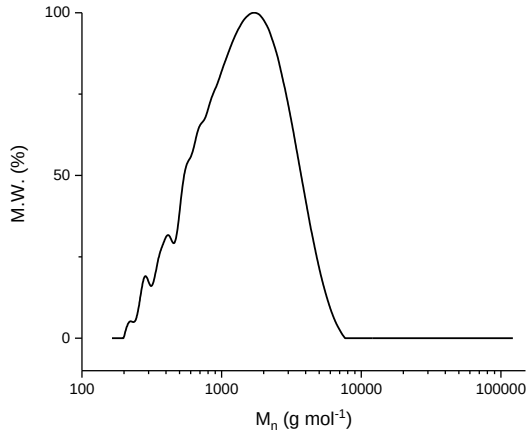


*Figure C.25 – SEC plot of M_n for catalyst **[LZnMg(OBz^{OMe})$_2$]** with ETHF at 80 °C under 1 bar CO_2 for 6 hours at 0.1 mol% catalyst loading.*

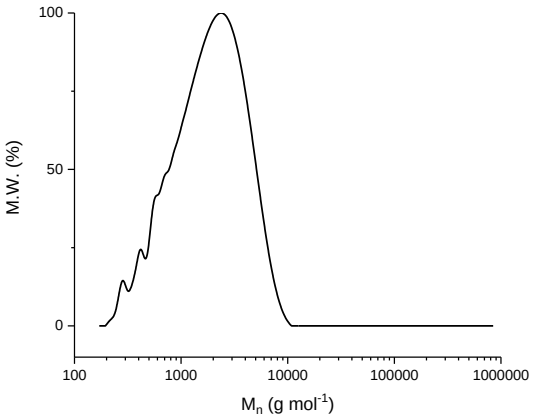


*Figure C.26 – SEC plot of M_n for catalyst **[LZnMg(OBz^{OMe})$_2$]** with ETHF at 80 °C under 1 bar CO_2 for 24 hours at 0.1 mol% catalyst loading.*

C.7 Data for Table 4.9

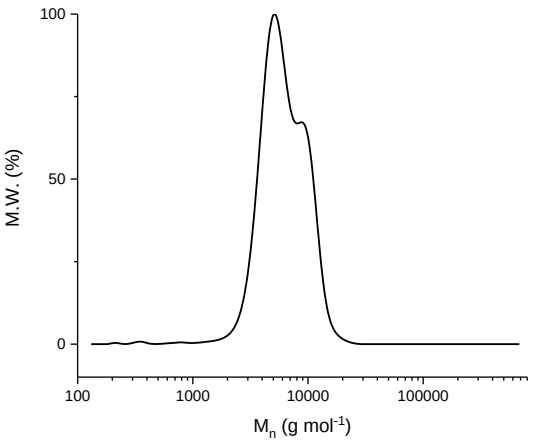


*Figure C.27 – SEC plot of M_n for catalyst **[LZnMg(OBz^{OMe})$_2$]** with CPO at 80 °C under 1 bar CO_2 for 6 hours at 0.1 mol% catalyst loading.*

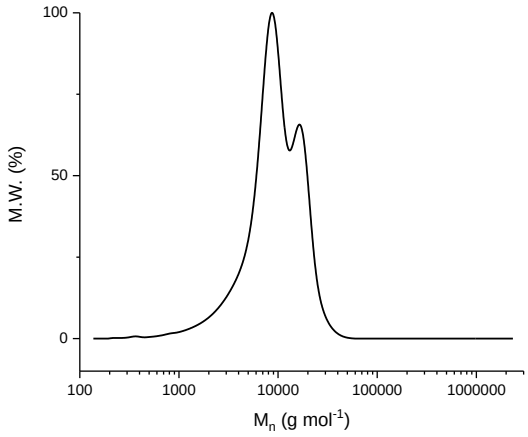


*Figure C.28 – SEC plot of M_n for catalyst **[LZnMg(OBz^{OMe})$_2$]** with CPO at 80 °C under 1 bar CO_2 for 24 hours at 0.1 mol% catalyst loading.*

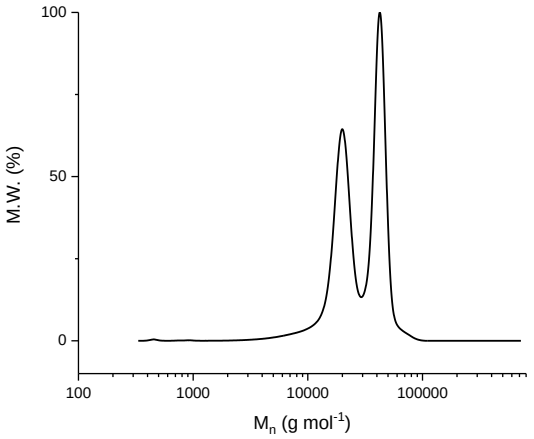


*Figure C.29 – SEC plot of M_n for catalyst **[LZnMg(OBz^{OMe})$_2$]** with CPO at 80 °C under 20 bar CO_2 for 24 hours at 0.01 mol% catalyst loading.*

C.8 Data for Table 4.11

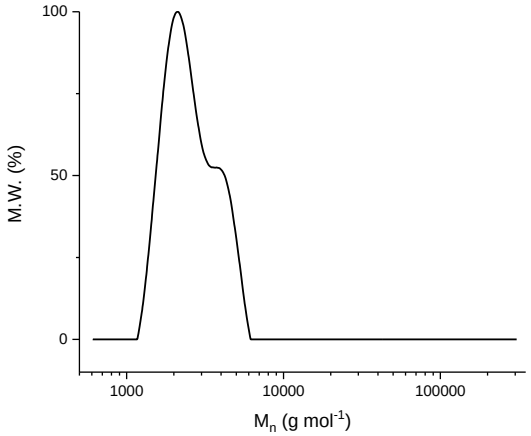


Figure C.30 – SEC plot of M_n for catalyst ***[LZnMg(OBz^{OMe})$_2$]*** *with CHO/NA at 100 °C under for 1 hour at a catalyst:anhydride:CHO molar ratio of 1:100:800.*

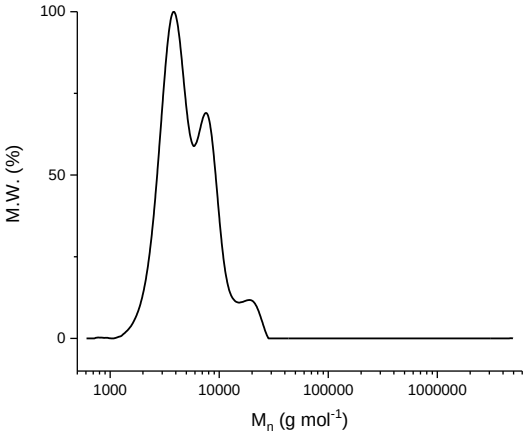


Figure C.31 – SEC plot of M_n for catalyst ***[LZnMg(OBz^{OMe})$_2$]*** *with CHO/NA at 100 °C under for 2 hours at a catalyst:anhydride:CHO molar ratio of 1:100:800.*

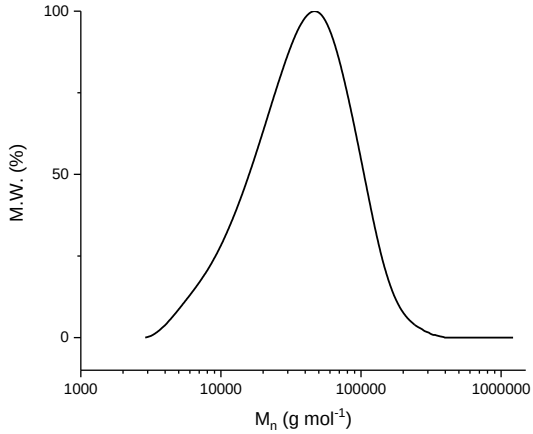


Figure C.32 – SEC plot of M_n for catalyst ***[LZnMg(OBz^{OMe})$_2$]*** *with CHO/MA at 45 °C under for 22 hours at a catalyst:anhydride:CHO molar ratio of 1:100:800.*

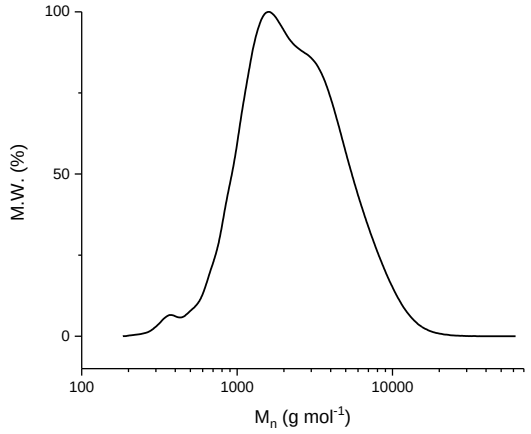


Figure C.33 – SEC plot of M_n for catalyst ***[LZnMg(OBz^{OMe})$_2$]*** *with CHO/SA at 100 °C under for 30 hours at a catalyst:anhydride:CHO molar ratio of 1:100:800.*

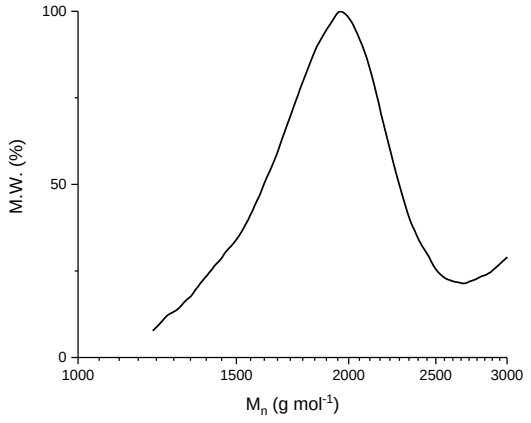


Figure C.34 – SEC plot of M_n for catalyst ***[LZnMg(OBz^{OMe})$_2$]*** *with CHO/GA at 100 °C under for 1 hour at a catalyst:anhydride:CHO molar ratio of 1:100:800.*

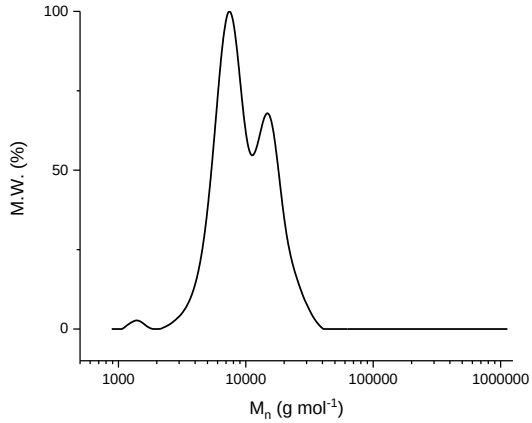


Figure A.C.35 – SEC plot of M_n for catalyst ***[LZnMg(OBz^{OMe})$_2$]*** *with CHO/DPA at 100 °C under for 1 hour at a catalyst:anhydride:CHO molar ratio of 1:100:800.*

C.9 Data for Figure 4.3

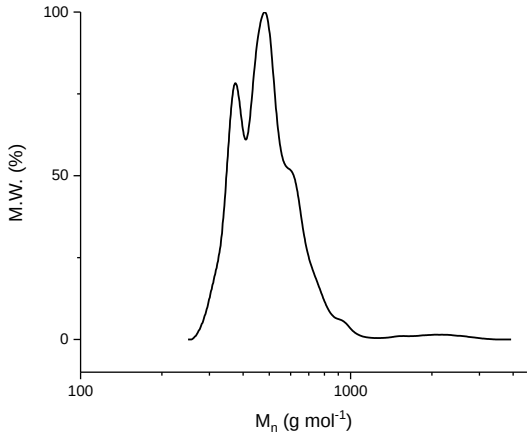


Figure C.36 – SEC plot of M_n for catalyst ***[LZnMg(OBz^{OMe})$_2$]*** *under 1 bar CO_2. Reaction conditions:* ***[LZnMg(OBz^{OMe})$_2$]****/CHO/CHD = 1/1000/10, 80 °C, 5M in toluene. Conversion = 1.5 %.*

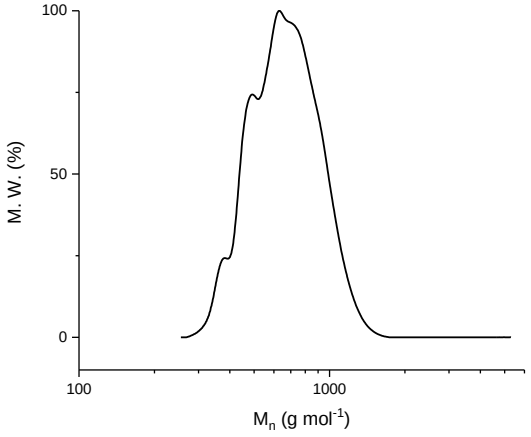


Figure C.37 – SEC plot of M_n for catalyst ***[LZnMg(OBz^{OMe})$_2$]*** *under 1 bar CO_2. Reaction conditions:* ***[LZnMg(OBz^{OMe})$_2$]****/CHO/CHD = 1/1000/10, 80 °C, 5M in toluene. Conversion = 7.0 %.*

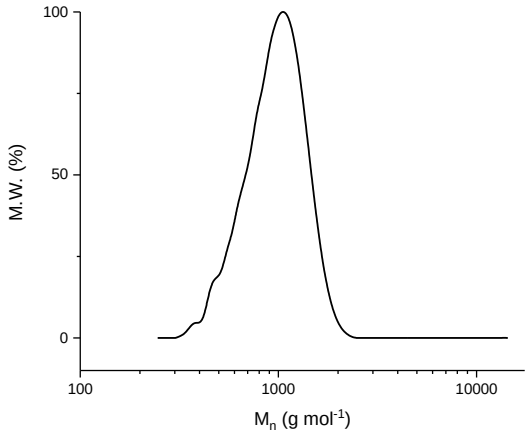


Figure C.38 – SEC plot of M_n for catalyst ***[LZnMg(OBz^{OMe})$_2$]*** *under 1 bar CO_2. Reaction conditions:* ***[LZnMg(OBz^{OMe})$_2$]****/CHO/CHD = 1/1000/10, 80 °C, 5M in toluene. Conversion = 14.8 %.*

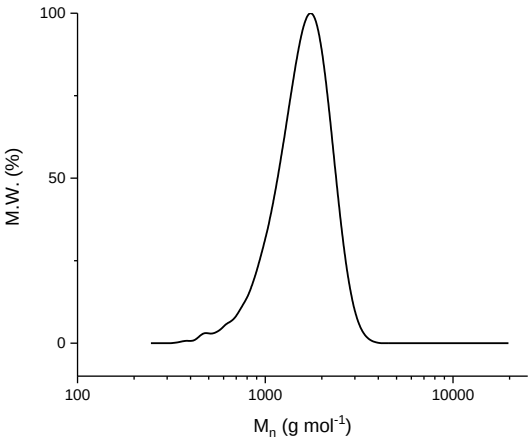


Figure C.39 – SEC plot of M_n for catalyst ***[LZnMg(OBz^{OMe})$_2$]*** *under 1 bar CO_2. Reaction conditions:* ***[LZnMg(OBz^{OMe})$_2$]****/CHO/CHD = 1/1000/10, 80 °C, 5M in toluene. Conversion = 33.3 %.*

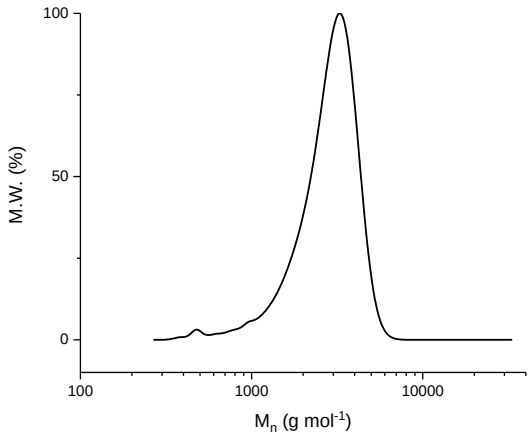


Figure C.40 – SEC plot of M_n for catalyst ***[LZnMg(OBz^{OMe})$_2$]*** *under 1 bar CO_2. Reaction conditions:* ***[LZnMg(OBz^{OMe})$_2$]****/CHO/CHD = 1/1000/10, 80 °C, 5M in toluene. Conversion = 74.8 %.*

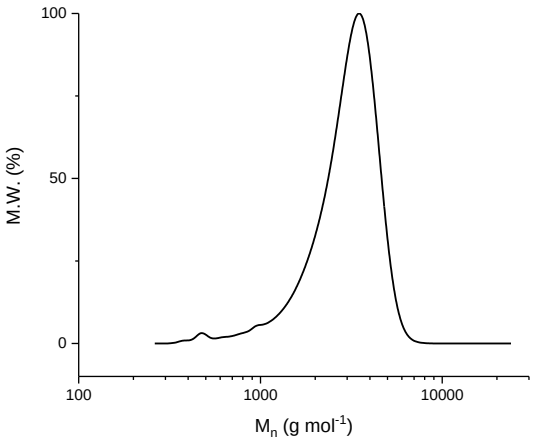


Figure C.41 – SEC plot of M_n for catalyst ***[LZnMg(OBz^{OMe})$_2$]*** *under 1 bar CO_2. Reaction conditions:* ***[LZnMg(OBz^{OMe})$_2$]****/CHO/CHD = 1/1000/10, 80 °C, 5M in toluene. Conversion = 78.8 %.*

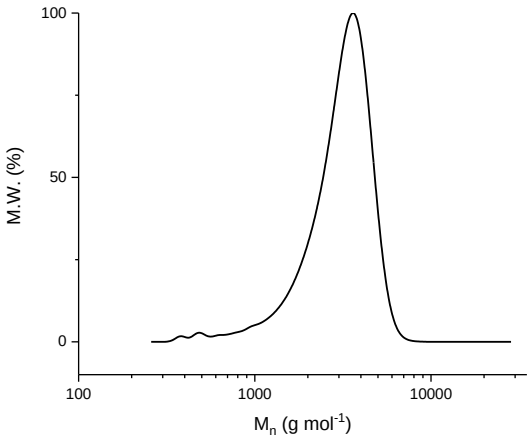


Figure C.42 – SEC plot of M_n for catalyst ***[LZnMg(OBz^{OMe})$_2$]*** *under 1 bar CO_2. Reaction conditions:* ***[LZnMg(OBz^{OMe})$_2$]****/CHO/CHD = 1/1000/10, 80 °C, 5M in toluene. Conversion = 85.0 %.*

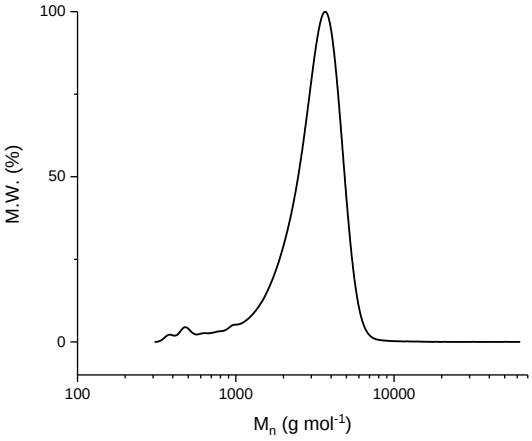


Figure C.43 – SEC plot of M_n for catalyst ***[LZnMg(OBz^{OMe})$_2$]*** *under 1 bar CO_2. Reaction conditions:* ***[LZnMg(OBz^{OMe})$_2$]****/CHO/CHD = 1/1000/10, 80 °C, 5M in toluene. Conversion = 90.5 %.*

C.10 Data for Figure 4.11

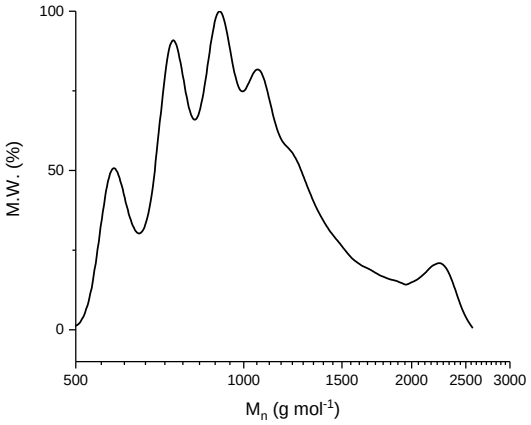


Figure C.44 – SEC plot of M_n for catalyst ***[LZnMg(OBz^{OMe})$_2$]*** *with CHO/PA at 100 °C with a catalyst:PA:CHO molar ratio of 1:100:800. Conversion = 9 %.*

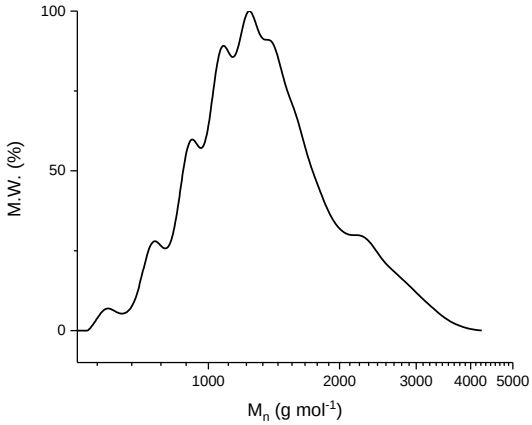


Figure C.45 – SEC plot of M_n for catalyst ***[LZnMg(OBz^{OMe})$_2$]*** *with CHO/PA at 100 °C with a catalyst:PA:CHO molar ratio of 1:100:800. Conversion = 17 %.*

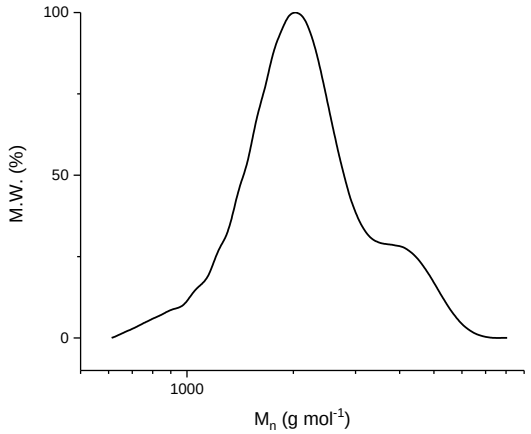


Figure C.46 – SEC plot of M_n for catalyst ***[LZnMg(OBz^{OMe})$_2$]*** *with CHO/PA at 100 °C with a catalyst:PA:CHO molar ratio of 1:100:800. Conversion = 29 %.*

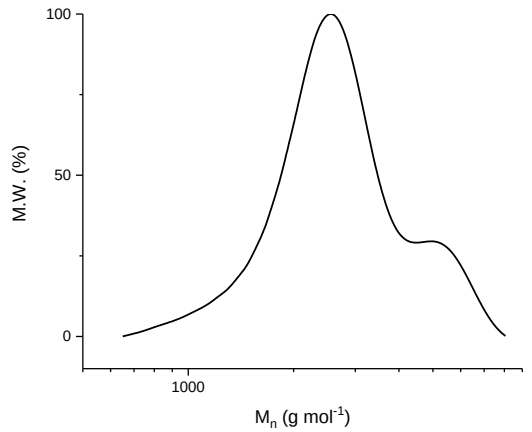


Figure C.47 – SEC plot of M_n for catalyst ***[LZnMg(OBz^{OMe})$_2$]*** *with CHO/PA at 100 °C with a catalyst:PA:CHO molar ratio of 1:100:800. Conversion = 42 %.*

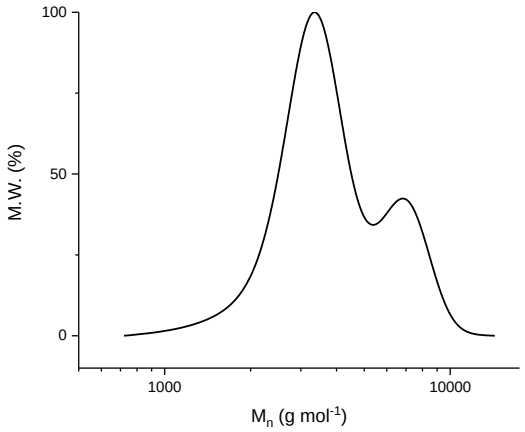


Figure C.48 – SEC plot of M_n for catalyst ***[LZnMg(OBz^{OMe})$_2$]*** *with CHO/PA at 100 °C with a catalyst:PA:CHO molar ratio of 1:100:800. Conversion = 57 %.*

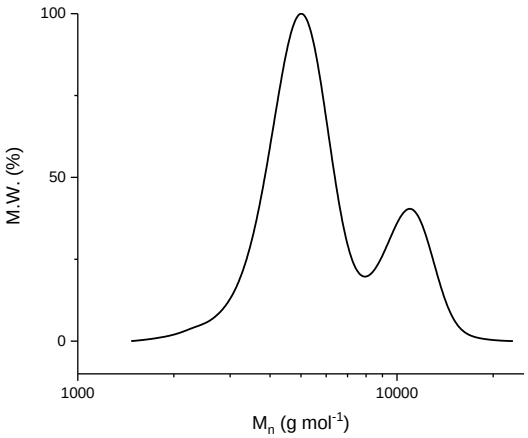


Figure C.49 – SEC plot of M_n for catalyst ***[LZnMg(OBz^{OMe})$_2$]*** *with CHO/PA at 100 °C with a catalyst:PA:CHO molar ratio of 1:100:800. Conversion = 88 %.*

Appendix D: ATR-IR Spectroscopy Plots

D.1 Data for Table 4.1

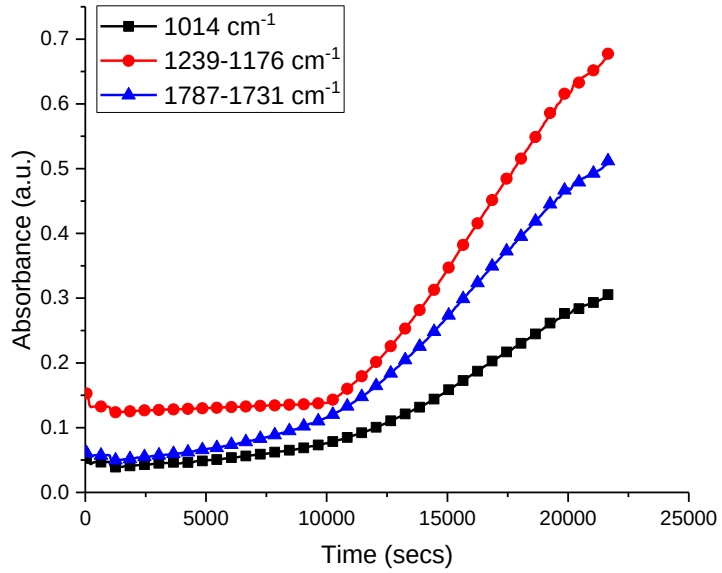


Figure D.1 – ATR-IR spectroscopy plot showing the change in absorbance vs. time plot for three vibrational modes during the CHO/CO_2 copolymerisation catalysed by ***[LZnMgBr$_2$]****. Reaction conditions: 1:1000 catalyst:CHO, 80 °C at 1 bar CO_2 pressure. For clarity, only every 10th data point is shown.*

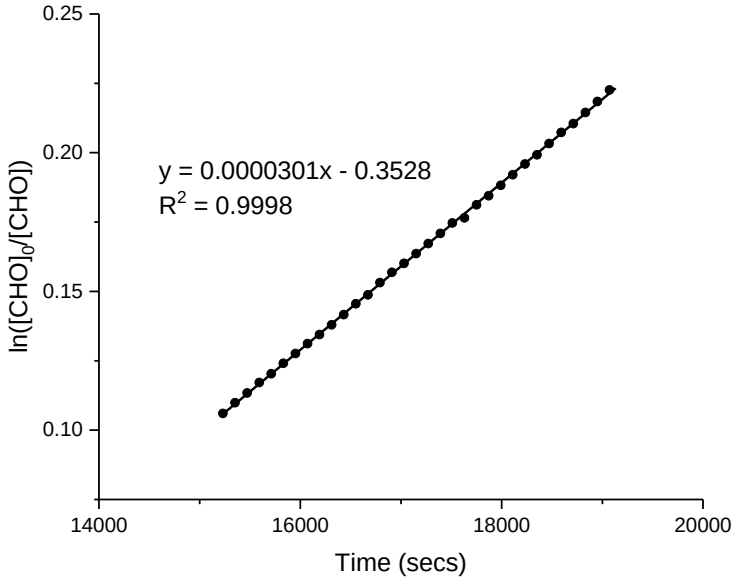


Figure D.2 – Plot of ln([CHO]$_0$/[CHO]) vs time for CHO/CO_2 copolymerisation catalysed by ***[LZnMgBr$_2$]****, for 10-20 % conversion. The gradient of the graph represents k_{obs}, assuming a first order dependence on epoxide. Reaction conditions: 1:1000 catalyst:CHO, 80 °C at 1 bar CO_2 pressure. For clarity, only every 2nd data point is shown.*

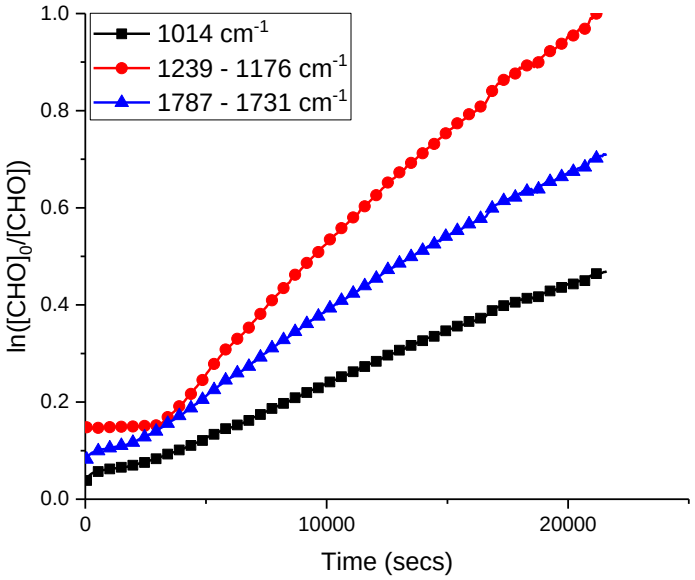


Figure D.3 – ATR-IR spectroscopy plot showing the change in absorbance vs. time plot for three vibrational modes during the CHO/CO_2 copolymerisation catalysed by ***[LZnMg(OAc)$_2$]****. Reaction conditions: 1:1000 catalyst:CHO, 80 °C at 1 bar CO_2 pressure. For clarity, only every 8th data point is shown.*

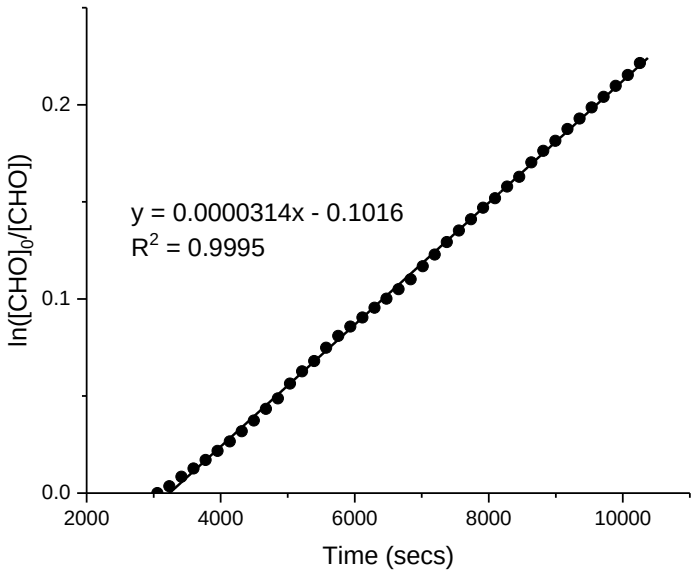


Figure D.4 – Plot of ln([CHO]$_0$/[CHO]) vs time for CHO/CO_2 copolymerisation catalysed by ***[LZnMg(OAc)$_2$]****. The gradient of the graph represents k_{obs}, assuming a first order dependence on epoxide. Reaction conditions: 1:1000 catalyst:CHO, 80 °C at 1 bar CO_2 pressure. For clarity, only every 3rd data point is shown.*

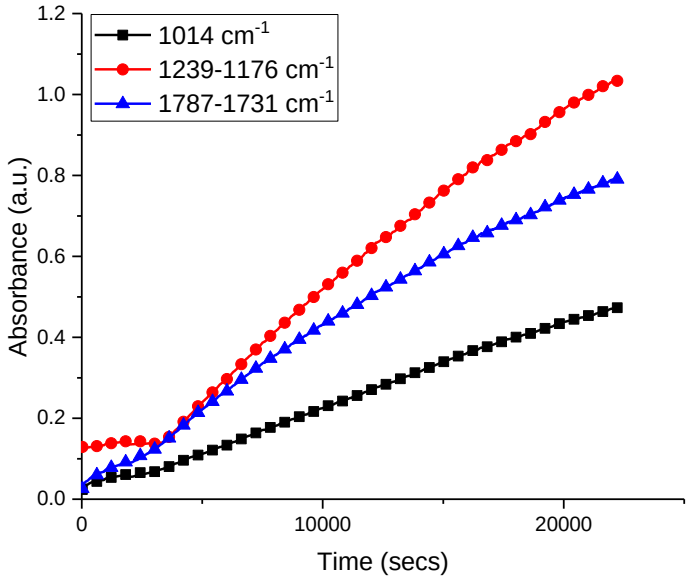


Figure D.5 – ATR-IR spectroscopy plot showing the change in absorbance vs. time plot for three vibrational modes during the CHO/CO_2 copolymerisation catalysed by ***[LZnMg(OBz)$_2$]****. Reaction conditions: 1:1000 catalyst:CHO, 80 °C at 1 bar CO_2 pressure. For clarity, only every 20th data point is shown.*

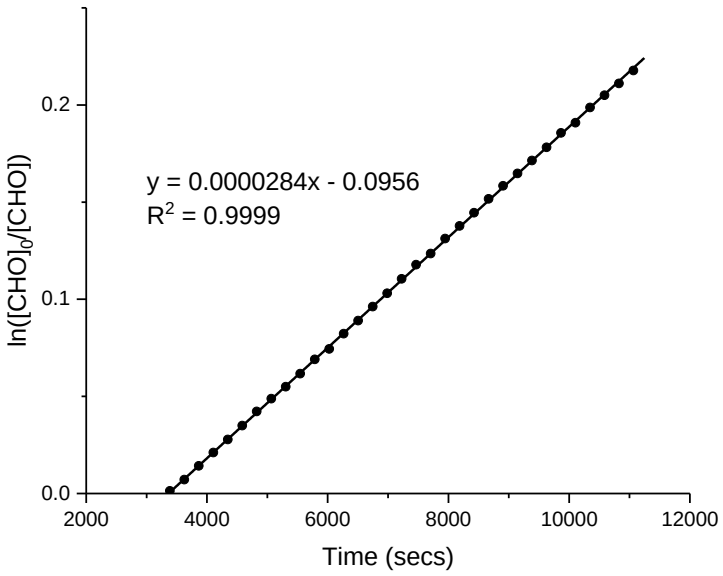


Figure D.6 – Plot of ln([CHO]$_0$/[CHO]) vs time for CHO/CO_2 copolymerisation catalysed by ***[LZnMg(OBz)$_2$]****. The gradient of the graph represents k_{obs}, assuming a first order dependence on epoxide. Reaction conditions: 1:1000 catalyst:CHO, 80 °C at 1 bar CO_2 pressure. For clarity, only every 9th data point is shown.*

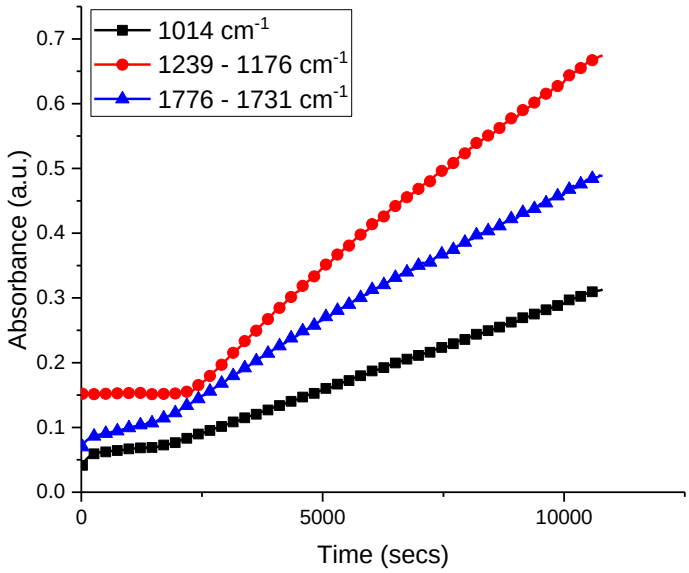


Figure D.7 – ATR-IR spectroscopy plot showing the change in absorbance vs. time plot for three vibrational modes during the CHO/CO_2 copolymerisation catalysed by ***[LZnMg(OBz^{OMe})$_2$]****. Reaction conditions: 1:1000 catalyst:CHO, 80 °C at 1 bar CO_2 pressure. For clarity, only every 8th data point is shown.*

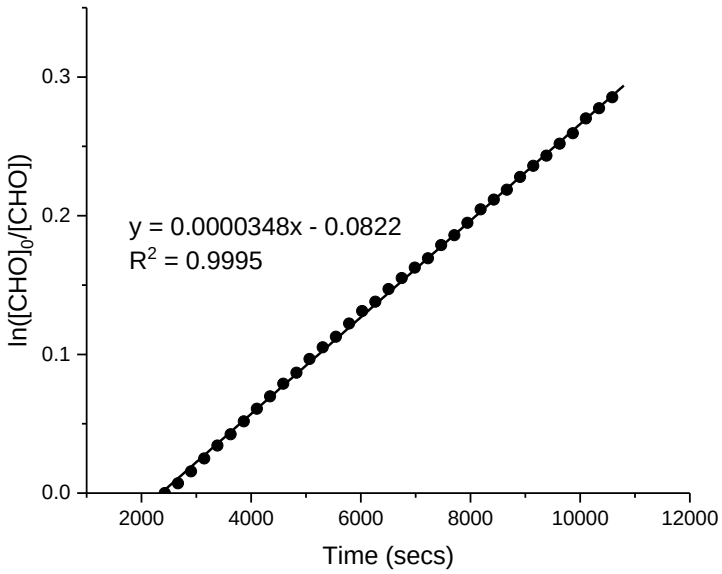


Figure D.8 – Plot of ln([CHO]$_0$/[CHO]) vs time for CHO/CO_2 copolymerisation catalysed by ***[LZnMg(OBz^{OMe})$_2$]****. The gradient of the graph represents k_{obs}, assuming a first order dependence on epoxide. Reaction conditions: 1:1000 catalyst:CHO, 80 °C at 1 bar CO_2 pressure. For clarity, only every 8th data point is shown.*

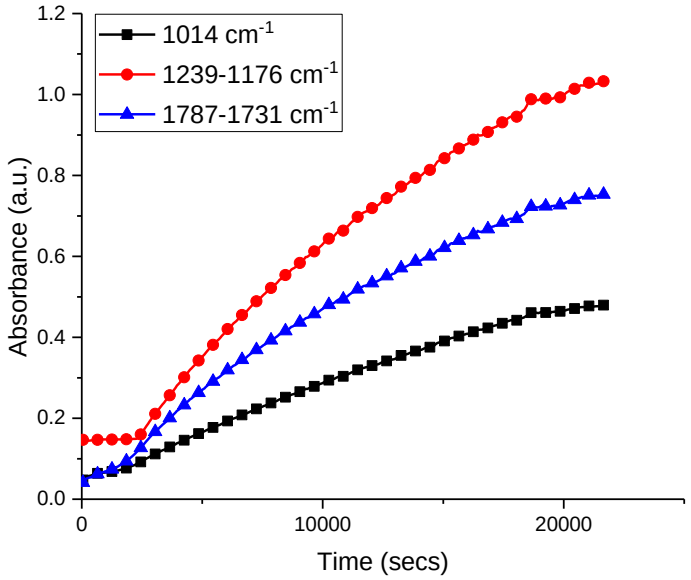


Figure D.9 – ATR-IR spectroscopy plot showing the change in absorbance vs. time plot for three vibrational modes during the CHO/CO_2 copolymerisation catalysed by ***[LZnMg(OBz^{CF3})$_2$]****. Reaction conditions: 1:1000 catalyst:CHO, 80 °C at 1 bar CO_2 pressure. For clarity, only every 10th data point is shown.*

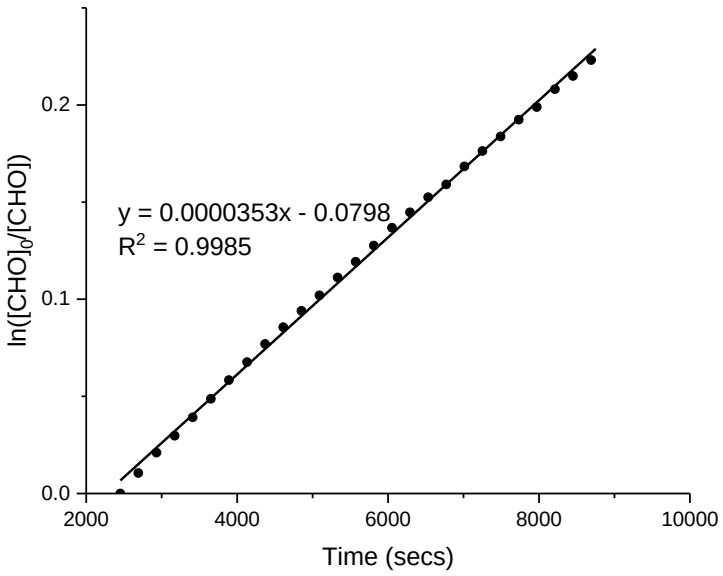


Figure D.10 – Plot of ln([CHO]$_0$/[CHO]) vs time for CHO/CO_2 copolymerisation catalysed by ***[LZnMg(OBz^{CF3})$_2$]****. The gradient of the graph represents k_{obs}, assuming a first order dependence on epoxide. Reaction conditions: 1:1000 catalyst:CHO, 80 °C at 1 bar CO_2 pressure. For clarity, only every 4th data point is shown.*

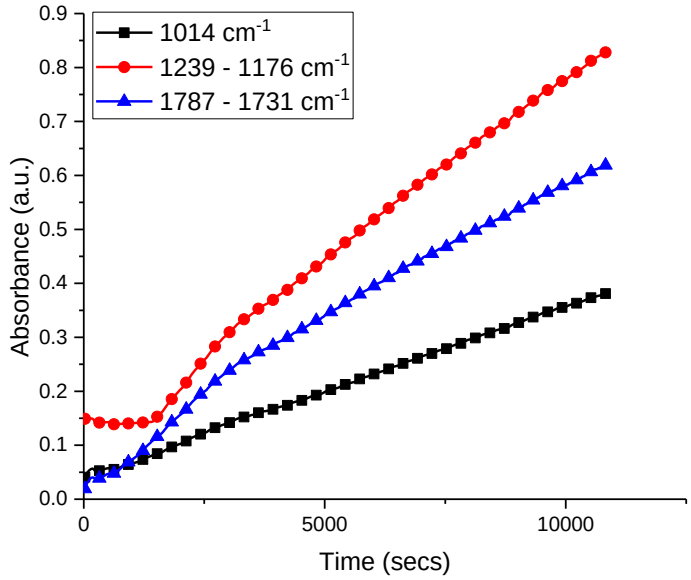


Figure D.11 – ATR-IR spectroscopy plot showing the change in absorbance vs. time plot for three vibrational modes during the CHO/CO_2 copolymerisation catalysed by ***[LZnMg(OBz^{NO2})$_2$]****. Reaction conditions: 1:1000 catalyst:CHO, 80 °C at 1 bar CO_2 pressure. For clarity, only every 10th data point is shown.*

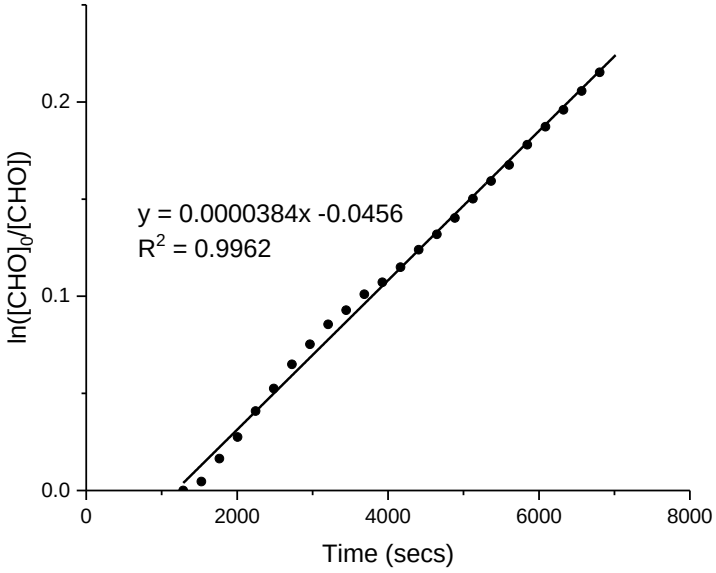


Figure D.12 – Plot of ln([CHO]$_0$/[CHO]) vs time for CHO/CO_2 copolymerisation catalysed by ***[LZnMg(OBz^{NO2})$_2$]****. The gradient of the graph represents k_{obs}, assuming a first order dependence on epoxide. Reaction conditions: 1:1000 catalyst:CHO, 80 °C at 1 bar CO_2 pressure. For clarity, only every 8th data point is shown.*

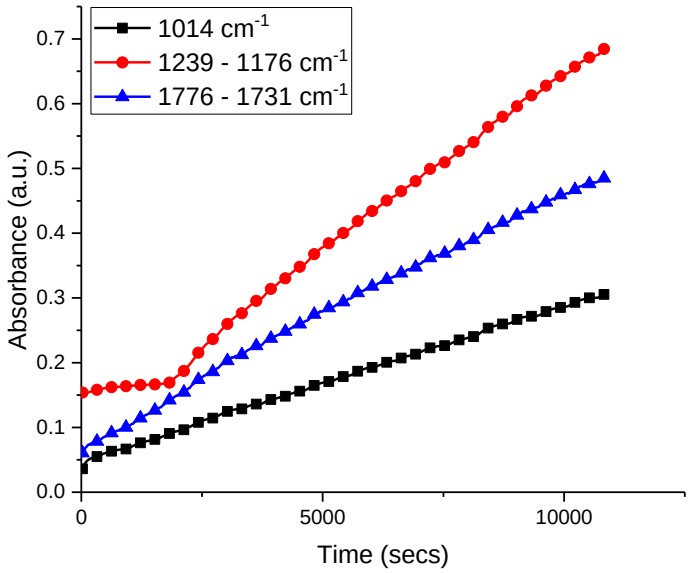


Figure D.13 – ATR-IR spectroscopy plot showing the change in absorbance vs. time plot for three vibrational modes during the CHO/CO_2 copolymerisation catalysed by ***[LZnMg(OBz^{NMe2})$_2$]****. Reaction conditions: 1:1000 catalyst:CHO, 80 °C at 1 bar CO_2 pressure. For clarity, only every 10th data point is shown.*

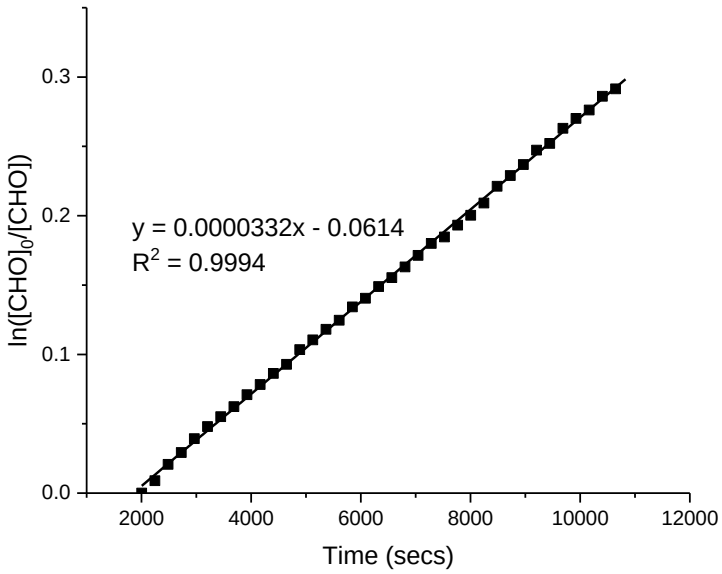


Figure D.14 – Plot of ln([CHO]$_0$/[CHO]) vs time for CHO/CO_2 copolymerisation catalysed by ***[LZnMg(OBz^{NMe2})$_2$]****. The gradient of the graph represents k_{obs}, assuming a first order dependence on epoxide. Reaction conditions: 1:1000 catalyst:CHO, 80 °C at 1 bar CO_2 pressure. For clarity, only every 8th data point is shown.*

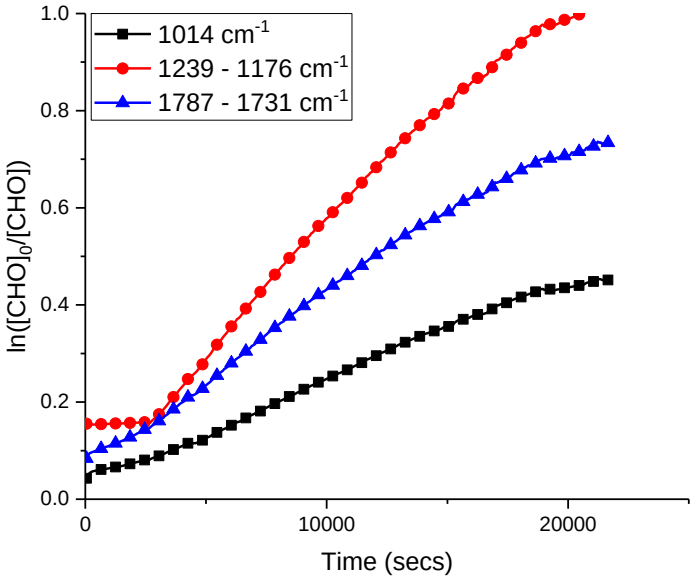


Figure D.15 – ATR-IR spectroscopy plot showing the change in absorbance vs. time plot for three vibrational modes during the CHO/CO_2 copolymerisation catalysed by ***[LZnMg(OBz^F)$_2$]****. Reaction conditions: 1:1000 catalyst:CHO, 80 °C at 1 bar CO_2 pressure. For clarity, only every 10th data point is shown.*

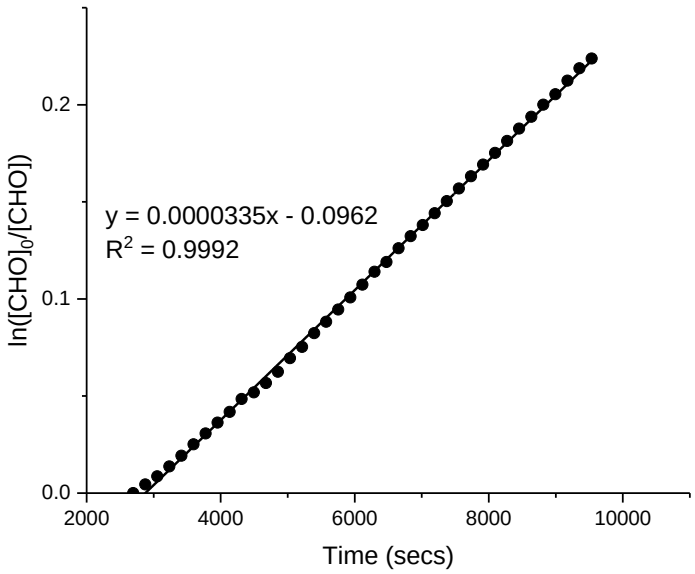


Figure D.16 – Plot of ln([CHO]$_0$/[CHO]) vs time for CHO/CO_2 copolymerisation catalysed by ***[LZnMg(OBz^F)$_2$]****. The gradient of the graph represents k_{obs}, assuming a first order dependence on epoxide. Reaction conditions: 1:1000 catalyst:CHO, 80 °C at 1 bar CO_2 pressure. For clarity, only every 3rd data point is shown.*

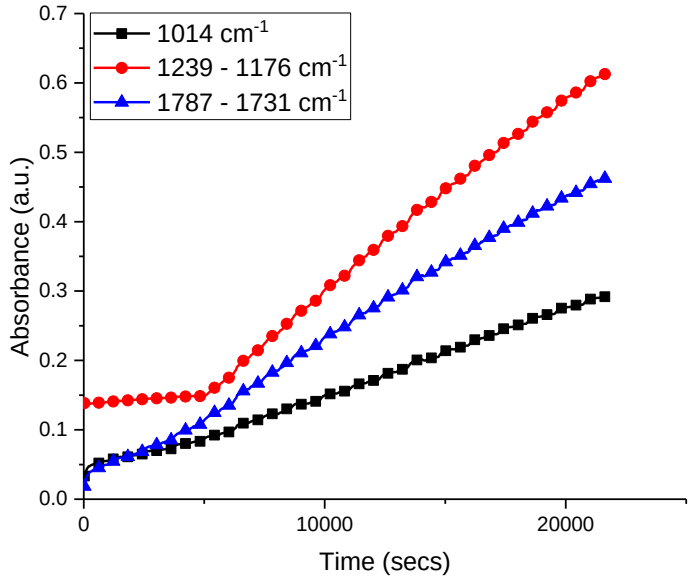


Figure D.17 – ATR-IR spectroscopy plot showing the change in absorbance vs. time plot for three vibrational modes during the CHO/CO_2 copolymerisation catalysed by ***[LZnMg(OBz^{F5})$_2$]****. Reaction conditions: 1:1000 catalyst:CHO, 80 °C at 1 bar CO_2 pressure. For clarity, only every 20th data point is shown.*

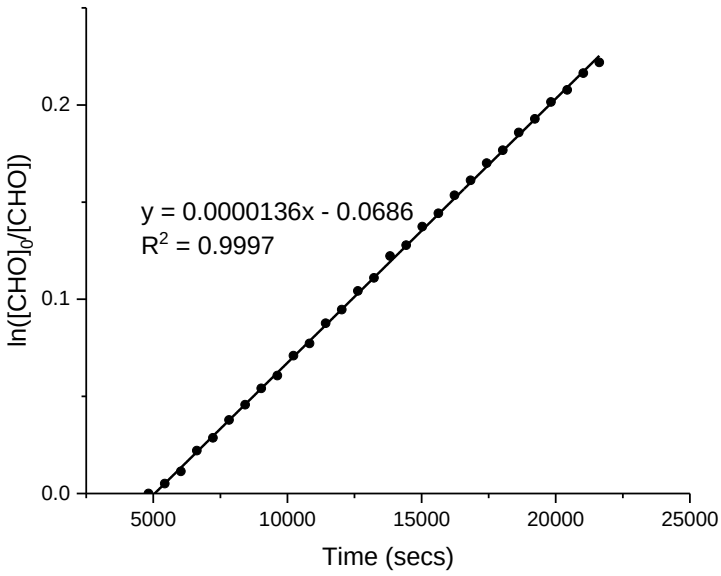


Figure D.18 – Plot of ln([CHO]$_0$/[CHO]) vs time for CHO/CO_2 copolymerisation catalysed by ***[LZnMg(OBz^{F5})$_2$]****. The gradient of the graph represents k_{obs}, assuming a first order dependence on epoxide. Reaction conditions: 1:1000 catalyst:CHO, 80 °C at 1 bar CO_2 pressure. For clarity, only every 20th data point is shown.*

D.2 Data for Table 4.2

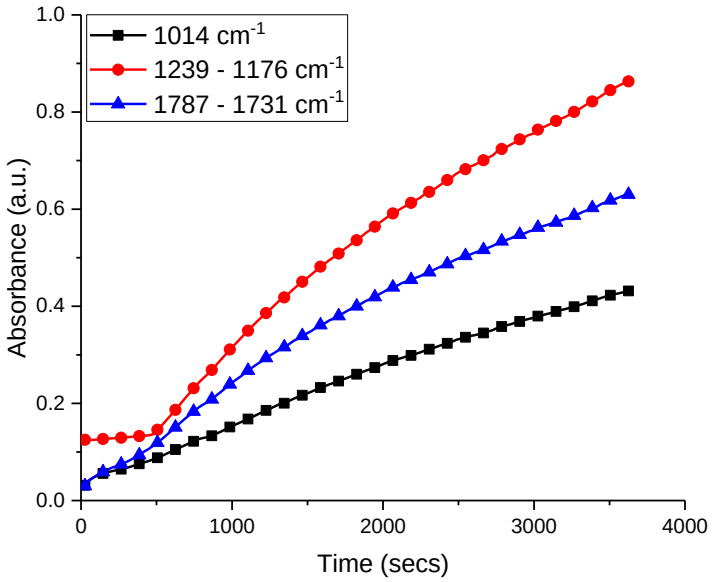


Figure D.19 – ATR-IR spectroscopy plot showing the change in absorbance vs. time plot for three vibrational modes during the CHO/CO_2 copolymerisation catalysed by ***[LZnMg(OBz^{OMe})$_2$]****. Reaction conditions: 1:1000 catalyst:CHO, 120 °C at 1 bar CO_2 pressure. For clarity, only every 4th data point is shown.*

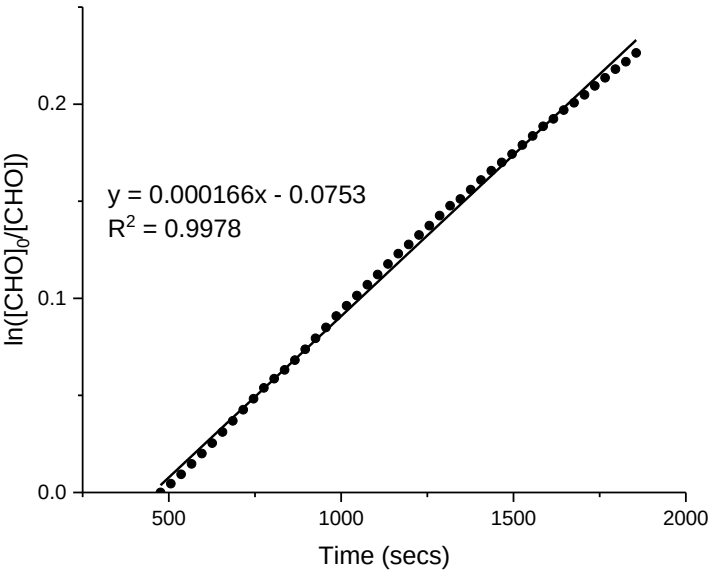


Figure D.20 – Plot of ln([CHO]$_0$/[CHO]) vs time for CHO/CO_2 copolymerisation catalysed by ***[LZnMg(OBz^{OMe})$_2$]****. The gradient of the graph represents k_{obs}, assuming a first order dependence on epoxide. Reaction conditions: 1:1000 catalyst:CHO, 120 °C at 1 bar CO_2 pressure.*

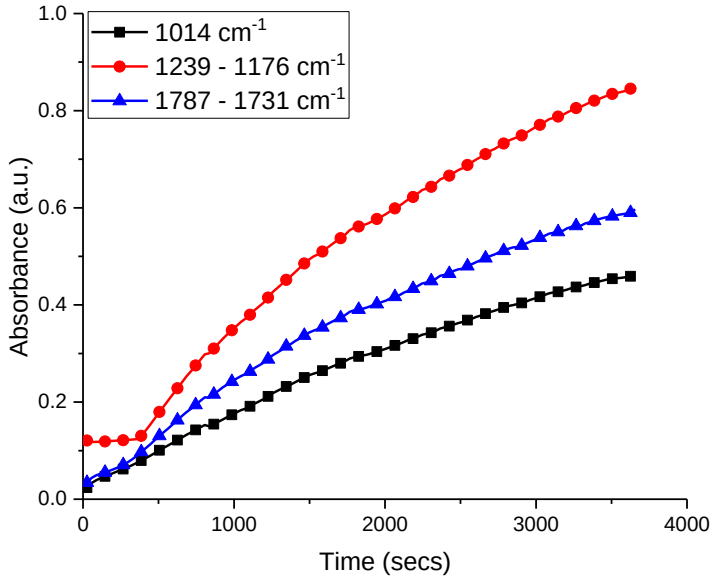


Figure D.21 – ATR-IR spectroscopy plot showing the change in absorbance vs. time plot for three vibrational modes during the CHO/CO_2 copolymerisation catalysed by ***[LZnMg(OBz^{CF3})$_2$]****. Reaction conditions: 1:1000 catalyst:CHO, 120 °C at 1 bar CO_2 pressure. For clarity, only every 4th data point is shown.*

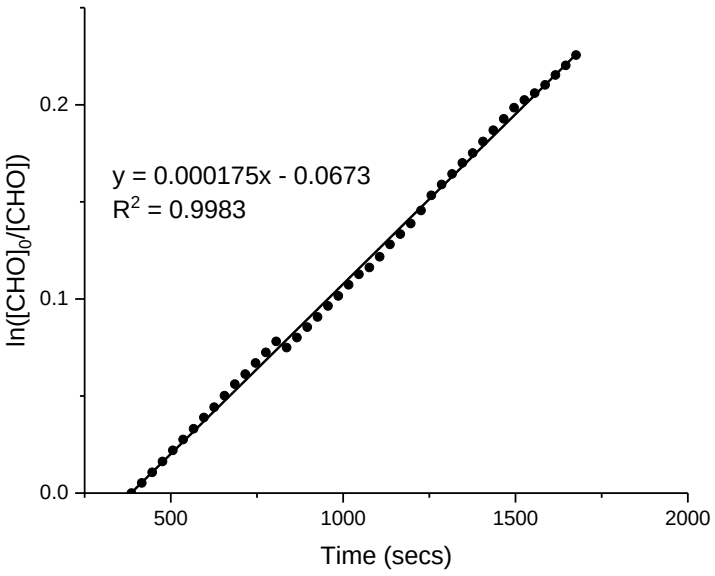


Figure D.22 – Plot of ln([CHO]$_0$/[CHO]) vs time for CHO/CO_2 copolymerisation catalysed by ***[LZnMg(OBz^{CF3})$_2$]****. The gradient of the graph represents k_{obs}, assuming a first order dependence on epoxide. Reaction conditions: 1:1000 catalyst:CHO, 120 °C at 1 bar CO_2 pressure.*

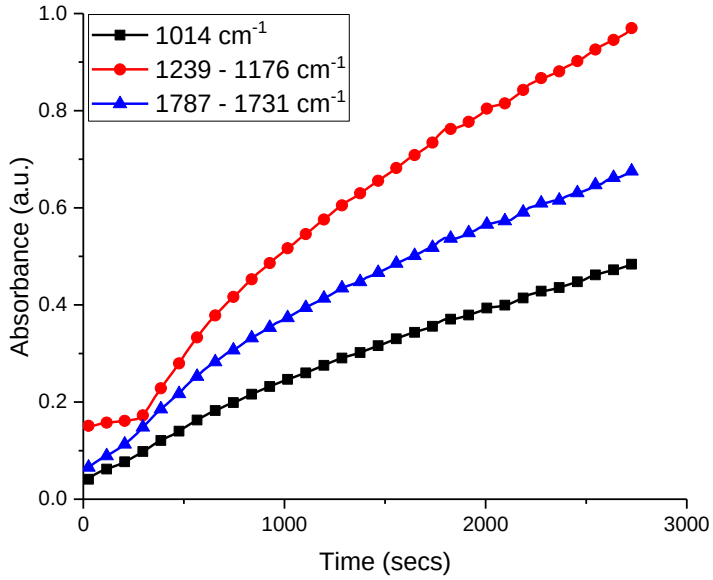


Figure D.23 – ATR-IR spectroscopy plot showing the change in absorbance vs. time plot for three vibrational modes during the CHO/CO_2 copolymerisation catalysed by ***[LZnMg(OBz^{NMe2})$_2$]****. Reaction conditions: 1:1000 catalyst:CHO, 120 °C at 1 bar CO_2 pressure. For clarity, only every 3rd data point is shown.*

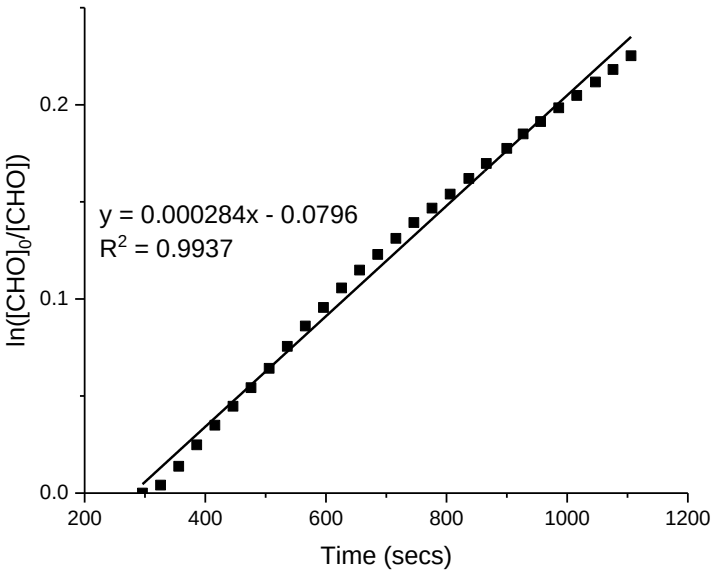


Figure D.24 – Plot of ln([CHO]$_0$/[CHO]) vs time for CHO/CO_2 copolymerisation catalysed by ***[LZnMg(OBz^{NMe2})$_2$]****. The gradient of the graph represents k_{obs}, assuming a first order dependence on epoxide. Reaction conditions: 1:1000 catalyst:CHO, 120 °C at 1 bar CO_2 pressure.*

D.3 Data for Figure 4.12

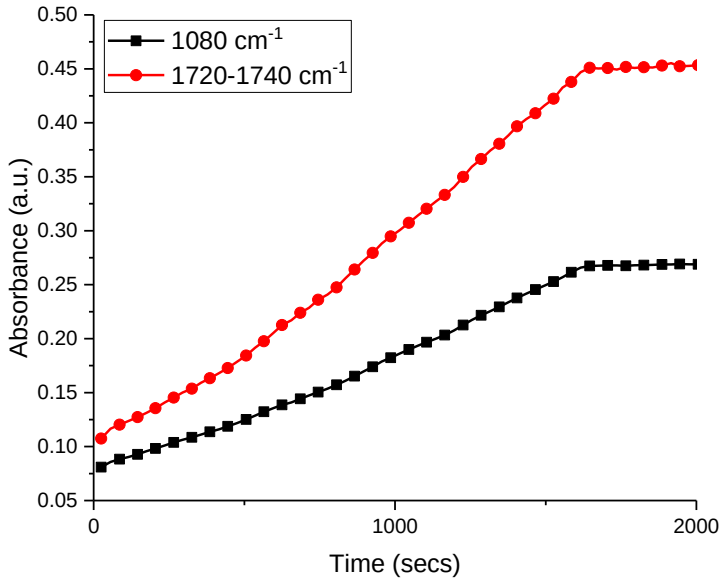


Figure D.25 – ATR-IR spectroscopy plot showing the change in absorbance vs. time plot for two vibrational modes during the CHO/PA copolymerisation catalysed by ***[LZnMg(OBz)$_2$]****. Reaction conditions: 1:100:800 catalyst:PA:CHO and 100 °C. For clarity, only every 2nd data point is shown.*

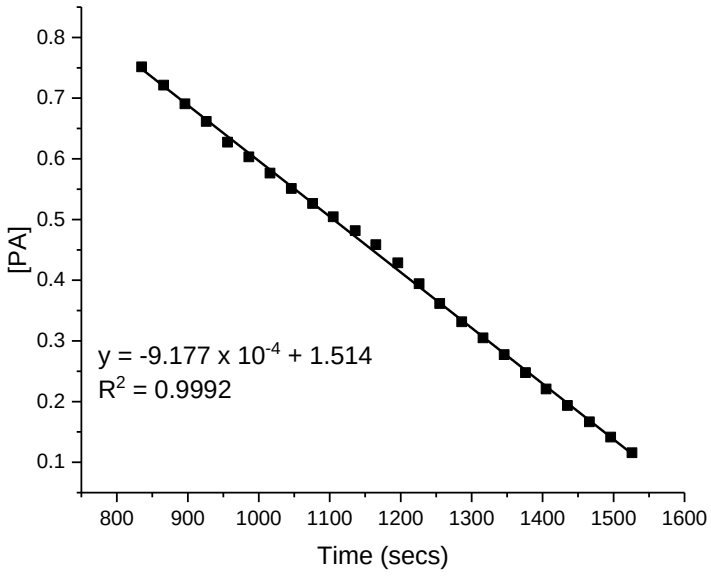


Figure D.26 – Plot of [PA] vs time for CHO/PA copolymerisation catalysed by ***[LZnMg(OBz)$_2$]****. The gradient of the graph represents k_{obs}, assuming a zero order dependence on PA, using data from 40-90 % conversion. Reaction conditions: 1:100:800 catalyst:PA:CHO and 100 °C.*

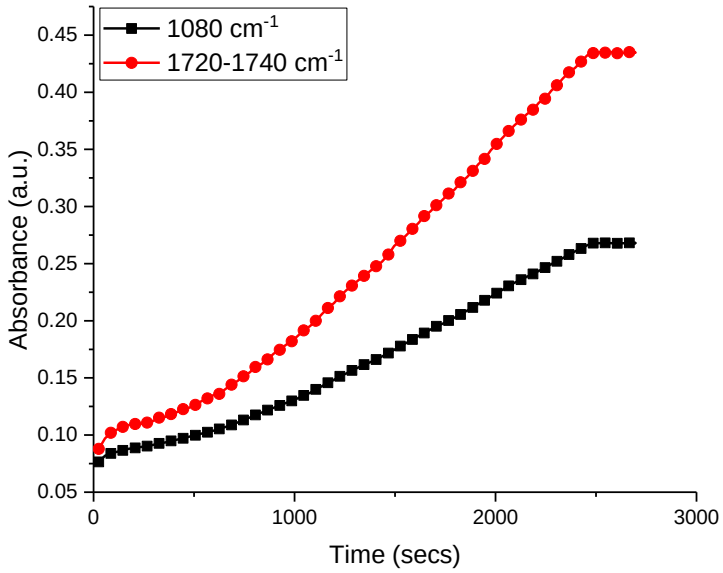


Figure D.27 – ATR-IR spectroscopy plot showing the change in absorbance vs. time plot for two vibrational modes during the CHO/PA copolymerisation catalysed by ***[LZnMg(OBz^{OMe})$_2$]****. Reaction conditions: 1:100:800 catalyst:PA:CHO and 100 °C. For clarity, only every 2nd data point is shown.*

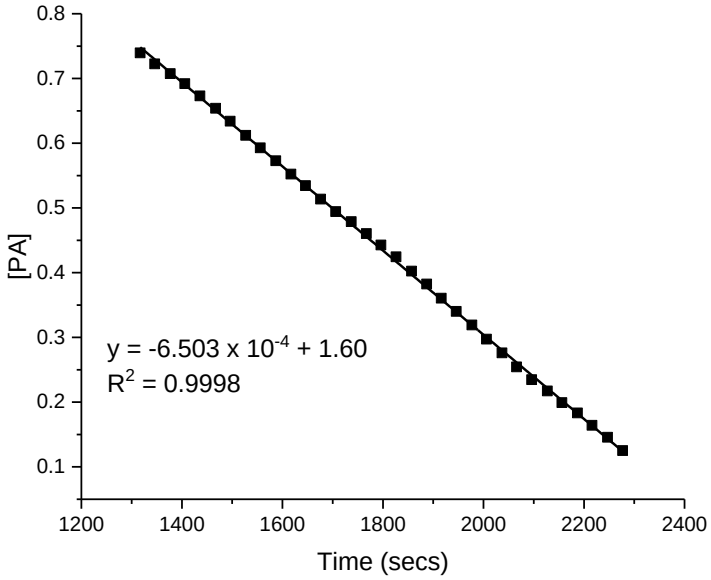


Figure D.28 – Plot of [PA] vs time for CHO/PA copolymerisation catalysed by ***[LZnMg(OBz^{OMe})$_2$]****. The gradient of the graph represents k_{obs}, assuming a zero order dependence on PA, using data from 40-90 % conversion. Reaction conditions: 1:100:800 catalyst:PA:CHO and 100 °C.*

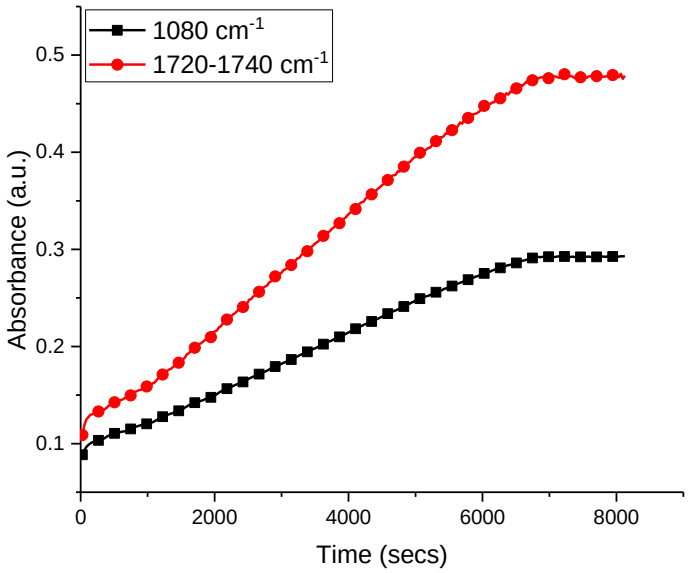


Figure D.29 – ATR-IR spectroscopy plot showing the change in absorbance vs. time plot for two vibrational modes during the CHO/PA copolymerisation catalysed by ***[LZnMg(OBz^{CF3})$_2$]****. Reaction conditions: 1:100:800 catalyst:PA:CHO and 100 °C. For clarity, only every 8th data point is shown.*

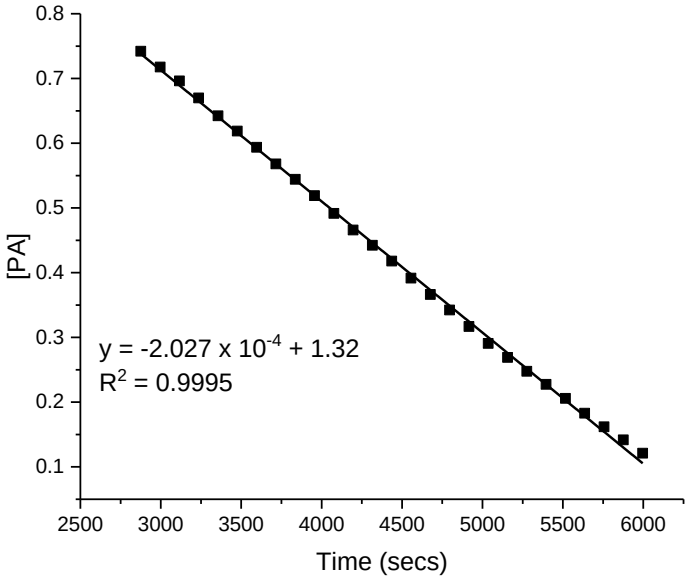


Figure D.30 – Plot of [PA] vs time for CHO/PA copolymerisation catalysed by ***[LZnMg(OBz^{CF3})$_2$]****. The gradient of the graph represents k_{obs}, assuming a zero order dependence on PA, using data from 40-90 % conversion. Reaction conditions: 1:100:800 catalyst:PA:CHO and 100 °C. For clarity, only every 4th data point is shown.*

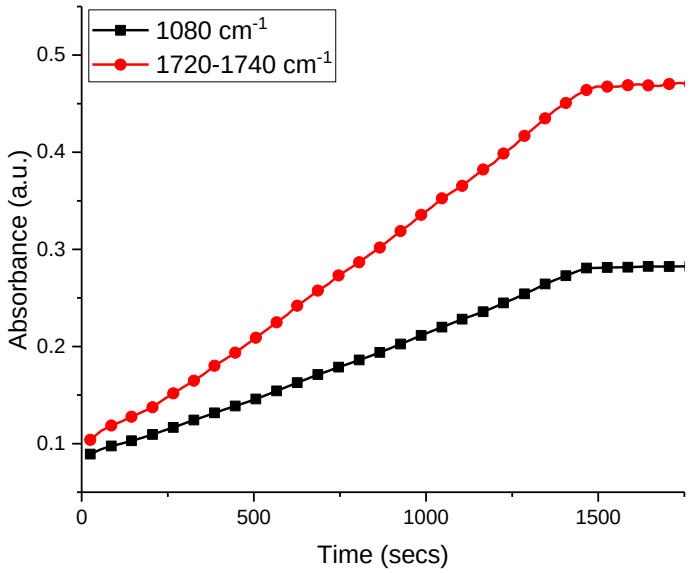


Figure D.31 – ATR-IR spectroscopy plot showing the change in absorbance vs. time plot for two vibrational modes during the CHO/PA copolymerisation catalysed by ***[LZnMg(OBz^{NO2})$_2$]****. Reaction conditions: 1:100:800 catalyst:PA:CHO and 100 °C. For clarity, only every 2nd data point is shown.*

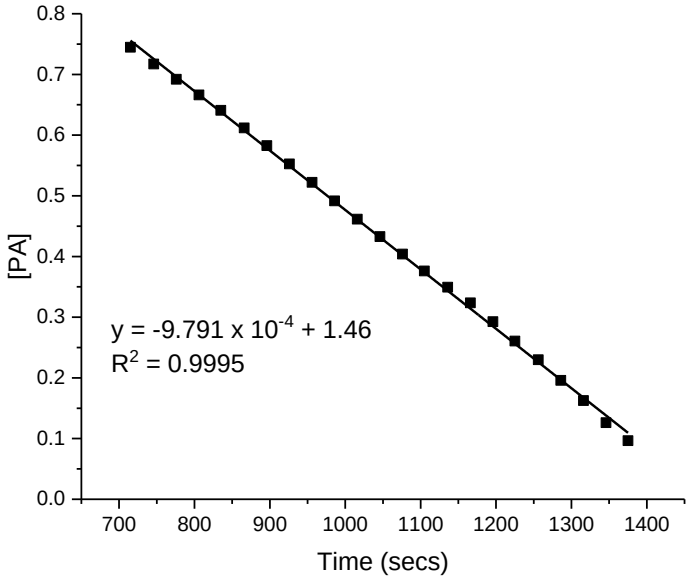


Figure D.32 – Plot of [PA] vs time for CHO/PA copolymerisation catalysed by ***[LZnMg(OBz^{NO2})$_2$]****. The gradient of the graph represents k_{obs}, assuming a zero order dependence on PA, using data from 40-90 % conversion. Reaction conditions: 1:100:800 catalyst:PA:CHO and 100 °C.*

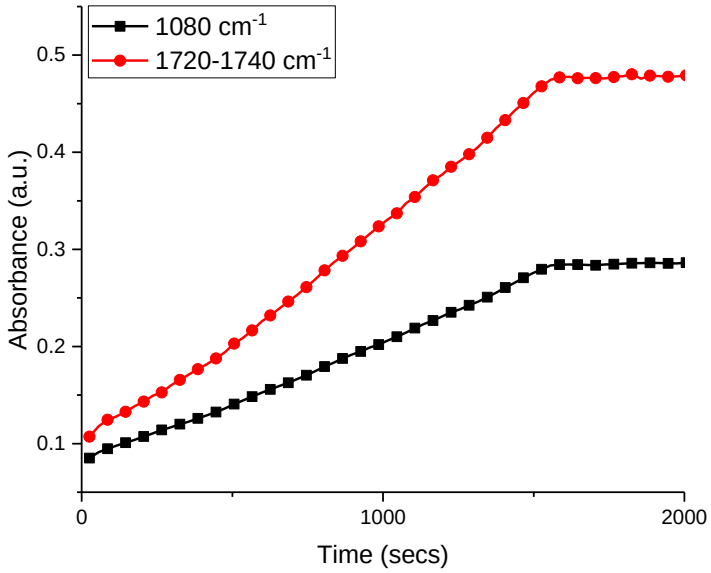


Figure D.33 – ATR-IR spectroscopy plot showing the change in absorbance vs. time plot for two vibrational modes during the CHO/PA copolymerisation catalysed by ***[LZnMg(OBz^{NMe2})$_2$]****. Reaction conditions: 1:100:800 catalyst:PA:CHO and 100 °C. For clarity, only every 2nd data point is shown.*

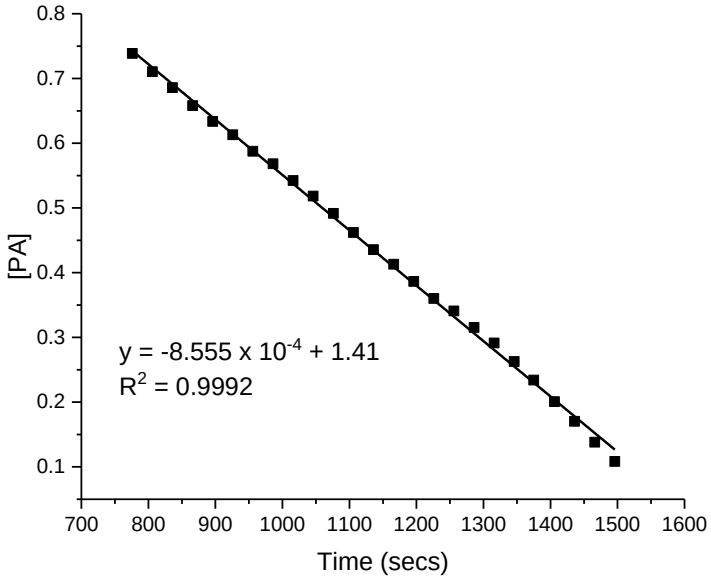


Figure D.34 – Plot of [PA] vs time for CHO/PA copolymerisation catalysed by ***[LZnMg(OBz^{NMe2})$_2$]****. The gradient of the graph represents k_{obs}, assuming a zero order dependence on PA, using data from 40-90 % conversion. Reaction conditions: 1:100:800 catalyst:PA:CHO and 100 °C.*

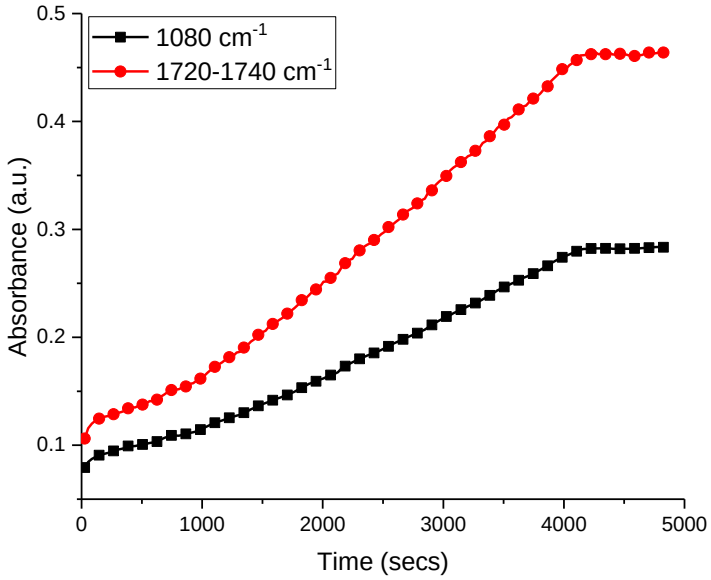


Figure D.35 – ATR-IR spectroscopy plot showing the change in absorbance vs. time plot for two vibrational modes during the CHO/PA copolymerisation catalysed by ***[LZnMg(OBz^F)$_2$]****. Reaction conditions: 1:100:800 catalyst:PA:CHO and 100 °C. For clarity, only every 4th data point is shown.*

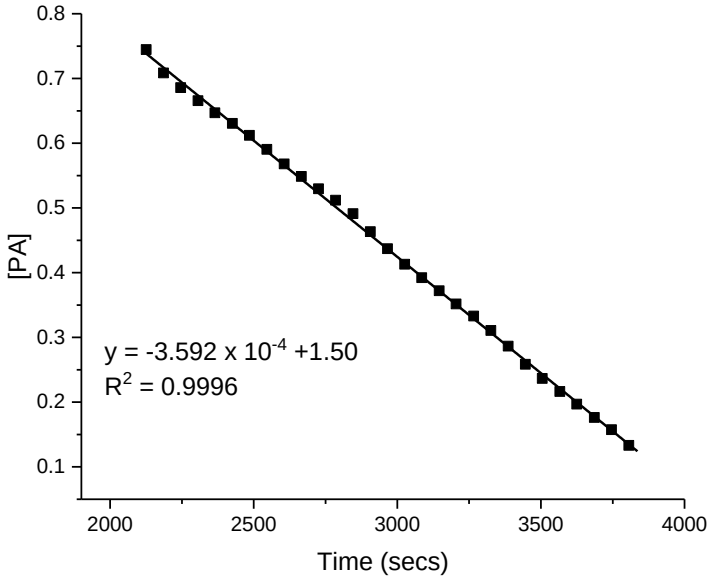


Figure D.36 – Plot of [PA] vs time for CHO/PA copolymerisation catalysed by ***[LZnMg(OBz^F)$_2$]****. The gradient of the graph represents k_{obs}, assuming a zero order dependence on PA, using data from 40-90 % conversion. Reaction conditions: 1:100:800 catalyst:PA:CHO and 100 °C.*

D.4 Data for Figure 5.2

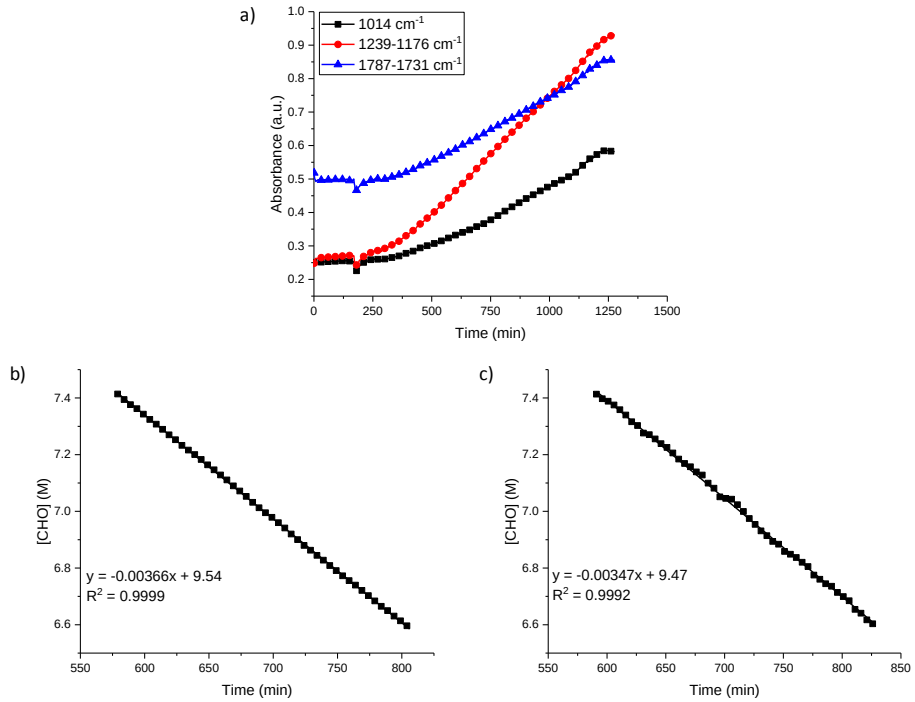


Figure D.37 – Reaction conditions: ***[LZnMgBr$_2$]*** *= 4.2 mM, [CHO]$_0$ = 8.24 M in DEC, at 80 °C and 1 bar pressure. a) ATR-IR spectroscopy raw data plot showing the change in absorbance vs. time plot for three vibrational modes during the CHO/CO$_2$ copolymerisation. For clarity, only every 30th data point is shown. b) and c) Plots showing the change in absorbance vs. time plot, from 10 to 20 % conversion, for the vibrational modes at 1239-1176 cm^{-1} (b) and 1787-1731 cm^{-1} (c). For clarity, only every 5th data point is shown. The gradient value = initial rate.*

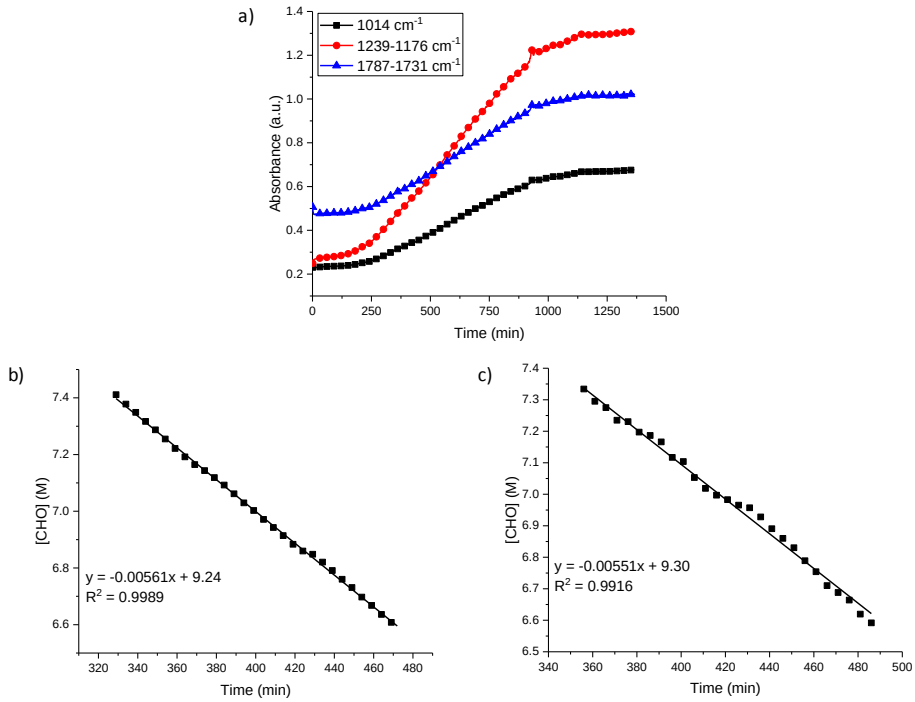


Figure D.38 – Reaction conditions: ***[LZnMgBr$_2$]*** *= 4.2 mM, [CHO]$_0$ = 8.24 M in DEC, at 80 °C and 1 bar pressure. a) ATR-IR spectroscopy raw data plot showing the change in absorbance vs. time plot for three vibrational modes during the CHO/CO$_2$ copolymerisation. For clarity, only every 30th data point is shown. b) and c) Plots showing the change in absorbance vs. time plot, from 10 to 20 % conversion, for the vibrational modes at 1239-1176 cm^{-1} (b) and 1787-1731 cm^{-1} (c). For clarity, only every 5th data point is shown. The gradient value = initial rate.*

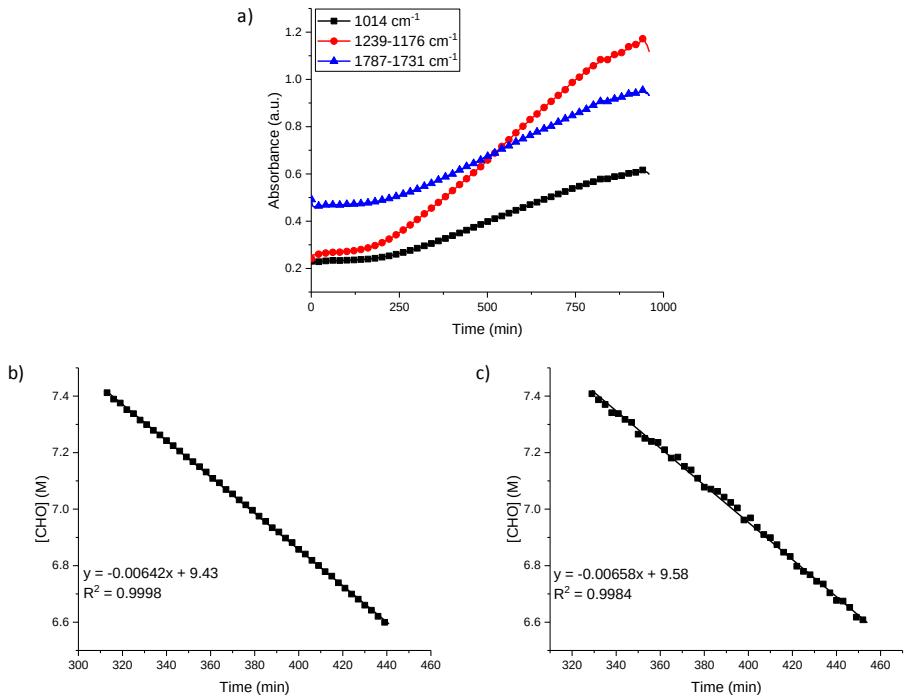


Figure D.39 – Reaction conditions: ***[LZnMgBr$_2$]*** *= 4.2 mM, [CHO]$_0$ = 8.24 M in DEC, at 80 °C and 1 bar pressure. a) ATR-IR spectroscopy raw data plot showing the change in absorbance vs. time plot for three vibrational modes during the CHO/CO$_2$ copolymerisation. For clarity, only every 20th data point is shown. b) and c) Plots showing the change in absorbance vs. time plot, from 10 to 20 % conversion, for the vibrational modes at 1239-1176 cm^{-1} (b) and 1787-1731 cm^{-1} (c). For clarity, only every 3rd data point is shown. The gradient value = initial rate.*

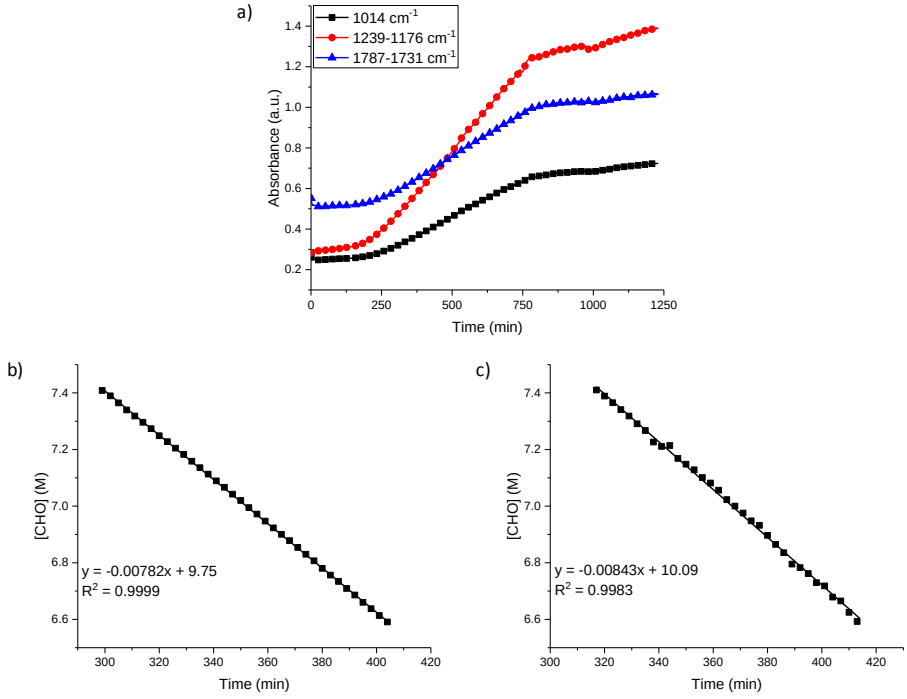


Figure D.40 – Reaction conditions: ***[LZnMgBr$_2$]*** *= 8.3 mM, [CHO]$_0$ = 8.24 M in DEC, at 80 °C and 1 bar pressure. a) ATR-IR spectroscopy raw data plot showing the change in absorbance vs. time plot for three vibrational modes during the CHO/CO$_2$ copolymerisation. For clarity, only every 25th data point is shown. b) and c) Plots showing the change in absorbance vs. time plot, from 10 to 20 % conversion, for the vibrational modes at 1239-1176 cm^{-1} (b) and 1787-1731 cm^{-1} (c). For clarity, only every 3rd data point is shown. The gradient value = initial rate.*

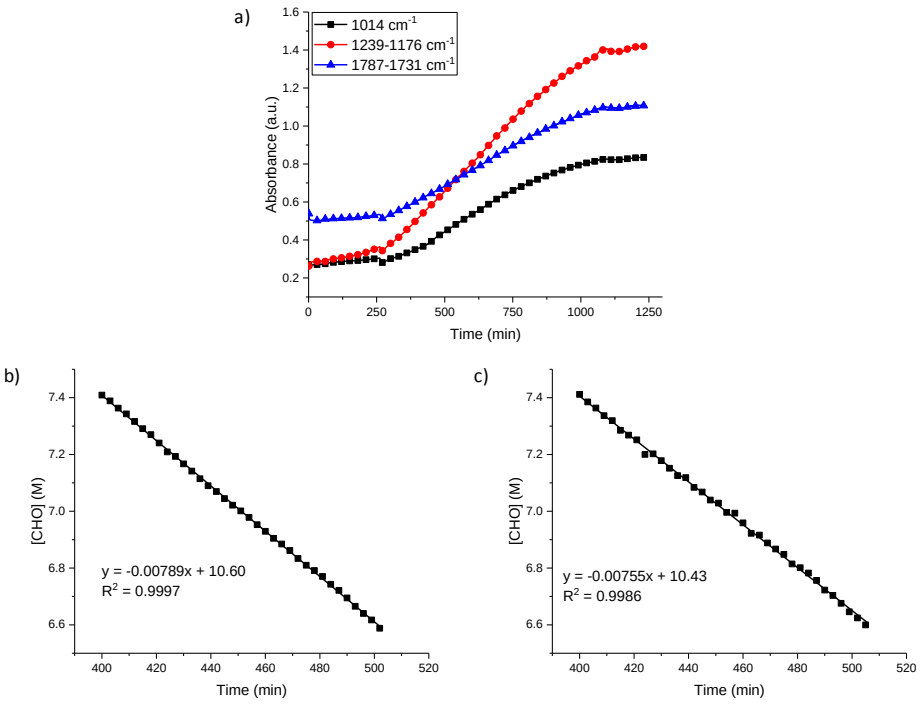


Figure D.41 – Reaction conditions: ***[LZnMgBr$_2$]*** *= 8.3 mM, [CHO]$_0$ = 8.24 M in DEC, at 80 °C and 1 bar pressure. a) ATR-IR spectroscopy raw data plot showing the change in absorbance vs. time plot for three vibrational modes during the CHO/CO$_2$ copolymerisation. For clarity, only every 30th data point is shown. b) and c) Plots showing the change in absorbance vs. time plot, from 10 to 20 % conversion, for the vibrational modes at 1239-1176 cm^{-1} (b) and 1787-1731 cm^{-1} (c). For clarity, only every 3rd data point is shown. The gradient value = initial rate.*

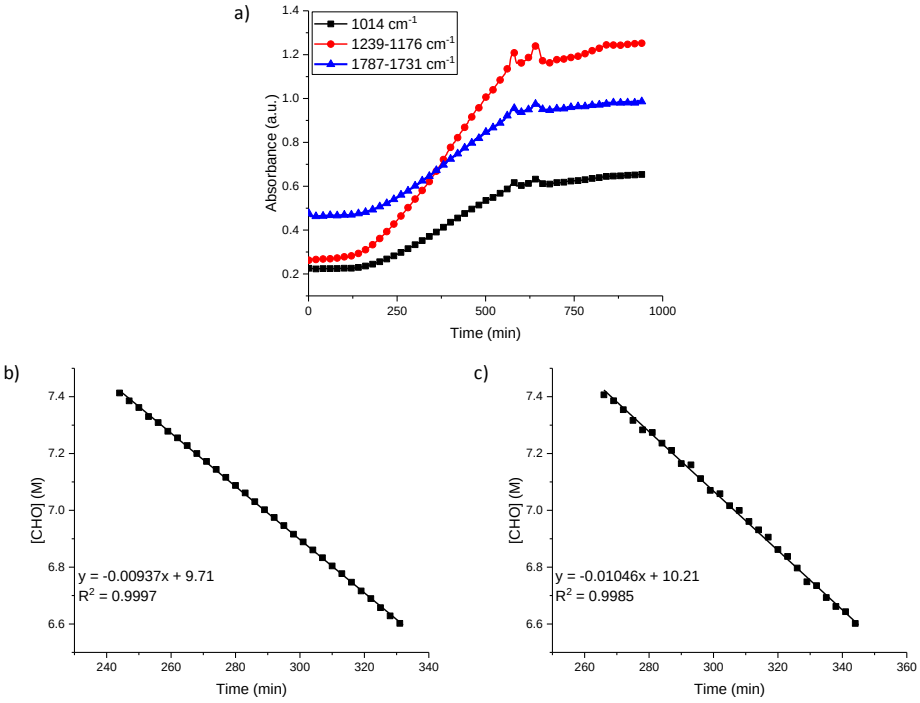


Figure D.42 – Reaction conditions: ***[LZnMgBr$_2$]*** *= 8.3 mM, [CHO]$_0$ = 8.24 M in DEC, at 80 °C and 1 bar pressure. a) ATR-IR spectroscopy raw data plot showing the change in absorbance vs. time plot for three vibrational modes during the CHO/CO$_2$ copolymerisation. For clarity, only every 20th data point is shown. b) and c) Plots showing the change in absorbance vs. time plot, from 10 to 20 % conversion, for the vibrational modes at 1239-1176 cm^{-1} (b) and 1787-1731 cm^{-1} (c). For clarity, only every 3rd data point is shown. The gradient value = initial rate.*

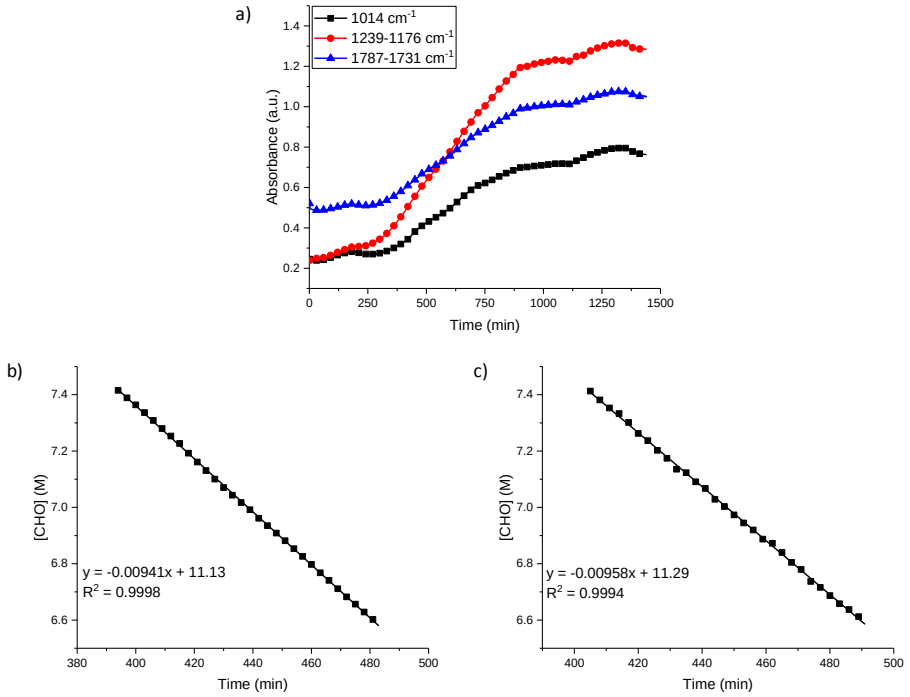


Figure D.43 – Reaction conditions: ***[LZnMgBr$_2$]*** *= 12.5 mM, [CHO]$_0$ = 8.24 M in DEC, at 80 °C and 1 bar pressure. a) ATR-IR spectroscopy raw data plot showing the change in absorbance vs. time plot for three vibrational modes during the CHO/CO$_2$ copolymerisation. For clarity, only every 30th data point is shown. b) and c) Plots showing the change in absorbance vs. time plot, from 10 to 20 % conversion, for the vibrational modes at 1239-1176 cm^{-1} (b) and 1787-1731 cm^{-1} (c). For clarity, only every 3rd data point is shown. The gradient value = initial rate.*

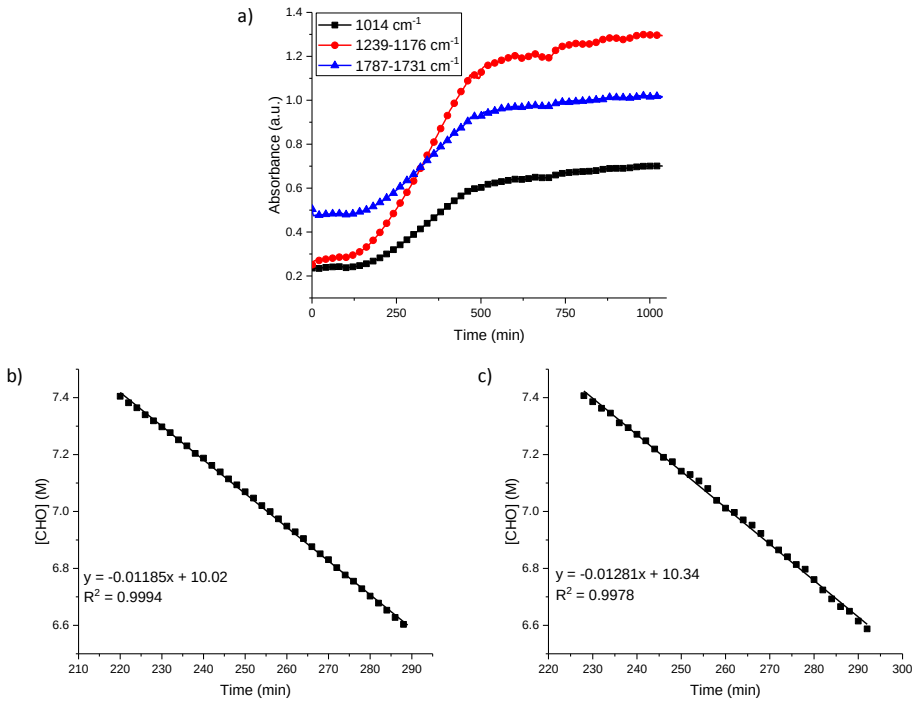


Figure D.44 – Reaction conditions: ***[LZnMgBr$_2$]*** *= 12.5 mM, [CHO]$_0$ = 8.24 M in DEC, at 80 °C and 1 bar pressure. a) ATR-IR spectroscopy raw data plot showing the change in absorbance vs. time plot for three vibrational modes during the CHO/CO$_2$ copolymerisation. For clarity, only every 20th data point is shown. b) and c) Plots showing the change in absorbance vs. time plot, from 10 to 20 % conversion, for the vibrational modes at 1239-1176 cm^{-1} (b) and 1787-1731 cm^{-1} (c). For clarity, only every 2nd data point is shown. The gradient value = initial rate.*

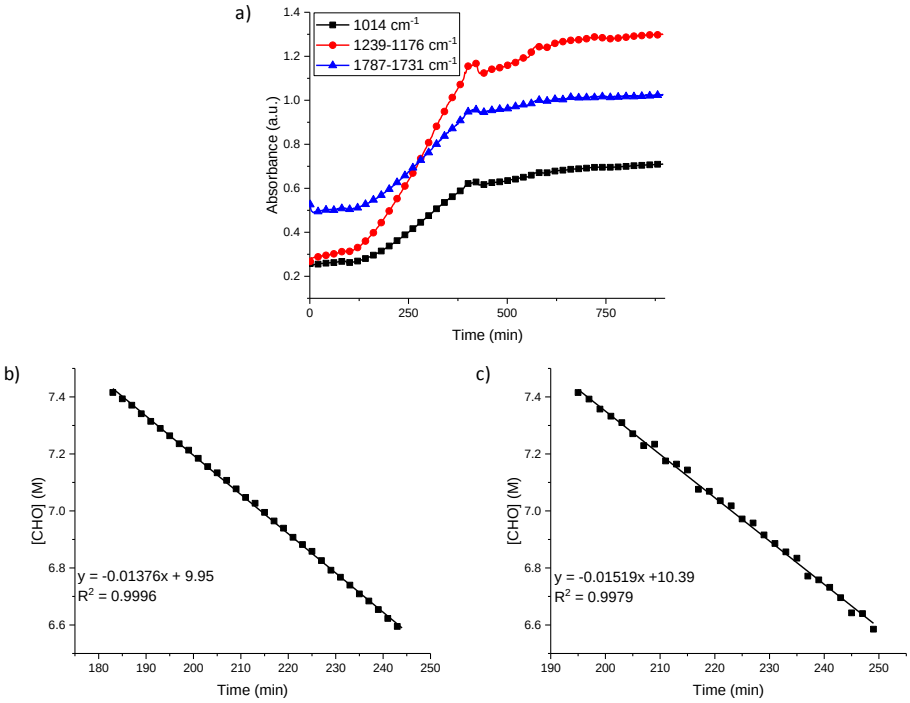


Figure D.45 – Reaction conditions: ***[LZnMgBr$_2$]*** *= 12.5 mM, [CHO]$_0$ = 8.24 M in DEC, at 80 °C and 1 bar pressure. a) ATR-IR spectroscopy raw data plot showing the change in absorbance vs. time plot for three vibrational modes during the CHO/CO$_2$ copolymerisation. For clarity, only every 20th data point is shown. b) and c) Plots showing the change in absorbance vs. time plot, from 10 to 20 % conversion, for the vibrational modes at 1239-1176 cm^{-1} (b) and 1787-1731 cm^{-1} (c). For clarity, only every 2nd data point is shown. The gradient value = initial rate.*

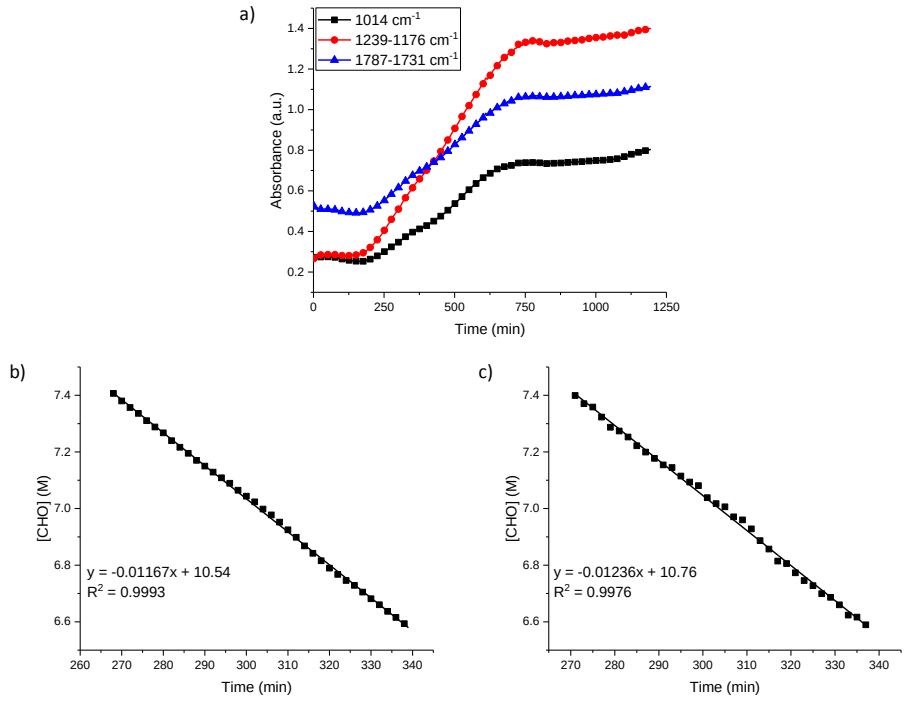


Figure D.46 – Reaction conditions: ***[LZnMgBr$_2$]*** *= 16.6 mM, [CHO]$_0$ = 8.24 M in DEC, at 80 °C and 1 bar pressure. a) ATR-IR spectroscopy raw data plot showing the change in absorbance vs. time plot for three vibrational modes during the CHO/CO$_2$ copolymerisation. For clarity, only every 25th data point is shown. b) and c) Plots showing the change in absorbance vs. time plot, from 10 to 20 % conversion, for the vibrational modes at 1239-1176 cm^{-1} (b) and 1787-1731 cm^{-1} (c). For clarity, only every 2nd data point is shown. The gradient value = initial rate.*

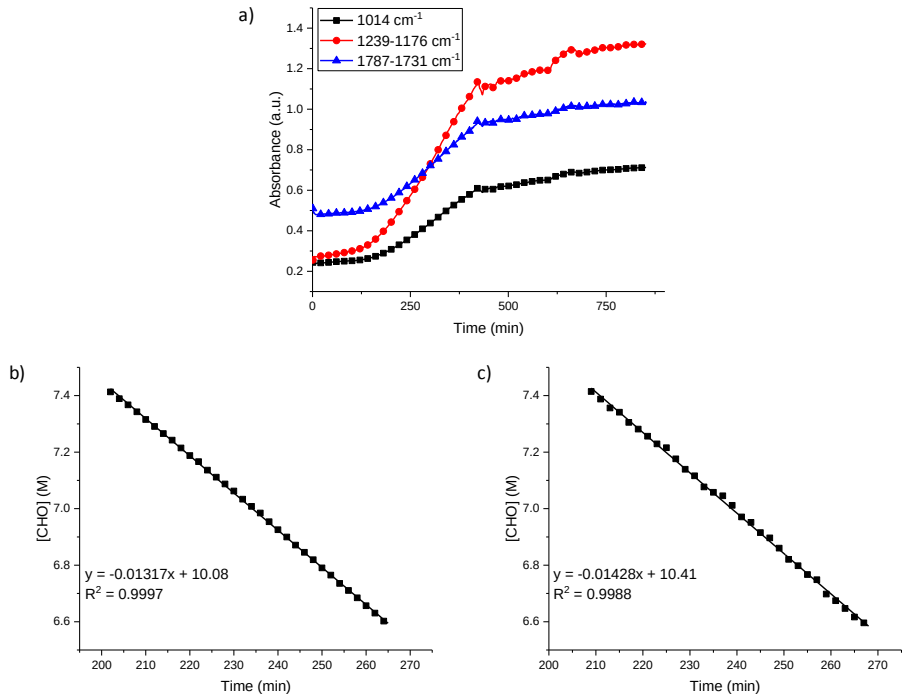


Figure D.47 – Reaction conditions: ***[LZnMgBr$_2$]*** *= 16.6 mM, [CHO]$_0$ = 8.24 M in DEC, at 80 °C and 1 bar pressure. a) ATR-IR spectroscopy raw data plot showing the change in absorbance vs. time plot for three vibrational modes during the CHO/CO$_2$ copolymerisation. For clarity, only every 20th data point is shown. b) and c) Plots showing the change in absorbance vs. time plot, from 10 to 20 % conversion, for the vibrational modes at 1239-1176 cm^{-1} (b) and 1787-1731 cm^{-1} (c). For clarity, only every 2nd data point is shown. The gradient value = initial rate.*

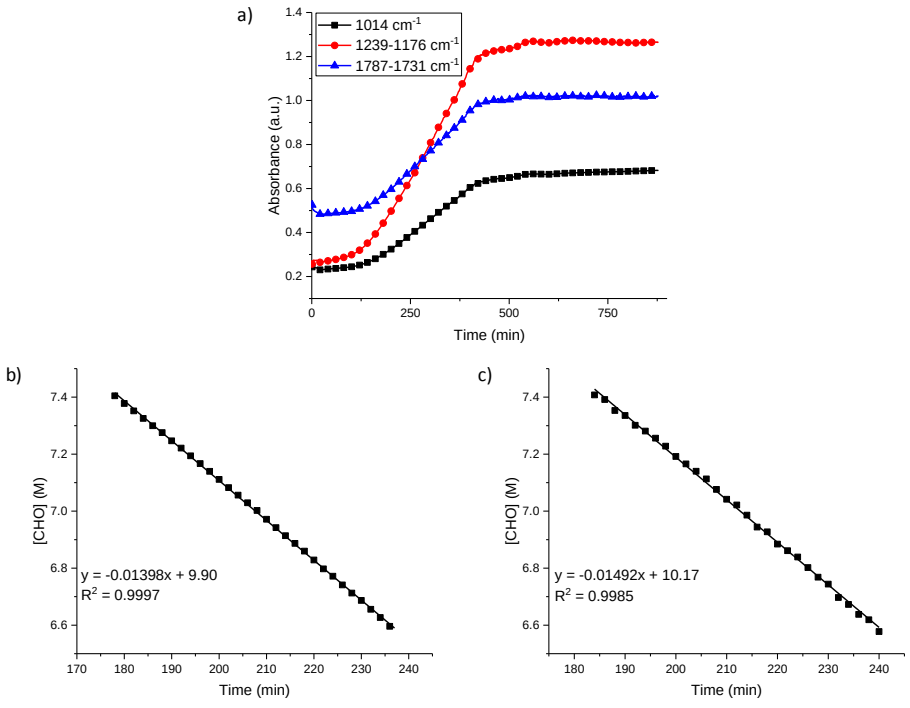


Figure D.48 – Reaction conditions: ***[LZnMgBr$_2$]*** *= 16.6 mM, [CHO]$_0$ = 8.24 M in DEC, at 80 °C and 1 bar pressure. a) ATR-IR spectroscopy raw data plot showing the change in absorbance vs. time plot for three vibrational modes during the CHO/CO$_2$ copolymerisation. For clarity, only every 20th data point is shown. b) and c) Plots showing the change in absorbance vs. time plot, from 10 to 20 % conversion, for the vibrational modes at 1239-1176 cm^{-1} (b) and 1787-1731 cm^{-1} (c). For clarity, only every 2nd data point is shown. The gradient value = initial rate.*

Table D.1 – Table of errors comparing the calculated initial rates for catalyst ***[LZnMgBr$_2$]***.

Concentration (mM)	Calculated Initial Rate (M·min^{-1})		Standard Deviation		Coefficient of Variation	
	1239 cm^{-1}	1787 cm^{-1}	1239 cm^{-1}	1787 cm^{-1}	1239 cm^{-1}	1787 cm^{-1}
4.2	0.00366	0.00347	0.00116	0.00129	0.22	0.25
	0.00561	0.00549				
	0.00642	0.00658				
8.3	0.00798	0.00755	0.00069	0.00121	0.08	0.14
	0.00782	0.00843				
	0.00936	0.01044				
12.5	0.00941	0.00958	0.00178	0.00243	0.15	0.19
	0.01375	0.01515				
	0.01185	0.01281				
16.6	0.01167	0.01236	0.00096	0.00109	0.07	0.08
	0.01398	0.01492				
	0.01317	0.01428				

D.5 Data for Figure 5.6

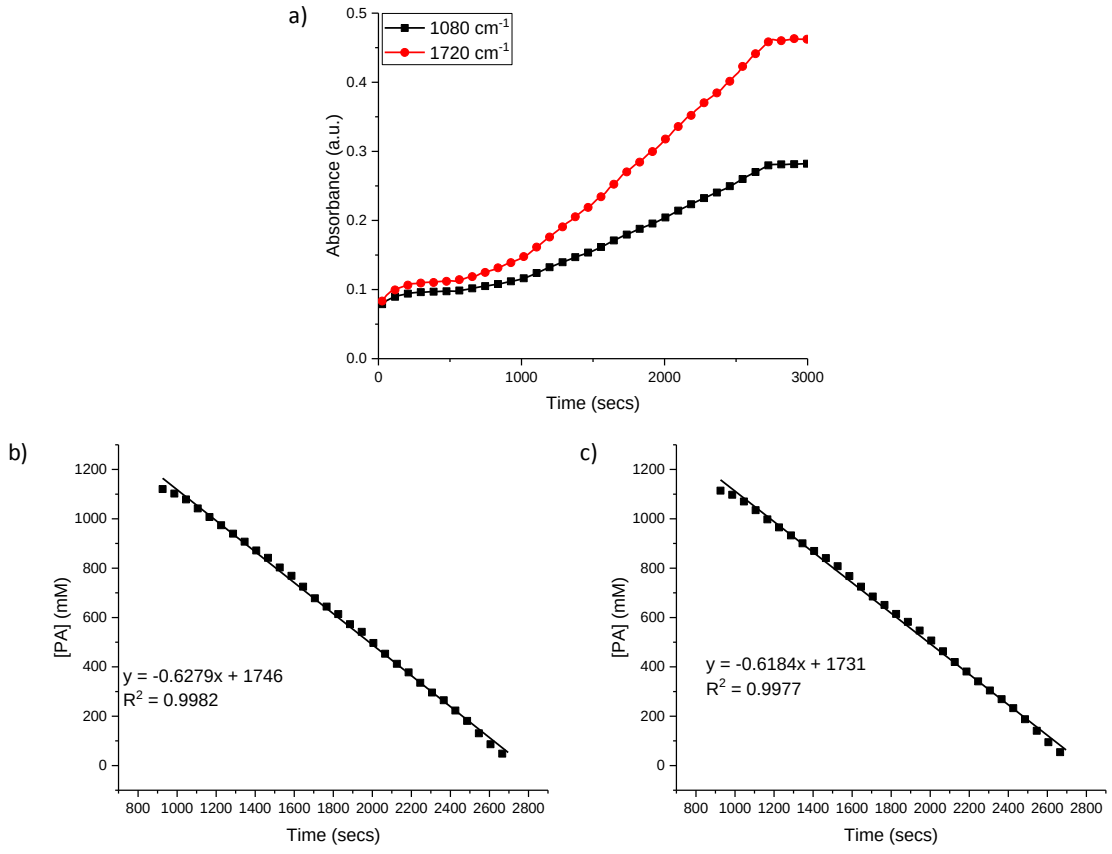


Figure D.49 – Reaction conditions: ***[LZnMgBr$_2$]*** *= 9.3 mM, [PA]$_0$ = 1.24 M in CHO, at 100 °C. a) ATR-IR spectroscopy raw data plot showing the change in absorbance vs. time plot for three vibrational modes during the CHO/PA copolymerisation. For clarity, only every 3rd data point is shown. b) and c) Plots showing the change in absorbance vs. time plot, from 10 to 99 % conversion, for the vibrational modes at 1720 cm^{-1} (b) and 1080 cm^{-1} (c). For clarity, only every 2nd data point is shown. The gradient value = initial rate.*

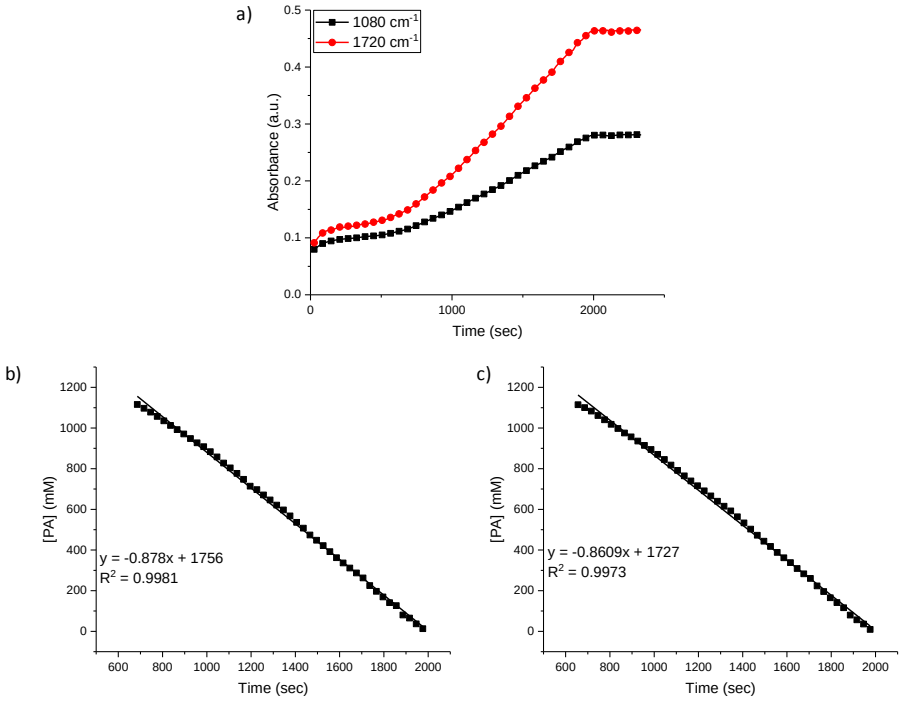


Figure D.50 – Reaction conditions: ***[LZnMgBr$_2$]*** *= 12.6 mM, [PA]$_0$ = 1.24 M in CHO, at 100 °C. a) ATR-IR spectroscopy raw data plot showing the change in absorbance vs. time plot for three vibrational modes during the CHO/PA copolymerisation. For clarity, only every 2nd data point is shown. b) and c) Plots showing the change in absorbance vs. time plot, from 10 to 99 % conversion, for the vibrational modes at 1720 cm^{-1} (b) and 1080 cm^{-1} (c). The gradient value = initial rate.*

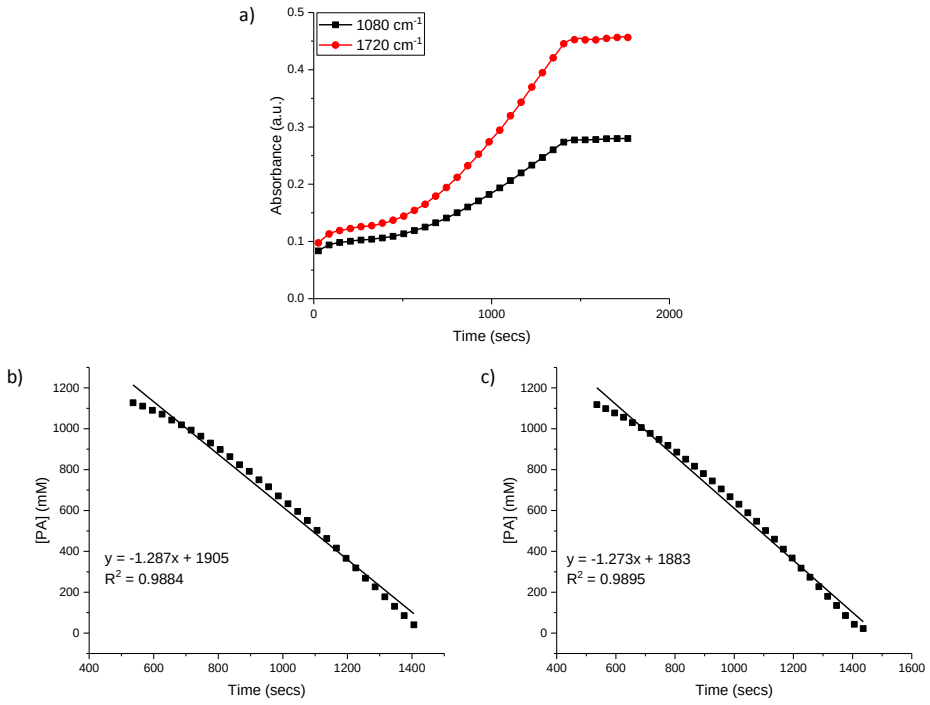


Figure D.51 – Reaction conditions: ***[LZnMgBr$_2$]*** *= 18.7 mM, [PA]$_0$ = 1.24 M in CHO, at 100 °C. a) ATR-IR spectroscopy raw data plot showing the change in absorbance vs. time plot for three vibrational modes during the CHO/PA copolymerisation. For clarity, only every 2nd data point is shown. b) and c) Plots showing the change in absorbance vs. time plot, from 10 to 99 % conversion, for the vibrational modes at 1720 cm^{-1} (b) and 1080 cm^{-1} (c). The gradient value = initial rate.*

D.6 Data for Figure 5.8

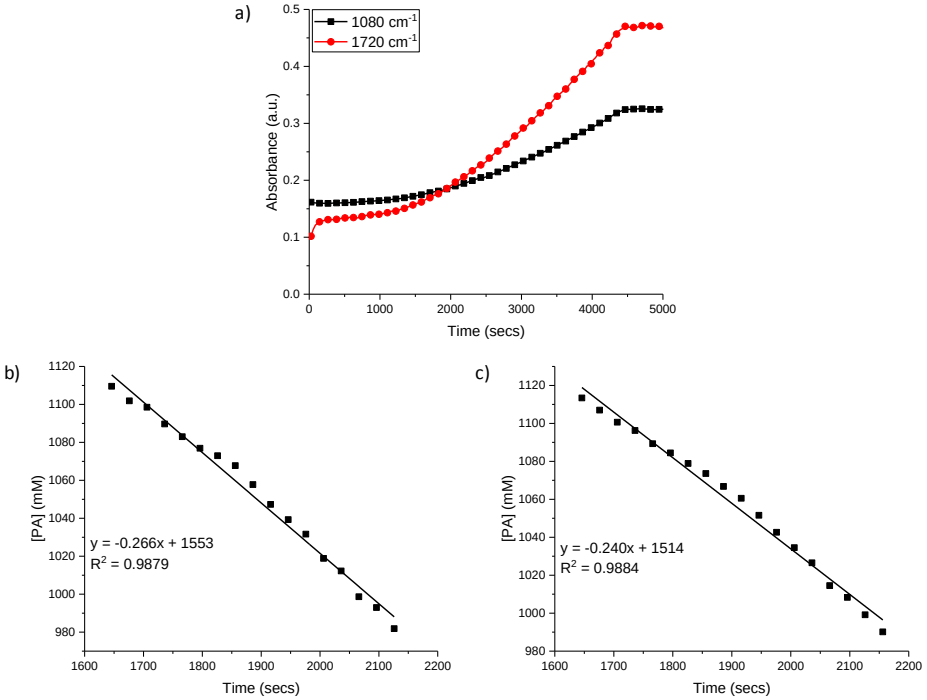


Figure D.52 – Reaction conditions: ***[LZnMgBr$_2$]*** *= 12.6 mM, [PA]$_0$ = 1.24 M, [CHO]$_0$ = 2.48 M in toluene, at 100 °C. a) ATR-IR spectroscopy raw data plot showing the change in absorbance vs. time plot for three vibrational modes during the CHO/PA copolymerisation. For clarity, only every 4th data point is shown. b) and c) Plots showing the change in absorbance vs. time plot, from 10 to 20 % conversion, for the vibrational modes at 1720 cm^{-1} (b) and 1080 cm^{-1} (c). The gradient value = initial rate.*

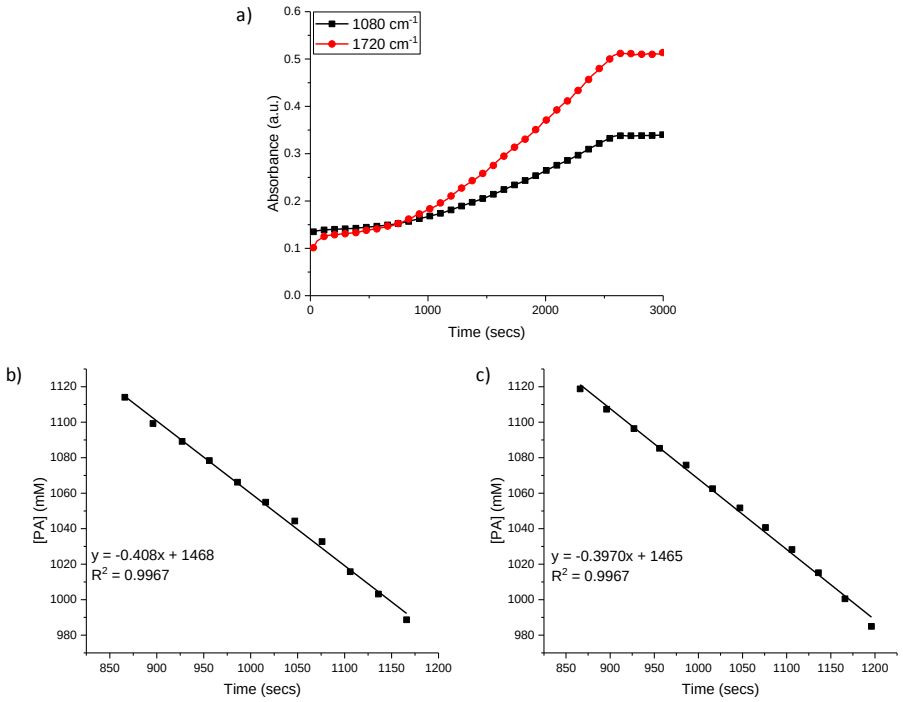


Figure D.53 – Reaction conditions: ***[LZnMgBr$_2$]*** *= 12.6 mM, [PA]$_0$ = 1.24 M, [CHO]$_0$ = 4.97 M in toluene, at 100 °C. a) ATR-IR spectroscopy raw data plot showing the change in absorbance vs. time plot for three vibrational modes during the CHO/PA copolymerisation. For clarity, only every 3rd data point is shown. b) and c) Plots showing the change in absorbance vs. time plot, from 10 to 20 % conversion, for the vibrational modes at 1720 cm^{-1} (b) and 1080 cm^{-1} (c). The gradient value = initial rate.*

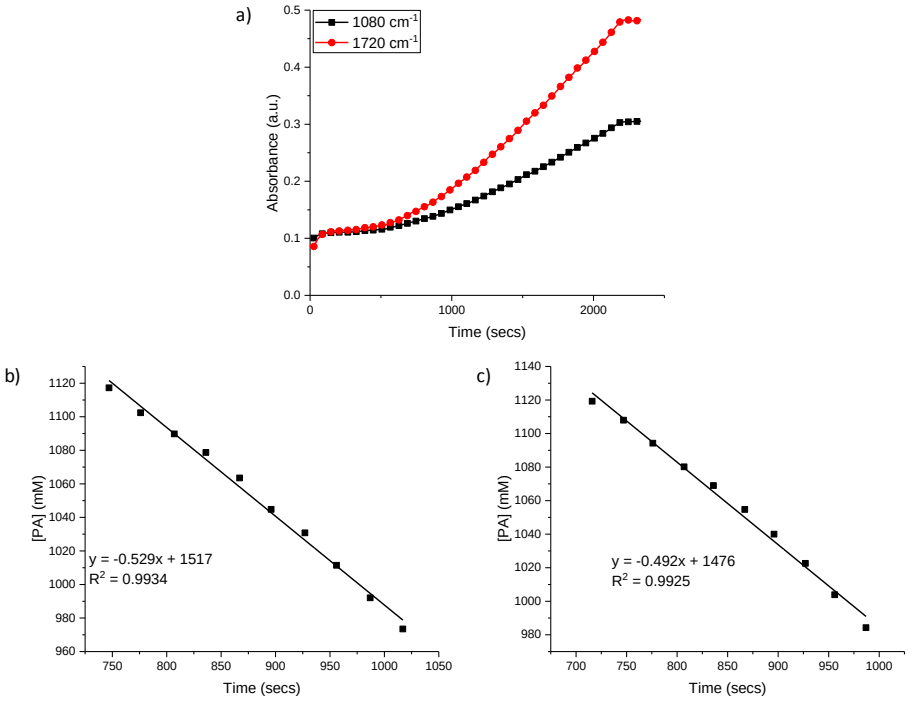


Figure D.54 – Reaction conditions: ***[LZnMgBr$_2$]*** *= 12.6 mM, [PA]$_0$ = 1.24 M, [CHO]$_0$ = 7.45 M in toluene, at 100 °C. a) ATR-IR spectroscopy raw data plot showing the change in absorbance vs. time plot for three vibrational modes during the CHO/PA copolymerisation. For clarity, only every 2nd data point is shown. b) and c) Plots showing the change in absorbance vs. time plot, from 10 to 20 % conversion, for the vibrational modes at 1720 cm^{-1} (b) and 1080 cm^{-1} (c). The gradient value = initial rate.*

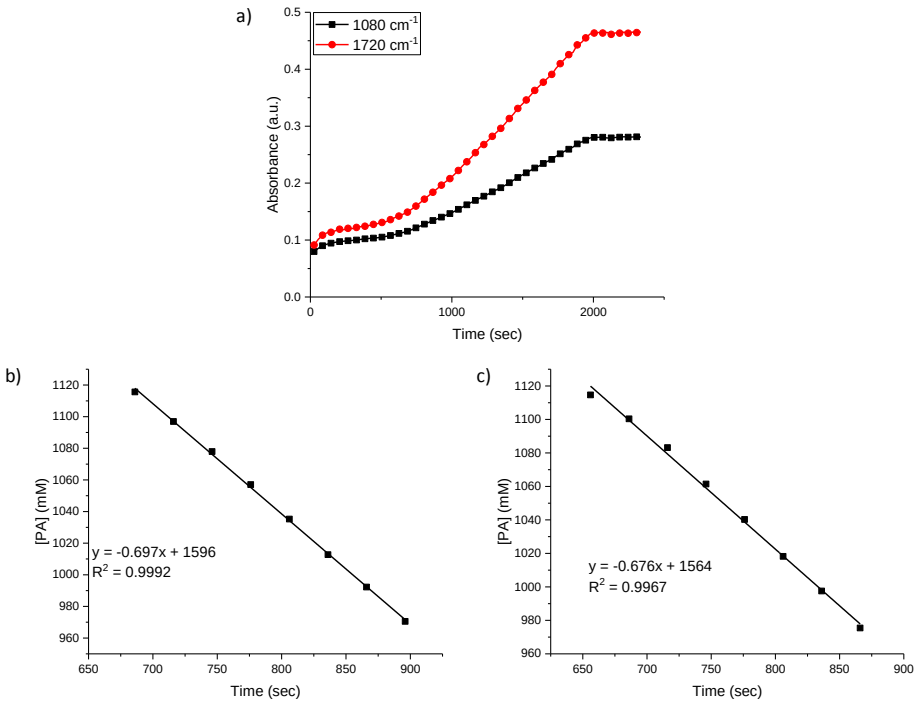


Figure D.55 – Reaction conditions: ***[LZnMgBr$_2$]*** *= 12.6 mM, [PA]$_0$ = 1.24 M, [CHO]$_0$ = 9.93 M in toluene, at 100 °C. a) ATR-IR spectroscopy raw data plot showing the change in absorbance vs. time plot for three vibrational modes during the CHO/PA copolymerisation. For clarity, only every 2nd data point is shown. b) and c) Plots showing the change in absorbance vs. time plot, from 10 to 20 % conversion, for the vibrational modes at 1720 cm^{-1} (b) and 1080 cm^{-1} (c). The gradient value = initial rate.*

Appendix E: Concentration vs Time Plots for Table 4.10

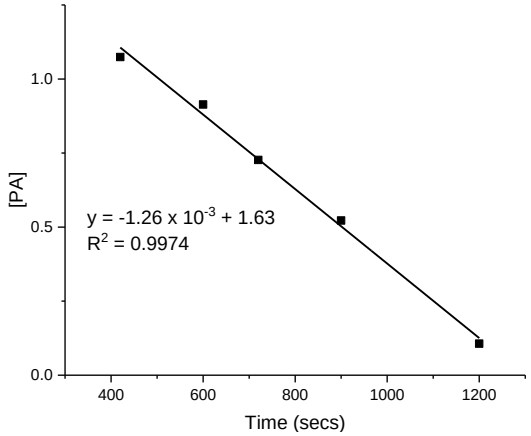


Figure E.1 – Plot of [PA] against time for a series of aliquots for catalyst ***[LZnMgBr$_2$]*** *with CHO/PA at 100 °C with a catalyst:PA:CHO molar ratio of 1:100:800.*

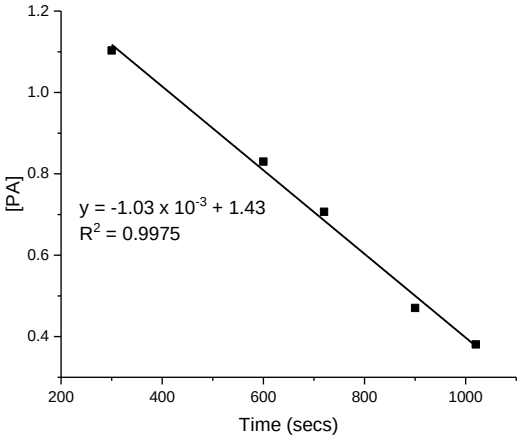


Figure E.2 – Plot of [PA] against time for a series of aliquots for catalyst ***[LZnMg(OBz)$_2$]*** *with CHO/PA at 100 °C with a catalyst:PA:CHO molar ratio of 1:100:800.*

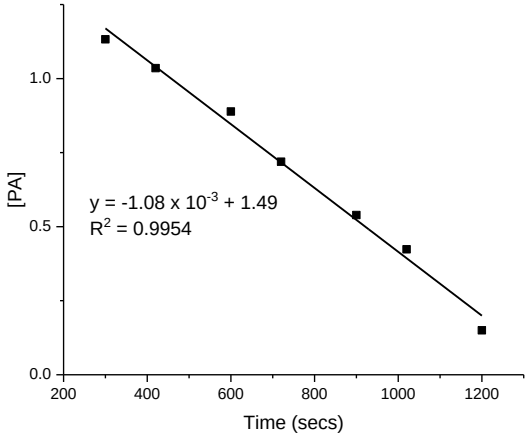


Figure E.3 – Plot of [PA] against time for a series of aliquots for catalyst ***[LZnMg(OBz^{OMe})$_2$]*** *with CHO/PA at 100 °C with a catalyst:PA:CHO molar ratio of 1:100:800.*

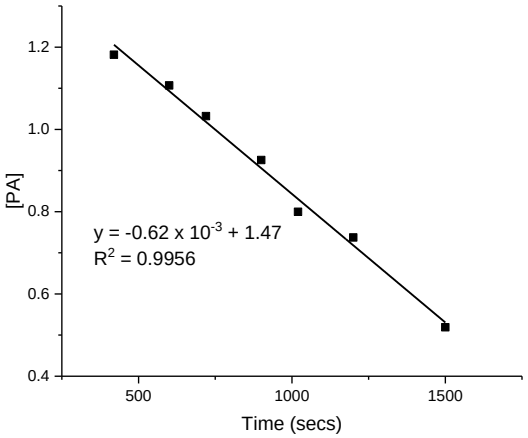


Figure E.4 – Plot of [PA] against time for a series of aliquots for catalyst ***[LZnMg(OBz^{CF3})$_2$]*** *with CHO/PA at 100 °C with a catalyst:PA:CHO molar ratio of 1:100:800.*

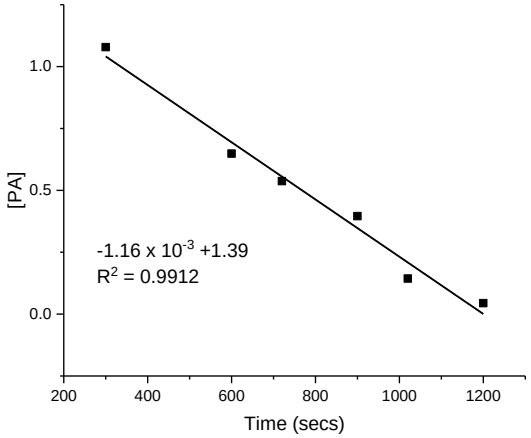


Figure E.5 – Plot of [PA] against time for a series of aliquots for catalyst ***[LZnMg(OBz^{NO2})$_2$]*** *with CHO/PA at 100 °C with a catalyst:PA:CHO molar ratio of 1:100:800.*

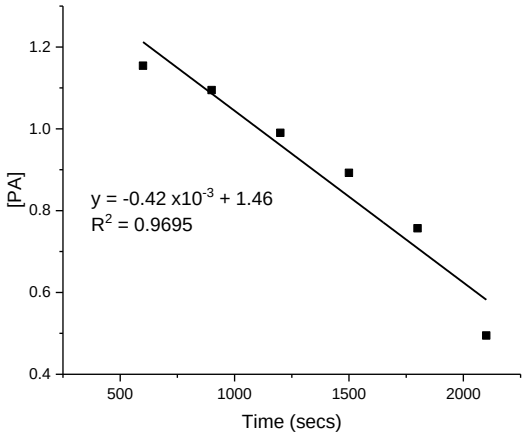


Figure E.6 – Plot of [PA] against time for a series of aliquots for catalyst ***[LZnMg(OBz^{F5})$_2$]*** *with CHO/PA at 100 °C with a catalyst:PA:CHO molar ratio of 1:100:800.*

Appendix F: IRC Plot

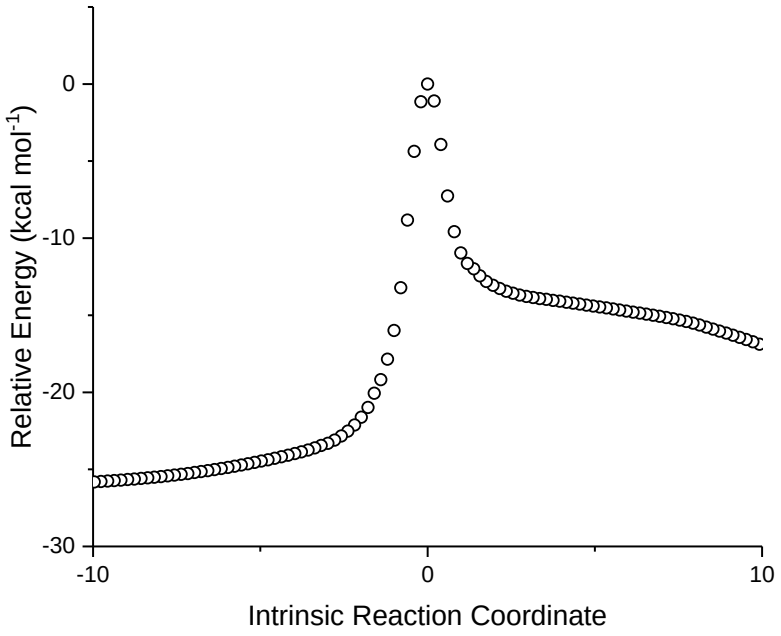


Figure F.1 – Plot of Intrinsic Reaction Coordinate against relative energy for the reaction pathway of ***3TS*** *(**[LMg$_2$(OAc)$_2$]**).*

Appendix References

(1) Garden, J. A.; Saini, P. K.; Williams, C. K. *J. Am. Chem. Soc.* **2015**, *137*, 15078.